



RIJKSUNIVERSITEIT GRONINGEN

**Host galaxies and environments of  
compact extragalactic radio sources**

PROEFSCHRIFT

ter verkrijging van het doctoraat in de  
Wiskunde en Natuurwetenschappen  
aan de Rijksuniversiteit Groningen  
op gezag van de  
Rector Magnificus, dr. F. Zwarts,  
in het openbaar te verdedigen op  
vrijdag 24 februari 2006  
om 10:30 uur

door

**Álvaro Labiano Ortega**

geboren op 14 januari 1977  
te Madrid, Spanje

Promotor: Prof. Dr. P. D. Barthel  
Co-promotores: Dr. C. P. O'Dea  
Dr. R. C. Vermeulen

Beoordelingscommissie: Prof. Dr. A. G. de Bruyn  
Prof. Dr. J. M. van der Hulst  
Prof. Dr. R. F. Peletier

**ISBN-nummer:**

*To my parents*

*Cover Image: Artistic representation of the center of an AGN.*

*Credit: Sonoma State University, NASA E/PO, Aurore Simonnet. <http://epo.sonoma.edu>*

*Back-cover Image: God laughing at a general physics book.*

*Credit: © Joaquín Salvador Lavado (QUINO), *Humano se Nace*. Editorial Lumen, 1991.*

*Cover design: Abril González Aragón.*

# Contents

<b>1</b>	<b>Introduction</b>	<b>1</b>
1.1	What are the AGN? . . . . .	2
1.2	Radio galaxies . . . . .	5
1.3	What are the GPS and CSS sources? . . . . .	6
1.3.1	Recurrent or smothered sources . . . . .	7
1.3.2	Transient sources . . . . .	7
1.3.3	Frustrated scenario . . . . .	7
1.3.4	Young scenario . . . . .	7
1.4	Current model of the GPS and CSS sources . . . . .	8
1.5	The spectral shape. Synchrotron self-absorption . . . . .	9
1.6	GPS quasars . . . . .	10
1.7	Thesis project . . . . .	13
1.8	Thesis outline . . . . .	14
<b>2</b>	<b>Compact and extended radio sources in the southern sky</b>	<b>15</b>
2.1	Introduction . . . . .	16
2.2	The Molonglo Southern 4 Jy Sample . . . . .	16
2.3	VLA observations of MS4 compact sources . . . . .	17
2.4	Data reduction and mapping . . . . .	17
2.5	Notes on individual sources . . . . .	17
2.6	Results . . . . .	21
2.7	Summary . . . . .	22
<b>3</b>	<b>Optical imaging and spectroscopy of candidate GPS radio sources</b>	<b>33</b>
3.1	Introduction . . . . .	34
3.2	Observations and data reduction . . . . .	34
3.3	Results . . . . .	35
3.3.1	Identifications . . . . .	35
3.3.2	Magnitudes . . . . .	35
3.3.3	Spectra and redshifts . . . . .	36
3.3.4	Stellar synthesis models . . . . .	36
3.4	Notes on individual sources . . . . .	38
3.5	Summary . . . . .	43

<b>4</b>	<b>HST/STIS low dispersion spectroscopy of three CSS sources: Evidence for jet-cloud interaction</b>	<b>53</b>
4.1	Introduction . . . . .	54
4.2	Observations . . . . .	55
4.3	Data reduction . . . . .	55
4.4	Results . . . . .	60
4.4.1	Ionization diagnostics . . . . .	60
4.4.2	Can the central AGN power the emission line luminosity in the extended nebulae? . . . . .	61
4.4.3	Diagnostic ratios vs. kinematics and distance . . . . .	64
4.4.4	Cloud properties . . . . .	68
4.5	Summary . . . . .	68
<b>5</b>	<b>H I absorption in 3C 49 and 3C 268.3</b>	<b>71</b>
5.1	Introduction . . . . .	72
5.2	Observations and data reduction . . . . .	73
5.2.1	Spectrum analysis . . . . .	73
5.3	Results . . . . .	75
5.3.1	The Milliarcsecond Scale Continuum Structure . . . . .	76
5.3.2	The H I Absorption . . . . .	79
5.4	Discussion . . . . .	80
5.5	Summary . . . . .	81
<b>6</b>	<b>H I in the one-sided “compact double” radio galaxy B2050+364</b>	<b>83</b>
6.1	Introduction . . . . .	84
6.2	Observations and data processing . . . . .	85
6.2.1	Observations . . . . .	85
6.2.2	Initial calibration and data averaging . . . . .	86
6.2.3	Self-calibration; continuum imaging and modeling . . . . .	87
6.2.4	Spatially resolved spectroscopy . . . . .	88
6.3	Results . . . . .	91
6.3.1	VLBI continuum structure of B2050+364 at 1 GHz . . . . .	91
6.3.2	H I absorption distribution . . . . .	92
6.4	Multi-frequency Radio Continuum Structure . . . . .	93
6.5	Discussion . . . . .	95
6.5.1	B2050+364: a one-sided core-jet structure ? . . . . .	95
6.5.2	The optical redshifts and H I: infall or outflow ? . . . . .	97
6.5.3	The locations of the H I absorbers relative to the radio source . . . . .	98
6.6	Summary . . . . .	100
<b>7</b>	<b>Star formation in hosts of compact radio galaxies</b>	<b>103</b>
7.1	Introduction . . . . .	104
7.2	Observations and data reduction . . . . .	104
7.3	Nuclear and emission line contamination . . . . .	106
7.4	UV morphology . . . . .	107
7.4.1	Notes on individual sources . . . . .	107

---

7.5	UV and radio properties . . . . .	110
7.6	Stellar synthesis models . . . . .	112
7.7	Summary . . . . .	113
<b>8</b>	<b>Concluding remarks</b>	<b>129</b>
8.1	Developments in the field . . . . .	129
8.2	Detailed contributions by this thesis . . . . .	133
8.3	The bottom line: Strong interaction between radio source and host . . . . .	134
8.4	Ongoing and future work . . . . .	135
	<b>Nederlandse samenvatting</b>	<b>139</b>
	<b>English Summary</b>	<b>141</b>
	<b>Bibliography</b>	<b>153</b>
	<b>List of Publications</b>	<b>155</b>
	<b>Acknowledgements</b>	<b>157</b>



*Though this be madness,  
yet there is method in 't.*

William Shakespeare  
Hamlet, II, 2.

# 1

## Introduction

IN 1908, Edward Arthur Fath took an optical spectrum of a galaxy, NGC 1068, and found that the "spectrum is composite, showing both bright and absorption lines" (Fath 1909). In 1917, higher resolution spectra showed that these emission lines were similar to those observed in planetary nebulae (Slipher 1917). During the next decades, astronomers observed nuclear emission lines in several *spiral nebula* (see Fig 1.1). Thirty five years after Fath's observations, Carl Keenan Seyfert realized that several of these galaxies formed a different group (Seyfert 1943). They had very broad emission lines (up to  $8500 \text{ km s}^{-1}$ ) and the Hydrogen lines sometimes were broader than the other lines: the *Seyfert galaxies*. Although these discoveries still did not launch the study of active galaxies, astronomers were about to find that there was a whole hidden Universe waiting for them at long wavelengths.

In 1932, Karl Guthe Jansky, working for Bell Labs on transatlantic radio communications, discovered a "faint, steady hiss of unknown origin" (Jansky 1932). He found that this *static* was coming from our own galaxy and was stronger towards the constellation of Sagittarius, towards the center of the Milky Way. Radio astronomy was born.

Radio astronomy had a slow beginning, partly because of World War II, as most of the efforts in science and technology were put into military development. The good part is that once the war was over, some of these technologies were inherited by science<sup>1</sup>. The first discoveries were performed by engineers that (most of them) had turned into astronomers after World War II. New phenomena started to show up and, during the 1950s, it all finally started: pulsars, the cosmic microwave background, the 21 cm Hydrogen line and last but not least, quasars and active galactic nuclei, AGN.

It took some twenty to thirty years for astronomers to combine radio astronomy and active galaxies and realize what they had just discovered (even accidentally) but those

---

<sup>1</sup>A curious anecdote: Some of the first radio telescopes in England and The Netherlands built right after the war used German-made radar dishes.

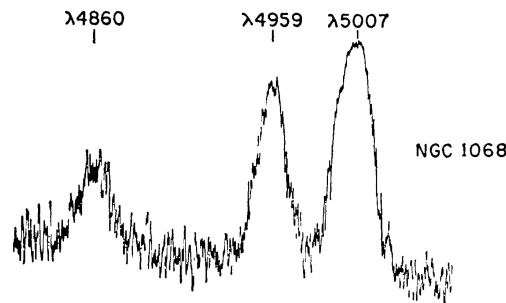


**Figure 1.1**— Spectrum of NGC 1068, from Seyfert (1943).

pioneers opened the doors for what has become one of the most fascinating and studied subjects in modern astronomy (see Shields 1999, for a review on history of AGN).

## 1.1 What are the AGN?

An active galactic nucleus is an object in the center of a galaxy whose spectrum cannot be explained just by starlight. The light emitted by the nucleus equals (Seyfert galaxy) or even exceeds (quasi stellar object, QSO) the total emission of the rest of the galaxy. This led to the idea that these QSOs were "stars with peculiar properties" (Matthews et al. 1961), as they looked like a star (they were point sources) but their spectra showed unusual properties for a star.

There are several types of AGN, classified according to their radio luminosity (radio loud or radio quiet) and spectral characteristics (Types 0, 1 or 2). The division in radio loud or radio quiet corresponds to objects *bright* or *faint* in radio compared to their own optical emission (Kellermann et al. 1989). Type 1 AGN are those with bright continuum and broad emission lines, Type 2 AGN have weak continuum and only narrow emission lines. The most active and variable AGN are sometimes classified as Type 0 but usually referred to by their names (BL Lacs, core dominated, etc, see Table 1.1).

Despite all these different types, there is light in the darkness. During the late 70s and 80s, astronomers realized that, in some cases, observations of AGN of a certain type resembled the properties of AGN of a different type. For instance, Antonucci & Miller (1985) found a hidden broad line region (BLR) in a Seyfert 2 galaxy; the polarised spectrum resembled that from a Seyfert 1. The absence of a BLR in Type 2 AGN could be explained if the central region of the AGN was "hidden" behind a screen (the torus) surrounding the nucleus. The properties of blazars (Type 0, radio loud AGN) could be easily explained if these AGN were Type 1 or Type 2 but observed along the radio axis. As the years passed, more types of AGN appeared to be related. In the early 90s, these *unification models* were so evolved that it seemed that there were only two really different classes of AGN, the radio loud and radio quiet, while the rest could be explained as being the same phenomenon, observed with different orientations.

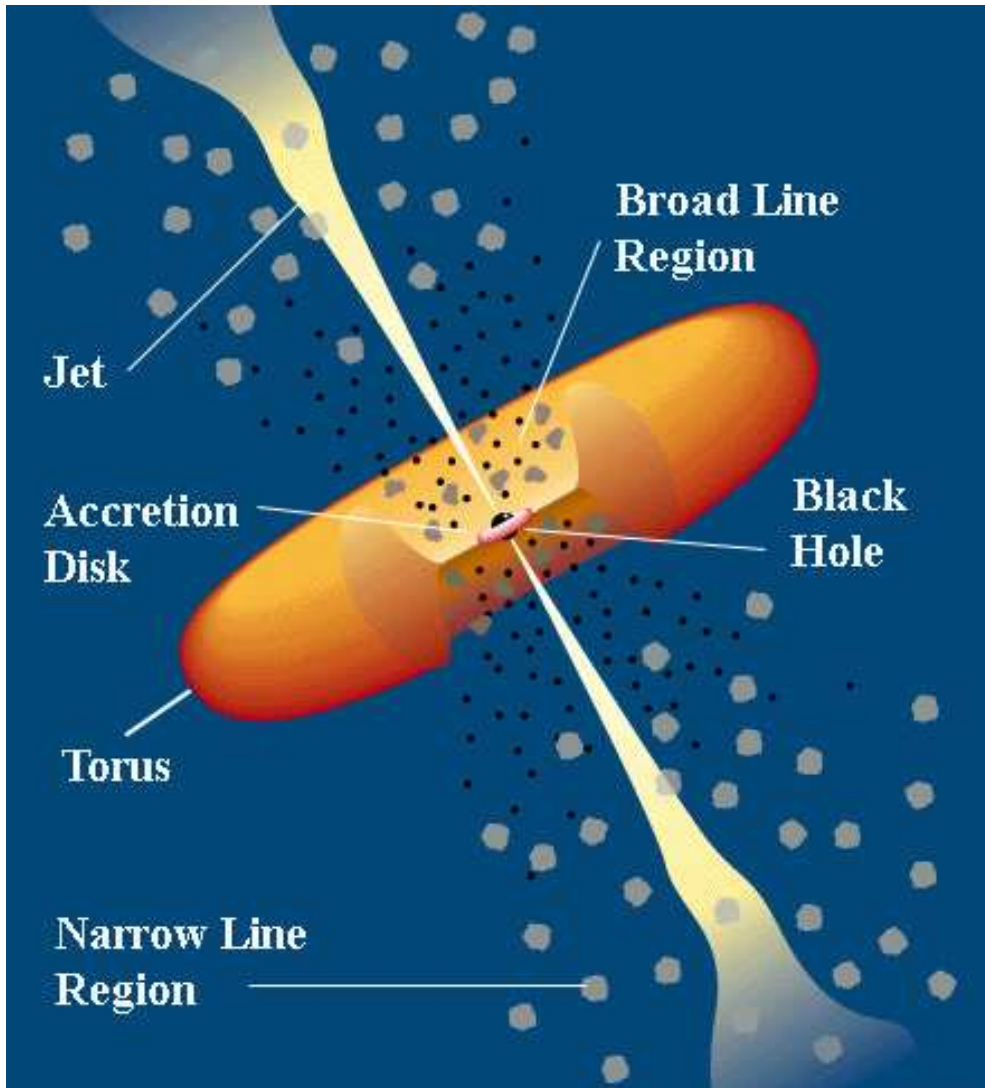


**Figure 1.2**— Artistic view of an AGN, from Urry & Padovani (1995). © PASP, reprinted with permission of the author.

	Type 2	Type 1	Type 0
Radio quiet	LINER		
	Seyfert 2	Seyfert 1	
		Radio quiet quasars	
Radio loud	NLRG FR I	BLRG	BL Lacs/Blazars
	NLRG FR II	Lobe dominated quasars	Core dominated quasars

**Table 1.1–. Classification of AGN.** This classification is orientative and objects show overlap. The line of sight decreases to the right of the table. Luminosity increases from top to bottom. Based on Urry & Padovani (1995) and Krolik (1999).

The Unification model is currently the most accepted model to explain the different AGN. It says that Type 0, 1 and 2 AGN, with the same radio loudness, might be the same phenomenon, but seen with different orientations (i.e. Barthel 1989; Antonucci 1993; Urry & Padovani 1995). Table 1.1 shows schematically how the type of AGN depends on the orientation towards the observer. Astronomers are also trying to understand what produces the difference between radio loud and radio quiet AGN and attempting to unify them according to their radio loudness. A very interesting model explains the difference in loudness with the spin of the central black hole, where fast spinning (Rees et al. 1982; Wilson & Colbert 1995; Meier 2002) central black holes would produce radio loud AGN while slow spinning central black holes would produce a radio quiet AGN. However, X-ray observations (Elvis et al. 2002) suggest that the majority of super-massive black holes rotate rapidly. Furthermore, the evolution of massive black holes in galactic nuclei is still not well understood and the difference between loud and quiet AGN is more complicated. Other phenomena must be taken into account, such as the size of the accretion disk, mass-to-energy conversion efficiency of the AGN, merging rates, size and angular momentum of the black hole (e.g Peterson 1997; Véron-Cetty & Véron 2000; Yu & Tremaine 2002).

The physics are still not completely understood, but the current, most accepted model for the AGN consists of a super-massive black hole in the center, surrounded by a small ( $< 1$  pc) accretion disk, which is responsible for the huge amount of radiation we observe, (e.g., Rees 1984; Magorrian et al. 1998). The accretion disk widens in the outer regions, forming a torus (at 1 to a few tens of parsecs) that surrounds the whole AGN (see Figure 1.2). As the matter falls into the central hole, some of it will escape from the disk forming jets (which can extend for megaparsecs in the largest radio sources). The inner clouds (roughly the central 1 parsec) of the host galaxy form the broad line region (BLR) as the gas rotates faster closer to the black hole and the Doppler effect widens the emission lines of these clouds, and the outer clouds form the narrow line region (NLR), which can extend for a few kpc.

Although the basics of the model are probably correct, recent observations (e.g., Konradt et al. 2005) suggest that some modifications must be made. The accretion mechanism could be more complicated than just a simple thin disk (e.g., Frank et al. 2002), the torus scenario is slowly being substituted by matter dragged by outflowing winds and creating the

obscuring region. This winds could also affect the emission mechanisms of the inner regions (e.g., Elvis 2000). The Unification model still has flaws beyond these *corrections*. While it explains most of the observed AGN, there are exceptions. Some of these exceptions can be explained as *special cases* where the source lacks a BLR, a special distribution of dust, etc. However, the Unification model does not consider factors that should be important in the life of AGN and their host galaxy, such as age, evolution and interaction with other objects.

## 1.2 Radio galaxies

Very simply put, a radio galaxy is a radio loud AGN where the optical nucleus is, at least, partially obscured. They are usually associated with elliptical galaxies and usually have radio jets that can extend for kiloparsecs or even megaparsecs. Their radio emission is thought to be mostly due to the synchrotron emission of relativistic electrons.

In 1974, Fanaroff and Riley classified morphologically the 3CR sources that were known to have two or more radio components (Fanaroff & Riley 1974). They measured the distance between the two brightest peaks and compared it with the total extent of the radio source. Those sources where the ratio was lower than 0.5 were classified as *class I*, those with ratio greater than 0.5 were classified as *class II*. Nowadays this classification is known as Fanaroff-Riley I and Fanaroff-Riley II, or shortly, FR I and FR II sources. FR II sources are also known as *classical doubles*.

Once a radio source is resolved, it can quickly be classified, in principle, as an FR I or FR II: FR I are usually weaker<sup>2</sup> and show more distorted structures than the FR II. In FR I sources, the radio luminosity dims as we move away from the nucleus and most of them show two jets emerging from the core and ending in diffuse lobes or extended emission. We see the opposite effect in FR II, usually having a faint or undetected core, with jets or lobes that increase in luminosity with distance, and end in hot spots at the edges of the radio structure.

In the last 30 years, more differences have been found between FR I and FR II sources. Their radio and optical line emission luminosity show different correlations. There are also differences in the relation between line luminosity and optical magnitude of the galaxy (FR I show a correlation while the FR II do not). FR II are generally brighter than FR I for similar core and/or total radio powers (more details on these and other wavelength differences can be found in e.g. Baum et al. 1995, and references therein). The properties of the jets or how they are affected by the host galaxy must also be different (e.g., Bridle 1984; O’Dea 2002). At low redshift, FR II seem to be found in poorer clustering environments than FR I, while at higher redshift ( $z \sim 0.5$ ), both classes are usually found in rich environments.

The literature contains many models and explanations trying to unify the Fanaroff-Riley sources, or explain the reason for their differences. I will just list a few here. In FR I galaxies the environments could be denser, slowing the jets to subsonic speeds while in FR II the

---

<sup>2</sup>The limit is set by an absolute luminosity of  $P_{1.4\text{GHz}} \sim 10^{25} \text{ W Hz}^{-1}$ . Later, it was found that FR II are also brighter in optical wavelengths (e.g., Ledlow & Owen 1996) and infrared (Heckman et al. 1994).

surrounding media would not be dense enough to slow the jets down and they would manage to keep their supersonic velocities (detailed models on jets and FR sources can be found in e.g. Laing & Bridle 2004; Bicknell 1995). In this scenario, the supersonic jets of the FR II would end up hitting the external medium surrounding the source (e.g., De Young 1993; Peterson 1997). Also the *fueling* of the source and powering of the emission line gas seem to be different in FR I and FR II. FR I would be fueled slowly from the ISM and ICM, maybe through a cooling flow, while in FR II the accretion would occur rapidly. The emission lines of FR I would be powered by processes associated with the host galaxy (such as a cooling flow or photoionization by stars) and FR II would be powering their emission line gas with photons from the AGN (e.g., Baum et al. 1995; O’Dea 2002).

There are radio galaxies that do not fall exactly on the FR I or FR II class and other classifications can be found in the literature (e.g., Owen & Laing 1989; Gopal-Krishna & Wiita 2002). However, the Fanaroff-Riley classification is probably the most common. Another frequently used classification (that overlaps with the Fanaroff-Riley) is based on the spectral properties: if the spectrum shows broad emission lines we will have a *Broad Line Radio Galaxy*, if it only displays narrow lines we will have a *Narrow Line Radio Galaxy*. In the literature, they are usually referred by their acronyms NLRG and BLRG.

### 1.3 What are the GPS and CSS sources?

The Fanaroff-Riley classification is independent of size. If we classify radio galaxies according to their size, we will find that there is a sub-class of objects that have subgalactic scales, although the rest of their properties are basically the same of those of larger size radio galaxies. These *small radio galaxies* are the Gigahertz peaked-spectrum (GPS) and compact steep spectrum (CSS) sources.

GPS and CSS sources are types of radio loud AGN that constitute a significant fraction of the extragalactic radio sources (10% and 30%, respectively, in high frequency radio surveys). They are characterized by their convex (*peaked*) radio spectra, powerful emission ( $P_{1.4\text{GHz}} \gtrsim 10^{25} \text{ W Hz}^{-1}$ ), low radio polarization and small size ( $\lesssim 1$  kpc for GPS and from 1 to 20 kpc for the CSS sources). The GPS sources show their peak between 500 MHz and 10 GHz while the CSS have it at  $\lesssim 500\text{MHz}$ , down to  $\sim 30\text{MHz}$ , although these upper (10 GHz) and lower (30MHz) limits are more due to observing and sample limitations than to physics or properties of the sources. The division between the two classes, GPS and CSS, is somewhat arbitrary and we can find different names or classifications depending on the morphologies or the authors, but basically they all comprehend the same objects: compact and medium symmetric objects (CSO and MSO), compact doubles or triples (i.e. Lister et al. 2003; Wilkinson et al. 1994; Conway et al. 1994; Phillips & Mutel 1981). For a review, see O’Dea (1998). I will adopt the GPS and CSS classification, as described, throughout the thesis.

There is still uncertainty about the relation between GPS/CSS sources and the larger radio galaxies, and how they relate with the other AGN. Several scenarios have been proposed, the most accepted of these is the *young* scenario, followed by the *frustration* scenario (e.g.,

Stanghellini et al. 2005). There are also other suggestions but these two seem to be the most accepted ones and, in the last years, the trends seem to favor the young scenario. I will discuss them separately below.

### 1.3.1 Recurrent or smothered sources

In this scenario, the nuclear activity stopped at some point and has recently started again forming a GPS or CSS source in the center (Baum et al. 1990; Stanghellini et al. 1990). This scenario is supported by the fact that  $\sim 18\%$  of the GPS sources show large scale diffuse radio structure which could be the relic of the past nuclear activity (Stanghellini et al. 2005). Baum et al. (1990) also suggested the possibility that the expansion of the GPS sources being interrupted by a sudden increase in density in the central part of the source, instead of the nuclear activity being recurrent, what they call a *smothered source*. Many GPS sources also show complex VLBI morphologies (e.g., Stanghellini et al. 1997, 2001) which could support this model. However, there is much controversy surrounding the nature of some GPS sources with core-jet or complex morphologies: we could be observing large, beamed radio galaxies instead (see Section 1.6 for a detailed discussion).

### 1.3.2 Transient sources

In this scenario, GPS sources (CSO, e.g., Readhead et al. 1994, 1996a) are transient events ( $\lesssim 10^4$  yr) in the life of the host. There are no strong arguments supporting or against this model.

### 1.3.3 Frustrated scenario

In this scenario, the GPS and CSS sources are old, evolved sources that have not been able to expand beyond the host galaxy (e.g., van Breugel et al. 1988; O’Dea et al. 1991; De Young 1993; Carvalho 1994, 1998). A very dense ISM could prevent the radio source expansion. Although the young scenario seems to be widely accepted, this old, frustrated version has not been completely ruled out yet.

### 1.3.4 Young scenario

In this scenario, the GPS sources would evolve into CSS sources in  $\sim 10^6$  yr and then would evolve into FR I or FR II radio galaxies, once the jets break through the ISM surrounding the source and escape into the intergalactic medium. It was first suggested by Blake (1970) and has been developed along the years by different authors (i.e. Readhead & Hewish 1976; Phillips & Mutel 1982; Carvalho 1985; Hodges & Mutel 1987; Fanti et al. 1995; Readhead et al. 1996b; O’Dea & Baum 1997; Alexander 2000; Snellen & Schilizzi 2002).

The main arguments supporting this scenario are the similar properties and morphology of the sources, relation between the peak frequency and size, the absence of enough dense gas around the source to confine it (which is required by the other scenarios). The latest measurements of GPS expansion velocities (i.e. Polatidis & Conway 2003) are consistent with GPS sources being young ( $\lesssim 10^3$  yr) and evolving into CSS, but they would need to slow down after the CSS phase to match the speeds measured in the larger radio galaxies.

The sources must undergo other changes in their evolution, as some of their properties (expansion velocities, luminosity or size distributions) do not match those observed in larger radio galaxies. The simplest explanation is that the interaction with the host is responsible for making these changes. However, this explanation has yet to be confirmed, and there is no definitive evidence of the link between GPS/CSS sources and large radio galaxies, as the studies are based on the similarity of properties and extrapolation of the relation between GPS and CSS.

#### 1.4 Current model of the GPS and CSS sources

Although there are still uncertainties, many GPS and CSS sources are likely to be young radio galaxies expanding through the host, to become FR sources (e.g., de Vries 1999; Snellen et al. 2003b; Polatidis & Conway 2003). However, there is not a solid model that describes how this expansion takes place.

Quite a few models are still qualitative, but there have been different attempts to make an analytic model. Most of these have been developed based on self-similar expansion of the radio source. They are mainly variations on the Begelman (1996) model, including free-free absorption or synchrotron self-absorption and varying the jet or host physical parameters as new observations were obtained.

The main criticism is that the self-similarity is usually introduced empirically to explain the observations but with no solid physical argument to support self-similarity. It seems a little *ad hoc* to force a jet to cross a galaxy and maintain geometric relationships. Furthermore, it is not clear if other effects other than self-similarity could reproduce the observations and some models developed in the last years (e.g., Carvalho & O’Dea 2003; Tinti & De Zotti 2005) seem to match the data better without including self-similar growth.

Almost until middle of the 90s, astronomers did not realize that GPS and CSS could form a class of radio sources by themselves. It is not yet clear, especially for GPS, that all sources classified as GPS and CSS really fall in this group. This has created a difficult to avoid inertia, that we are only now being able to abandon. If we don’t know what is really a GPS/CSS source, we cannot plan systematic surveys to observe these sources, or certain properties, and test our models. Now that we are slowly starting to understand them, this is changing; but almost until mid 90s, all GPS/CSS samples were selected from surveys targeting general radio sources (3CR for example). These surveys had selection criteria that not necessarily would apply to GPS and CSS. For example, the steepness of the spectra and position of the peak would make a certain type of GPS/CSS not fall into the selection criteria of some surveys. Then, we could only test our models on certain GPS/CSS without knowing if they were representative of the whole GPS/CSS population or if the selection criteria had cut out a certain type that would not fit our model and could be more representative of the GPS/CSS population. Most of the uncertainties in the nature of GPS/CSS still come from not knowing what we are missing in our samples or if everything that looks as GPS or CSS really fits the definition. Chapters 2 and 3 of this thesis re-classify some of these objects.

Taking all of the above into account, the most accepted models of GPS and CSS sources agree that the peak in the radio spectra is due to synchrotron self-absorption and that the radio source strongly interacts with the host while it expands. GPS sources seem to increase in radio luminosity as they cross the core of the host. Once they leave the core (their size makes them now CSS) the radio source starts dimming as it grows (and the density of the host decreases). This scenario, although still with some problems, could unify GPS, CSS and FR galaxies. A good model unifying GPS/CSS galaxies and quasars or the different distributions with redshift is still needed.

## 1.5 The spectral shape. Synchrotron self-absorption

The spectral shape of GPS and CSS sources is thought to be due to synchrotron emission and self-absorption (Figure 1.3, Snellen et al. 2000). Where the source is optically thin, the spectrum is produced by *normal* synchrotron emission and follows a power law (e.g., Kellermann 1964; Ginzburg & Syrovatskii 1965):

$$F_\nu \sim \nu^\alpha$$

where  $\alpha$  is called *spectral index* and lies between  $-1.7$  and  $-0.5$  for the optically thin region of most extragalactic radio sources, depending on source morphology and observing frequency.

The cloud where the synchrotron emission is produced may reabsorb the lower frequencies of its own emission (e.g., Ginzburg & Syrovatskii 1969). This phenomenon is called *synchrotron self-absorption* and produces a spectrum of the form:

$$F_\nu \sim \nu^{5/2}$$

This produces a spectrum with the shape shown in Figure 1.3. The frequency corresponding to the maximum flux emission, the *turnover frequency*,  $\nu_m$ , is given by:

$$\nu_m \sim B^{1/5} S_m^{2/5} \theta^{-4/5} \quad (1.1)$$

where  $B$  is the magnetic field,  $S_m$  is the flux density at the peak and  $\theta$  is the angular size of the source (e.g., Pacholczyk 1970). The position of the turnover frequency carries information on the source size (which has the largest contribution) and physical properties, so studying the turnover frequency of a source will yield information on its properties:

- *Redshift.* It has been found that GPS sources happen preferentially at higher redshifts (e.g., O'Dea et al. 1990; de Vries et al. 1997a) so we would expect them to be more compact, as the turnover frequency is proportional to  $\theta^{-4/5}$ , and it would imply denser environments at high redshifts. However, this result might be due to detection limits, as for the steep spectrum sources, the redshift could move the spectra far enough so the flux density of the source at our observed frequencies is below the detection limits.
- *Linear size.* Fanti et al. (1990) found an anti-correlation between the linear size and turnover frequency of CSS sources. O'Dea & Baum (1997) studied the relation

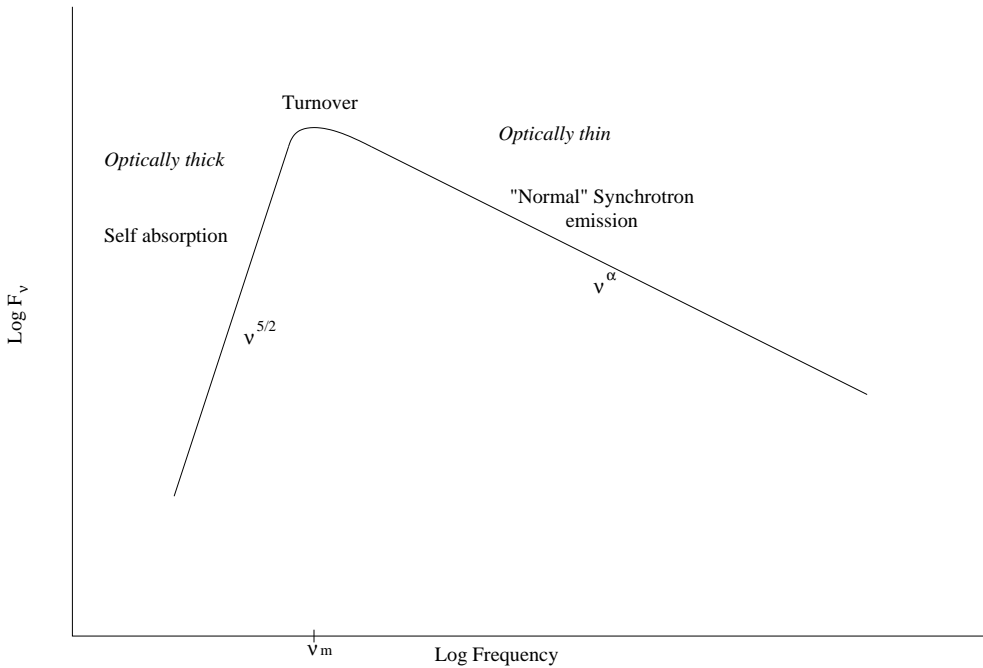


**Figure 1.3**— Schematics of a spectrum with synchrotron self absorption.

between linear size of the source and intrinsic turnover frequency, but now combining both GPS and CSS sources in the sample. They found that the anti-correlation also occurred for the combined sample, suggesting similar properties for GPS and CSS sources (although nothing directly implies that the sources evolve following this correlation), and that this correlation was the same also for quasars and radio galaxies:

$$\nu_m \propto (\text{Linear Size})^{-0.65}$$

The spectral shape observed in GPS and CSS sources can also be reproduced by free-free absorption processes (e.g. Tingay et al. 1997; Bicknell et al. 1997) but to reproduce the observations, another factor must be invoked (i.e. an absorption screen). Although there are still authors supporting the free-free absorption as the process causing the spectrum shape, the main stream seems to favor the synchrotron self-absorption (e.g., Snellen et al. 2003b), as it is a much simpler argument and can reproduce the observations without including other factors in the source. However, free-free absorption cannot completely be ruled out nor can a combination of both processes.

## 1.6 GPS quasars

There is substantial controversy surrounding GPS quasars (e.g., Snellen 1997). According to the unification model, they should be the same type of object as the GPS galaxies with different orientation. However, observations seem to disagree:

- GPS quasars are clearly more abundant than galaxies (e.g., Dallacasa et al. 2000) and are found at all redshifts (peaking at  $z \sim 2 - 3$ ) while GPS galaxies appear only below  $z \sim 1$  (O’Dea et al. 1991). This difference in redshift is likely to be genuine and not due to selection or similar effects (Snellen et al. 1999).
- GPS quasars show higher values of intrinsic and observed turnover frequencies than GPS galaxies suggesting that GPS quasars may be more compact than the GPS galaxies (e.g., Stanghellini et al. 1998).
- Observations suggest that the spectra of GPS quasars originate in compact regions, close to the nucleus while in galaxies it seems to come from hot spots with large range of sizes (e.g., Stanghellini 2003).

These differences have led to the hypothesis that GPS quasars could be a different type of object, not related to CSS sources or GPS galaxies or the models discussed in Sections 1.3 and 1.4 (Stanghellini et al. 2005).

What then are the GPS quasars? It has been widely accepted that CSS and GPS sources are not affected by Doppler boosting<sup>3</sup>. Most of the CSS sources have lobes of similar intensities and their jet velocities are not relativistic. This is also true for GPS galaxies. However, GPS quasars may be affected by beaming (de Vries et al. 1997a; Stanghellini et al. 1998). This beaming can make a flat-spectrum quasar look like a GPS quasar and vice-versa.

If a flat-spectrum quasar has its jets close to the line of sight, Doppler boosting can be important enough to change its spectrum (e.g., Lister 2003; Melrose 1996), as Doppler boosting would move the individual spectra of each component (equation 1.1). At some stage, variation in the intensity of components of the jet (a perturbation or shock wave moving along the jet, a single homogeneous component dominating the radio spectrum) can modify the spectra of the components in such a way that the total composite spectrum of the quasar will look like a *real* GPS spectrum. It is possible that most (if not all) observed GPS quasars could be large quasars with apparent GPS source spectra (Snellen 2004, private communication, see also e.g., Snellen et al. 1999).

So far, all the GPS samples may be contaminated by these non-GPS quasars. However there are ways of unveiling them. The conditions for a flat-spectrum quasar to create a GPS looking spectrum are rather random and temporal. Then, we expect to observe variability, which would not be present in a GPS source. The closer we are to the jet line, the faster the variations in the jet propagate, so we should be able to observe variations in the quasar radio spectra in (astronomically) short periods of time. Some work has already been done in this line finding that, in fact, sources that some years ago looked as GPS quasars, now show a completely different, non-GPS, radio spectrum (e.g., Tinti et al. 2005, and Chapter 3 of this thesis).

Some GPS and CSS quasars with core-jet or complex morphologies could be large sources observed along the radio axis. The high redshift of the GPS quasars could make extended radio emission to fall under the detection limits (Stanghellini 2003). High resolution,

---

<sup>3</sup>Enhancement of radiation from material moving towards the observer at relativistic speeds.

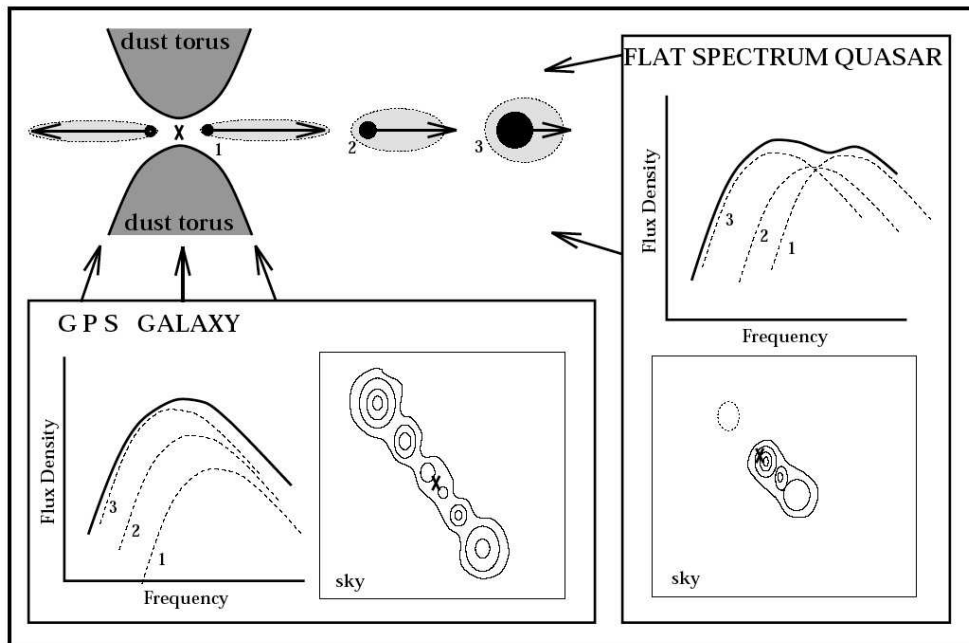


**Figure 1.4–.** Snellen et al. (1998b) model and representation of how Doppler boosting can change the spectrum of a source. The length of the arrows is proportional to the speed of the component. Doppler boosting is not important in galaxies but it can completely change the spectrum and appearance of a source when observed along the jet axis. Reprinted with permission of the author.

deep VLBI imaging of these sources should also help decontaminating the samples.

It is worth noting that the opposite effect can also be present. A GPS source could look like a flat-spectrum quasar. Snellen et al. (1998b) have proposed a model where the jets decelerate as they expand. In this model the inner components of the jet propagate faster than the outer ones and are, therefore, more affected by Doppler boosting. The Doppler boosting effect is mainly noticed along the line of propagation, and decreases with viewing angle. So, combining both effects, a galaxy with a GPS spectrum can look like a flat-spectrum quasar (probably core-jet) when observed along the jet line (see Figure 1.4). A direct consequence is that we may (and most likely do) have GPS quasars hiding in flat-spectrum quasar samples.

## 1.7 Thesis project

By the beginning of this thesis, GPS and CSS sources stood as different classes of objects by themselves, and a lot of research had just been carried out. However, there were still questions to be answered. In my opinion, the two main questions concerning GPS and CSS sources were:

- 1) Where do they stand in relation with the other radio sources and AGN?
- 2) How do GPS/CSS interrelate with their host?

Both questions had been around for some time, however, the first one was sooner to be answered. There were two important workshops held in 1999 (*Life cycles of radio galaxies*<sup>4</sup>) and 2002 (*The Third Workshop on CSS and GPS radio sources*<sup>5</sup>). In the first one, participants showed growing evidence supporting the young scenario. By the end of the 2002 workshop, most participants were convinced that GPS and CSS sources are (or seem to be) young.

Research had been carried out focussing on the interrelation between the radio source and the host. However it was a by far less active field. The main developments on this subject were done on alignment effect of the radio source and the line emission gas. This thesis takes it from there and advances in our understanding of the interrelation between the radio source and the host and how it is affecting both.

Other issues addressed in the thesis:

- 3) Mapping of compact radio sources.
- 4) Enlargement and improvement of GPS and CSS samples.
- 5) Properties of the gas and stellar population of the host.
- 6) Ionization mechanisms of the gas in the host.

---

<sup>4</sup>Proceedings published in *New Astronomy Reviews*, editors: J.A. Biretta, A.M. Koekemoer, E.S. Perlman, C.P. O'Dea. May 2002, Vol. 46, Nos. 2–7

<sup>5</sup>Proceedings published by PASA, 2003, Vol. 20, editors: T. Tzioumis, W. de Vries, A.M. Koekemoer, I. Snellen

- 7) Gas content and distribution in the host.
- 8) First near-UV study of GPS and CSS sources.
- 9) AGN–starburst connection.

## 1.8 Thesis outline

Chapter 2 presents radio maps of compact sources in the Southern hemisphere. The data are being compared with other measurements to classify and look for unidentified GPS and CSS sources in the sample. Number statistics of GPS and CSS quasars and galaxies are presented and compared with the Northern hemisphere.

Chapter 3 presents optical observations of hosts of candidate GPS radio sources. Identification and spectroscopy of the hosts are carried out, aiming to complete the GPS identification and redshift entries of the O’Dea et al. (1991) GPS master list. New identifications, magnitudes, redshifts and emission line gas properties are reported. Models of stellar populations are compared with the observations. Literature data are collected to study previous GPS identifications.

Chapter 4 presents Hubble Space Telescope long slit spectroscopy of CSS sources, studying the ionization mechanisms of the emission line gas, as well as its properties. All sources show a combination of photoionization and –fast– shock ionization. The expansion of the radio source is clearly affecting the optical emission properties of the host.

Chapters 5 and 6 present high resolution radio imaging and spectroscopy of two CSS sources and a GPS source, and study the contents, distribution and properties of cold gas in the host, revealing that it seems to be associated with the emission line gas and presenting a completely new interpretation of an old known GPS source.

Chapter 7 presents the first study of the near-UV emission in hosts of GPS and CSS sources. Alignment between the radio source and UV emission of the host is found, as well as small UV emitting regions, consistent with recent star formation. A comparative study with large radio sources is presented. The connection between bursts of star formation and the presence of a powerful radio source is explored.

Chapter 8 summarizes the main results of this thesis and discusses its implications. It also describes the work carried out by other groups concerning GPS and CSS sources and attempts to make a coherent picture. The last section of the chapter suggests possible lines of future research.

# 2

---

## Compact and extended radio sources in the southern sky

*Preliminary version of a paper to be co-authored by:*

A. Labiano, P.D. Barthel, R.W. Hunstead, R.T. Schilizzi, J. Bland-Hawthorn

**W**E present Very Large Array (VLA) observations of a subset of southern extragalactic sources selected from the Molonglo Southern 4 Jy (MS4) Sample, demonstrating that MS4 is comparable to the northern Third Cambridge Revised catalogue. Several interesting individual objects are discussed, including new galactic sized CSS objects. New CSS sources are found: B0614–349, B0615–365, B0646–398, B0707–359, B1015–314, B2259–375 and B2339–353 as well as a CSS candidate in the core of B0618–371.

## 2.1 Introduction

In the last fifty years, several surveys in radio wavelengths have been performed. The most used and better studied is the Third Cambridge Catalogue (3C; Edge et al. 1959) and its revisions (3CR and 3CRR; Bennett 1962; Laing et al. 1983). The 3C catalogues were made selecting radio sources (both galactic and extragalactic) with  $S_{178\text{MHz}} \geq 10 \text{ Jy}$ ,  $\delta \geq 10^\circ$ ,  $|b| \geq 10^\circ$ . The latest revision, 3CRR (Laing et al. 1983) comprises almost two hundred extragalactic radio sources. The majority (85%) are large FR I (edge darkened, Fanaroff & Riley 1974) and FR II (edge brightened) radio sources. 15% of the 3CRR sample are Compact Steep Spectrum (CSS) sources (Nan et al. 1991; Sanghera et al. 1995) and no Gigahertz Peaked Spectrum (GPS) sources are found (see Table 2.2 for more detailed statistics). The absence of GPS sources in the 3CR catalogues is most likely due to the spectral shape of these sources: the position of the peak makes them too faint around 178MHz to be included in the 3C catalogues. They are however generally present in radio source samples selected at cm or dm wavelengths (e.g de Vries et al. 1997b)

The 3C catalogue was the first detailed catalogue of extragalactic radio sources. It has been used extensively in the last 50 years, and still is. However, there was no equivalent of the 3C catalogues in the southern sky until 1998, when R.W. Hunstead and A.M. Burgess (Burgess 1998) presented a comparison sample in the southern hemisphere: the Molonglo Southern 4 Jy Sample (see also Burgess & Hunstead 2006a).

## 2.2 The Molonglo Southern 4 Jy Sample

The Molonglo Southern 4 Jy Sample (MS4) consists of 229 radio sources selected from the 408 MHz Molonglo Reference Catalogue (MRC; Large et al. 1981), with a flux density  $\gtrsim 4 \text{ Jy}$ . It covers declinations between  $-85^\circ$  and  $-30^\circ$  and a galactic latitude  $|b| > 10^\circ$ . The Magellanic Clouds were excluded because sources found there would be very complicated to identify as extragalactic. The 229 sources in MS4 were imaged with the Molonglo Observatory Synthesis Telescope (MOST) at 843MHz at a resolution of  $43'' \times 43'' \cos \delta$ , yielding radio positions accurate to a few arcsec, crude angular sizes and flux densities. Sources with angular sizes  $< 35''$  were imaged at 5 GHz with the Australia Telescope Compact Array (ATCA) in snapshot mode at a resolution of 2–8''. The optical identifications were done using UK Schmidt plates for the brighter objects and AAT<sup>1</sup> R-band CCD images for the fainter ones, along with the MOST and ATCA positions. Only half of the MS4 sources, mostly quasars and nearby galaxies, have published spectroscopic redshifts (after optical identification, e.g., Burgess 1998). Optical magnitudes were used to estimate the redshift of the sources without spectroscopic data (see column 13 of Table 2.1). Comparing the MS4 and 3CRR catalogues should be, in principle, straightforward, as both catalogues cover equivalent regions of the sky and the flux density limits (10 Jy at 178 MHz and 4Jy at 408 MHz) are comparable for a spectral slope  $F \propto \nu^{-1}$ .

---

<sup>1</sup>Anglo-Australian Telescope

### 2.3 VLA observations of MS4 compact sources

In order to increase the number of known GPS and CSS sources, study basic radio parameters (e.g. angular size) and test number statistics, we observed a complete sub-sample of the MS4 catalogue using the Very Large Array (VLA) in the X-band (3.5 cm), with the BnA configuration. We obtained 1'' resolution images of 26 MS4 sources with angular size between  $\sim 2$  and  $\sim 30$  arcsec, in the  $-30^\circ$  to  $-40^\circ$  declination strip. The strip contains 74 sources in total. In addition to our 26 sources, there are 39 radio sources with size  $> 30''$  and 9 with size  $\lesssim 2''$ .

### 2.4 Data reduction and mapping

The 26 southern MS4 radio sources were observed with the VLA, in its BnA configuration, on June 24 and 26, 1998, employing the standard X-band (8.4GHz, 2x50MHz) receiver system. Two snapshots of typically ten minutes each, at different source hour angles were made. Each program source was observed with an associated phase calibrator, whereas calibrator 3C 286 was used to establish the absolute flux scale. The BnA configuration (east and west arms in "B", the second longest configuration, and the northern arm in "A", the longest configuration), of the VLA was chosen to optimize the beam shape for observations of sources in the southern sky. The typical beamsize in the final images is 1 x 0.5 arcsec (see Table 2.1). The radio data were of high quality, and there was no need for extensive flagging of discrepant data points. Reduction of the data was performed using standard NRAO AIPS image processing routines, including several steps of self-calibration (phase only, followed by amplitude self-calibration). Several successive self-calibration and cleaning cycles generally led to a rapid convergence towards the images presented below. The resulting radio maps are shown in figures 2.3 to 2.7. Figures 2.8 and 2.9 present overlays of the radio maps and available optical R-band images. Table 2.1 summarizes the source and map properties.

### 2.5 Notes on individual sources

Before discussing the sample properties, we proceed by describing the individual sources imaged with the VLA. The spectral indices have been estimated using our VLA observations (8.4 GHz) and the MOST measurements (843MHz) for the integrated emission of the source. ATCA data (4.8 GHz) were used to estimate the spectral indices of the cores (Table 2.1). We assume that the spectra of the sources behave as a power law between the available frequencies. Many of the sources in our strip only had observations with MOST.

*B0012-383*: Lobe dominated triple source associated with an intermediate redshift galaxy ( $z=0.65$ ). ATCA observations show just the lobes while our observations bring up a possible core, consistent with the optical observations (Figure 2.8). Both lobes show tails of extended emission and misalignment of the three components.

*B0036-392*: ATCA observation showed a double source associated with an optical quasar. Our observations confirm it but reveal a structured center of the source with a big twist, almost in a "z" shape.

*B0042–357*: ATCA observations showed a compact asymmetric double source associated with a  $z_R = 1.259$  (Burgess 1998) galaxy: a very bright spot in the south with extended bright emission to the north. Our higher resolution map shows that this extended emission is a compact bright component separated  $\sim 50$  kpc from the southern component, aligned north-south with the other component.

*B0157–311*: A highly structured source with very extended emission and several hot spots, associated with a quasar. Burgess (1998) identifies the central, brightest component as the core of the source. We compute  $\alpha_{4.8}^{8.4} \simeq -0.4$ , ( $F \propto \nu^{-\alpha}$ ), which could be produced by the variability of the core, resolution effects or contamination from the extended emission in our estimation of the flux density. The complex structure of the radio jets suggests a dense ISM.

*B0340–0372*: A CSS source ( $\alpha_{0.843}^{8.4} \simeq 1$ ) with several compact components aligned in the NE-SW direction and extended emission to the NW. The optical identification corresponds to a quasar coincident with the central component of the VLA map (White et al. 1988).

*B0411–346*: The ATCA map shows a single bright component CSS source ( $\alpha_{0.843}^{8.4} \simeq 1$ ) in the radio map of this  $z \sim 1$  galaxy. Our higher resolution separates the source in two components.

*B0427–366*: An extended, linear triple source with some faint extended emission towards the south of the central component. The ATCA map showed a lobe dominated triple source connected by extended emission. The optical image (Burgess & Hunstead 2006b) shows a stellar source slightly south of the central component but there is no available spectrum for the source so it could be classified as a quasar candidate.

*B0601–344*: A faint compact source, associated with a galaxy, with some faint extended emission towards the north east. There are no ATCA maps of this source. The MOST map showed a similar morphology.

*B0602–319*: A bright source with a peak in the center and extended emission to the south. The shape of the central component suggests an unresolved secondary component. Higher resolution maps would be needed to check it. Burgess (1998) suggests that the brightest radio component is the core of the quasar but we estimate  $\alpha \sim 2$  which seems too far from the flat, expected, value.

*B0614–349*: An unresolved CSS source associated with a galaxy. We compute a spectral index  $\alpha_{0.843}^{8.4} \simeq 0.66$ .

*B0615–365*: An unresolved CSS source,  $\alpha_{0.843}^{8.4} \simeq 0.91$ , associated with an optical galaxy.

*B0618–371*: The VLA map shows a very extended source with two components separated  $\sim 30$  arcsec, associated with a galaxy. The brightest component is also very compact and the eastern component shows extended emission, probably the end of the jet. There are

no good estimations of the flux density of the Western (compact) component which could be the core and/or a CSS source. Parma et al. (1991) shows a wider field map of this source revealing a 2' long triple, almost symmetric, FR II source with very wide extended emission around the lobes. Parma et al. (1991) place the optical counterpart (a  $b_J = 14.8$  dumb-bell galaxy) in our VLA compact component.

*B0646–398*: An unresolved faint CSS source, computed  $\alpha_{0.843}^{8.4} \simeq 2$ , associated with a possible quasar (no optical spectrum of the optical -compact- counterpart). The high value of the spectral index can be due to variations in the emission of the source.

*B0707–359*: An unresolved CSS source for which we compute  $\alpha_{0.843}^{8.4} \simeq 1.8$  with a bright optical galaxy counterpart. As with the previous source, the high value of the spectral index can be due to variations in the emission of the source.

*B1015–314*: An unresolved CSS source,  $\alpha_{0.843}^{8.4} \simeq 0.86$ , with a quasar counterpart.

*B1206–337*: A highly aligned four component source associated with a faint distant galaxy. ATCA observations only reveal two components. Our map shows two faint hotspots between the brightest components. The optical overlay indicates the absence of a radio core.

*B1247–401*: A highly structured lobe dominated source with a galaxy counterpart. ATCA observations only reveal two components, which we manage to separate. Our map suggests a twist in the center of the source but it can be due to the shape of the beam.

*B1346–391*: ATCA observations show a  $\sim 8''$  double source that our higher resolution reveals as a triple source. The southern component seems to be made of two radio components which we do not resolve completely. The optical image shows emission close to the compact component in the center of the radio map. We only compute an upper limit to the spectral index of the possible core:  $\alpha_{4.8}^{8.4} < 1.3$ .

*B1359–358*: ATCA observations suggest a  $\sim 8''$  double source associated with an optical galaxy. We resolve both components and some extended emission between them.

*B1955–357*: The ATCA map shows a double source which we separate into a three component source with the central component coincident with the optical quasar counterpart suggesting we are resolving a core (with  $\alpha_{4.8}^{8.4} < 2.2$ ) and two lobes.

*B2049–368*: A  $\sim 5''$  compact double both in the ATCA and our map, associated with a galaxy. The beam shape makes it very difficult to interpret the map. Burgess (1998) places the core in the southwestern component ( $\alpha_{4.8}^{8.4} < 1.1$ ).

*B2128–315*: A triple source with a compact lobe component in the south west and an extended component with two compact bright components towards the north east. The optical position of the quasar coincides with the central radio component suggesting a core (although we compute  $\alpha_{4.8}^{8.4} \simeq 1$ ) and two lobes, the northern one connected to the core by jet emission.



*B2226–386*: A double source, associated with an optical galaxy, with a bright component in the south and a fainter hotspot in the northern connected by some faint extended emission. Burgess (1998) places the core of this source in the southern, brightest component, for which we compute  $\alpha_{4.8}^{8.4} < -0.5$ . This negative value can be due to variability of the core or overestimation (due to "contamination" from the surrounding extended emission) of our 8.4GHz flux density.

*B2259–375*: An unresolved CSS source,  $\alpha_{0.843}^{8.4} \simeq 1.1$ , with a galaxy counterpart.

*B2323–407*: A lobe dominated triple source with a very faint central component, coincident with the optical galaxy, suggesting a core ( $\alpha < 0.6$ ).

*B2339–353*: An unresolved CSS source,  $\alpha_{0.843}^{8.4} \simeq 1.4$ , associated with an optical galaxy.

## 2.6 Results

Table 2.2 shows a summary of the occurrence of galaxies, quasars and CSS/GPS sources in the 3CRR catalogue (173 sources) and the strip between  $-30^\circ < \delta < -40^\circ$  from the MS4 (74 sources out of the 229 of the complete catalogue). We have used the redshifts and identifications of optical counterparts in Burgess (1998). We define a CSS source to have projected linear size  $\lesssim 15$  kpc ( $H_0 = 71 \text{ km s}^{-1} \text{ Mpc}^{-1}$  and  $\Omega_\Lambda = 0.73$ ,  $\Omega_M = 0.73$ ) with  $\alpha > 0.5$ , and GPS sources those with size below 1 kpc. We have classified the unresolved objects as CSS sources. Higher resolution imaging would be needed to classify them as GPS. The complete MS4 catalogue only has two sources classified as GPS so far (B0008–421 and B1934–638), 0.9% of the total sample. Our VLA observations reveal several CSS sources: B0411–346, B0614–349, B0615–365, B0646–398, B0707–359, B1015–314, B2259–375 and B2339–353. The core of B0618-371 may harbor a CSS source too, although more spectral data is needed to confirm it. The data for the 3CRR have been taken from Laing et al. (1983) and <http://www.3crr.dyndns.org/>, as well as Nan et al. (1991) and Sanghera et al. (1995) for the CSS occurrences.

About 8% of the MS4 strip has not been identified as quasar or galaxy, therefore the percentages of each type in the sample can change when the remaining objects are classified. Ignoring these unidentified sources, the MS4 strip and the 3CRR catalogue have the same fraction of galaxies ( $\sim 76\%$  and  $\sim 75\%$  respectively) and the MS4 strip lacks of quasars (16%) compared to the 3CRR (25%). If most of the unidentified objects in the MS4 strip were classified as quasars, the occurrence be similar to the 3CRR quasars. However, the complete MS4 catalogue lacks of quasars (20%) compared to the 3CRR (25%).

Regardless of optical identification, both catalogues show a similar occurrence of CSS sources (15% in the MS4 strip and 15% in 3CRR) and lack GPS sources. The lack of GPS sources can be due to their spectrum (steep and peaked at  $\sim 1$  GHz), as GPS are expected to be weak at low frequencies. There is a clear discrepancy in the occurrence of CSS galaxies and quasars in both catalogues: almost all the CSS sources in the MS4 strip are galaxies

Object	ID	MS4 strip	Stat. Err.	3CRR	Stat. Err.	Ratio
	Total	74 (100%)	0	173 (100%)	0	2.3
Complete	Galaxies	56 (76%)	4	129 (75%)	6	2.3
Sample	Quasars	12 (16%)	3	43 (25%)	6	3.6
	Unidentified	6 (8%)	2	1 (<1%)	1	0.17
	Total	11 (15%)	3	26 (15%)	5	2.4
CSS	Galaxies	9 (12%)	3	12(7%)	3	1.3
	Quasars	2 (4%)	1	14(8%)	4	7.0
GPS	Total	0	0	0	0	–

**Table 2.2.– Statistics of the different objects in MS4 and 3CRR.** Comparison between the different object IDs in the 3CRR and our MS4  $-40 < \delta < -30$  sample. The first part of the table gives the numbers for the total samples and the second part the CSS and GPS statistics. Columns *Stat. Err.* give the statistical errors associated to the number of sources in each category. The last column gives the ratio 3CRR / MS4 of identification in each sample for each type of object. We also give the percentage to the total sample for each object. MS4 statistics from our VLA data and Burgess (1998). 3CRR statistics from Laing et al. (1983) and <http://www.3crr.dyndns.org/>.

while CSS sources are evenly spread in galaxies and quasars for the 3CRR. This discrepancy can be due to the definition of the optical counterparts in MS4 which would confuse, for instance, broad line galaxies, galaxies with compact appearance, quasars with narrow line spectra or with extended emission (Burgess 1998).

Figure 2.1 shows the distribution of sizes in the MS4 strip and the complete 3CRR catalogue. The behavior is similar: high occurrences of small sources and decreasing with size. Both catalogues show a trend to increase around the 350 kpc region, although the MS4 strip seems to lack sources between 350 and 400 kpc. Otherwise, the distribution is, in general, similar, specially taking into account that we are using low number statistics. Burgess (1998) finds comparable linear size distribution for the sources in the complete MS4 and 3CRR so we must attribute this "gap" between 350 and 400 kpc to the selection of just a strip in the sky instead of the complete MS4 catalogue or the low number statistics. The Kolmogorov-Smirnov test seems to support the similarity of catalogues. However, it is not conclusive (Figure 2.2).

## 2.7 Summary

We carried out a comparison study between a MS4 strip and the 3CRR catalogue and improved the classification of CSS sources in the MS4 catalogue. We find that although there are slight differences, these are mainly due to small number statistics; both catalogues show the same general distributions. The  $-30^\circ < \delta < -40^\circ$  strip of the MS4 catalogue is more abundant in CSS galaxies but contains fewer CSS quasars. The MS4 strip also lacks sources with diameters between 350 and 400 kpc compared to the 3CRR.

We find new CSS sources in the MS4 strip: B0614–349, B0615–365, B0646–398, B0707–359, B1015–314, B2259–375 and B2339–353 and a CSS candidate in the core of B0618–371.



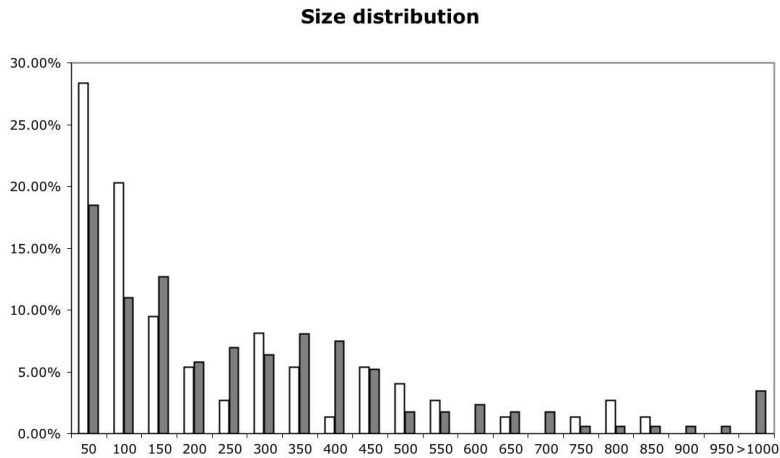


**Figure 2.1**— Comparison of the distribution of sizes (in kpc) in the 3CRR (shaded bars) and MS4 strip (white bars) samples: 173 and 74 radio sources respectively. The sources have been grouped in 50 kpc bins. The first column contains all the sources with sizes below 50 kpc; the second one sizes between 50 and 100 kpc, and so on. The last column represents sources with sizes bigger than 1 Mpc.

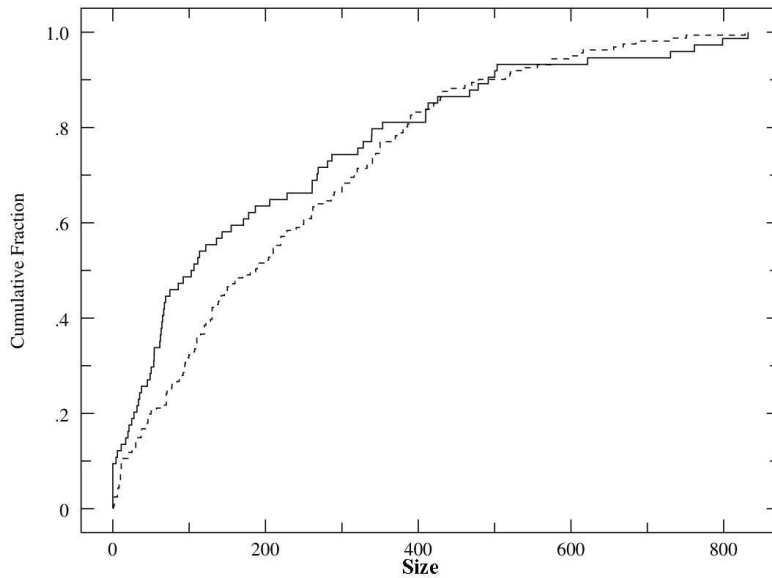


**Figure 2.2**— Cumulative histogram for sizes of MS4 strip (solid line) and 3CRR (dashed line) sources.

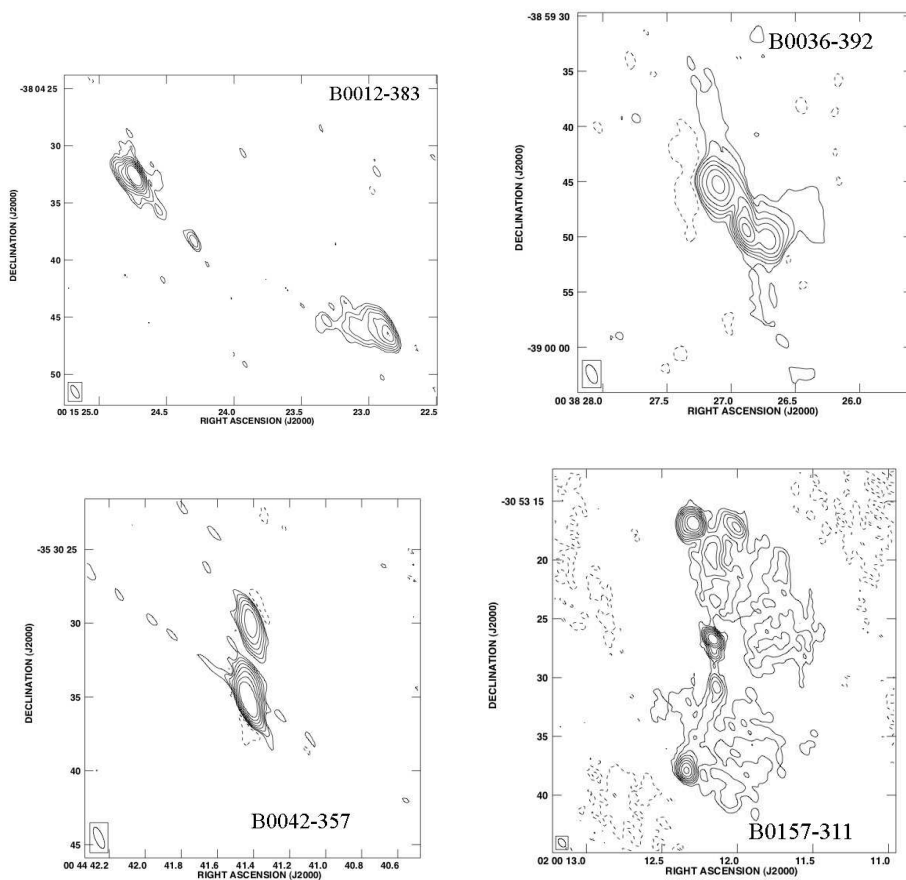


**Figure 2.3.**— VLA 8.4GHz maps of MS4 sources. Contours are -3, 3, 6, 12, 24, 48, 96, 192, 384 multiples of the rms noise in the images (see table 2.1). Typical noise levels of  $\sim 0.1\%$  peak flux were reached. Only resolved sources are shown.

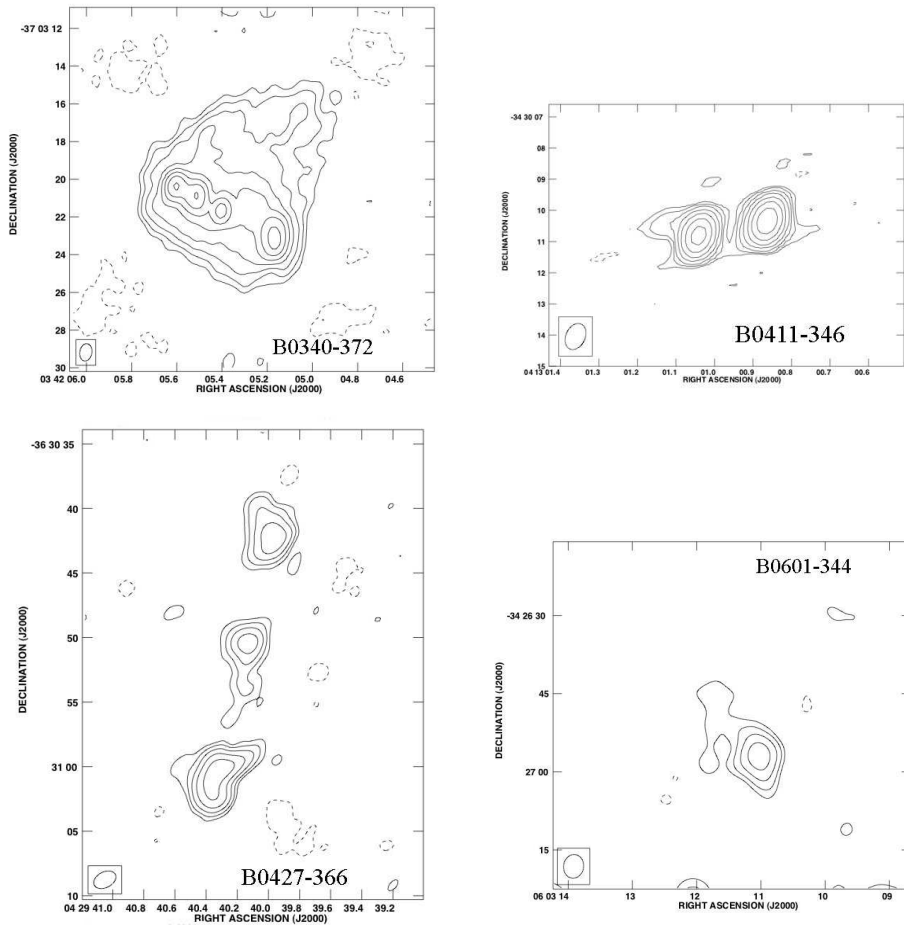


**Figure 2.4.**— Same as Figure 2.3.

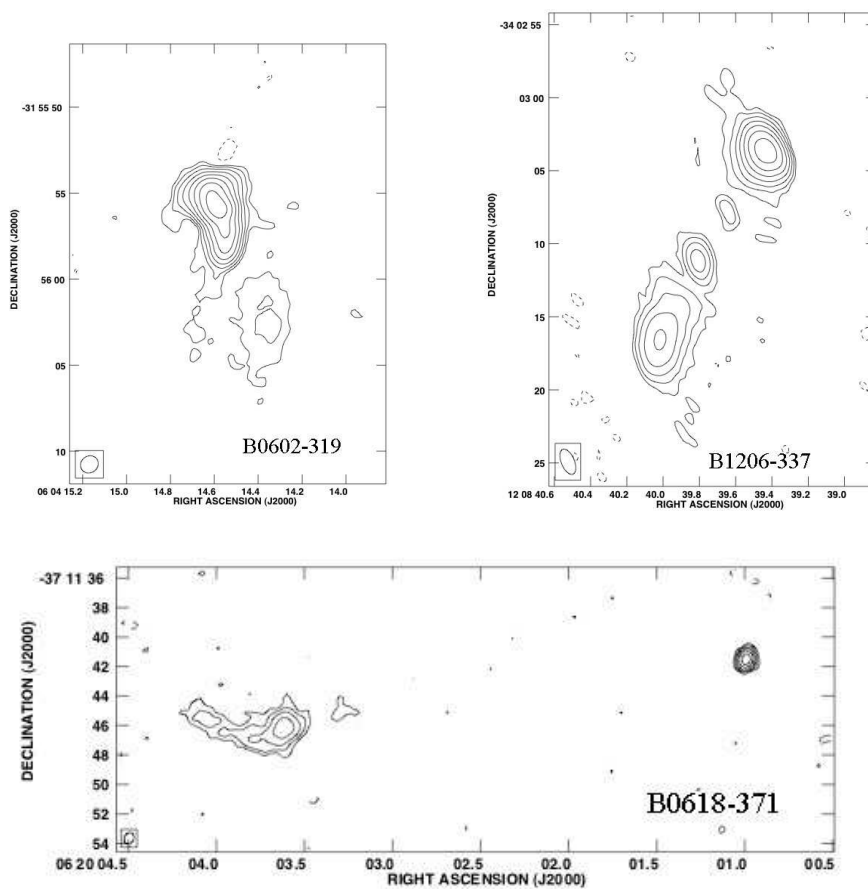
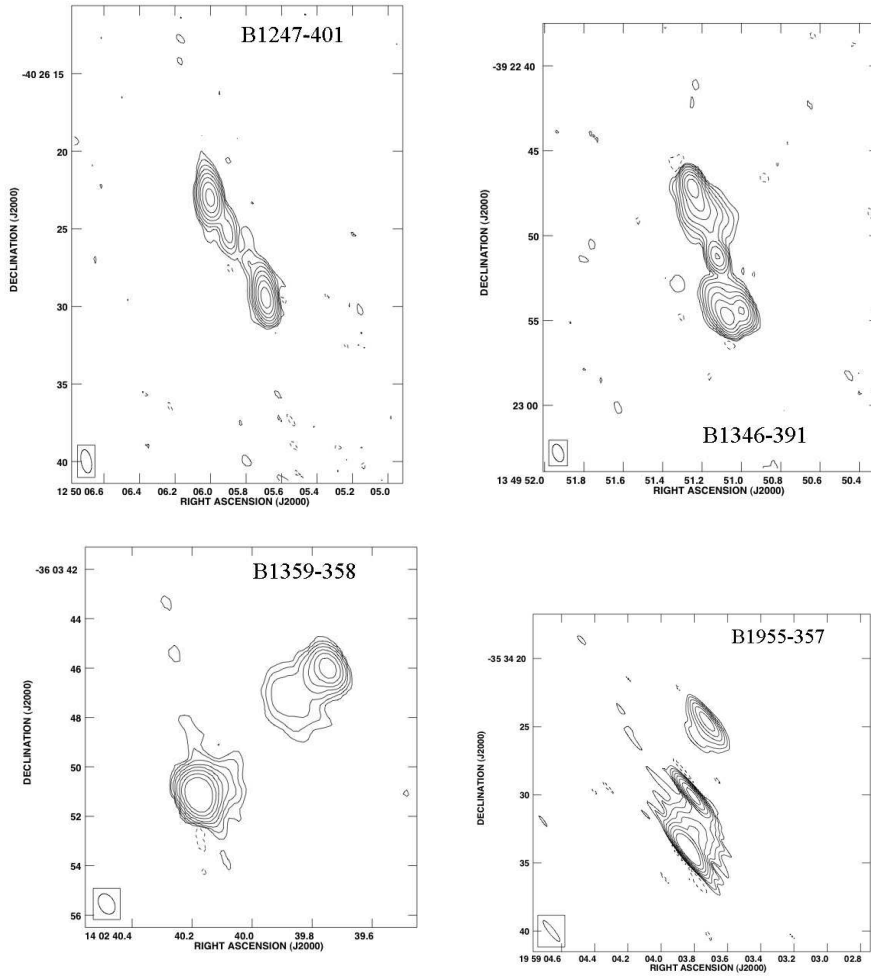
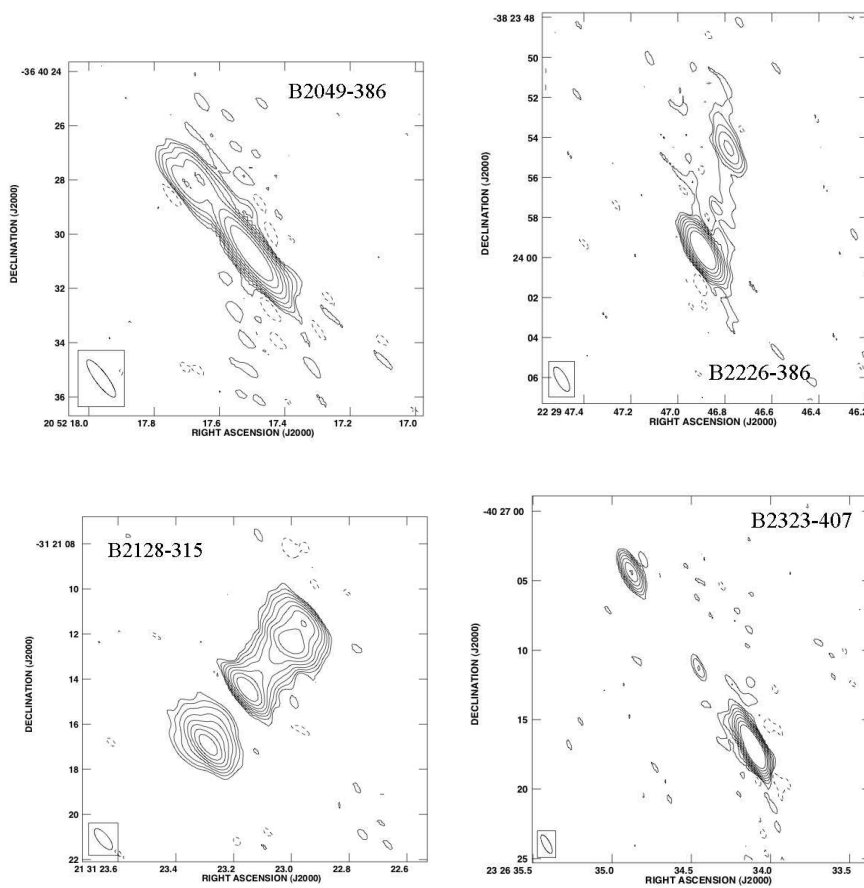


Figure 2.5—. Same as Figure 2.3.



**Figure 2.6.**— Same as Figure 2.3.



**Figure 2.7**–. Same as Figure 2.3.

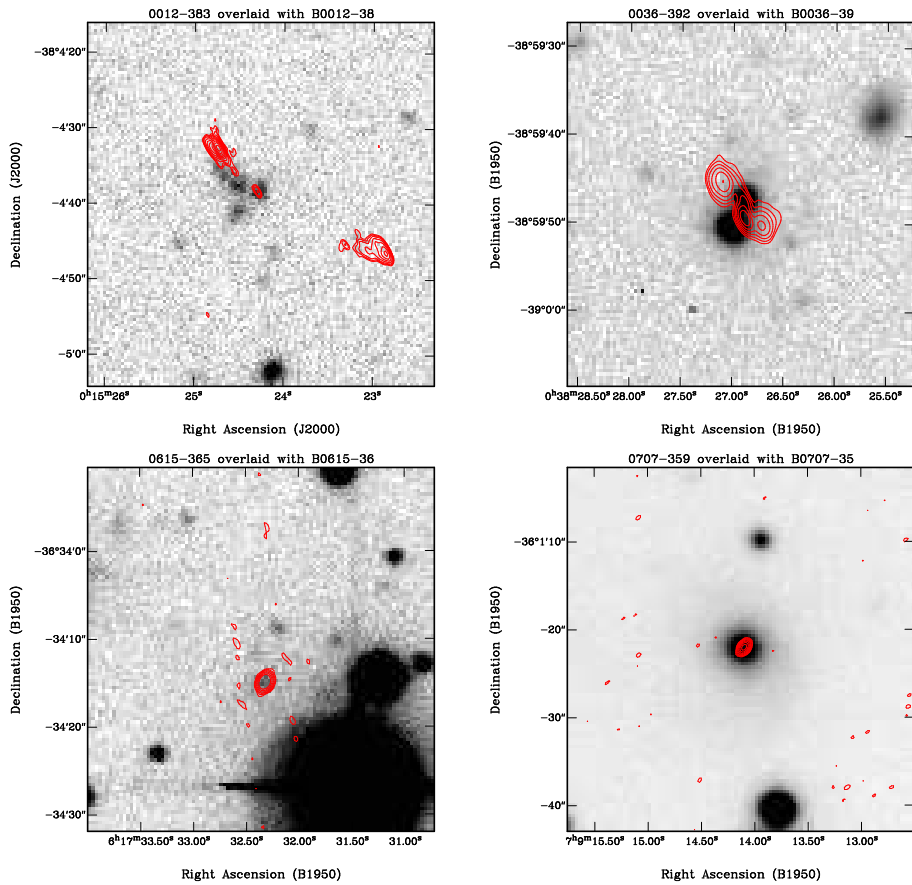


**Figure 2.8.**— Overlays of our VLA images and *R*-band overlays of MS4 sources observed with the Anglo-Australian Telescope.

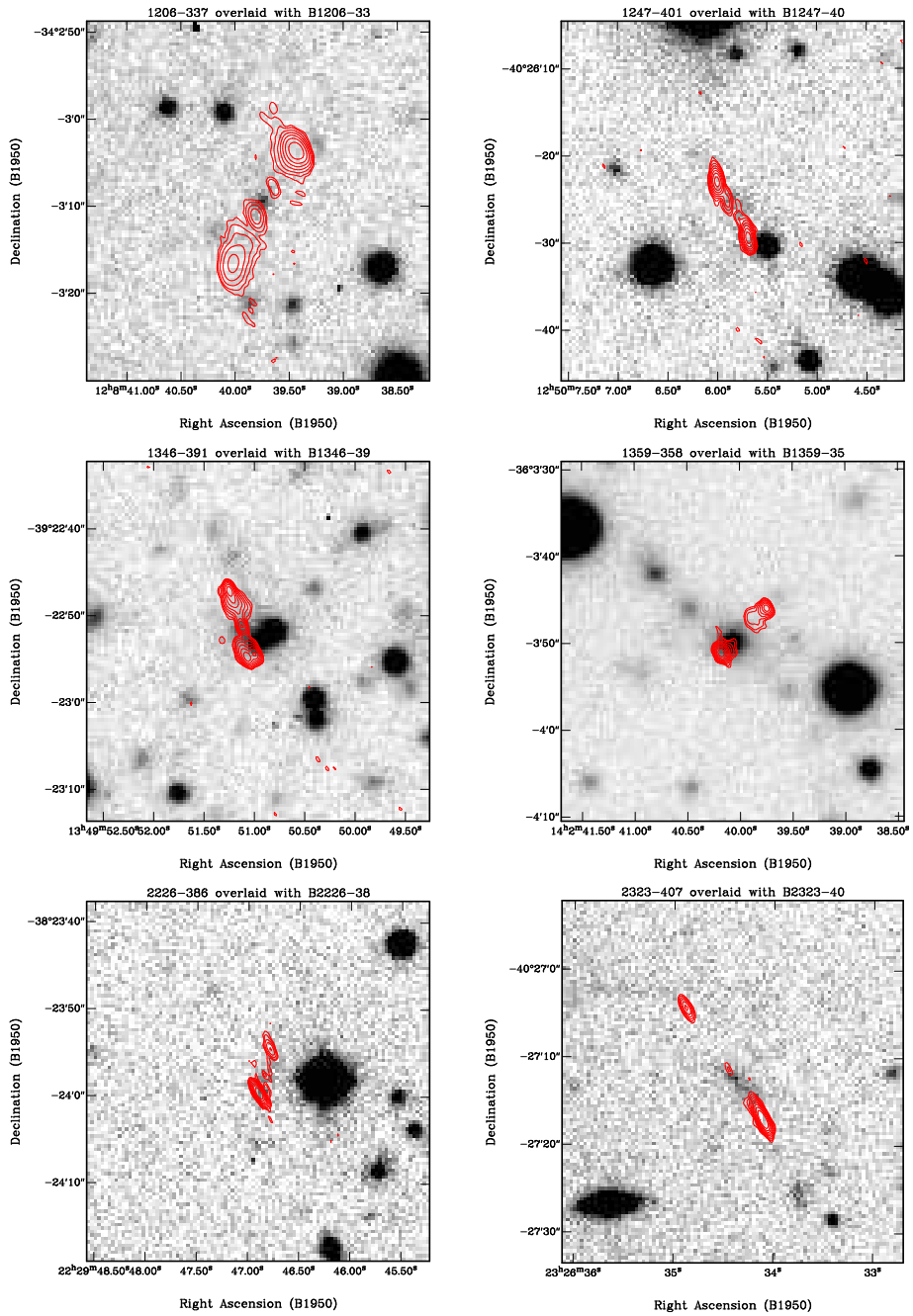


Figure 2.9-. Same as Figure 2.8.



# 3

---

## Optical imaging and spectroscopy of candidate GPS radio sources

A. Labiano, P.D. Barthel, C.P. O’Dea, W.H. de Vries, I. Pérez, S.A. Baum

**D**EEP optical imaging and spectroscopy, obtained with the Very Large Telescope (VLT), is presented, targeting the host galaxies of candidate GPS radio sources from the master list of O’Dea et al. (1991). Our goal is to measure new redshifts, identify optical counterparts and address uncertain identifications. We measure redshifts for B0316+161, B0407–658, B0904+039, B1433–040, and identify the optical counterparts of B0008–421, B03161+161, B0407–658, B0554–026, B0742+103, B0904+039. We find that the previous identification for B0914+114 is incorrect. Using literature data we furthermore show that the following sources are not GPS: B0407–658, B0437–454, B1433–040, B1648+015.

### 3.1 Introduction

GPS radio sources are fairly common – O’Dea (1998) lists a 10% fraction in high frequency selected catalogs. It is fairly well established now that the extended radio galaxies and quasars should be unified with the compact, core-dominated quasars and BL Lac-objects through the combined effects of radio jet orientation and anisotropic obscuration (e.g., Urry & Padovani 1995). These objects are considered to be mature, well developed radio sources. It is likely that GPS objects are young radio sources that will evolve into the 10 – 100 kpc scale objects. Both theoretical work and observational studies of GPS host galaxies support this picture. As for the former, model and data require declining radio luminosity with age. As for the latter, multi-color optical as well as near-IR imaging (e.g., de Vries et al. 2000a) have shown that host galaxy colors of nearby GPS objects are indeed consistent with non- or passively evolving ellipticals, with absolute magnitudes comparable to brightest cluster members, similar to the hosts of intermediate sized and large radio source classes. Determination of the rest-frame broad-band colors (which requires redshifts) in connection with stellar synthesis modeling has proven essential for these investigations<sup>1</sup>.

O’Dea et al. (1991) presented a list of candidate GPS radio sources. About half of those sources had unknown redshifts and several lacked an optical counterpart. Our goal in this chapter is to increase the number of optical identifications, measure new redshifts and remove non GPS sources present in the list (with the currently available radio data). The sample under consideration is comprised of the unidentified objects from the master list of O’Dea et al. (1991), updated by de Vries et al. (1997a), and consists of all peaked spectrum radio sources having cm flux densities in excess of 0.5 Jy. Here present VLT observations of sources with unknown redshifts or optical counterparts and increase the number of GPS sources (up to  $\sim 90\%$ ) of the complete O’Dea et al. (1991) list. We give new host identifications (down to  $R \sim 25$ ) and obtain several new redshifts. We use  $H_0=71$ ,  $\Omega_M = 0.27$ ,  $\Omega_\Lambda = 0.73$  (Spergel et al. 2003) throughout the chapter.

### 3.2 Observations and data reduction

The sample was observed during two nights (January 30 to 31, 2000, and December 16 to 17, 2001) using VLT’s FORS1/UT1 and FORS2/UT4. We obtained long slit spectroscopy using grism 150I with order separators OG590 and GG375, obtaining a 230 Å/mm dispersion (5.52Å/pix) and covering wavelengths 6000–11000Å(OG590) and 3850–7500Å(GG375). For the photometry we used a *R*-Johnson-Cousins filter for the January 2000 run. For the December run, we used *B*, *V*- Johnson-Cousins and the *R*-Special filters<sup>2</sup>. We covered a 6.8 arcmin field with seeing ranging from 0.5” to 0.7 ” for the January run and 0.5” to 1.1” for the December run.

Standard data reduction was performed using IRAF routines. All the spectra were corrected for bias, flat-field and sky lines. Wavelength calibration was done using internal arc lamps. The flux calibration and removal of atmospheric features were performed using

<sup>1</sup>Chapter 7 presents a study on star formation in hosts of GPS and CSS.

<sup>2</sup>The *R*-Special filter on FORS2 is a Johnson-Cousins filter with a slightly shortened red end to avoid sky emission lines.

the spectrophotometric standards GD50 and GD108.

The calibration of the imaging data was different for the January and December runs. The January observations were done during a photometric night. We took flat field images and observed the Landolt (1992) standard fields PG1323–086 and SA 95. No useful standard fields or flat fields were observed for the –non photometric– December run. To calibrate these images, we averaged all the observations in each filter separately to create *artificial* flat-field images, which we used for the calibration. As standard stars, we chose unsaturated field stars with data in the GSC2.2 catalog ( $\sim 40$  stars in total). The GSC stars have available magnitudes in the photographic F and J bands. The transformation to the Johnson-Cousins filters was performed following Kent (1985). The January images were taken only in R-band. For the December run, most of the standards lacked color information to perform (first order) color coefficient corrections to our apparent magnitudes. We could only fit the zero point magnitudes in each band.

### 3.3 Results

#### 3.3.1 Identifications

The astrometry was performed using the GSC2.2 catalog as reference. It was possible to make accurate (usually with  $1\sigma$  error  $< 0.5$  arcsec) positional determinations for the candidate optical counterparts. As in de Vries et al. (1995) and de Vries et al. (2000a), we use the *likelihood ratio* defined by de Ruiter et al. (1977):

$$R = \sqrt{\frac{\Delta\alpha^2}{\sigma_\alpha^2} + \frac{\Delta\delta^2}{\sigma_\delta^2}} \quad (3.1)$$

where  $\Delta\alpha$  and  $\Delta\delta$  are the measured offsets in RA and Dec between the optical and radio positions,  $\sigma_\alpha^2$  and  $\sigma_\delta^2$  are the sums of the squared  $1\sigma$  errors in the optical and radio positions. An  $R$ -value less than three indicates a probability of less than 1% to miss a true identification (assuming that the optical counterpart is the object closest to the radio position). The probability that a true optical counterpart has an  $R$ -value larger than some  $R_0$  is given by  $P(R > R_0) = e^{-0.5R_0^2}$ . Most of our identifications have  $R$ -values smaller than 3 and are likely to be correct. The optical position used in the calculation of  $R$  and listed in Table 3.1 corresponds to the pixel of the optical object closest to the radio position. The identification results are listed in Table 3.1 and finding charts for the sources are presented in Figure 3.5.

#### 3.3.2 Magnitudes

The magnitudes were extracted performing aperture photometry. We used apertures large enough to include all light from the object (typically a diameter of  $\sim 10$  pixels) but minimizing the contribution from sky. As judged from internal consistency of field stars with known magnitudes, our photometric accuracy varies between 0.1 and 0.4 magnitudes. The main source of error, except for B0008–421, comes from the uncertainties in the magnitudes of the stars used in the calibration. B0008–421 and B0742+103 were observed in the  $R$ -Johnson-Cousins filter in the January 2000 night. It was a photometric night and

Source	Radio (J2000)		Optical (J2000)		R	Magnitude
	RA	Dec	RA	Dec		
B0008-421	00:10:52.52	-41:53:10.8	00:10:52.53	-41:53:10.6	2.1	R 24.3±0.3±0.04
B0316+161	03:18:57.80	+16:28:32.7	03:18:57.82	+16:28:32.9	2.0	B 23.0±0.1±0.2
B0316+161	"	"	03:18:57.82	+16:28:32.6	2.0	V 23.4±0.1±0.1
B0407-658	04:08:20.38	-65:45:09.1	04:08:20.37	-65:45:09.0	1.3	B 22.5±0.04±0.2
B0407-658	"	"	04:08:20.41	-65:45:08.6	3.4	V 21.4±0.03±0.1
B0407-658	"	"	04:08:20.41	-65:45:09.4	3.4	R 20.2±0.06±0.4
B0554-026	05:56:52.62	-02:41:05.5	05:56:52.61	-02:41:05.3	2.6	B 18.3±0.01±0.2
B0554-026	"	"	05:56:52.59	-02:41:05.5	3.3	V 17.5±0.02±0.1
B0554-026	"	"	05:56:52.62	-02:41:05.5	3.2	R 16.4±0.01±0.4
B0742+103	07:45:33.06	+10:11:12.7	07:45:33.06	+10:11:12.5	1.9	B 24.0±0.1±0.2
B0742+103	"	"	07:45:33.06	+10:11:12.3	0.9	V 23.8±0.2±0.1
B0742+103	"	"	07:45:32.97	+10:11:12.8	3.9	R 23.1±0.1±0.04
B0904+039	09:06:41.05	+03:42:41.5	09:06:41.43	+03:42:41.7	2.1	V 24.9±0.3±0.1
B0914+114	09:17:16.39	+11:13:36.5	09:17:16.53	+11:13:31.4	52.6	B 21.3±0.04±0.2
B0914+114	"	"	09:17:16.54	+11:13:32.3	44.4	V 19.9±0.01±0.1

**Table 3.1— Positions of the optical counterparts.** The radio positions are from NED. The ‘R’ factor is the likelihood ratio (see text for details). The optical coordinates of B0914+114 correspond to the galaxy previously - and incorrectly - identified as the counterpart (see notes on individual source). The errors in the magnitudes are divided in photon noise (first error) and calibration (second error). The magnitudes are corrected from galactic extinction, following Schlegel et al. (1998). B0316+161 magnitudes may be affected by close-by ( $\sim 3''$ ) objects.

the larger error in the magnitude of B0008-421 is due to the faintness of the source. The rest of the observations were done in the December 2001 run, which was not photometric. A conservative ( $5\sigma$ ) detection limit is magnitude 25.5 for each band.

Comparison with the Hubble diagram (O’Dea et al. 1996a; Snellen et al. 2002) show that the R magnitudes we measure are consistent with previous observations of GPS hosts. We measure V magnitudes consistent with those from di Serego-Alighieri et al. (1994) although ours tend to be slightly fainter. We have not found published B magnitudes for comparison.

### 3.3.3 Spectra and redshifts

We took spectra of 16 sources to measure their redshifts. Table 3.2 and Figure 3.4 show those sources where emission features were found. We measure redshifts for B0316+161, B0407-658, B0904+039, B1433-040 (with a conservative error of  $\pm 0.001$ ) and B0914+114. Some sources show possible emission lines but their redshifts are uncertain (see notes on each individual object below): B0008-421, 1300-059, and B1045+019. The spectra were too noisy to find emission features for B0437-454, B0742+103, B1601-222 and B1648+015.

### 3.3.4 Stellar synthesis models

We have compared our redshift and magnitude measurements with the Bruzual & Charlot (2003) stellar population synthesis models. Most of our objects are radio galaxies so we expect the contribution from the AGN emission to be minimal: most of the radiation would

Name	ID	Line	Wavelength(Å)	Redshift	Mean	Flux	FWHM	Log Power 5GHz	
B0008-421	G	H $\beta$ 4861	7084	0.457	0.457*	0.2	13	26.7	
		[O III] 5007	7294	0.457		0.3	29		
B0316+161	Q	[O II] 3727	7102	0.906	0.907	5.4	21	27.6	
		[Ne III] 3869	7381	0.908		1.8	32		
		H $\beta$ 4861	9277	0.908		4.7	49		
		[O III] 4959	9464	0.908		8.3	35		
		[O III] 5007	9544	0.906		33	51		
B0407-658	G	[Ne V] 3425	6721	0.962	0.962	11	25	27.7	
		[O II] 3727	7314	0.962		6.9	29		
		[Ne III] 3869	7595	0.963		2.0	44		
		[Ne III] 3967	7787	0.963		0.7	29		
		H $\gamma$ 4102	8048	0.962		0.3	18		
		H $\beta$ 4861	9538	0.962		4.4	52		
		[O III] 4959	9731	0.962		43	51		
		[O III] 5007	9823	0.962		16	54		
		B0904+039	G	[O II] 3727		6822	0.830		0.830
[O III] 4959	9078			0.831	1.8	26			
[O III] 5007	9162			0.830	4.4	26			
B0914+114	G	Break 4000	4711	0.178	0.178	–	–	–	
		H $\beta$ 4861	5690?	0.171?	$\pm 0.005$	–	–		
		Mgb 5200	6115	0.183	–	–			
		[N II] 6548	7667	0.171	–	–			
		H $\alpha$ 6563	7772	0.184	–	–			
		[S II] 6716	7952	0.184	–	–			
B1045+019		[O II] 3727	6297	0.689	0.689*	0.4	12	26.6	
		H $\gamma$ 4102	7327	0.688		0.3	12		
		[He II] 4686	7918	0.689		0.3	29		
1300-1059	Q?	[Mg II] 2799	6385	1.283	1.283*	10	125	–	
B1433-040	Q	[O II] 3727	6694	0.796	0.795	17	19	26.3	
		[Ne III] 3869	6949	0.796		32	54		
		[Ne III] 3967	7122	0.795		10	21		
		H $\delta$ 4102	7355	0.794		23	84		
		H $\gamma$ 4341	7790	0.795		76	113		
		H $\beta$ 4861	8724	0.795		347	192		
		[O III] 4959	8900	0.795		63	30		
		[O III] 5007	8987	0.795		121	27		

**Table 3.2.— Line identifications and redshifts.** For B1433–040, the redshift is measured with the narrow emission profiles. The \* means the redshift estimation is uncertain for that source, see text for details. The FWHM listed is the observed FWHM corrected from the FWHM of the instrumental spectrum. Fluxes in  $10^{-16}$  erg/cm<sup>2</sup>/s. A conservative error for  $z$  is  $\pm 0.001$ . The B0914+114 results correspond to the unrelated galaxy. It shows emission and absorption lines mixed so the centers are more uncertain than in the other sources (the  $1\sigma$  error in  $z$  is listed below the mean value) and line properties will depend on the stellar population model. The last column lists the radio power in W/Hz of the source for the redshifts listed. The 5GHz fluxes are from O’Dea (1998) and Wright & Otrupcek (1990).

be associated with stars in the host. Furthermore, previous work (O’Dea et al. 1996a; Snellen et al. 1996) find the R (and K) band magnitudes to be dominated by the host’s stellar population for these sources.

The models have been run using the Chabrier (Chabrier 2003) initial mass function, metallicities  $Z=0.008$ ,  $Z=0.02$ ,  $Z=0.05$  and ages (time since the initial starburst) ranging from 5 to 12.5 Gyr. Different star formation histories have been used: instantaneous burst, exponentially declining, and constant star formation. We fitted colors B-V and V-R for those sources where the color information was available, and magnitudes when color information was not available. The hosts of GPS/CSS are usually massive elliptical galaxies (e.g., de Vries et al. 2000a) so we used masses of  $10^{11}$  and  $10^{12} M_{\odot}$  to fit those sources without color information.

Constant and exponentially declining star formation models seem to be ruled out by our data. The data points and best models disagree by roughly 2 magnitudes for sources without color information and 0.5–1 magnitude for those sources with color information. The data show better agreement with the instantaneous burst models. However our observed colors are predicted by instantaneous burst models with ages of  $\sim 6$  Gyr and metallicity 0.05, as well as ages of  $\sim 12$  Gyr and metallicity 0.008; and consequently, all the intermediate models. The probable contribution from emission line gas and this degeneracy between metallicities and ages makes it almost impossible to choose among the instantaneous burst models.

### 3.4 Notes on individual sources

*B0008–421*: Following unsuccessful attempts by di Serego-Alighieri et al. (1994), de Vries et al. (1995) and Costa (2001), we have now identified the bright radio source B0008–421 with an  $R=24.3$ , somewhat diffuse galaxy. We detect a faint object,  $0.2''$  from the VLBI position. The spectrum is consequently faint and very noisy making it difficult to distinguish real emission lines from noise. We only find one possibility for redshift:  $z=0.457$ . Comparison with the GPS Hubble diagram (O’Dea et al. 1996a) shows that for a redshift between 0.4 and 0.5, we would expect an apparent R magnitude around 19 or 20. Our magnitude is consistent with previous non-detections (with limits down to 23 magnitudes) and, according to O’Dea et al. (1996a) the redshift of the object would be around 1.1.

*B0316+161*: Our deep image confirms the earlier identification of this well known GPS radio source, (also known as CTA21), by Stanghellini et al. (1993). We find a rather compact host, and note in passing that the object seen  $8''$  NNW of the CTA21 identification in the Stanghellini et al. image is spurious. The relative faintness of B0316+161, and the proximity ( $\sim 0.3''$ ) of other objects, may be affecting our measured magnitudes. The spectrum shows a weak continuum with bright [O II] and [O III] lines. We measure  $z=0.907$  based on five lines.

*B0407–658*: Stickel et al. (1996) identified the optical counterpart of this radio source as a galaxy. The spectrum shows a faint continuum spectrum where we identify nine emission lines at  $z=0.962$ . With this redshift, the emission line gas extends  $3.2'' = 25$  kpc

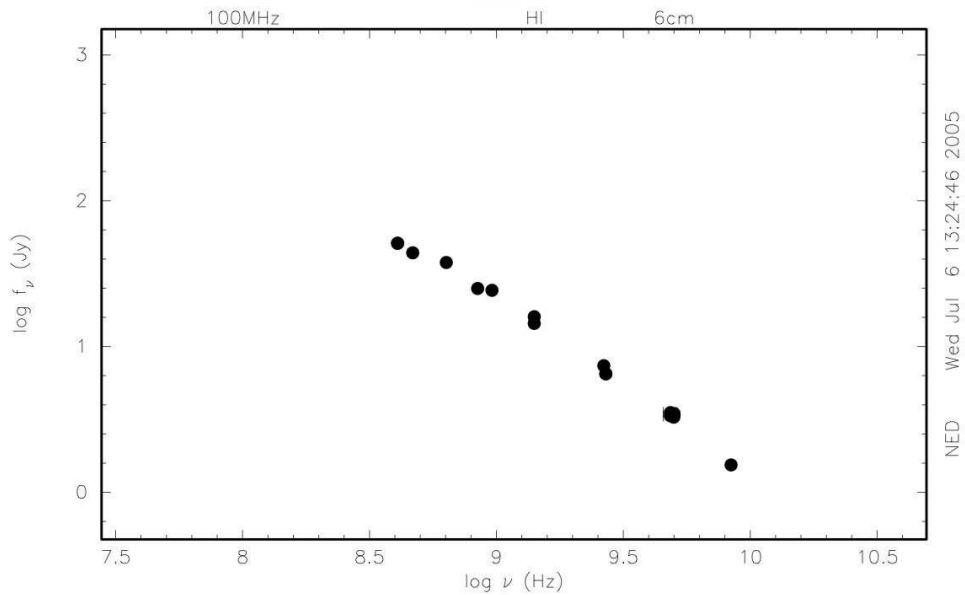


**Figure 3.1–.** Radio spectrum of B0407–658. From NED.

along the slit. We observe no shift in wavelength along the spatial direction in the spectra. A 2 pixel resolution yields a velocity resolution limit of  $\sim 500$  km/s for the central part of the spectrum. Although this source has been classified as GPS previously (e.g. O’Dea et al. 1991), the radio spectrum (Figure 3.1) shows no peak. It is probably a CSS source or a larger radio source. However, ATCA observations have not resolved it (resolution  $\sim 5 \times 3''$ , Morganti et al. 1993).

*B0437–454:* Bright continuum but no emission lines. One possible line at  $9539 \text{ \AA}$ , probably a cosmic ray. If it were [O III] (at  $z=0.905$ ), we would not be detecting [O II]  $3727$  (which should be at  $7100 \text{ \AA}$  for that redshift). A literature search indicated that the radio spectrum of B0437–454 is only marginally peaked. In addition, pronounced variability was reported: 0.6 Jy vs. 1.4 Jy at 5 GHz. Also given the identification with an optical point source, we conclude that the object is a BL Lac object and should be removed from the GPS list.

*B0554–026:* We confirm the identification of de Vries et al. (2000b) ( $z=0.283$ ) of this galaxy. We find a rather bright ( $B=18.3, V=17.5$ ) and extended source ( $\sim 5''$ ). We obtain  $R = 16.4$  but this band may be affected by calibration problems (see Section 3.3.2).

*B0742+103:* Neither Stickel et al. (1996) nor de Vries et al. (1995) were able to identify the host of this relatively bright radio source. Our UT1 image, which unambiguously identifies the source with a compact host galaxy, indicates that the Fugmann et al. (1988)

and de Vries et al. (2000b) near-identifications were correct: we establish  $R=23.1$ . We took long slit spectra of this source both in the January and the December run. Both observations show a faint spectrum and features which could be lines. However, none of these features are present in both spectra. Best et al. (2003) measure  $2.624 \pm 0.003$  based on Ly  $\alpha$ , C IV, He II and C III] between 4400 and 6920 Å. We detect a faint (slightly brighter than noise) emission at 6922 Å which could be the Best et al. (2003) C III]. Having only one emission feature, we cannot get an independent redshift measurement. If their redshift is correct, using the 5GHz flux density from O’Dea (1998), the source would have a radio power of  $2.1 \times 10^{28}$  W/Hz.

*B0904+039*: The deep UT1 image reinforces the earlier identification of this GPS radio source (de Vries et al. 2000a,  $I=22.5$ ) with a faint host ( $V=24.90$ ) in a group of faint galaxies. The spectrum shows a weak continuum. We measure  $z=0.830$  based on the [O II] and [O III] lines.

*B0914+114*: Our B and V band images show an empty field at the radio coordinates. Stanghellini et al. (1993) emphasize that the WSRT declination coordinate is affected by the elongated N-S beam for low declination sources and suggest that the disk galaxy  $\sim 6''$  south of the radio position could be the host of the radio source. The FIRST and NVSS surveys agree with the Texas/WSRT position for the radio source. Furthermore, this optical galaxy does not show a radio counterpart in the FIRST image ( $5\sigma$  detection limit of 0.9 mJy). Thus, the disk galaxy is not the optical identification. In fact our VLT observations show an empty field at the radio position. We did obtain a spectrum of the disk galaxy which shows a faint stellar dominated continuum. The low signal to noise makes it impossible to study the stellar population producing it. We observe a narrow H $\alpha$  in emission on top of a broad absorption which also may be affecting [N II] and [S II] emission. H $\beta$  also shows an emission line on on top an absorption line. The fainter emission and absorption of H $\beta$  and the low signal to noise makes it really hard to obtain an accurate center for this line. Lacking a good stellar population model for the object, we cannot measure accurate fluxes or FWHM for the lines. Averaging the redshifts of all the observed features, we obtain  $z=0.178$ . The H $\alpha$  emission at 7772 Å had been detected before (de Vries et al. 1998b). However, this galaxy is not the counterpart of the GPS source.

*B1045+019* The weak continuum and noisy spectrum makes it difficult to distinguish real emission lines from noise. We only find one –dubious– possibility for redshift ( $z=0.689$ ). If this redshift is correct, we are not detecting H $\beta$  and [O III] 5007 (at 8200 and 8550 Å respectively). Radio observations were discussed in de Vries et al. (2000a) suggesting that this radio source may not be a GPS.

*B1300–019*: We find one emission line at 6385 Å. The emission may consist on a narrow ( $\sim 80$  Å) and a broad ( $\sim 200$  Å) component but the edge of the chip is too close to deblend it accurately. We think this line may be Mg II  $\lambda$  2799 at  $z=1.283$ , and in that case the [O II] doublet at 3727 Å is not detected. If it were [C IV] $\lambda$ 1549, we would expect [C III] $\lambda$ 1909 at 7826 Å. The relatively bright continuum suggests a QSO, which would be consistent with broad Mg II .

*B1433–040*: de Vries et al. (2000a) already drew attention to the fact that the GPS source

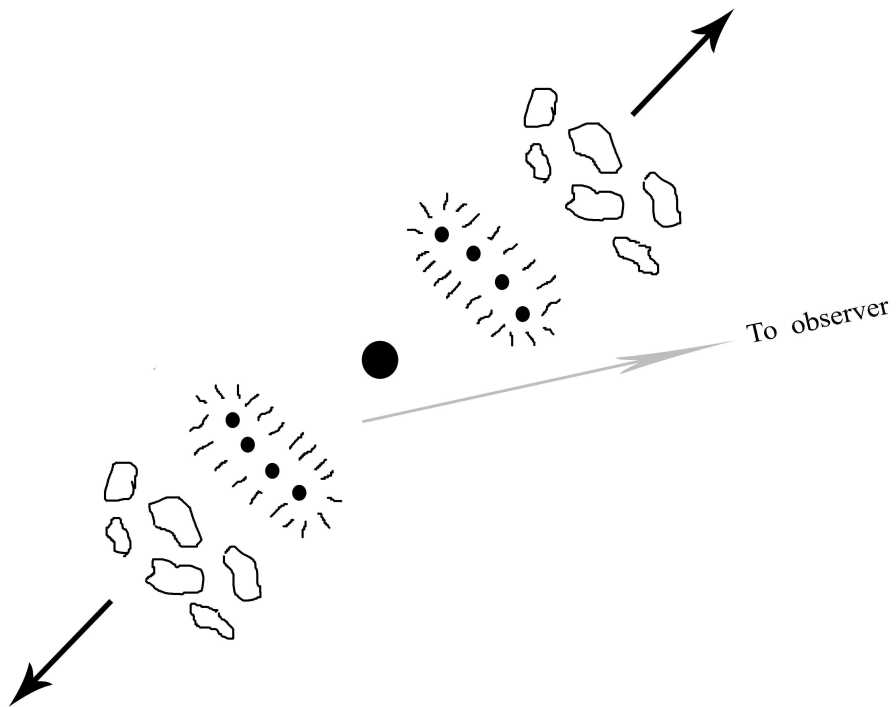


**Figure 3.2-** Model of how the asymmetry in emission gas can be produced (Whittle 1985). The black circle in the middle represents the center of the AGN. We have the two outgoing jets with emitting gas (small circles) and further away in the jet we have a line absorber (or scattering) source (white blobs) which blocks (or scatters) the emission in the direction of the jet. If the line of sight of the observer is close to the direction of the jet, the absorbing clouds block the emission of the incoming jet, but not from the furthest jet. This distribution (absorber in the jet *behind* the emitter) would produce the red asymmetry wing we see in 1433–040. If the absorber were *in front of* the emitter in the jet, we would see a blue wing.

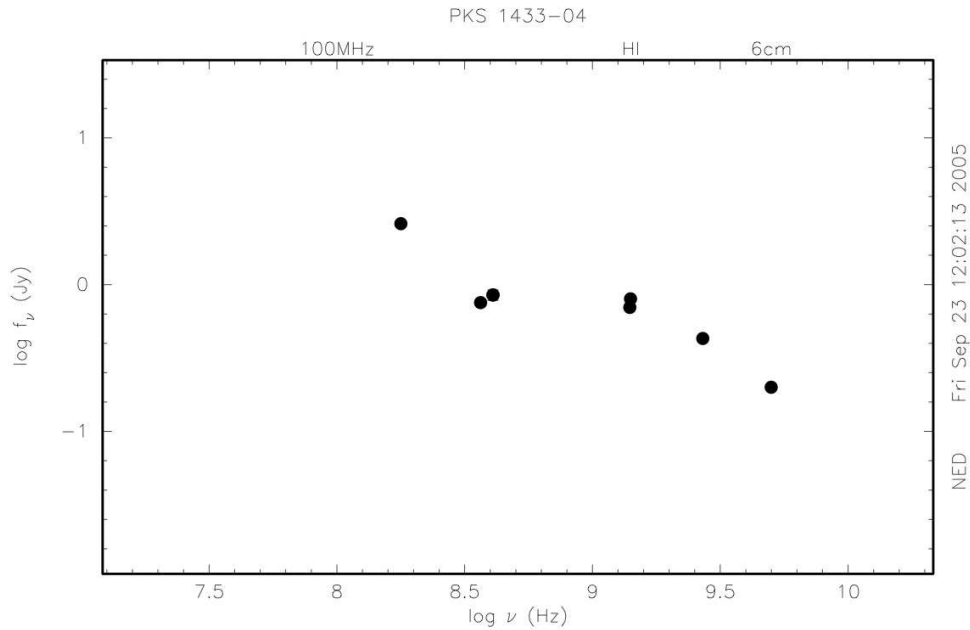


**Figure 3.3–.** Radio spectrum of B1433–040. From NED.

B1433–040 should not be identified with the considerably brighter radio source 4C–04.51. The optical spectrum shows a very strong continuum. Broad ( $\sim 200\text{\AA}$ ) and narrow ( $\sim 30\text{\AA}$ ) emission lines. The spectral shape and presence of bright broad lines is consistent with a QSO. We observe a strong asymmetry in the broad emission. The asymmetry index (AI20, Heckman et al. 1981) is defined as  $(W_{L20} - W_{R20}) / (W_{L20} + W_{R20})$ , where  $W_{L20}$  is the half width of the line to the left (L) and right (R) at the 20% intensity level. We measure  $AI_{20} \sim 0.35$ , towards the red, for  $H_{\beta}$  (and  $H_{\gamma}$ ), which is large, but not unusual. This asymmetry can be explained by inflow or outflow of gas, together with a line opacity (or scatter) cloud which blocks the emission at one side of the AGN (e.g Whittle 1985, and references therein; see Figure 3.2). The optical spectrum of this radio source displays hydrogen emission lines of striking velocity width: we measure 28000 km/sec FWZI for  $H_{\beta}$ , and note in addition its double-peaked nature. Although the radio spectrum seems to peak around 1 GHz (Figure 3.3, the high flux observed at 178 MHz suggests that B1433–040 is not a GPS source. It may be a flat spectrum quasar where Doppler boosting is affecting the spectrum, or even a BL Lac: there seems to be some variability in the 408 MHz and  $\sim 1.4\text{GHz}$  (Large et al. 1981; Wright & Otrupcek 1990; White & Becker 1992) observed fluxes. Given the unresolved optical host, we suggest that the optical counterpart of B1433–040 is a quasi-stellar object at  $z=0.796$ .

*B1601–222*: Featureless, very noisy spectrum with a moderately bright continuum. Snellen et al. (2002) measure  $z = 0.141$  based on G 4300, Mgb 5169, Na 5899 and  $H_{\beta}$  which

correspond to  $\sim 4900\text{--}5550\text{\AA}$ . We covered the range between 5700 and 9200  $\text{\AA}$  and observe no emission ( $H\alpha$  with their redshift would be at 7488 $\text{\AA}$ ).

*B1648+015*: Featureless with a not very bright continuum. Stickel et al. (1996) identifies this source as a quasar. The radio spectrum shows a very variable source so it is probably a flat spectrum quasar or a BL Lac object.

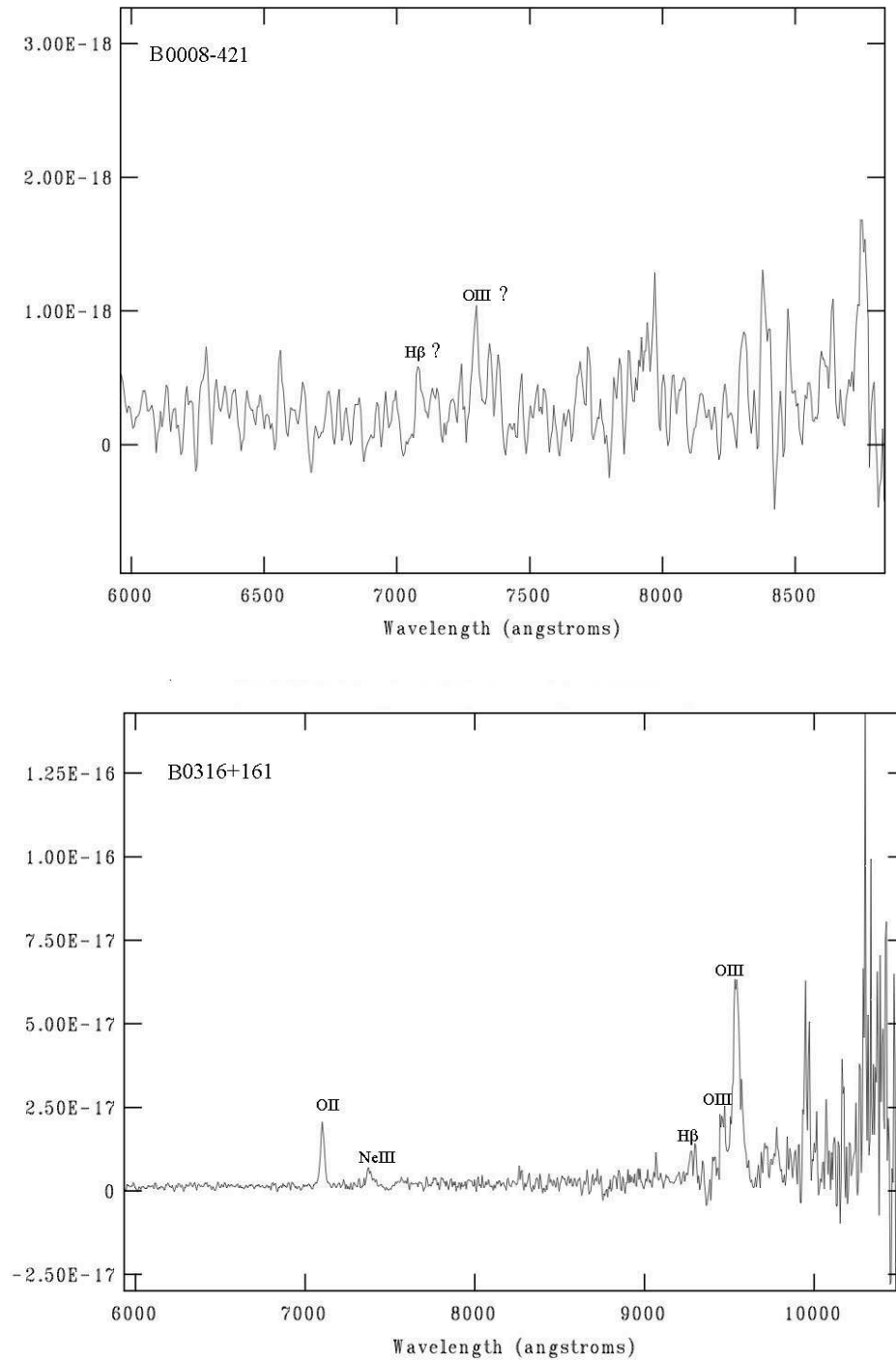
### 3.5 Summary

We presented VLT deep optical imaging and spectroscopy targeting the host galaxies of GPS radio sources. The sample was comprised of unidentified objects from the master list of O’Dea et al. (1991), updated by de Vries et al. (1997a).

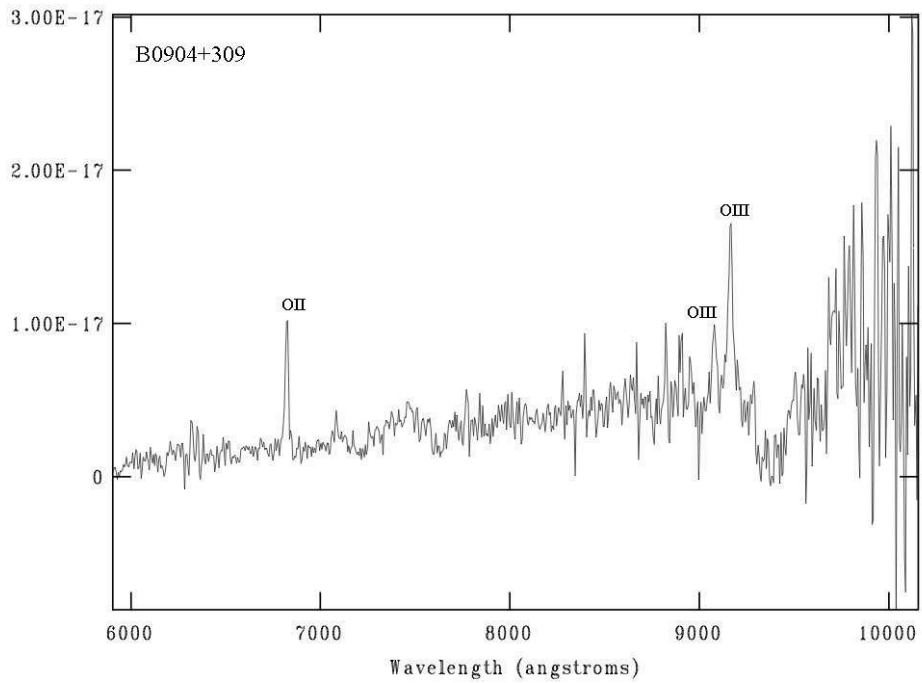
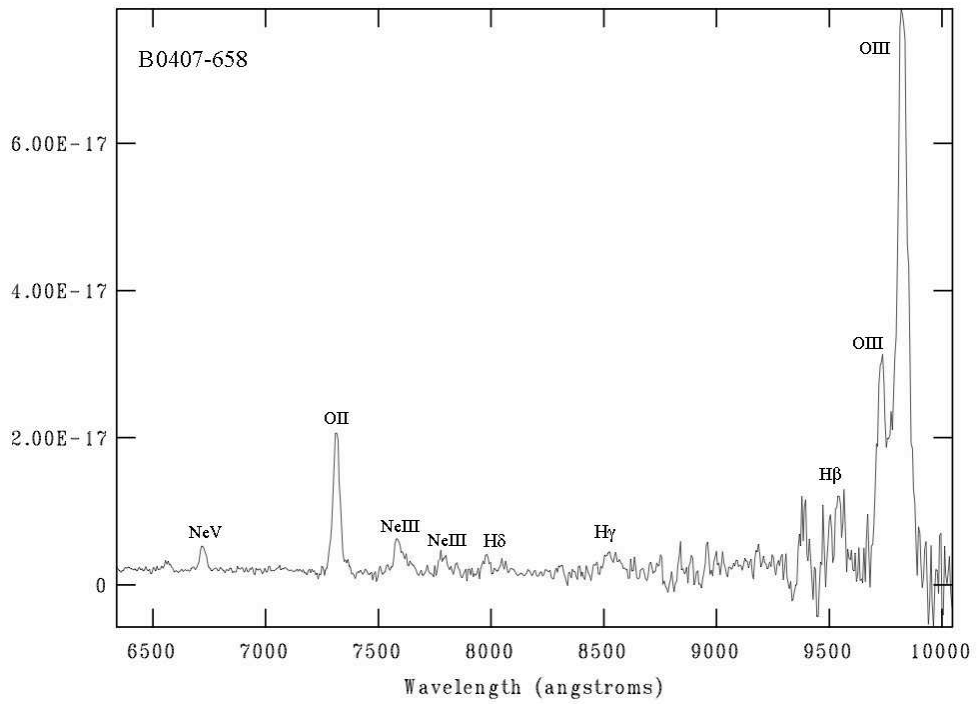
We have found new optical counterparts (down to magnitudes  $\sim 25$ ) of GPS sources B0008–421 and B0742+103 and confirmed previous identifications of GPS sources: B0316+161, B0407–658, B0554–026, B0904+039. The radio spectra of B0407–658, B0437–454, B1433–040 and 1648+015 suggest that these sources are not GPS. However, high resolution radio observations are needed to confirm it. We cannot find the optical counterpart of B0914+114 and suggest that previous *identifications* correspond to an unrelated galaxy (at  $z=0.178$ ), 6’’ south of the radio position.

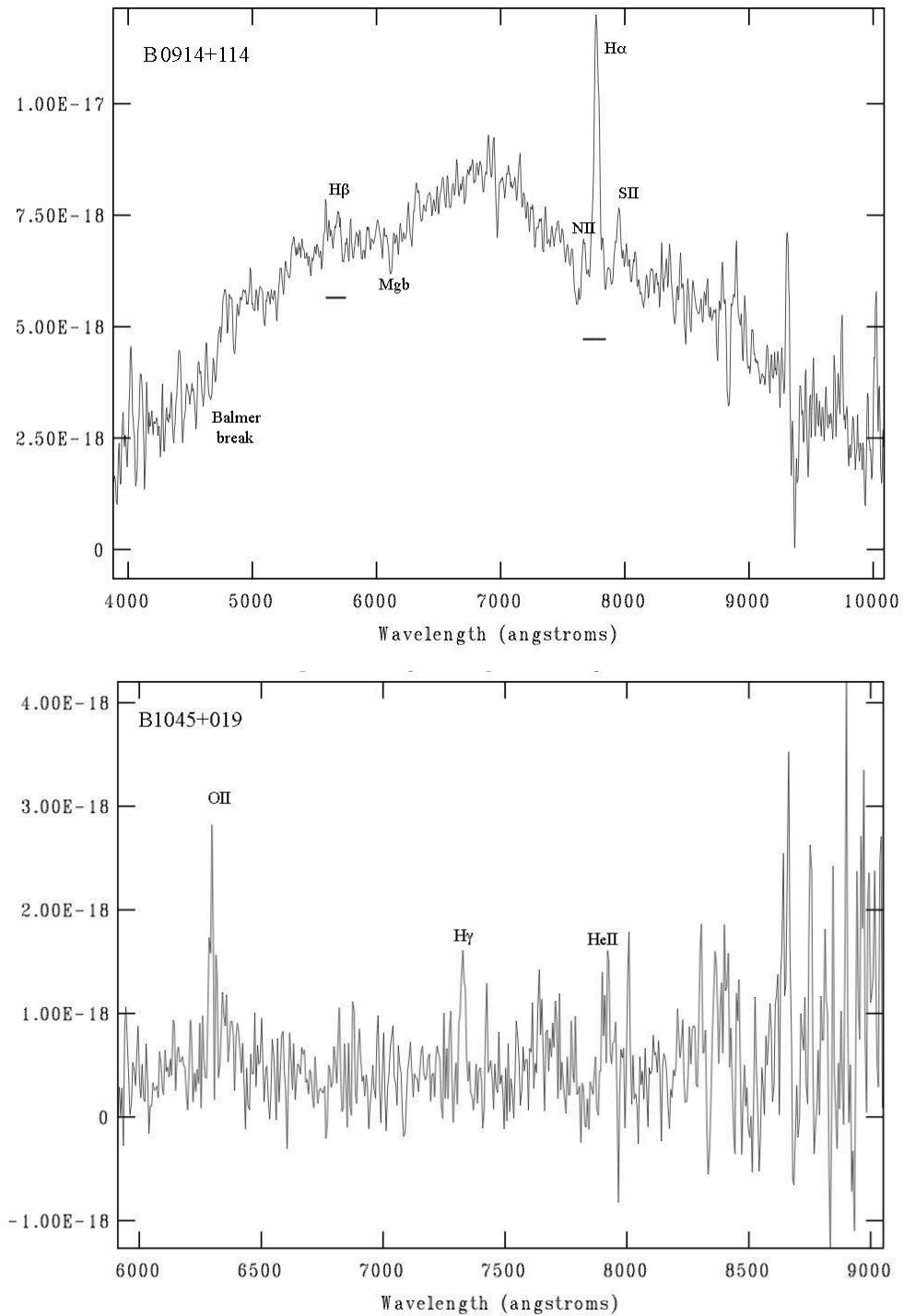
We measure new redshifts for B0316+161, B0407–658, B0904+039, B0914+114 (unrelated galaxy) and B1433–040, uncertain redshifts for B0008–421, B1045+019, 1300–059. The following sources remain with undetermined redshift: B0437–454, B0914+114 and B1648+015. We cannot confirm previous redshifts of: B0742+103, B1601–222.

Our magnitudes seem to be consistent with previous measurements of GPS counterparts. We find redder V–R colors for some sources but this can be due to problems in the calibration of the *R*-band observations. Comparison with stellar population synthesis models seem to rule out constant or exponentially declining star formation in the host. The data generally agree with single instantaneous burst models but do not yield useful information on age or metallicity.

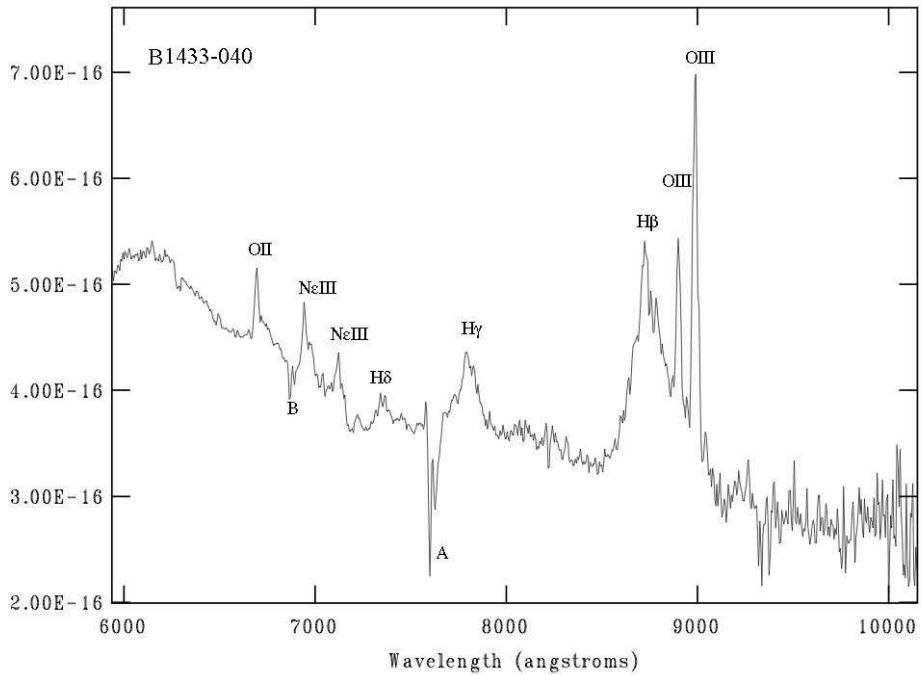
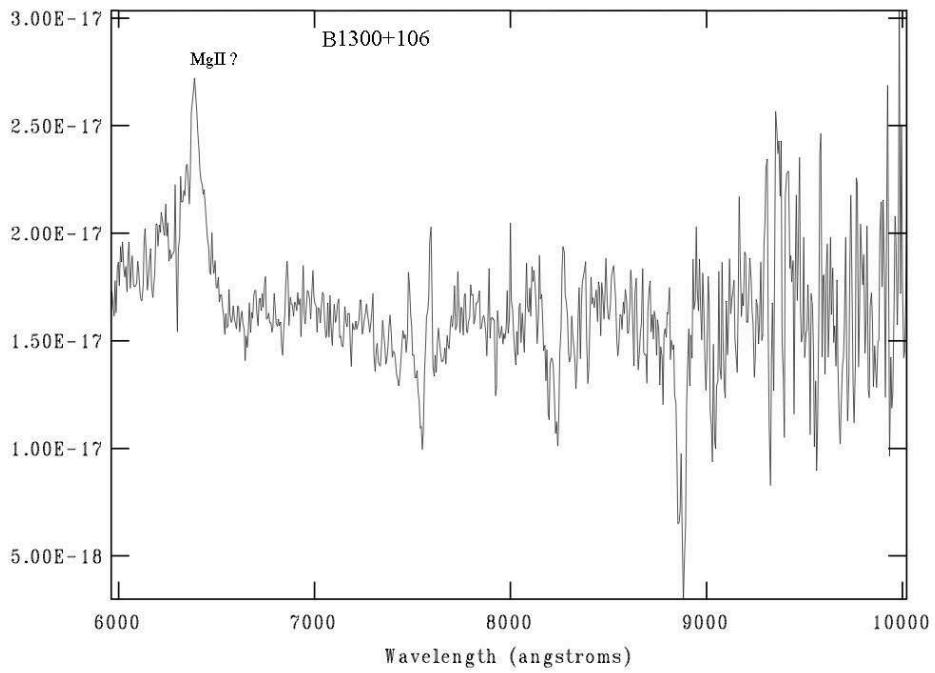


**Figure 3.4.** Spectra of the sources with identified emission lines. Flux is in  $\text{erg cm}^{-2} \text{s}^{-1} \text{\AA}^{-1}$ .

**Figure 3.4.-** Continued.



**Figure 3.4-.** Continued. B0914+114: The horizontal lines show an estimation of the possible extent of the absorption Hydrogen lines.

**Figure 3.4-** Continued.

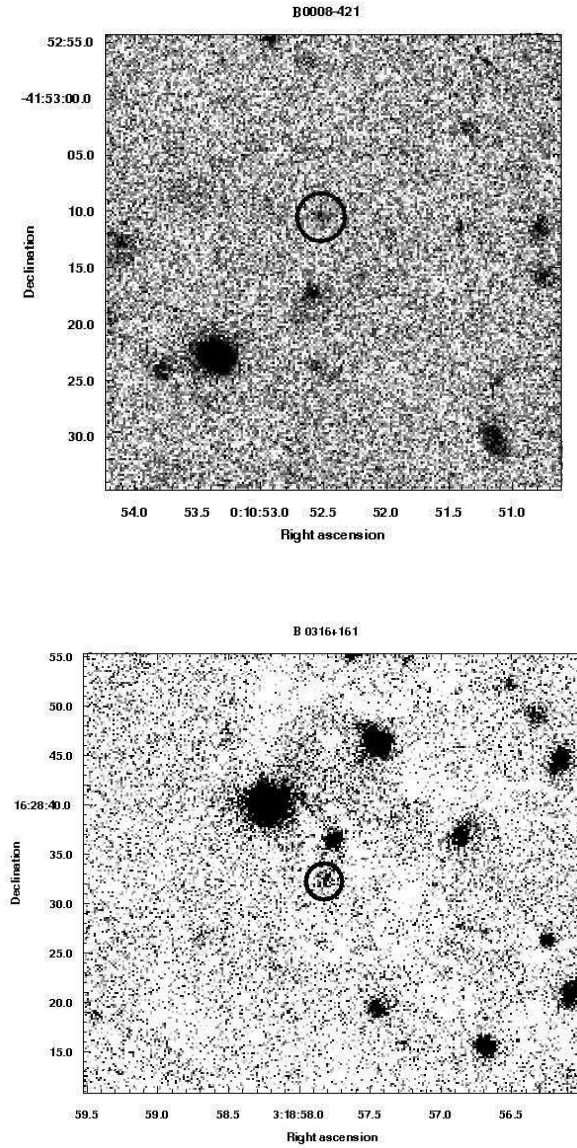


**Figure 3.5**— Finding charts for the identified sources. The images correspond to the band of our VLT observations where sources were brighter.

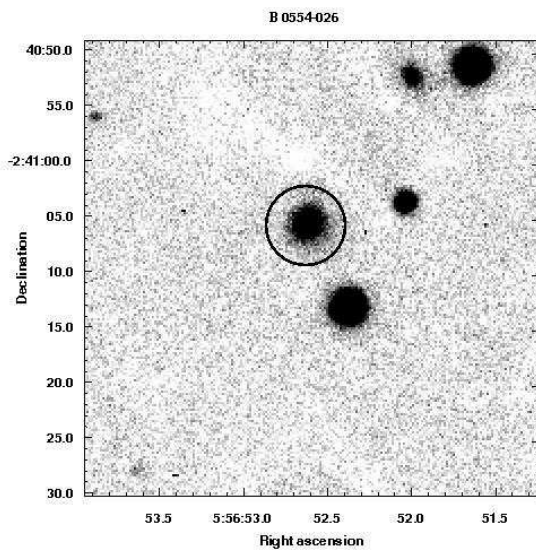
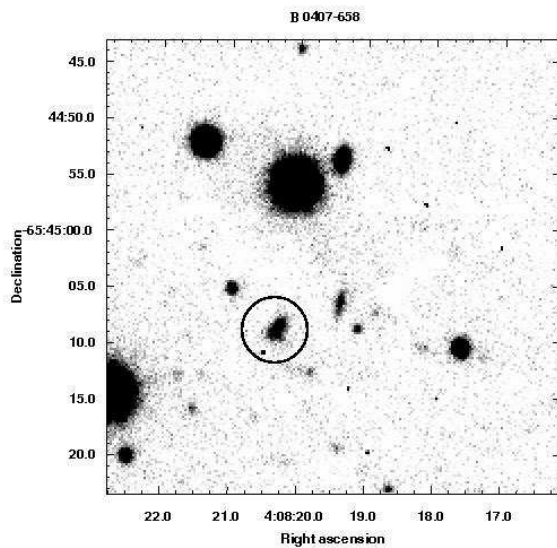


Figure 3.5-. Continued.

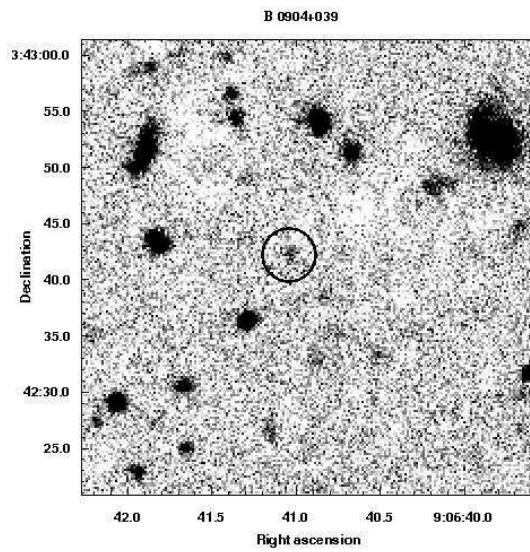
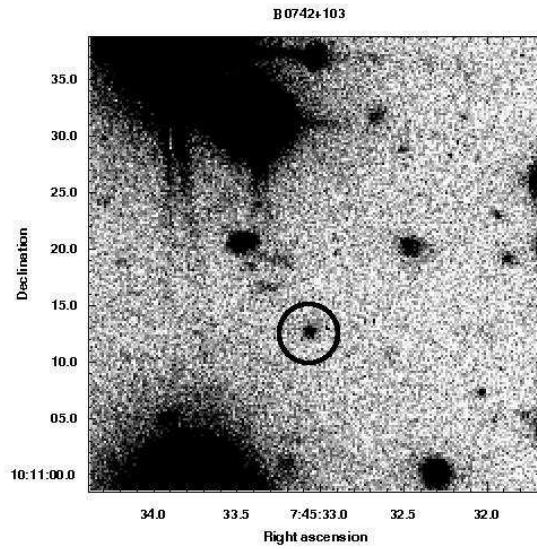
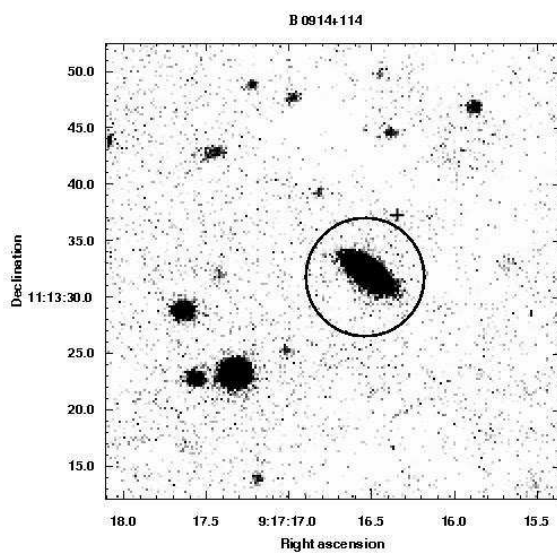


Figure 3.5-. Continued.



**Figure 3.5-.** Continued. The radio position of 0914+114 is 6'' north of the observed galaxy (circled) which was previously - and incorrectly - identified as the optical counterpart (see text). The radio position is marked with a cross.



# 4

---

## HST/STIS low dispersion spectroscopy of three CSS sources: Evidence for jet-cloud interaction

A. Labiano, C.P. O’Dea, R. Gelderman, W.H. de Vries, D.J. Axon, P.D. Barthel, S.A. Baum,  
A. Capetti, R. Fanti, A.M. Koekemoer, R. Morganti, C.N. Tadhunter.  
ASTRONOMY & ASTROPHYSICS, 436, 493 (2005)

**W**E present Hubble Space Telescope Imaging Spectrograph long-slit spectroscopy of the emission line nebulae in the compact steep spectrum radio sources 3C 67, 3C 277.1, and 3C 303.1. We derive BPT (Baldwin- Philips-Terlevich; Baldwin et al. 1981) diagnostic emission line ratios for the nebulae which are consistent with a mix of shock excitation and photo-ionization in the extended gas. In addition, line ratios indicative of lower ionization gas are found to be associated with higher gas velocities. The results are consistent with a picture in which these galaxy scale radio sources interact with dense clouds in the interstellar medium of the host galaxies, shocking the clouds thereby ionizing and accelerating them.

## 4.1 Introduction

Powerful radio galaxies play a critical role in our understanding of both galaxy evolution and the phenomenon of activity in galactic nuclei. Yet we know little about how the radio galaxies are born and how they subsequently evolve. Recent work has identified the GHz Peaked Spectrum (GPS) and Compact Steep Spectrum (CSS) radio sources as the most likely candidates for the progenitors of the large scale powerful classical double (FR2) sources (e.g. O’Dea et al. 1991; Fanti et al. 1990, 1995; Readhead et al. 1996b,a; O’Dea & Baum 1997); for a review see O’Dea (1998). The GPS and CSS sources are powerful but compact radio sources whose spectra are generally simple and convex with peaks near 1 GHz and 100 MHz respectively. The GPS sources are contained within the extent of the optical narrow emission line region ( $\lesssim 1$  kpc) while the CSS sources are contained within the host galaxy ( $\lesssim 15$  kpc).

Current models for the evolution of powerful radio galaxies suggest that these sources propagate from the  $\sim 10$  pc to Mpc scales at roughly constant velocity through an ambient medium which declines in density as  $\rho(R) \propto R^{-2}$  while the sources decline in radio luminosity as  $L_{rad} \propto R^{-0.5}$  (Fanti et al. 1995; Begelman 1996; Readhead et al. 1996a; De Young 1997; Kaiser et al. 1997; Kaiser & Alexander 1997; Snellen et al. 2000). Such a scenario is consistent with the observed number densities of powerful radio sources as a function of linear size (from tens of parsecs to hundreds of kpc) (e.g. O’Dea & Baum 1997; Fanti et al. 2001). However, the situation must be more complicated than this simple picture. We give two reasons: (1) The GPS and CSS sources must interact with the host galaxy as they propagate through it. The discovery of emission line gas aligned with and presumably co-spatial with the CSS radio sources and the presence of broad and complex integrated emission line profiles (Gelderman & Whittle 1994) indicates that the radio source is strongly interacting with the ambient gas (de Vries et al. 1997b, 1999; Axon et al. 2000). Therefore, we would expect shocks to contribute strongly to the ionization of the gas (e.g. Bicknell et al. 1997). (2) The GPS sources are observed to have expansion velocities several times higher (Conway 1998, private communication) than the estimated advance speeds of large scale classical doubles (Alexander & Leahy 1987). This would require the evolving GPS sources to decelerate as they propagate through the host galaxy and would require the radio sources to dim faster than the simple models predict. It may be that the deceleration takes place via interaction with ambient gas (see De Young 1993; Carvalho 1994, 1998).

We are carrying out a study of the kinematics and ionization of the aligned emission line nebulae in three CSS radio sources: 3C 67 (galaxy,  $z = 0.310$ , linear size  $D=10.1$  Kpc), 3C 277.1 (quasar,  $z = 0.321$ ,  $D=6.9$  Kpc), 3C 303.1 (galaxy,  $z = 0.267$ ,  $D=6.2$  Kpc)<sup>1</sup> with HST/STIS long-slit spectroscopy. In O’Dea et al. (2002) we presented our results on the kinematics of the [O III]  $\lambda 5007$  emission line and found complex emission line profiles and large differences in velocity offset on the two sides of the nucleus, suggesting that the cloud motions are being driven by shocks induced by the expanding radio lobes. In O’Dea et al. (2003) we discussed two models for the cloud kinematics - (1) acceleration by the radio source bow shock and (2) acceleration by the post bow shock wind, and concluded that the bow shock acceleration was favored. Here we present the results of our low dispersion

---

<sup>1</sup>We adopt a Hubble constant of  $H_0 = 75 \text{ km s}^{-1} \text{ Mpc}^{-1}$  and a deceleration parameter of  $q_0 = 0.0$ .

Source	Grism	Central $\lambda$ Å	PA Degrees	Time Sec
3C 67	G750L	7751	17	2160
3C 67	G430L	4300	17	2660
3C 277.1	G750L	7751	311	2340
3C 277.1	G430L	4300	311	2800
3C 303.1	G750L	7781	331	2900
3C 303.1	G430L	4300	331	5300

**Table 4.1–. Journal of HST/STIS Observations.** HST proposal ID=8104. The slit was placed parallel to the radio source axis.

spectra of several diagnostic emission lines. We compare our results with shock and photo-ionization models and examine the relationships between the ionization diagnostics and the gas kinematics.

## 4.2 Observations

We obtained STIS long slit spectra through the  $52'' \times 0.1''$  slit through several gratings. The instrumental parameters are summarized in Table 4.2. The observations through the medium dispersion G750M grism has been used primarily to study the kinematics of the nebula and are discussed by O’Dea et al. (2002). For the study of the ionization, we observed through the low dispersion G750L (5236 to 10266Å) and G430L (2900 to 5700Å) grisms centered on 7751Å and 4300Å, respectively, with a spectral resolution of 5Å/pixel and a Line Spread Function (LSF) of 2.0 pixels resulting in a velocity resolution of  $\sim 700$  km/s at the center of the blue side of the spectra and  $\sim 390$  km/s at the center of the red side<sup>2</sup>. The spatial resolution is given by the Point Spread Function (PSF) of the detector, with a FWHM of 2.3 pixels.

We integrated for one orbit on each slit position ( $\sim 2500$ – $3000$  sec) with the orientation taken roughly parallel to the radio source axis. In each source one slit was centered on the source nucleus and aligned along the radio axis. In 3C 67 and 3C 303.1, where the emission line gas is slightly misaligned with respect to the radio axis, we rotated the slit to place it along the emission-line nebula axis, rather than the radio source axis.

## 4.3 Data reduction

The standard STIS reduction pipeline was used to remove detector signatures such as bias, dark current, and flat fielding and to apply the flux calibration. Cosmic ray hits can be quite numerous over the course of orbit-long exposures. We therefore split each exposure per orbit into two equal-length parts in order to allow removal of cosmic rays. Any surviving cosmic rays were removed and replaced by the average of the flux values in the adjacent pixels

<sup>2</sup>Corrected for redshift.

around the cosmic ray.

To correct the spatial dispersion of the light produced by the spectrograph (given by the PSF) we have averaged (weighted by the flux errors given by the spectrograph) three pixels in the spatial direction for every source. We also averaged all the rows in each lobe for each source, to produce an *average* lobe spectrum for each side of the source.

We used the IRAF/STSDAS *Specfit* (Kriss 1994) software to fit Gaussians to the profile of each emission line in our sources (Table 4.2 and Figures 4.1, 4.2 and 4.3) measuring each line's integrated flux, full width at half maximum (FWHM) and central wavelength (i.e., velocity offset relative to the nucleus). Some constraints were adopted to reduce the number of free parameters and limit our options to "physically consistent models", as follows: We classified the detected lines in the spectrum as either high or low ionization (see Table 4.2). We required all gas with same ionization state to have the same FWHM and velocity offset, and took as free parameters the widths and velocities of  $H\beta$  and  $[O\text{ III}]\lambda 5007$ . The integrated fluxes of every line were free to vary except for those with known ratios (from atomic physics, see e.g., Osterbrock 1989), in this case: the  $[N\text{ II}]\lambda\lambda 6548,84$  and  $[O\text{ III}]\lambda\lambda 4959,5007$  doublets. We used a power law to fit the continuum. Whenever this model was not accurate enough in parts of the spectrum, we limited the fit to the adjacent regions of each emission line, improving our continuum model and producing accurate fits for the line profiles. Only a few of the potential emission lines (Table 4.2) were detected in the extended nebulae (signal to noise ratio  $> 3$ ) – the  $[O\text{ II}]\lambda\lambda 3727,29$  doublet,  $H\alpha$ ,  $H\beta$ ,  $[O\text{ III}]\lambda\lambda 4959,5007$  and the  $[N\text{ II}]\lambda\lambda 6548,84$ ,  $[S\text{ II}]\lambda\lambda 6716,31$  doublets<sup>3</sup>. Upper limits were defined to be three times the noise of the spectrum, multiplied by the width of the line:  $3 \times \text{RMS} \times \text{FWHM}$ . We used the width we measured in the resolved lines of the same ionization status.

*Specfit* is known to overestimate the errors for flux and central wavelength measurements in our data. To improve the estimation of our error bars we created over one hundred artificial spectra consisting of a perfect Gaussian with known random white Gaussian noise added, which covered the parameter space of our data in signal to noise ratios and resolution. We created ten artificial spectra for each different signal to noise ratio and ran *Specfit* on each spectrum. We compared the *Specfit* derived errors with those expected based on the parameters of the artificial spectra and estimated a correction to the *Specfit* errors. The final step in the data reduction was correcting the data for reddening, using the Galactic dereddening curve in Cardelli et al. (1989) and the measured Galactic extinction values of Schlegel et al. (1998).

O'Dea et al. (2002) searched for the possible presence of faint, broad wings ( $\gtrsim 1500 - 2000$  km/s) using the low dispersion data, that might have been undetected in the higher dispersion data. They found no strong evidence for broad, non-Gaussian components substantially above  $\sim 1500$  km/s in any of these galaxies.

---

<sup>3</sup>We have detected the  $[S\text{ II}]\lambda\lambda 6716,31$  emission in very few points of the sources and our low wavelength resolution does not allow us to deblend the doublet components.

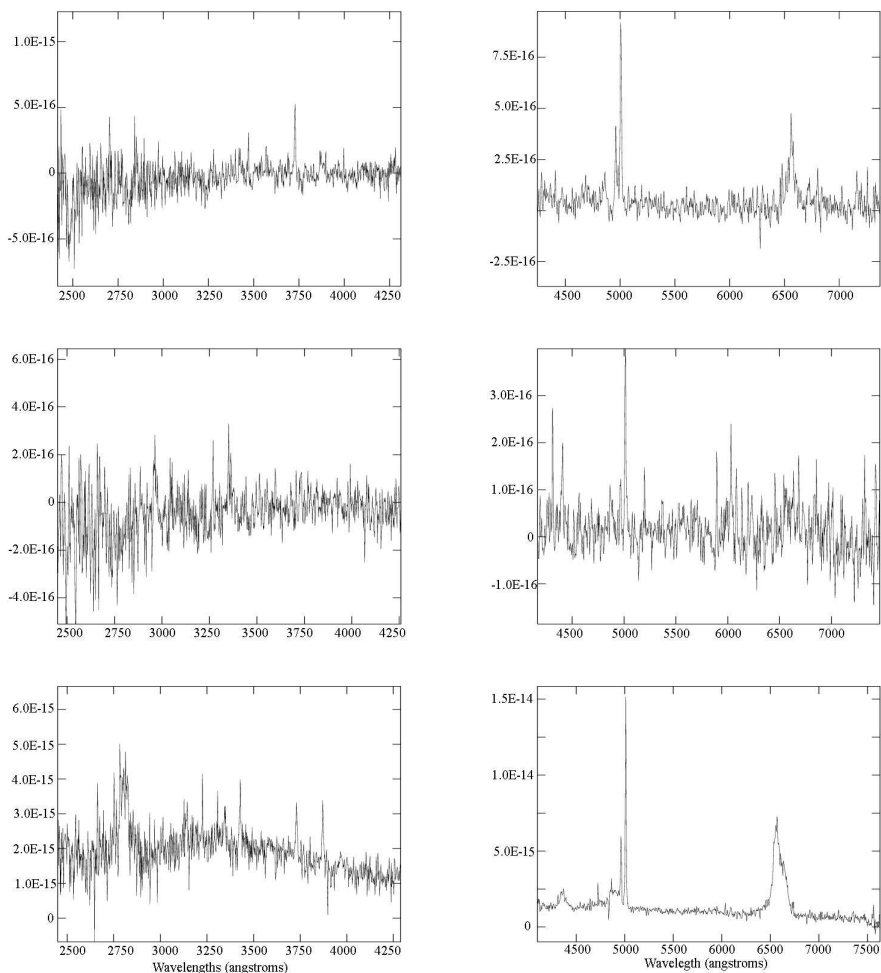


**Figure 4.1**— Spectra of the lobes and nucleus of 3C 67. Left is G430L and right is G750L. The top row corresponds to the spatially averaged spectra of the southern lobe, the middle row to the averaged spectra of the northern lobe and the bottom row corresponds to the nucleus. We have trimmed the sides of some spectra for clarity but all the wavelengths of interest are shown. The units of flux are  $\text{erg s}^{-1} \text{cm}^{-2} \text{arcsec}^{-2} \text{\AA}^{-2}$ .

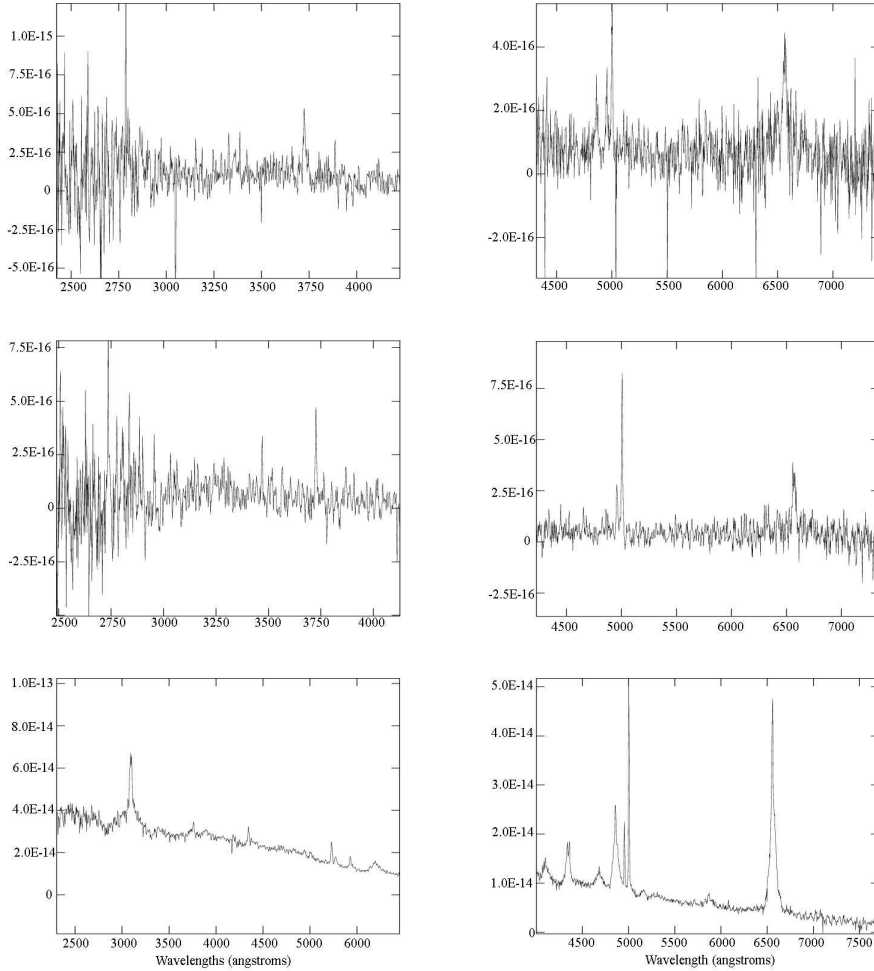


**Figure 4.2.** Spectra of the lobes and nucleus of 3C 277.1. Left is G430L and right is G750L. The top row corresponds to the spatially averaged spectra of the southern lobe, the middle row to the averaged spectra of the northern lobe and the bottom row corresponds to the nucleus. We have trimmed the sides of some spectra for clarity but all the wavelengths of interest are shown. The units of flux are  $\text{erg s}^{-1} \text{cm}^{-2} \text{arcsec}^{-2} \text{\AA}^{-2}$ .

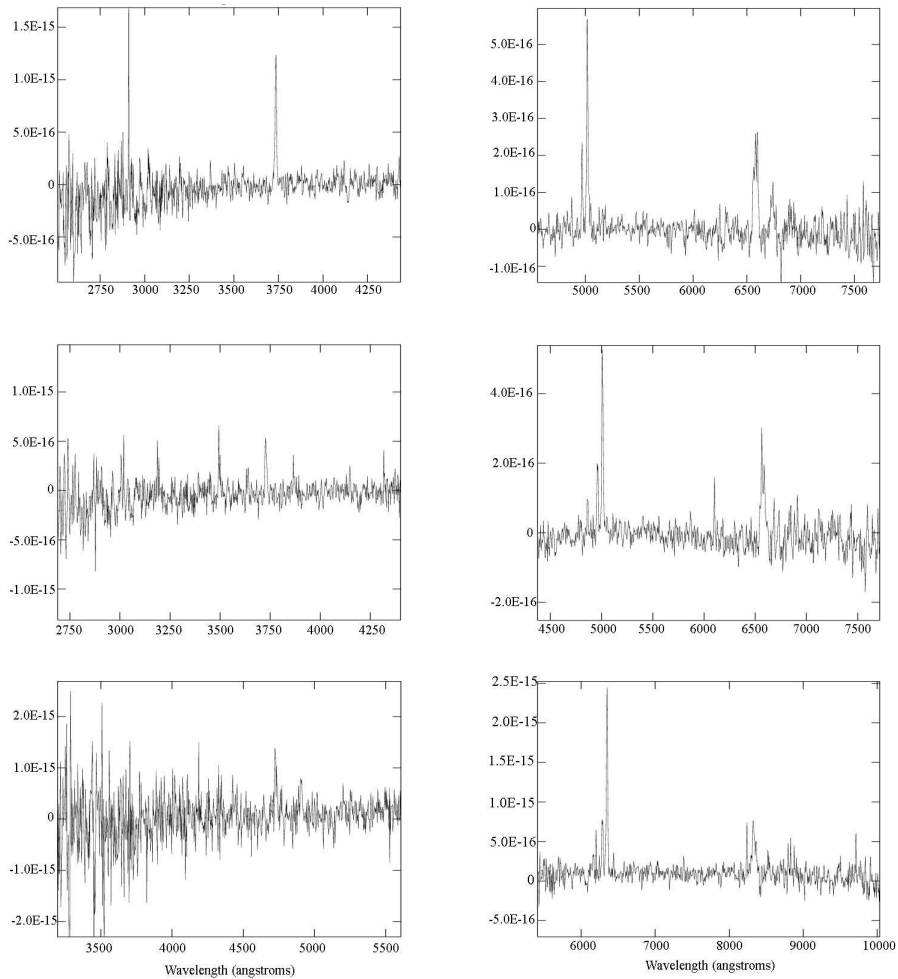


**Figure 4.3.** Spectra of the lobes and nucleus of 3C 303.1. Left is G430L and right is G750L. The top row corresponds to the spatially averaged spectra of the southern lobe, the middle row to the averaged spectra of the northern lobe and the bottom row corresponds to the nucleus. We have trimmed the sides of some spectra for clarity but all the wavelengths of interest are shown. The units of flux are  $\text{erg s}^{-1} \text{cm}^{-2} \text{arcsec}^{-2} \text{\AA}^{-2}$ .

Line	$\lambda$ (Å)	Ion.	3C 67			3C 277.1			3C 303.1		
			Nuc	S	N	Nuc	S	N	Nuc	S	N
[Mg II]	2799.12	Low	24.0±0.7	-	-	2738±40	-	-	-	-	-
[Ne V]	3425.90	High	143.9±6.3	23.2±1.4	-	427±18	-	-	-	-	-
[O II]	3727.37	Low	111.2±4.6	57.1±9.8	20.3±1.5	188.9±15	65.0±1.8	33.8±0.6	275.4±3.6	144.2±1.4	63.1±1.3
[Ne III]	3868.76	High	133.6±6.0	-	-	627±17	-	-	52.4±1.8	-	-
[Ne III]	3967.47	High	13.2±4.1	-	-	412±26	-	-	-	-	-
H $\delta$	4101.73	Low	-	-	-	212.8±3.3	-	-	-	-	-
H $\gamma$	4340.47	Low	-	-	-	343.1±4.0	-	-	25.1±1.1	-	-
[O III]	4363.21	High	-	15.4±1.1	-	332.7±3.4	-	-	-	-	-
[He II]	4685.68	Low	-	-	-	57.7±3.7	-	-	23.7±1.1	-	-
H $\beta$	4861.33	Low	95.9±2.7	33.4±1.4	-	281.0±4.1	30.4±1.6	-	72.7±1.5	13.7±0.6	18.9±0.8
[O III]	4958.92	High	54.0±3.2	67.9±1.2	25.2±0.9	1031.3±4.7	27.4±1.2	35.7±0.8	258.9±1.6	32.3±0.6	35.9±0.6
[O III]	5006.85	High	1566.8±5.7	196.7±1.4	73.0±1.0	2998.3±9.2	79.7±1.3	103.9±0.9	752.1±2.8	95.3±0.6	104.4±0.7
[He I]	5875.70	Low	45.2±3.1	-	-	98.4±4.5	-	-	-	-	-
[O I]	6300.31	Low	-	-	-	-	-	-	-	-	-
[N II]	6548.06	Low	-	-	-	181.6±5.1	-	-	59.6±2.7	16.8±0.8	-
H $\alpha$	6562.82	Low	372.0±3.7	103.4±1.7	37.6±1.3	2923.3±12.6	94.1±2.5	88.7±2.0	210.6±2.3	39.7±0.9	59.4±1.1
[N II]	6583.39	Low	75.2±3.3	58.9±1.6	-	527.4±5.9	4.9±2.4	36.1±2.0	193.5±3.1	48.9±0.9	34.5±1.0
[S II]	6716.42	Low	-	-	-	160.6±5.2	-	-	56.2±16	32.7±1.1	-
[S II]	6731.78	Low	-	-	-	-	-	-	-	-	-

**Table 4.2–. Emission lines master list.** List of the emission lines we searched for in our sample. The first column gives the species; the second column the rest-frame wavelength; the third column the ionization status. For wavelength and ionization references see Eracleous & Halpern (2004). For each source we present the integrated flux (in  $10^{-16}$  erg s $^{-1}$  cm $^{-2}$  arcsec $^{-2}$ ) for the detected lines in the nucleus (Nuc) and southern (S) or northern (N) lobes. Non detections are indicated by “-”. For the lobes we have used the spatially averaged spectra. However, a line marked in the table as a non detection in the averaged spectra might have been detected in a couple of very localized positions. We require  $3\sigma$  for a detection. See also Figures 4.1, 4.2 and 4.3 for spectra of the sources.

## 4.4 Results

We have detected several lines in the extended nebulae of all three CSS sources – [O II], [O III], H $\beta$ , H $\alpha$ , and [N II]. We have used these lines to determine the standard diagnostics of ionization and compared them to the predictions of shock and photo-ionization models. We have also compared the ionization levels with the gas kinematics, as presented and discussed by O’Dea et al. (2002).

### 4.4.1 Ionization diagnostics

Given our line detections we were able to construct one of the key diagnostic Baldwin-Philips-Terlevich (BPT) diagrams (Baldwin et al. 1981; Veilleux & Osterbrock 1987; Moy & Rocca-Volmerange 2002), namely the [O II]/[O III] vs. [O III]/H $\beta$  diagram (figures 4.4,4.5,4.6). Other potentially useful BPT diagrams (e.g., [S II]/H $\alpha$  vs. [N II]6583/H $\alpha$ , [O II] $\lambda\lambda$ 3727+29/[O III]5007 vs. [N II]6583/H $\alpha$ , [O III]5007/H $\beta$  vs. [S II]/H $\alpha$ , etc.) were not possible given the limited number of detected lines. We have compared our results with the two main classes of ionization mechanisms: shock ionization using MAPPINGS III ((Kewley et al. 2005 in prep.; Dopita & Sutherland 1996) and AGN photo-ionization using CLOUDY (Ferland et al. (1998)). The MAPPINGS shock code calculates the spectra from gas which has been directly ionized by the shock (*pure shock* models) and unshocked gas which has been ionized by the radiation emitted by the hot shocked gas (*pure precursor* models). In our BPT diagrams (figures 4.4,4.5,4.6) we show the predicted line ratios calculated by MAPPINGS for both a pure precursor and pure shock model, as well as linear combinations of these two (30%, 50%, 70% contribution to the emission line luminosity

from shocks), including a range of magnetic fields (MAPPINGS's magnetic parameter from 0.5 to 10) and shock velocities from 100 to 1000 km/s. In addition we include the predicted line ratios calculated by CLOUDY for a range of ionization parameter (Log U ranging from  $-2$  to  $-3.8$ ) and cloud density (Log  $n = 0, 2, 4$ ). We note that "real" radio galaxies are probably more complicated than assumed in the MAPPINGS and CLOUDY calculations and suggest that the results be taken with caution.

We find that the data points tend to spread across the diagrams (figures 4.4, 4.5, 4.6) covering about one dex in both dimensions. The nuclei lie to the lower right of the distribution of points (with the highest values of  $[\text{O III}]/\text{H}\beta$ , and lowest values of  $[\text{O II}]/[\text{O III}]$ ) consistent with the nuclei containing the highest ionization gas. The data for the extended emission clearly indicate lower ionization than the nuclei. In addition the data for the extended emission are at higher ionization than the 100% shock models from MAPPINGS and are at lower ionization than the CLOUDY AGN photo-ionization models. In general the extended emission lines are consistent with a mixture of shocked and photo-ionized gas. In 3C 67, the data lie between the MAPPINGS models for a contribution to the observed luminosity from shocked gas ranging from 0 to 50%. In 3C 303.1, the contribution to the luminosity from shocked gas is between 30 and 70%. In 3C 277.1, the data scatter around the model for 100% contribution to the luminosity from precursor gas. Thus, the contribution from shocks increases from 3C 277.1 to 3C 67 to 3C 303.1. The sources tend to lie in the regions for moderate to high shock velocities (500 to +1000 km/s) and we do not obtain any useful constraints on magnetic field strengths in the MAPPINGS models. We note that these results are consistent with previous work on CSS radio sources using ground based data (Gelderman & Whittle 1994; Morganti et al. 1997). We also used the observed  $\text{H}\alpha/\text{H}\beta$  ratios to test the hypothesis that the low values of the  $[\text{O II}]/[\text{O III}]$  ratio are produced by large amounts of reddenning. However, the observed Balmer ratios (or even values 10% higher than observed) are not consistent with significant reddenning effects on the  $[\text{O II}]/[\text{O III}]$  ratio (except possibly in the nucleus of 3C277.1).

#### 4.4.2 Can the central AGN power the emission line luminosity in the extended nebulae?

We compared the number of ionizing photons produced by the nucleus of the source, with the number of photons needed to produce the observed emission line luminosity (see e.g. Wilson et al. 1988; Baum & Heckman 1989; Axon et al. 2000; O'Dea et al. 2000). Assuming radiative recombination under case B conditions, the number of ionizing photons  $N_{\text{H}\beta}$  needed to produce the observed  $\text{H}\beta$  luminosity  $L_{\text{H}\beta}$  is:

$$N_{\text{H}\beta} = 2.1 \times 10^{12} L_{\text{H}\beta} \text{ photons s}^{-1}$$

We use the integrated  $[\text{O III}]\lambda 5007$  fluxes measured by Gelderman & Whittle (1994) (see Table 4.4.2) and scale using the typical ratio for the narrow line components in CSS sources (see also Gelderman & Whittle 1994):  $\text{H}\beta/[\text{O III}]\lambda 5007 = 0.18 \pm 0.02$ .

The number of photons in the continuum, between frequencies  $\nu_1$  and  $\nu_2$  are given by:

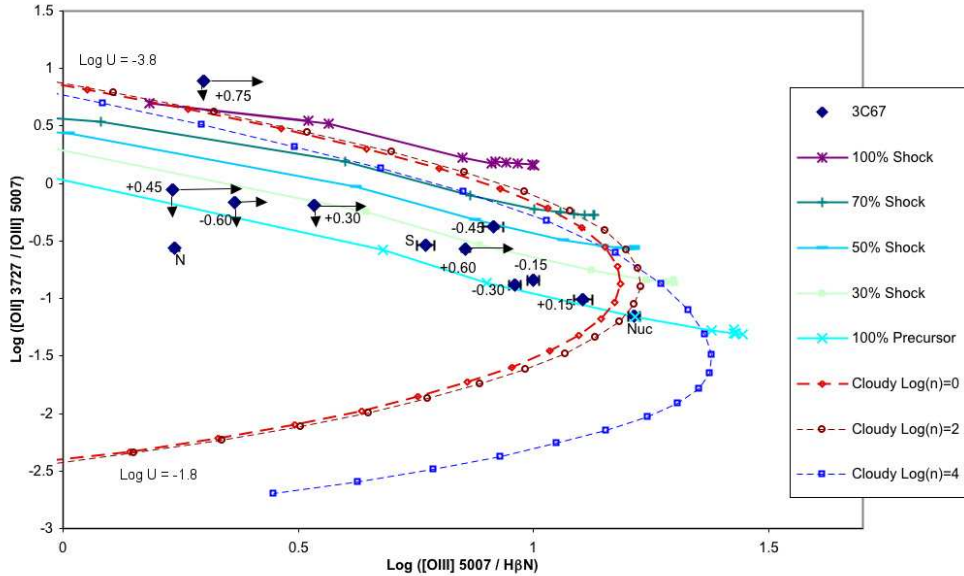


**Figure 4.4.** 3C 67. Reddening-corrected  $[O II] \lambda\lambda 3727+29/[O III] \lambda 5007$  vs.  $[O III] \lambda 5007/H\beta N$  intensity ratios. Symbols for the models are shown in key to the figure. Data is shown for the nucleus (Nuc) and at each 0.15 arcsec along the slit in the extended region, labeled with their distance to the nucleus. We also show the points for the averaged extended emission in the northern (N) and southern (S) lobes. The arrows in the plot represent those points where lines were not detected, using an upper limit of  $(3 \times RMS \times FWHM)$ . We compare our results with the two main classes of ionization mechanisms: MAPPINGS III (Kewley et al. 2005 in prep.); Dopita & Sutherland 1996) shock models (solid lines) and CLOUDY (Ferland et al. (1998)) AGN photo-ionization models (dashed lines). For the shock models from MAPPINGS we included both pure precursor and pure shock models, as well as linear combinations of these two (30%, 50%, 70% contribution to the emission line luminosity from shocks). The results do not depend on magnetic field strength, and so for simplicity we show models with  $B = 10$ . Shock velocity in this models ranges from 100 to 1000 km/s and increases to the right. For the CLOUDY AGN photoionization models we include a range of ionization parameter (Log U ranging from -1.8 to -3.8) and cloud density (Log n = 0,2,4).

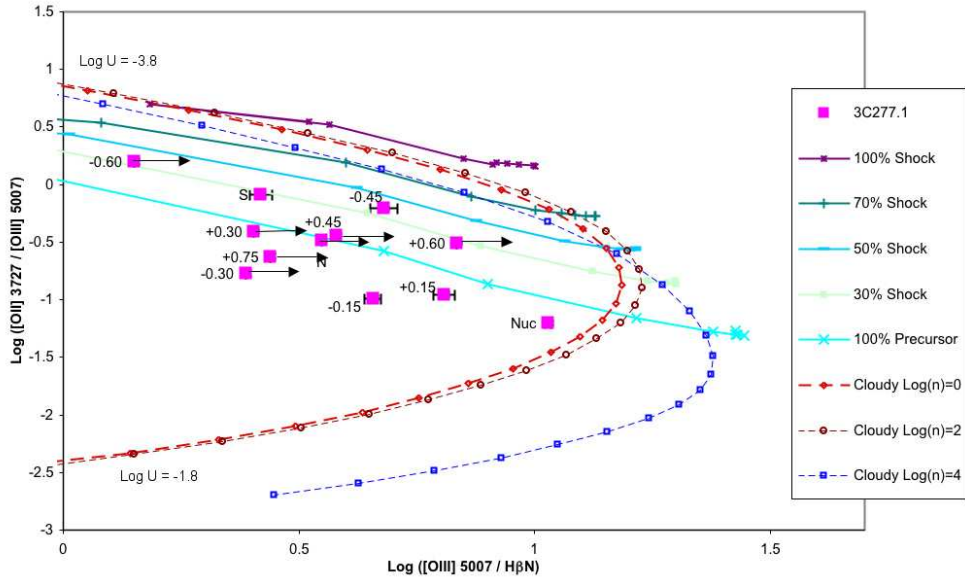


Figure 4.5-. Same as Figure 4.4, but for 3C 277.1.

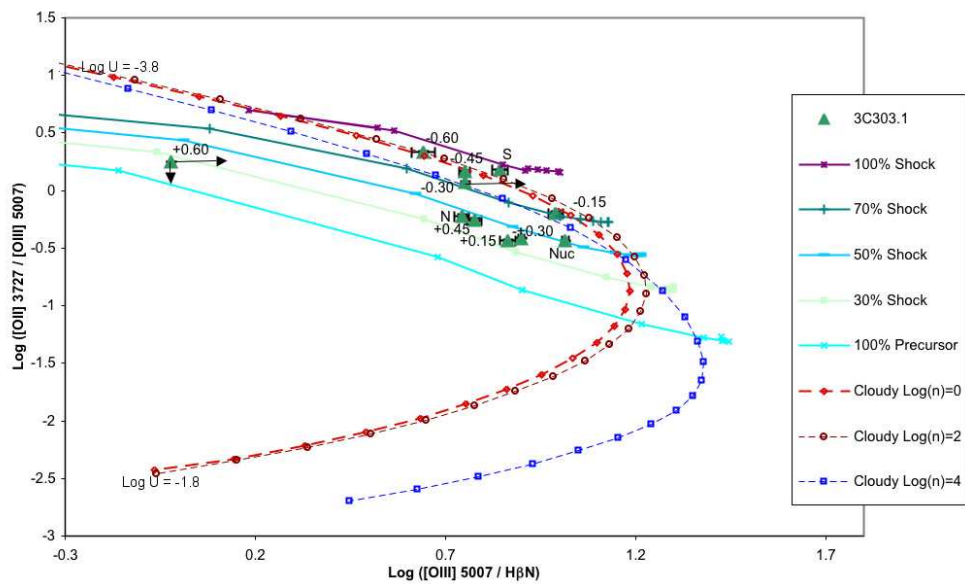


Figure 4.6-. Same as Figure 4.4, but for 3C 303.1.

Parameter	3C 67	3C 277.1	3C 303.1
ID	G	Q	G
redshift	0.310	0.321	0.267
scale (kpc/arcsec)	4.04	4.13	3.65
radio power $\log_{10} P_{5GHz}$ (Watts $\text{Hz}^{-1}$ )	26.3	26.4	26.0
angular size $\theta$ (arcsec)	2.5	1.67	1.7
linear size $D$ (kpc)	10.1	6.9	6.2
integrated emission line flux F(O III $\lambda$ 5007) ( $10^{-15}$ ergs $\text{s}^{-1} \text{cm}^{-2}$ )	22	31	28
integrated ([O III $\lambda$ 5007) line width at 50% of line peak ( $\text{km s}^{-1}$ )	$600 \pm 42$	$510 \pm 19$	$815 \pm 18$
integrated (O III $\lambda$ 5007) line width at 20% of line peak ( $\text{km s}^{-1}$ )	$915 \pm 85$	$740 \pm 50$	$1170 \pm 41$
spectral age (yr)	$5 \times 10^4$	$2 \times 10^5$	$1 \times 10^5$
advance speed (v/c)	0.22	0.04	0.07

**Table 4.3.— Source Properties.** We adopt a Hubble constant of  $H_o = 75 \text{ km s}^{-1} \text{ Mpc}^{-1}$  and a deceleration parameter of  $q_o = 0.0$ . The integrated emission line flux and width are from Gelderman & Whittle (1994). The spectral age is estimated by fitting a continuous injection model to the integrated radio spectrum and is taken from Murgia et al. (1999). The advance speed is estimated using  $2v = \text{linear size} / \text{spectral age}$ .

$$N_{\text{Nuc}} = 4\pi D^2 S_0 (\alpha h)^{-1} (\nu_1^\alpha - \nu_2^\alpha) \text{ photons s}^{-1}$$

where  $D$  is the luminosity distance, the flux density spectrum is given by  $F_\nu = S_0 \nu^{-\alpha}$  (we adopt  $\alpha=1$ ) and  $h$  is Planck's constant. We are only interested in the photons with enough energy to ionize Hydrogen, so we choose  $\nu_1 = 3.3 \times 10^{15} \text{ Hz}$  ( $912 \text{ \AA}$  or  $13.6 \text{ eV}$ ) and  $\nu_2 = 4.8 \times 10^{17} \text{ Hz}$  ( $17 \text{ keV}$ ). For our spectral index,  $\alpha=1$ , higher frequencies do not add a significant number of photons. Note that this analysis is subject to the caveat that the continuum emission may not be emitted isotropically, and the extended nebulae may see a different luminosity than we do (e.g. Penston et al. 1990)

The results are shown in Table 4.4. We find that the nucleus apparently produces enough ionizing photons to power the emission line luminosity in 3C 277.1 and possibly 3C 67, but not 3C 303.1. This is consistent with the results from our BPT diagrams.

Source	Distance	Log $N_{H\beta}$	Log $N_{\text{Nuc}}$	$N_{H\beta}/N_{\text{Nuc}}$
3C 67	1620	54.4	54.3	1.3
3C 277.1	1700	54.6	55.1	0.35
3C 303.1	1350	54.4	53.1	17.0

**Table 4.4.— Photon counting.** Source, distance to the source in Mpc ( $H_0=75 \text{ km/s/Mpc}$ ) and number of photons needed to ionize  $H_\beta$ , ionizing photons produced by the nucleus, and the ratio between the last two. If the ratio is  $\leq 1$ , the nucleus is producing enough photons to ionize  $H_\beta$ , if the ratio is higher than one, another source of ionization, such as shocks, is required.

#### 4.4.3 Diagnostic ratios vs. kinematics and distance

Here we look for additional clues to the nature of the ionization and acceleration of the emission line gas. In shock models, the ionization should be related to the gas kinematics

(e.g., Clark et al. 1998), while if the ionization is dominated by AGN photoionization, the ionization level and kinematics should be largely independent.

We have studied the behavior of the diagnostic ratios  $[\text{OIII}]\lambda 5007/\text{H}\beta$ ,  $[\text{O II}]\lambda\lambda 3727+29 / [\text{O III}]\lambda 5007$ ,  $[\text{NII}]\lambda 6583/\text{H}\alpha$ ,  $[\text{SII}]/\text{H}\alpha$  with distance to the nucleus of the source, and the gas kinematics (velocity offset relative to the nucleus, and FWHM). The kinematic data have been taken from the medium dispersion results (O’Dea et al. 2002) given their superior spectral resolution. The low dispersion data give consistent results. The relationships are plotted in Figures 4.7 to 4.8 and the results are summarized in Table 4.5. We have applied a Spearman rank test to search for correlations and regard correlations with a significance  $\geq 99\%$  as real.

Source	Plot	$[\text{OIII}]\lambda 5007/\text{H}\beta$	$[\text{O II}]/[\text{O III}]^a$	$[\text{NII}]\lambda 6583/\text{H}\alpha$	$[\text{SII}]/\text{H}\alpha$
3C 67	Dist	Decrease (99%)	Increase (95%)	Asymmetric <sup>(3)</sup> (95%)	No trend <sup>1</sup>
	VO	Decrease <sup>2</sup> (99%)	Increase <sup>2</sup> (85%)	Increase <sup>2</sup> (95%)	No trend <sup>1,2</sup>
	FWHM	No Trend	No Trend	No Trend	No trend <sup>1</sup>
3C 277.1	Dist	Decrease <sup>4</sup> (95%)	Increase (99.5% S)	Decrease (90% N) <sup>5</sup>	No trend <sup>1</sup>
	VO	Decrease <sup>4</sup> (90%)	Increase (90% S)	Increase (95% N) <sup>5</sup>	No trend <sup>1</sup>
	FWHM	No trend <sup>4</sup>	Increase (95% S)	No trend	No trend <sup>1</sup>
3C 303.1	Dist	Decrease (99.5%)	Increase (99%)	No trend <sup>3</sup>	Asymmetric <sup>3</sup> (99.5%)
	VO	Decrease (99%)	Increase (99.5%)	No trend	Increase (95%)
	FWHM	Increase (90%)	No Trend	No trend	No trend

<sup>a</sup> $[\text{O II}]\lambda\lambda 3727+29/[\text{O III}]\lambda 5007$

<sup>1</sup>Very few clear detections

<sup>2</sup>Most of the points around  $|VO| \sim 150$  km/s

<sup>3</sup>Increases to the south. Decreases to the north.

<sup>4</sup>Few clear detections of  $\text{H}\beta$

<sup>5</sup>Few clear detections of  $[\text{NII}]$  in the South Lobe.

**Table 4.5–. Behavior of diagnostic ratios with distance and kinematics.** Summary of the behavior of the different ratios with distance to the nucleus, velocity offset (relative to the nucleus) and FWHM. First column gives the name of the source, second column the “X” axis in the plot; the next four columns give the studied ratios. Asymmetric: Significantly different values in the two lobes. No trend: No observable trend. Increase/Decrease: Trend of the ratio with increasing values of distance, velocity offset or FWHM. Where trends were found, we note the –minimum– confidence level based on the Spearman’s Rank Correlation for that plot. A letter S or N means the correlation was only found in the southern (S) or northern (N) lobe. See the text for more detailed comments on each ratio and source.

The three sources show a decrease in ionization with distance from the nucleus (based on  $[\text{OIII}]\lambda 5007/\text{H}\beta$ ,  $[\text{OII}]\lambda\lambda 3727+29/[\text{OIII}]\lambda 5007$ ). This behavior (high ionization in the nucleus, low in the lobes) can be explained by (1) the influence of the central engine in the inner regions, and a low ionization source, like shocks, further out, and (2) dilution of photons from the nucleus with distance. The sources show a weak trend for ionization to decrease with increasing FWHM and a strong trend for ionization to decrease with increasing velocity offset. This relation between ionization level and the kinematics is consistent with shock ionization and acceleration of the gas (as suggested by O’Dea et al. 2002).

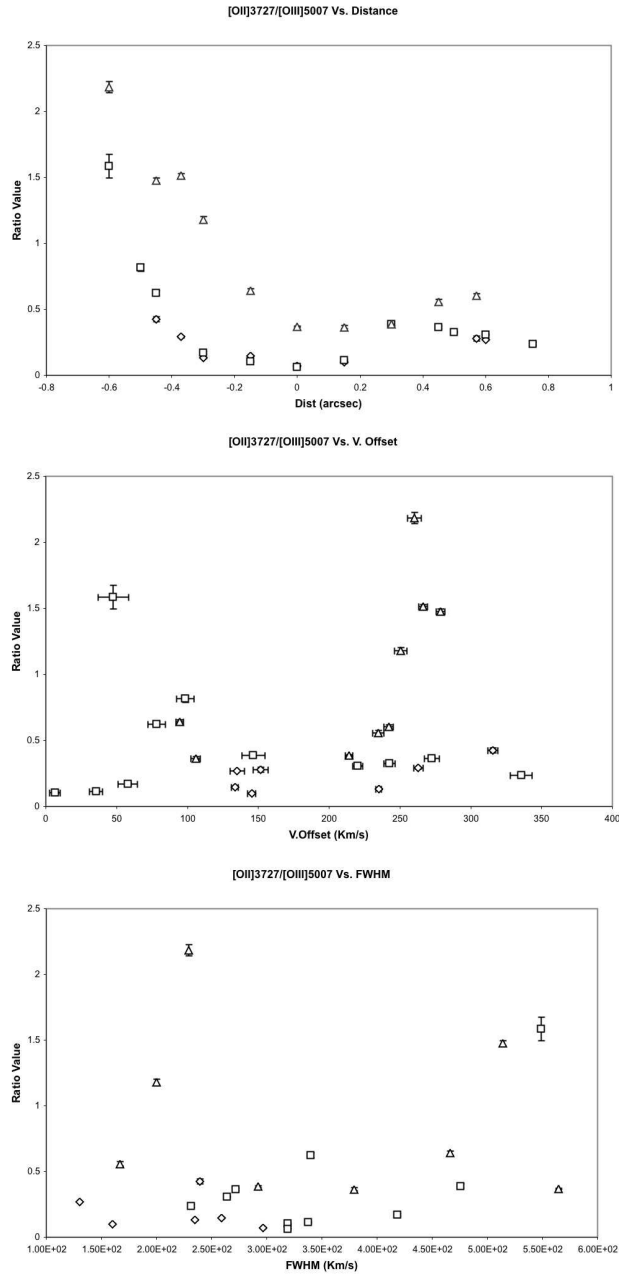


**Figure 4.7--.** Behavior of the diagnostic ratio  $[OII]\lambda\lambda 3727+29/[OIII]5007$  versus distance, velocity offset and FWHM. Diamonds represent 3C 67, squares 3C 277.1 and triangles 3C 303.1.

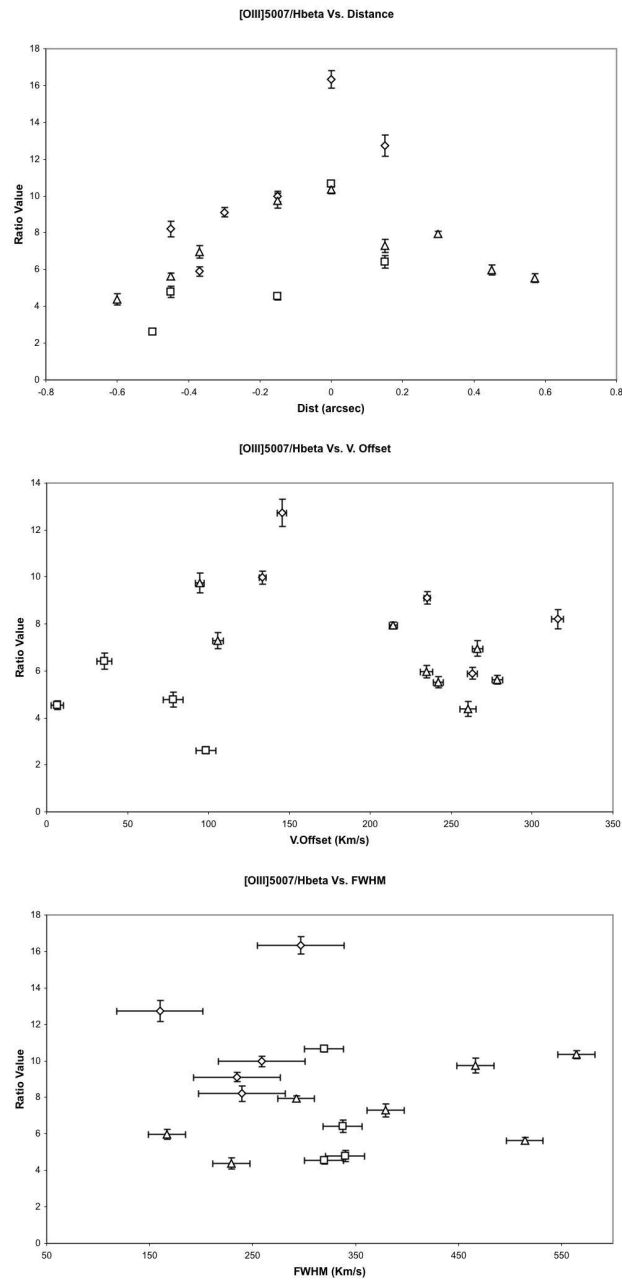


**Figure 4.8.** Behavior of the diagnostic ratio  $[OIII]5007/H\beta$  versus distance, velocity offset and full width half maximum. Diamonds represent 3C 67, squares 3C 277.1 and triangles 3C 303.1.

#### 4.4.4 Cloud properties

We have estimated the electron temperature using the  $[\text{O III}]\lambda 4363/[\text{O III}]\lambda 5007$  diagnostic lines. Given our limited signal-to-noise we derive an estimate of the  $e^-$  temperature in the nucleus of 3C 277.1 of  $\sim 20,000\text{K}$  and obtain lower limits ( $>7,000\text{K}$ ) for the rest of the sources. These temperatures are consistent with previous measurements of temperatures in the nucleus and extended emission-line regions of AGN (Clark et al. 1998; Wilson et al. 1997; Storchi-Bergmann et al. 1996). Tadhunter et al. (1989) showed that the observed ratio  $[\text{O III}]\lambda 4363/[\text{O III}]\lambda 5007$  implied for several extended emission-line regions electron temperatures ranging from  $12800\text{K}$  to  $22000\text{K}$ , whereas photoionization models predict much lower values. They discussed several possible explanations for this discrepancy between the results and the models, including additional heating sources such as cosmic rays or shocks, or metal abundances lower than the solar values assumed in the models.

In 3C 277.1 we also found high  $\text{H}\alpha/\text{H}\beta$  values for the nucleus ( $10.4 \pm 0.2$ ) consistent with the measurements of CSS quasars by Baker & Hunstead (1995), who argued for very dusty gas in these objects. On the other hand, 3C 67 and 3C 303.1 show  $\text{H}\alpha/\text{H}\beta$  ratios of  $\sim 3.1$ .

## 4.5 Summary

We present Hubble Space Telescope Imaging Spectrograph long-slit spectroscopy of the aligned emission line nebulae in three compact steep spectrum radio sources: 3C 67, 3C 277.1, and 3C 303.1. In previous papers we have reported evidence that the kinematics of the gas is consistent with being driven by shocks from the expanding radio lobes. Here we present the results of our low dispersion spectra of several diagnostic emission lines. We compare our results with shock and photo-ionization models and examine the relationships between the ionization diagnostics and the gas kinematics.

We find that the ionization diagnostics are consistent with a mix of shock and photoionization in the extended emission line gas. The data for the extended emission are at higher ionization than the 100% shock models from MAPPINGS and are at lower ionization than the CLOUDY AGN photo-ionization models. In general the extended emission lines are consistent with a mixture of shocked and photo-ionized gas. In 3C 67, the data lie between the MAPPINGS models for a contribution to the observed luminosity from shocked gas ranging from 0 to 50%. In 3C 303.1, the contribution to the luminosity from shocked gas is between 30 and 70%. In 3C 277.1, the data scatter around the model for 100% contribution to the luminosity from precursor gas. The sources tend to lie in the regions for moderate to high shock velocities (500 to 1000 km/s) and we do not obtain any useful constraints on magnetic field strengths in the MAPPINGS models.

The three sources show a decrease in ionization with distance from the nucleus (consistent with a decrease in photoionization with distance) a weak trend for ionization to decrease with increasing FWHM and a strong trend for ionization to decrease with increasing velocity

offset (which is consistent with shock ionization) .

These results are consistent with a picture in which the CSS sources interact with dense clouds as they propagate through their host galaxies, shocking the clouds thereby ionizing and accelerating them (as suggested by O’Dea et al. 2002).

### **Acknowledgements**

Support for this work was provided by NASA through grant number GO-08104.01-97A (PI C. O’Dea) from the Space Telescope Science Institute, which is operated by the Association of Universities for Research in Astronomy, Inc., under NASA contract NAS5-26555. These observations are associated with program 8104. WDV’s work was performed under the auspices of the U.S. Department of Energy, National Nuclear Security Administration by the University of California, Lawrence Livermore National Laboratory under contract No. W-7405-Eng-48. This research has made use of the NASA/IPAC Extragalactic Database (NED) which is operated by the Jet Propulsion Laboratory, California Institute of Technology, under contract with the National Aeronautics and Space Administration. This research has made use of NASA’s Astrophysics Data System. We thank the referee, Dr. Ignas Snellen, for useful comments on the manuscript.



# H I absorption in 3C 49 and 3C 268.3

*Accepted for publication in A&A. In press*

A. Labiano, R.C. Vermeulen, P.D. Barthel, C.P. O’Dea, J.F. Gallimore, S.A. Baum, W.H. de Vries

**W**E present and discuss European VLBI Network UHF band spectral line observations, made to localise the redshifted 21cm H I absorption known to occur in the subgalactic sized compact steep spectrum galaxies 3C 49 and 3C 268.3. We have detected H I absorption towards the western radio lobe of 3C 49 and the northern lobe of 3C 268.3. However, we cannot rule out the presence of similar amounts of H I towards the opposite and much fainter lobes. The radio lobes with detected H I absorption (1) are brighter and closer to the core than the opposite lobes; (2) are depolarized; and (3) are associated with optical emission line gas. The association between the H I absorption and the emission line gas, supports the hypothesis that the H I absorption is produced in the atomic cores of the emission line clouds. Our results are consistent with a picture in which compact steep spectrum sources interact with clouds of dense gas as they propagate through their host galaxy. We suggest that the asymmetries in the radio and optical emission can be due to interaction of a two sided radio source with an asymmetric distribution of dense clouds in their environment

## 5.1 Introduction

The GHz Peaked Spectrum (GPS) and Compact Steep Spectrum (CSS) radio sources make up significant fractions of the extragalactic bright (cm wavelength selected) radio source population ( $\sim 10\%$  and  $\sim 20\%$ , respectively), but are not well understood (e.g. O’Dea 1998). They are powerful but compact radio sources whose spectra are generally simple and convex with peaks near 1 GHz and 100 MHz respectively. The GPS sources are entirely contained within the extent of the nuclear narrow line region ( $\lesssim 1$  kpc, NLR) while the CSS sources are contained entirely within the host galaxy ( $\lesssim 15$  kpc). GPS and CSS sources are important because (1) they probe the NLR and interstellar medium (ISM) of the host galaxy and (2) they may be the younger stages of powerful large-scale radio sources – giving us insight into radio source genesis and evolution.

The currently favored hypothesis is that the GPS and CSS sources are indeed the young progenitors of the large scale powerful double sources (e.g. Carvalho 1985; Hodges & Mutel 1987; Begelman 1996; Fanti et al. 1995; Readhead et al. 1996a; O’Dea 1998; Snellen et al. 2000; Alexander 2000). In this model they propagate relatively quickly through the ISM of the parent galaxy with advance speeds of a few percent of the speed of light. Observed proper motions tend to be a bit higher - in the range  $0.05 - 0.2 h^{-1}c$ , e.g., Polatidis & Conway (2003), though the detections may be biased towards objects with the highest velocities.

Searches for 21 cm H I absorption have produced a 50% detection rate in GPS and CSS sources (Vermeulen et al. 2003; Pihlström et al. 2003) in contrast to normal elliptical radio galaxies, where the detection rate does not exceed  $\sim 10\%$  (van Gorkom et al. 1989). This indicates that clouds of atomic hydrogen are very common in the environments of GPS and CSS sources or that the geometry and/or morphology of GPS and CSS sources is very favorable for the detection of H I absorption. The close alignment and similar spatial extents of the radio continuum and optical emission line plasma suggests the existence of a close coupling between the thermal gas and the radio sources (de Vries et al. 1997b, 1999; Axon et al. 2000). The broad and highly structured spatially integrated [OIII] $\lambda 5007$  line widths observed by Gelderman & Whittle (1994) strongly suggest that the radio source is dominating the emission line kinematics. This has been confirmed by Hubble Space Telescope spectroscopy (O’Dea et al. 2002).

Thus, the simple picture of evolution may require the incorporation of interaction of the radio sources with dense gas clouds in their ISM (e.g., Jeyakumar et al. 2005). In order to probe the nature of the relationship between the gas clouds and the radio source we have obtained high resolution EVN observations of the redshifted 21 cm line seen in absorption against 1 GPS and 2 CSS radio galaxies in our WSRT spectra (Vermeulen et al. 2003). The results for 2050+364 are presented by Vermeulen et al. (2005). Here we present the results for 3C 49 and 3C 268.3.

## 5.2 Observations and data reduction

The 21cm H I absorption lines associated with the sources 3C 49 ( $z = 0.6207$ , 876.7 MHz) and 3C 268.3 ( $z = 0.37116$ , 1035.1 MHz)<sup>1</sup> were observed on 1999 September 14 and 09, respectively, for about 7 hours each, using the UHF receivers (800–1300 MHz) on the European VLBI Network (EVN). The sources J0249+063, 3C 84, J1048+717, 3C 286, DA 406, and 3C 454.3 were used as calibrators. The recorded bandwidth of 4 MHz was correlated at the NRAO, Socorro correlator with 256 spectral channels, for a resolution of  $5.3 \text{ km s}^{-1}$  and  $4.5 \text{ km s}^{-1}$  in 3C 49 and 3C 268.3, respectively.

At the time of these observations, we could only obtain data in left and right circular polarisations from the Effelsberg and Westerbork (Tied Array) telescopes, and two orthogonal linear polarisations from the Onsala (25m) telescope. For 3C 268.3, we obtained left circularly polarised data from the Lovell Telescope at Jodrell Bank in addition.

The NRAO Astronomical Image Processing Software (AIPS) package was used for the initial data processing (fringe fitting, spectral passband calibration and a priori gain calibration). The Caltech DIFMAP package (Shepherd 1997) was used for all further calibration and analysis (Cleaning, self-calibration, model-fitting). The data processing and analysis steps used to obtain final continuum images and radio spectra towards the various features in these images are explained in detail in our 2050+364 EVN UHF observations paper (Vermeulen et al. 2005). It should be noted in particular that all available polarization products were averaged together, including the cross-correlations between linear and circular polarisations. We believe the sensitivity gained to total intensity is more important than resultant limitations on absolute flux calibration accuracy or on (image or spectral) dynamic range; we think these are more affected by the sparseness of the array and the lack of complete system temperature data and gain curves. In fact, we caution that the absolute flux density scales for the data shown are uncertain even at the 50% level<sup>2</sup>. However, the main astrophysical results are unaffected, since they depend on opacities rather than on absolute flux densities. Furthermore, great effort was expended to obtain reliable *relative* (self)calibrations between the telescopes, in an extensive series of very gradual self-calibration iterations.

We believe the continuum structures and spectral line profiles obtained are robust against the overall calibration uncertainties. Indeed, the continuum structures obtained at these novel frequencies correspond well with those found at other frequencies, as discussed in Section 5.3.1. In order to restrict the number of free parameters, the sky model fitted to the visibility data during the self-calibration cycles consisted of a limited number of Gaussian components, which are shown overplotted on the continuum images in Figures 5.1 and 5.2; their parameters, fitted to the visibility data, are given in Tables 5.2 and 5.2.

### 5.2.1 Spectrum analysis

Given the sparseness of these VLBI datasets, the most robust way to derive line spectra of the various regions of the sources was to re-fit, separately for each of the line channels, the

<sup>1</sup>Redshifts from Spinrad et al. (1985) for 3C 49 and Gelderman & Whittle (1994) for 3C 268.3.

<sup>2</sup>This error is not included in our reported errors on flux densities.

Source	Freq. (GHz)	Time on source hh:mm:ss	Number of scans	RMS (Jy beam <sup>-1</sup> )	Cont. Peak (Jy beam <sup>-1</sup> )	Restoring beam (mas) (deg)	
3C 49	0.8767	07:26:18	4	$2.5 \times 10^{-3}$	6.550	105 x 51.5	-45.6
3C 268.3	1.0351	06:59:14	4	$1.4 \times 10^{-3}$	0.601	70.2 x 43.5	59.7

**Table 5.1.** Summary of the EVN observations of 3C 49 and 3C 268.3, in September, 1999. The first column gives the name of the source, the second column the frequency of our observations, the third column the exposure time, the fourth the number of scans made on each particular source (the exposure time shown is the sum of all the scans). The RMS column is the noise in an empty region of the map. *Cont. Peak* is the peak flux density of the continuum image. The *Beam* column gives the FWHM and orientation of the beam.

Source	GC	R (mas)	$\theta$ (deg)	Major (mas)	Minor (mas)	Flux <sup>a</sup> (Jy)	SC	$\Delta S/S_{cont}$	FWHM (km/s)	$\tau^b$	$N_{HI}^b$ (10 <sup>20</sup> (T <sub>S</sub> /100K) cm <sup>-2</sup> )	Center (km/s)
3C 49	1 (W)	1.24	133	24	24	$7.28 \pm 0.03$	1	$3.5\% \pm 0.4\%$	$20.9 \pm 3.7$	$0.036 \pm 0.003$	$1.5 \pm 0.3$	$-138 \pm 2 \pm 19$
3C 49	1 (W)	-	-	-	-	-	2	$1.9\% \pm 0.4\%$	$22.7 \pm 8.1$	$0.019 \pm 0.006$	$0.8 \pm 0.4$	$-160 \pm 5 \pm 19$
3C 268.3	3 (N)	3.9	-88	72	39	$1.10 \pm 0.01$	-	$2.5\% \pm 0.6\%$	$67.1 \pm 6.0$	$0.025 \pm 0.005$	$3.2 \pm 0.6$	$+190 \pm 2 \pm 12$

<sup>a</sup>: The errors in the absolute flux density scales include only the formal statistical error, and do not include the errors due to sparseness of the array (up to 50%, see Section 2.3).

<sup>b</sup>: Not taking into account the covering factor (See section 5.3.2).

**Table 5.2.** Components and absorption line properties. Detections. Columns 2 to 7 list the properties of the fitted Gaussian components (*GC*): distance (to coordinates (0,0)) and position (*R*,  $\theta$ ), axes size (*Major*, *Minor*), and integrated flux density. Columns 8 to 13 list the properties of the HI absorptions: spectral component (*SC*): peak depth divided by continuum level ( $\Delta S/S_{cont}$ ), width (*FWHM*), optical depth ( $\tau$ ), column density ( $N_{HI}$ ) and central wavelength (*Center*).

flux density of each of the Gaussian model components, as first derived for the line-free continuum. The positions and diameters of the model components were fixed at the continuum values. Resultant spectra are shown in Figures 5.3 for the locations where absorption was detected. Showing percentage absorption depth or opacity with respect to the continuum strength of the appropriate components avoids the uncertainties in the absolute flux density scale discussed above. Zero velocity was taken to be at the nominal redshift found in the literature; all calculations used the appropriate relativistic formulae.

We corrected the observed frequencies from redshift:

$$\nu_{sys} = \nu_{obs} (1 + z_{sys})$$

and then assumed that the velocity of the gas in the host galaxy is not relativistic. Then, the radial velocity of the gas in the systemic frame ( $V_{sys}$ ) and the associated error ( $\Delta V_{sys}$ ) are:

$$V_{sys} = c \left( \frac{\nu_{HI}}{\nu_{sys}} - 1 \right) \quad \text{and} \quad \Delta V_{sys} = c \nu_{HI} \sqrt{\left( \frac{\Delta \nu_{obs}}{\nu_{obs}^2 (1+z)} \right)^2 + \left( \frac{\Delta z}{\nu_{obs} (1+z)^2} \right)^2}$$

with  $\nu_{HI} = 1420.406$  MHz, the rest frequency of the HI ground state hyperfine transition.

Source	MC	R (mas)	$\theta$ (deg)	Major (mas)	Minor (mas)	Flux <sup>a</sup> (Jy)	$\Delta S/S_{cont}$	FWHM (km/s)	$\tau$ <sup>b</sup>	$N_{H I}$ <sup>b</sup> $10^{20} (T_S/100K) \text{ cm}^{-2}$
3C 49	2 (W)	54.5	58	4	4	0.13±0.02	< 31%	21.8	< 0.37	< 16
3C 49	3 (W)	92.6	149	4	4	0.05±0.02	< 100%	21.8	X	X
3C 49	4 (CW)	300	108	40	40	0.23±0.02	< 19%	21.8	< 0.21	< 8.7
3C 49	5 (CE)	509	109	14	14	0.04±0.02	< 100%	21.8	X	X
3C 49	6 (CE)	564	102	6	6	0.07±0.02	< 57%	21.8	< 0.85	< 36
3C 49	7 (E)	767	95	3	3	0.07±0.02	< 57%	21.8	< 0.85	< 36
3C 49	8 (E)	827	93	16	16	0.21±0.03	< 30%	21.8	< 0.36	< 15
3C 49	9 (E)	878	89	88	88	0.46±0.04	< 17%	21.8	< 0.19	< 8.1
3C 49	10 (E)	989	90	5	5	0.11±0.02	< 36%	21.8	< 0.45	< 19
3C 49	11 (E)	1003	85	41	41	0.81±0.03	< 7.4%	21.8	< 0.08	< 3.3
3C 49	East Int.	–	–	–	–	1.66±0.04	< 5.0%	21.8	< 0.05	< 2.1
3C 49	CE Int.	–	–	–	–	0.11±0.04	< 63%	21.8	< 1.00	< 42
3C 268.3	1 (N)	80	-7.2	100	45	0.24±0.01	< 10%	67.1	< 0.11	< 14
3C 268.3	2 (N)	69	-40	49	30	0.31±0.01	< 6.0%	67.1	< 0.06	< 8.1
3C 268.3	4 (N)	62	148	71	55	0.57±0.02	< 3.0%	67.1	< 0.03	< 4.0
3C 268.3	5 (N)	177	143	3	3	0.020±0.007	< 56%	67.1	< 0.82	< 107
3C 268.3	6 (N)	120	135	6	6	0.01±0.01	< 100%	67.1	X	X
3C 268.3	7 (S)	1339	162	90	35	0.104±0.007	< 13%	67.1	< 0.14	< 18

<sup>a</sup>: The errors in the absolute flux density scales include only the formal statistical error, but do not include the errors due to sparseness of the array (up to 50%, see Section 2.3).

<sup>b</sup>: Not taking into account the covering factor (see Section 5.3.2).

**Table 5.3.— Components and absorption line properties. Non detections.** As for Table 5.2 but for non detections. The numbers shown correspond to the  $2\sigma$  detection limits (maximum peak depth =  $2 \times \text{RMS}/\text{continuum}$ ). An "X" represents no value, as the absorption could be 100%. Rows 11 and 12, *East Int*, *CE Int*, correspond to the spectrum spatially integrated over the entire Eastern and CE component of 3C 49 respectively. For 3C 268.3, the South component consists of a single Gaussian component (7).

We fitted Gaussian profiles to the absorption towards our sources using standard, non-linear  $\chi^2$  minimization techniques. We measured the optical depth of each line (Figure 5.3), its full width at half maximum (FWHM), and its centroid. The values are listed with their formal fitting errors in Tables 5.2 and 5.2. The reduced  $\chi^2$  indicated that two Gaussian lines were needed to fit the absorption towards 3C 49 (Figure 5.3), while one was sufficient for 3C 268.3 (Figure 5.3). For all locations where the spectra showed no detectable absorption,  $2\sigma$  limits have been estimated from the spectral r.m.s. noise level, assuming that any putative line would occur at a similar velocity as the line detected for the same source, and with the same FWHM as for the detection (the average of the two detections for 3C 49). The resultant limits are given in Table 5.2.

### 5.3 Results

We have detected localized 21 cm H I absorption regions in both 3C 49 and 3C 268.3 consistent with the previously published WSRT observations (Vermeulen et al. 2003). The higher resolution of our VLBI observations allows us to locate the H I absorber and propose a physical scenario. We have studied the continuum milliarcsecond structure of the sources, as well as the properties of the H I absorption-line gas. Figures 5.1 and 5.2 show the clean maps, the Gaussian components used to model them, and the location of the H I absorption.

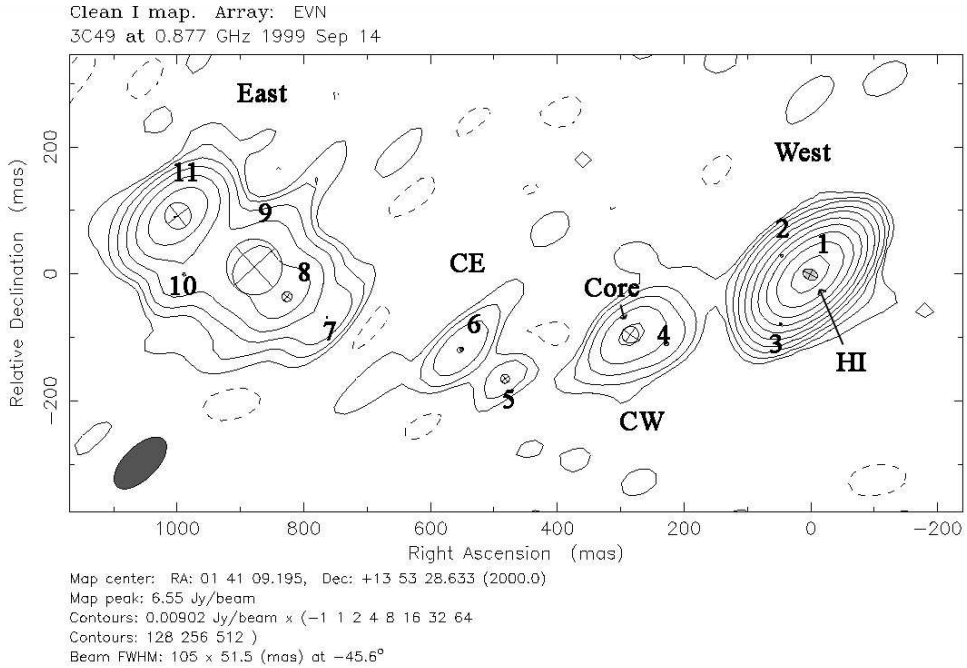


**Figure 5.1**–. Clean map of 3C 49 with the numbered Gaussian components drawn on top. We use letters for the major source regions (from left to right: E, CE, CW, W). The core of the source is in the center of the CW component (Ludke et al. 1998).

The coordinates (0,0) were driven by self-calibration to coincide with the brightest pixel in the image, rather than with the location of the brightest Gaussian component. Tables 5.2 and 5.2 list the details of all the Gaussian source components and their fitted absorption line properties.

### 5.3.1 The Millisecond Scale Continuum Structure

These radio sources have been previously imaged with high angular resolution (e.g., Ludke et al. 1998; Sanghera et al. 1995; Neff et al. 1995; van Breugel et al. 1992; Nan et al. 1991; Akujor et al. 1991). Our small array of telescopes did not allow us to perform a high quality calibration but we obtained continuum maps and structures consistent with those previously published.

#### 3C 49

3C 49 is a CSS galaxy (Spinrad et al. 1985) at a redshift  $z=0.6207$  with radio components extended mostly east-west over a total angular size of 1 arcsec or  $\simeq 6.8$  kpc<sup>3</sup>.

<sup>3</sup>Ho = 71 km s<sup>-1</sup>Mpc<sup>-1</sup>,  $\Omega_M = 0.27$  and  $\Omega_\Lambda = 0.73$

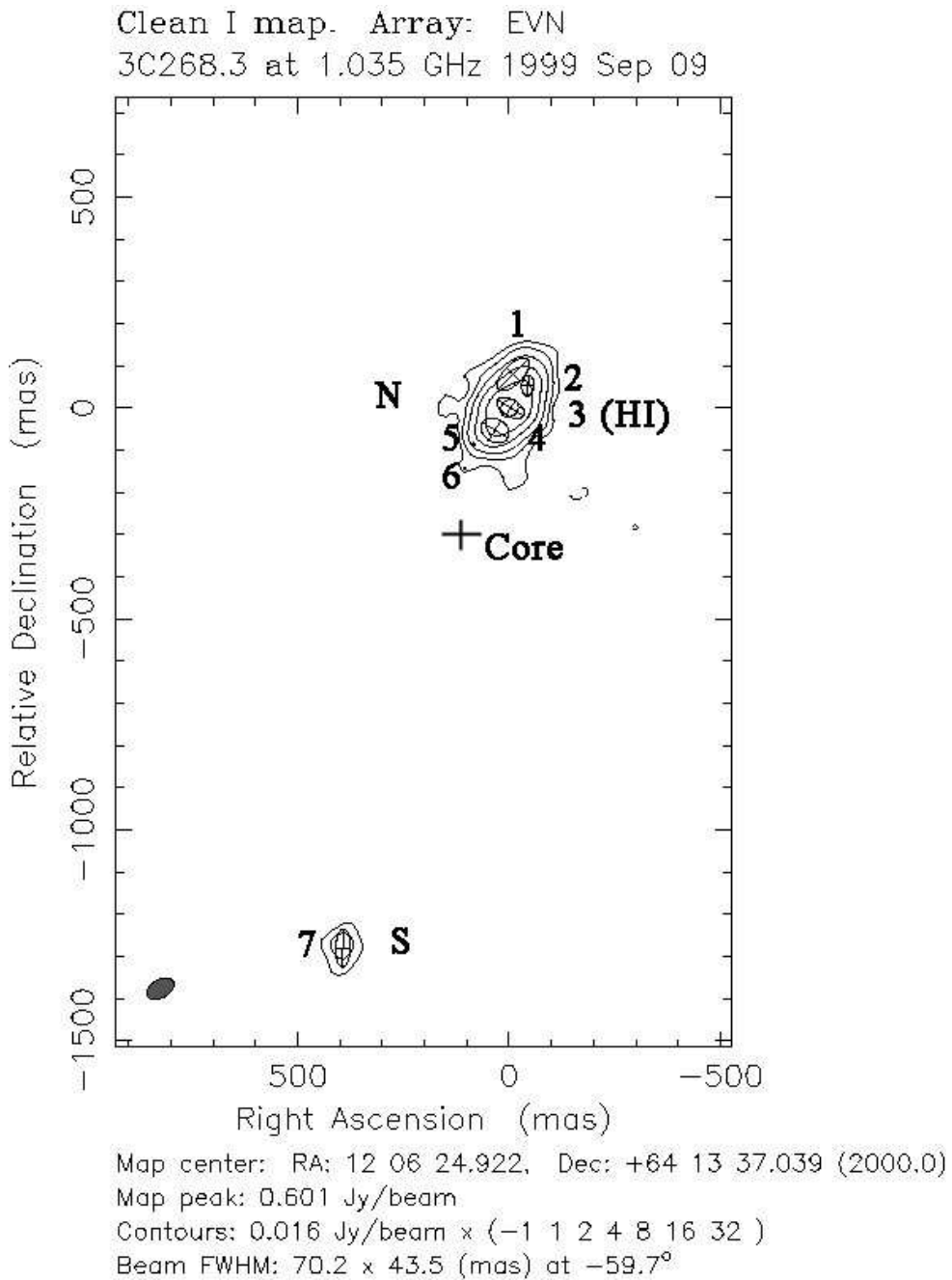


**Figure 5.2--.** Clean map of 3C 268.3 with the Gaussian components drawn on top. We use numbers to refer to the Gaussian model components (1 to 7, from top to bottom, being 1 the furthest north, and 7 the furthest south) and letters for the source *real* components (N for the Northern, S for the Southern). The position of the core detected at 5 GHz by (Ludke et al. 1998) has been marked with a cross.

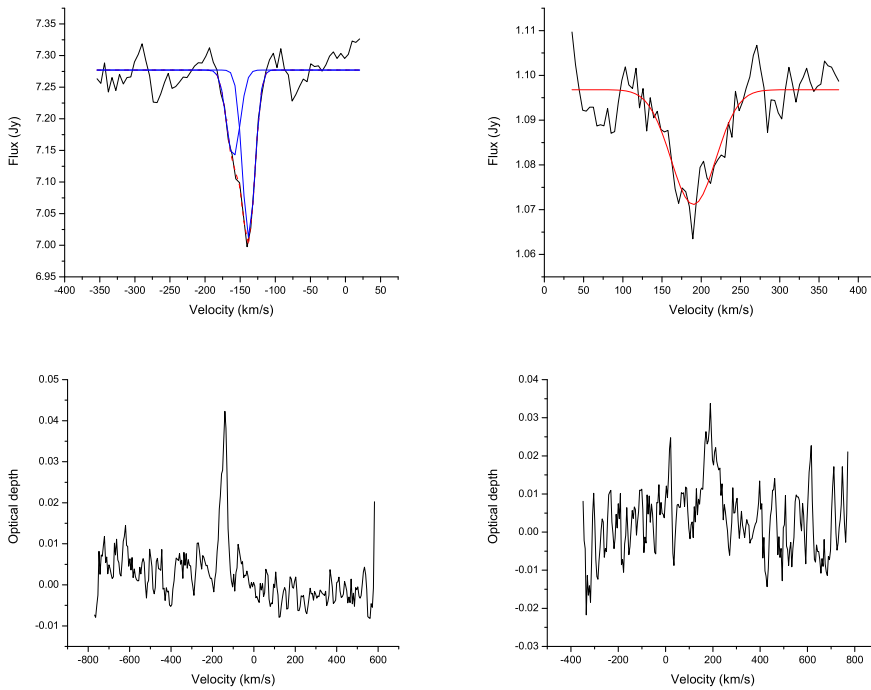


**Figure 5.3**— Left panels: Spectrum and optical depth of the absorption in the West component of 3C 49, with the de-blended lines and total fit over plotted. Right panels: Spectrum and optical depth of the absorption in the North component of 3C 268.3, with the fit over-plotted.

We detect the three components (labeled East, Center-West (CW) and West) which have been seen previously (i.e. Nan et al. 1991; van Breugel et al. 1992; Neff et al. 1995; Sanghera et al. 1995; Ludke et al. 1998). Multifrequency observations have shown that CW contains the flat spectrum core (Sanghera et al. 1995; Ludke et al. 1998). We also find an additional component labeled Center-East (CE) whose reality is uncertain. The CE component is faint but its inclusion in the clean components seemed to improve the final image. West is the brightest component in the map (integrated flux density =  $7.48 \pm 0.06$  Jy), which is roughly 66, 33 and 4.5 times more than the integrated flux density of CE, CW and East respectively.

### 3C 268.3

3C 268.3 is a CSS galaxy (Spinrad et al. 1985; Gelderman & Whittle 1994) at a redshift  $z=0.37116$ , with two main radio components oriented roughly north-south with a total angular size of 1.5 arcsec or  $\simeq 7.6$  kpc (i.e., Nan et al. 1991; van Breugel et al. 1992; Neff et al. 1995; Sanghera et al. 1995; Ludke et al. 1998). Our observations are consistent with the previous results. Ludke et al. (1998) have found a faint, possible core at 5 GHz, about 1.5 kpc south of the northern lobe.

The northern component has an integrated flux density of  $2.25 \pm 0.01$  Jy, which is roughly 22 times more than the southern component. The northern component also shows a more complex structure: 6 Gaussian components were required for it, as opposed to a single one for the southern feature.

As for the components of 3C 49, an offset between the brightest Gaussian component and the image peak brightness of 3C 268.3 is observed. In this case, the offset is even bigger, which is consistent with the North component being reproduced by more, brighter and bigger Gaussian components than W in 3C 49.

### 5.3.2 The HI Absorption

We have detected 21 cm HI absorption against the western lobe of 3C 49 and the northern lobe of 3C 268.3. Figure 5.3 shows the spectra and optical depth of these regions in 3C 49 and 3C 268.3.

The measured peak depth  $\Delta S$  of the absorption line depends on both the optical depth  $\tau$  and the covering factor of the hydrogen  $c_f$  (e.g. Wolfe & Burbidge 1975),

$$c_f = \frac{\Delta S}{S(1-e^{-\tau})} \quad \text{or} \quad \tau = -\ln \left( 1 - \frac{\Delta S}{Sc_f} \right)$$

where  $S$  is the continuum flux density. For a uniform source there is a minimum covering factor required by the observed ratio of line depth to continuum flux density  $c_f > \Delta S / S$  (e.g. O’Dea et al. 1994), and for a complete covering of the source  $c_f = 1$ .

The column density,  $N_{\text{HI}}$ , is given by:

$$N_{\text{HI}} = 0.18 \times 10^{21} (T_s/100\text{K}) \int \tau_\nu dv \text{ cm}^{-2}$$

(e.g., Dopita & Sutherland 2003; O’Dea et al. 1994), where  $T_s$  is the spin temperature,  $\tau$  the optical depth, and  $\nu$  is the velocity. For a Gaussian profile:

$$N_{\text{HI}} \simeq 1.94 \times 10^{20} (T_s/100\text{K}) \tau_0 \Delta V \text{ cm}^{-2}$$

where  $\tau_0$  is the peak optical depth in the line and  $\Delta V$  is the FWHM of the Gaussian line profile. A spin temperature  $T_s = 100$  K is applicable under typical ISM circumstances, although close to an AGN it could be higher (e.g. Morganti et al. 2001).

#### 3C 49

3C 49 shows HI absorption in the center of the Western component with a peak depth of  $\sim 4\%$  of the continuum level. The reduced  $\chi^2$  indicated that two Gaussian lines were needed to fit the absorption with peak depths of  $\sim 1.5\%$  and  $\sim 2.1\%$ . The column densities are 1.5 and  $0.8 \times 10^{20} (T_s/100\text{K}) \text{ cm}^{-2}$ . The absorption seems to be blueshifted in the host galaxy rest frame.

The covering factor,  $c_f$  for the absorption towards W in 3C 49 is  $1 > c_f > 0.04$ . If we assume the two absorption lines to be produced by spherical clouds of similar radius, equal to the measured FWHM of the component (24 mas = 163 pc at the source distance), then the density of these clouds would be  $220/c_f (T_s/100) \text{ cm}^{-3}$  and  $160/c_f (T_s/100) \text{ cm}^{-3}$ .

### 3C 268.3

3C 268.3 shows an absorption profile in the center of the northern lobe.  $\chi^2$  fitting shows that an adequate representation for the detection is just one Gaussian line redshifted in the host galaxy rest frame; the column depth is  $3.2 \times 10^{20} (T_s/100\text{K}) \text{ cm}^{-2}$ . Inspection of Table 5.2 shows that the limits on the other components are too high to rule out the presence of H I at similar levels in the southern component, which is much fainter than the northern component. The most intriguing  $2\sigma$  detection limit is 3.0% in component 4(N), which, compared to the detection in component 3(N), suggests that, possibly, the extent of the absorption towards the northern lobe is limited to  $72 \times 39 \text{ mas}$  ( $367 \times 199 \text{ pc}$  at the source distance).

The covering factor,  $c_f$ , for 3C 268.3 is  $1 > c_f > 0.025$ . If we assume the absorption line to be produced by a spherical cloud of a radius equal to the average of the measured FWHM of the component (55.5 mas = 283 pc), then the density of the cloud would be  $360/c_f (T_s/100) \text{ cm}^{-3}$ .

## 5.4 Discussion

We have detected H I absorption towards the western radio lobe of 3C 49 and the northern lobe of 3C 268.3. There are several possible hypotheses for the nature of the absorbing gas; e.g., (1) unrelated foreground clouds (e.g., in the ISM of the host galaxy) (2) an organized structure in the host galaxy such as a disk (as discussed by Pihlström et al. 2003), and (3) clouds which are interacting with the radio jet. We argue here that our results are consistent with the H I being produced in clouds which are in the environment of the radio source.

In 3C 49, the west lobe is  $\sim 4.5$  times brighter than the East lobe and  $\sim 3$  times closer to the core. Both radio lobes are unpolarized (Ludke et al. 1998). The emission line gas imaged by HST is very faint but seems to be asymmetric and is brighter near the west lobe (de Vries et al. 1997b, 1999; Axon et al. 2000).

In 3C 268.3, the northern radio lobe is roughly 22 times brighter than the southern lobe and  $\sim 3$  times closer to the core. In addition, Ludke et al. (1998) show that the radio polarization is asymmetric and that the northern lobe is much more strongly depolarized than the southern lobe. The emission line gas imaged by HST is also asymmetrically distributed and is much brighter near the northern lobe, while the southern lobe seems to extend beyond the line emission (de Vries et al. 1997b, 1999; Axon et al. 2000).

These correlated asymmetries in the radio and optical line emission are similar to those seen by McCarthy et al. (1991) in samples of powerful high redshift radio galaxies. We suggest that these data are consistent with a picture in which one side of the radio source is

strongly interacting with dense clouds of gas. The interaction causes the lobe to propagate more slowly, resulting in a smaller separation distance from the core (e.g., De Young 1991; Carvalho 1998; Jeyakumar et al. 2005). The higher radio luminosity could be due to smaller adiabatic expansion losses or to increased energy production efficiency due to compression and shocks (e.g., Jeyakumar et al. 2005). The clouds will also act as a Faraday screen, causing the observed depolarization as seen in 3C 268.3. The association of the optical emission line clouds and the H I absorption suggests that the H I absorption is produced in the atomic cores of the clouds which are seen in the emission line images (as may be the case in PKS2322-123, O’Dea et al. 1994). However, we caution that the data do not exclude the existence of H I on both sides of 3C 49 and 3C 268.3. An alternate scenario would be that the brighter lobe is beamed towards us and we are seeing H I absorption produced in clouds which are swept up by the radio lobes. However, if the brightness asymmetry is due to beaming we would expect the brighter lobe to be further from the core than the weaker lobe (due to the difference in light travel time), which is the opposite of what is observed.

A study of the emission line nebulae in three CSS sources – 3C 67, 3C 277.1 and 3C 303.1 – using HST long slit spectroscopy has shown that the kinematics of the gas are consistent with the clouds having been accelerated to velocities of several hundred km/s by shocks induced by the expanding radio lobes (O’Dea et al. 2002). The ionization diagnostics of the gas in CSS sources are also consistent with a contribution from shock-ionized gas (Labiano et al. 2005; Morganti et al. 1997; Gelderman & Whittle 1994). Thus, the observed blue and redshifts of the H I clouds of several hundred km/s in 3C 49 and 3C 268.3 could be attributed to bow shock induced velocities. It seems likely that both positive and negative velocities can result, depending on whether the H I absorption occurs in gas pushed towards the observer or in gas being entrained away from the observer.

## 5.5 Summary

We present European VLBI Network spectral line observations in the UHF band of the redshifted 21 cm H I line in two compact steep spectrum radio galaxies. We have detected H I absorption towards the western radio lobe of 3C 49 and the northern lobe of 3C 268.3. The radio lobes with H I absorption (1) are brighter and closer to the core than the opposite lobes; (2) are more depolarized (in 3C 268.3); and (3) are preferentially associated with optical emission line gas. The association between the H I absorption and the emission line gas, supports the hypothesis that the H I absorption is produced in the atomic cores of the emission line clouds, but we cannot rule out the existence of H I elsewhere. We suggest that the asymmetries in the radio and optical emission are due to interaction of the radio source with an asymmetric distribution of dense clouds in their environment. Our results are consistent with a picture in which CSS sources interact with clouds of dense gas as they propagate through their host galaxy.



# 6

---

## H I in the one-sided ‘compact double’ radio galaxy B2050+364

*Accepted for publication in A&A. In press*

R.C. Vermeulen, A. Labiano, P.D. Barthel, C.P. O’Dea, J.F. Gallimore, S.A. Baum, W.H. de Vries

EUROPEAN VLBI Network spectral imaging of the ‘compact double’ radio source B2050+364 in the UHF band at 1049 MHz has resolved the H I absorbing region, and has shown a faint continuum component to the North (N), in addition to the well-known East-West double (E, W).

Re-examination of VLBI continuum images at multiple frequencies suggests that B2050+364 may well be a one-sided core-jet source, which appears as a double over a limited frequency range. One of the dominant features, W, would then be the innermost visible portion of the jet, and could be at or adjacent to the canonical radio core. The other, E, is probably related to shocks at a sudden bend of the jet, towards the extended steep-spectrum region N.

A remarkably deep and narrow H I absorption line component extends over the entire projected extent of B2050+364. It coincides in velocity with the [O III] optical doublet lines to within  $10 \text{ km s}^{-1}$ . This H I absorption could arise in the atomic cores of NLR clouds, and the motion in the NLR is then remarkably coherent both along the line-of-sight and across a projected distance of  $> 300 \text{ pc}$  on the plane of the sky.

Broader, shallower H I absorption at lower velocities covers only the plausible core area W. This absorption could be due to gas which is either being entrained by the inner jet or is flowing out from the accretion region; it could be related to the BLR.

## 6.1 Introduction

B2050+364 (J2052+3635, DA 529; J2000 coordinates  $20^{\text{h}}52^{\text{m}}52.0549^{\text{s}}$   $+36^{\circ}35'35.300''$ , Beasley et al. (2002)), is one of the original members of the group of radio sources described as “Compact Doubles” (CDs) by Phillips & Mutel (1981), and then studied in more detail by Mutel et al. (1985). Phillips & Mutel (1981) suggested that, in contrast to most of the radio-loud AGN imaged with VLBI at GHz frequencies, CDs are “mini-lobes”, on (sub)galactic scales, at the ends of bi-directional outflows from an unseen central (“core”) component. The spectrum of the two components in compact doubles is typically not flat but peaked at a frequency around a GHz; such sources are termed Gigahertz Peaked Spectrum (GPS) sources (see the review by O’Dea (1998). The spectral shape can often be reasonably well understood from synchrotron self-absorption in  $\sim 1$  GHz radio emitting regions of  $\sim 100$  mas cross-section, but there are indications that in some sources, the low-frequency spectral shape is also determined (at least in part) by free-free absorption (e.g., Bicknell et al. 1997; Risaliti et al. 2003; Kameno et al. 2003, hereafter K03).

The CD and GPS source classes are related to the group of Compact Symmetric Objects (CSOs), first so termed by Conway et al. (1994) and Wilkinson et al. (1994). In CSOs, a central compact core component is visible in between two lobe-like components, albeit usually only faintly and often only at high observing frequencies. Thus, in CSOs the two-sidedness of the radio emission is proven beyond reasonable doubt. Models have been considered in which the lobes are kept to subgalactic dimensions by a dense confining medium (e.g., De Young 1993; Carvalho 1994, 1998). However, in a number of CSOs (e.g., Owsianik & Conway 1998; Polatidis & Conway 2003; Gugliucci et al. 2005) lobe advance velocities of a few tenths  $c$  have now been observed, and this provides powerful evidence that CSOs structures signify young radio sources, some with kinematic ages as low as a few hundred years.

GPS radio sources at moderate redshifts ( $z < 1$ ) are typically identified with passively evolving elliptical galaxies (e.g., Snellen et al. 1998a). The lifecycle of these sources is a subject of current interest, and is not well understood: at least some of them probably evolve to become fully fledged double-lobed FR I or perhaps even FR II radio sources, which typically have linear sizes of 100 kpc or even up to 1 Mpc, although, based on number counts, they should decrease in luminosity as they grow (e.g., Fanti et al. 1995; Readhead et al. 1996a; O’Dea & Baum 1997; Alexander 2000; Snellen et al. 2000). On the other hand, perhaps some compact sources may have multiple very short-lived active episodes (e.g., Gugliucci et al. 2005). Compact double radio sources are also particularly promising objects to study in the context of AGN fuelling and radio source evolution models, and the interaction between the interstellar medium and jets, because they lie entirely within the inner galaxy, on kpc or even sub-kpc scales.

One attractive possibility is to observe the 21cm hyperfine line of atomic hydrogen in absorption against bright radio structure, to study the kinematics and density distribution of the atomic gas. VLBI offers spatial resolution on the scales of the NLR and sometimes even the BLR, not accessible by any other means in galaxies at any appreciable redshift. However, for most CPS/CSO/CSS radio sources the frequency of this HI line is redshifted

outside the traditional observing band. But profiting from the advent of UHF receivers on interferometers, first at the Westerbork Synthesis Radio Telescope (WSRT), and then at many telescopes in the European VLBI Network (EVN), it has become possible to study the presence and distribution of associated H I in absorption against many compact radio sources.

A WSRT survey of a sample of compact radio sources was published by Vermeulen et al. (2003) (hereafter V03), and further analysed by Pihlström et al. (2003). About one third of the objects surveyed had detectable H I absorption, and the peak depth was found to be anti-correlated with linear size. A 16 % peak depth H I absorption line at  $z = 0.3547^1$  was discovered towards B2050+364. This is uncommonly deep; for sources of similar overall linear extent, absorption depths of 0.1–1 % (or upper limits at that level) were found to be rather more typical by V03. B2050+364 was therefore included in one of the first sessions with the new UHF receivers on the EVN, in order to resolve the H I absorption region spatially. We describe the data analysis procedure in Section 6.2, and present the results in Section 6.3.

B2050+364 has received comparatively little attention in its own right during the last two decades. Perhaps this was because of its low Galactic latitude,  $b = -5^\circ$ , in the Cygnus superbubble region ( $l = 79^\circ$ ), which is a handicap for obtaining a secure optical identification because of crowding, and hampers low frequency radio studies of the object because its image is broadened by interstellar scattering (Dennison et al. 1984; Mutel & Hodges 1986; Biretta et al. 1985; O’Dea et al. 1990) have both found a good match between the radio position and an  $m_r = 21.1$ ,  $(r - i) = 0.1$  galaxy. A spectrum was published by de Vries et al. (2000b) showing prominent H $\beta$  and [O III] emission lines. The latter have a redshift  $z = 0.3547$ ; we will critically review the redshift of B2050+364 in Section 6.5.2 and the optical identification in Section 6.5.3. Meanwhile, the low galactic latitude of B2050+364 has been turned into an advantage by using it as a background probe for interstellar scattering (e.g., Fey & Mutel 1993). This has culminated in a multi-frequency VLBI imaging study by Lazio & Fey (2001) (hereafter LF). Another multi-frequency VLBI data set is available from the investigation into possible free-free absorption in a sample of GPS sources by K03. Their results are described in Section 6.4, and used in our discussion on the nature of B2050+364 in Section 6.5.

## 6.2 Observations and data processing

### 6.2.1 Observations

On 1999 September 08–09, in one of the earliest sessions at UHF frequencies with the European VLBI Network (EVN), 14 hours were spent observing B2050+364, and the calibrators DA 406, 3C 454.3, and 3C 84. Four telescopes produced usable data: dual circular polarisations were available at Effelsberg and the WSRT, while Jodrell Bank had only LCP, and Onsala recorded dual linear polarisations. The (u,v)-coverage on B2050+364 is shown in Figure 6.1. The observing band, 1046.6 MHz to 1050.6 MHz, was centred on the absorption line discovered with the WSRT by V03.

<sup>1</sup> $H_0 = 70 \text{ km s}^{-1} \text{ Mpc}^{-1}$ ,  $\Omega_m = 0.27$ , and  $\Omega_\Lambda = 0.73$  are adopted throughout this paper, so that an angular size of 1 mas corresponds to 5.0 pc at  $z = 0.3547$ .

characteristics and data analysis procedures will be given in Vermeulen et al. (in preparation).

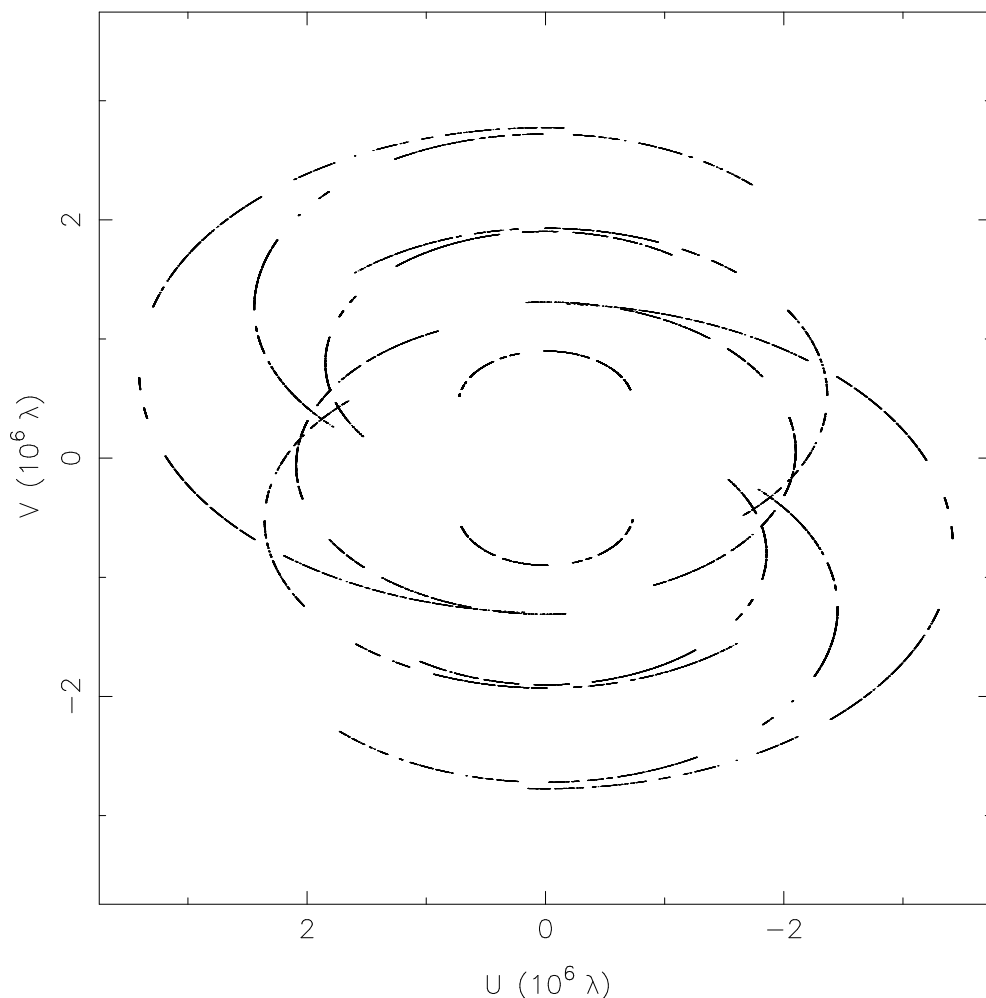


**Figure 6.1**–. The  $(u,v)$ -coverage obtained on 2050+364 with the EVN telescopes Effelsberg, Jodrell Bank, Onsala, and WSRT. Crossing points provide important self-calibration constraints.

### 6.2.2 Initial calibration and data averaging

The initial data processing (fringe fitting, spectral passband calibration, and a priori complex gain calibration) took place in the NRAO Astronomical Image Processing Software (AIPS), using the calibrator sources. After time-interpolated transfer of the solutions, and residual fringe-fitting on B2050+364, the data were averaged into 256 independent spectral channels (each  $4.5 \text{ km s}^{-1}$  wide), and 60 seconds time samples. This increased the sensitivity per

visibility. The target source, B2050+364, was detected on all baselines.

All available polarisation products were also averaged together, including the cross-correlations between the linear polarisations from Onsala and the circular polarisations from the other telescopes. We believe the sensitivity gained to the total intensity is more important than any possible resultant limitations on absolute flux calibration accuracy or on (image or spectral) dynamic range; we think these are more affected by the sparseness of the array and the lack of complete system temperature data and gain curves.

Much care was taken to obtain a consistent visibility calibration, for the rather sparse array, and in the occasional presence of external radio interference (although its impact is mitigated since it is typically not coherent over VLBI baselines). Relative antenna gains were derived from requiring consistent visibility amplitudes on the calibrator sources, while the overall flux density scale was set such that in the final self-calibrated image (see below) the total flux density is equal to 3.34 Jy at 1049 MHz, a value derived by interpolation from total flux densities at a number of other frequencies (Salgado et al. 1999; White & Becker 1992). We estimate the overall uncertainty in the flux scale of this UHF VLBI dataset to be as much as 20 %, but the main astrophysical results are unaffected, since they depend on opacities rather than on absolute flux densities.

### 6.2.3 Self-calibration; continuum imaging and modeling

The Caltech DIFMAP software package (Shepherd 1997) was used for all further calibration and analysis. A continuum dataset was formed by averaging all of the line-free channels on both sides of the HI absorption line, of which the location and width were taken from the WSRT survey (V03). The available VLBI array was sparse, but contained some crossing points (see Figure 6.1), and careful self-calibration was feasible. A double source structure was already evident in the first image made. After initial phase self-calibration, some additional flux density to the north-east quickly became apparent. At that time, we were unaware of the images published by LF, which at the lower frequencies also show emission in that area. Extensive tests of the reality of this third component were convincing: our data demand its presence. There are no major sidelobes of the dirty beam (shown in Figure 6.2) to affect its deconvolution with respect to the brighter parts of the source. We have performed careful iterative cycles of self-calibration with imaging/cleaning/modeling, both in trial runs where we kept excluding the third component from the models, and in runs where we admitted the presence of this additional continuum feature. The latter both gave cleaner-looking images and, more significantly, consistently required less extreme and more time-stable self-calibration coefficients.

In order to restrict the number of free parameters, the sky model fitted to the visibility data during iterative self-calibration cycles consisted of three circular Gaussian components: W(est), E(ast), and N(orth); their parameters, fitted to the visibility data, are given in Table 6.2.3. The final self-calibrated continuum visibility data were used to produce the cleaned and restored image displayed in Figure 6.3; symbols showing the three model components are overlotted.

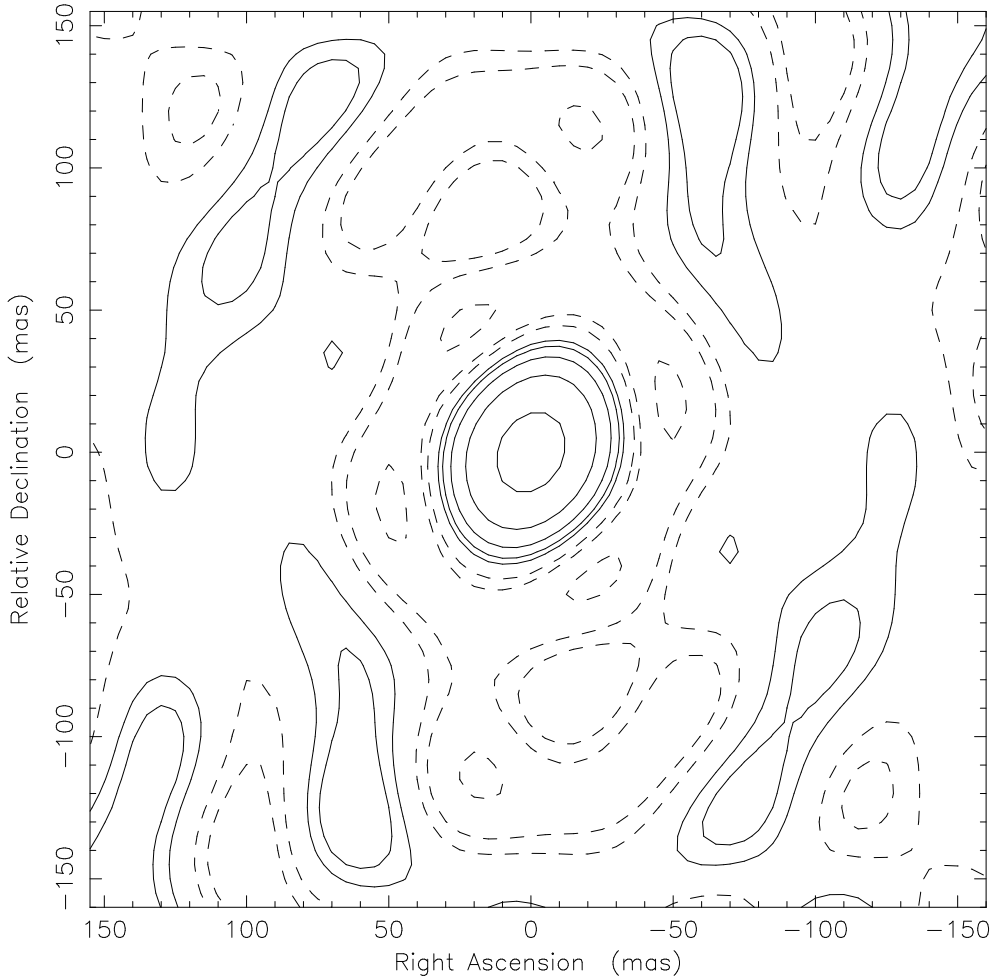


**Figure 6.2.**— The dirty beam obtained with the  $(u,v)$ -coverage shown in Fig. 6.1; contour levels are drawn at  $-0.2$ ,  $-0.1$ ,  $-0.05$ ,  $0.05$ ,  $0.1$ ,  $0.2$ ,  $0.4$ , and  $0.8$ . This beam is benign for deconvolution of the continuum structures in Fig. 6.3.

#### 6.2.4 Spatially resolved spectroscopy

The sensitivity of the data and the sparseness of the array did not allow generation of a full spectral image cube of acceptable signal-to-noise ratio. Instead, spectra of the W, E, and N areas of the source were determined by re-fitting the flux density of each of the three Gaussian model components derived for the line-free continuum, but then separately for each of the 256 spectral channels. The positions and diameters of the three components were

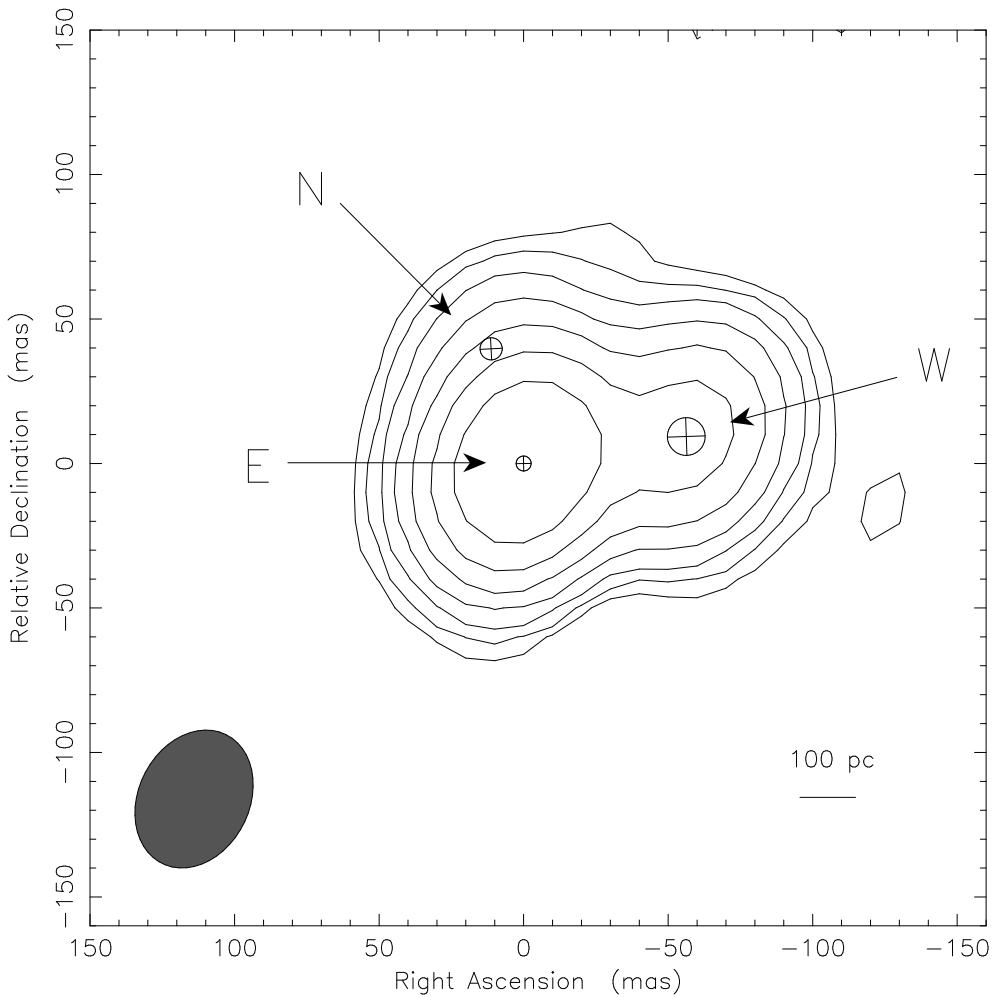


**Figure 6.3–.** Continuum VLBI image of B2050+364 at 1049 MHz. The restoring beam is  $50 \times 38$  mas in position angle  $-27^\circ$ . The peak flux density is 2.42 Jy/beam; contours start at 0.015 Jy/beam (3 times the r.m.s. fluctuation level away from the continuum structure), and increase in factors of 2. The absolute flux density scale is uncertain by 20 %, but this does not affect relative flux densities; see Section 6.2.2. The three circular Gaussian components used for modeling (Table 6.2.3) are overplotted.

not varied; they were fixed at the values derived from the continuum.

The resultant spectra are shown in Figures 6.4 and 6.5, as opacity with respect to the

Component	Flux (Jy)	Radial dist (mas)	P.A. (deg)	Diam (mas)
W	0.79	0	0	13.1
E	2.44	57	99	5.2
N	0.11	74	66	7.7

**Table 6.1**— The three circular Gaussian components used for modeling. Their continuum flux densities are listed. The absolute flux density scale is uncertain by 20 %, but this does not affect relative flux densities; see Section 6.2.2. These components are overplotted on the image in Fig. 6.3.

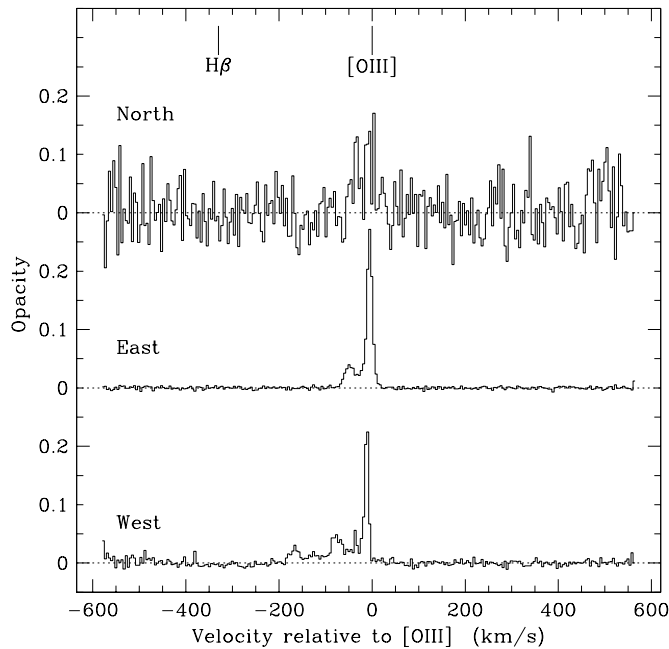


**Figure 6.4**— The H I absorption spectra, expressed in opacity, for the W, E, and N radio components of B2050+364. Zero velocity is chosen to be the [O III] redshift,  $z = 0.3547$  (see Section 6.5.2).

continuum strength of the appropriate components; this avoids the uncertainties in the absolute flux density scale, discussed in Section 6.2.2. Zero velocity for Figures 6.4 and 6.5 corresponds to the redshift of [O III],  $z = 0.3547$ , published de Vries et al. (2000b); this choice will be further discussed in Section 6.5.2. Note that a less precise value of the optical redshift was used by V03.

Gaussian line profiles were fitted to the most obvious features of the H I spectra at the three locations. The fitted profiles are overplotted on the data in Figure 6.6, and their parameters are listed in Table 6.2.4. These serve only to obtain a rough quantification of

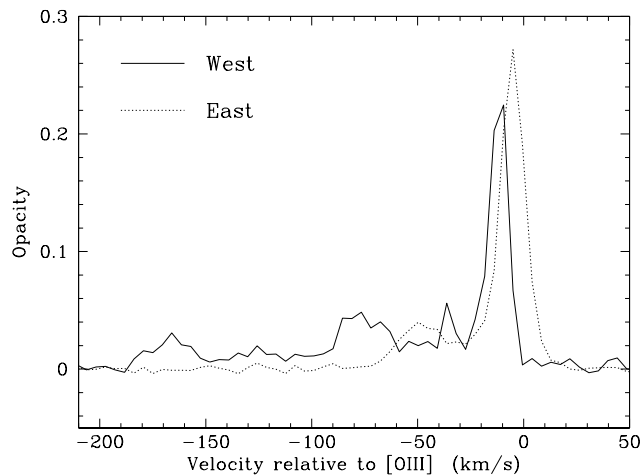


**Figure 6.5**–. Enlargement of part of Figure 6.4, to allow detailed comparison of the HI opacity profiles towards W and E.

the absorber properties; in particular, no attempt was made to find an optimally fitting set of Gaussians to cover the complex observed line spectrum at W.

## 6.3 Results

### 6.3.1 VLBI continuum structure of B2050+364 at 1 GHz

The 1049 MHz continuum VLBI image shows the W and E components, which constitute the well-known “classical double”. At this frequency the W:E flux density ratio is close to 1:3; this is constrained better than the flux densities themselves. The two components are separated by about 57 mas (285 pc) along a PA of  $\sim 100^\circ$ , which matches the relative locations found at other frequencies by LF. The component sizes we find at 1 GHz are only slightly larger than those found at 1.67 GHz by LF; we believe that the accuracy of our fitted component sizes is limited by the relatively poor resolution of our array (synthesised beam  $50 \times 38$  mas), although it is interesting that the angular diameter we find for E, 5.2 mas, is comparable to the scattering disk diameter determined by LF, 6–8 mas (as discussed below, this could be somewhat of an over-estimate since LF did not recognise sub-components which exist at the lowest frequencies).

We have also discovered with our data (before finding it in the low-frequency images published by LF) an additional emission region to the north/northeast, which we call N. While we are confident about the existence and approximate location of N, about 74 mas (370 pc) from W in PA  $\sim 66^\circ$ , its flux density ( $\sim 0.1$  Jy) is subject to considerable uncertainty, both in view of the overall flux scale uncertainty and because, with the sparse imaging array, some extended emission may have been missed. The relatively small array of EVN antennas used did not allow the presence of substructure within any of the three

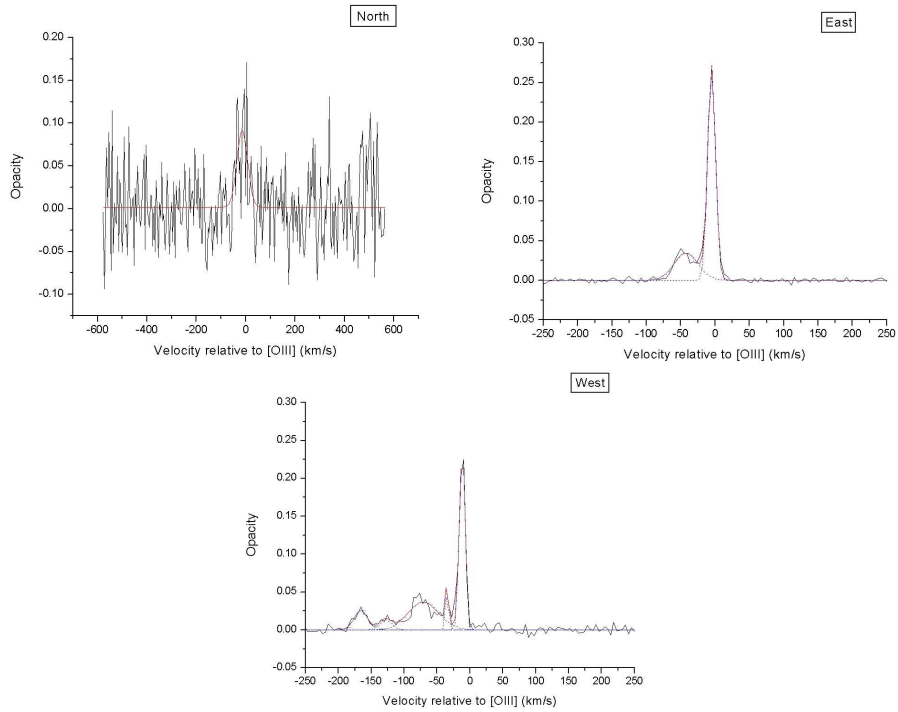


**Figure 6.6.** Fitted Gaussian line profiles overlapped onto the HI absorption spectra of the three regions. The parameters are listed in Table 6.2.4.

components to be investigated.

### 6.3.2 H I absorption distribution

The VLBI data reveal that the two most prominent H I absorption features (16 % and 4 % integrated opacity) found towards B2050+364 in the WSRT survey (V03) do not cover the sub-kpc scale radio source uniformly. The integrated (WSRT) profile is dominated by the absorption towards E, because that component is much brighter than the other radio source components.

The distinct, deep absorption feature at the high velocity end of the absorption spectrum shows a  $\sim 7 \text{ km s}^{-1}$  centroid velocity offset between W and E; see also Figure 6.5. This observed offset is highly significant, given the velocity resolution of  $4.5 \text{ km s}^{-1}$ , and the high signal-to-noise ratio of these absorption features. The line is also narrower at W than at E. At N, a corresponding absorption feature is also visible in the VLBI data (see Figures 6.5 and 6.6), but, due to the low background continuum flux density, the centroid velocity and the FWHM are too uncertain for a useful comparison. The peak opacity at N appears to be lower than at either W or E.

Region	Centre (km s <sup>-1</sup> )	FWHM (km s <sup>-1</sup> )	Peak opacity	$N_{\text{H I}}$ 10 <sup>20</sup> cm <sup>-2</sup>
W	-11.7 ± 0.1	10.3 ± 0.3	0.212 ± 0.010	4.2 ± 0.2
	-35.0 ± 0.7	5.8 ± 2.1	0.037 ± 0.022	0.4 ± 0.3
	-71.0 ± 2.3	55.0 ± 6.9	0.036 ± 0.006	3.9 ± 0.8
	-128.8 ± 3.6	20.7 ± 9.2	0.013 ± 0.008	0.5 ± 0.4
	-166.1 ± 1.9	24.1 ± 4.8	0.026 ± 0.007	1.2 ± 0.4
E	-5.1 ± 0.1	13.4 ± 0.2	0.263 ± 0.004	6.8 ± 0.1
	-42.4 ± 0.9	41.1 ± 2.4	0.034 ± 0.003	2.7 ± 0.3
N	-14.2 ± 5.1	51.5 ± 12.1	0.091 ± 0.028	9.1 ± 3.6

**Table 6.2.**— The parameters of the Gaussian line profiles fitted to the observed H I spectra of the three regions, as shown in Fig. 6.6. The derived column depths assume uniform coverage and  $T_{\text{sp}} = 100$  K.

The VLBI data show that the second absorption feature tabulated by V03 for the integrated WSRT spectrum (where it covers the observed velocity range  $-30$  km s<sup>-1</sup> to  $-60$  km s<sup>-1</sup> with respect to the [O III] redshift) has a peak opacity of  $\tau = 0.035$  at both W and E. But the detailed profile differs substantially between W and E; it is particularly irregular at W. The integrated profile shown in V03 is dominated by E, because it is the brightest feature. While the absorption at N was modeled with just a single Gaussian line, it is wider than the main component at E and W (see Table 6.2.4, and may therefore also encompass some secondary absorption features.

The VLBI data also show that there are further absorption features, extending to an observed velocity of nearly  $-200$  km s<sup>-1</sup>, at comparatively low opacities (a few percent, see Figure 6.6). These are all detected towards W only, and not towards E; towards N the signal-to-noise ratio is too poor to establish or delimit the presence of similarly shallow features. Since E dominates the total flux density, these features are not readily apparent in the integrated spectrum of V03.

## 6.4 Multi-frequency Radio Continuum Structure

The compact structure of B2050+364 was imaged with VLBI at multiple frequencies by both LF and K03. Their projects were aimed at studying interstellar scattering, or free-free absorption statistics, respectively, and the structure of B2050+364 itself was not analysed in detail. However, we give our own description of the images here, because we will then show in Section 6.5 that together with our own results, a surprising new interpretation emerges: B2050+364 could well be a one-sided core-jet source !

To support the discussion, we show in Figure 6.7 the flux densities at multiple frequencies as tabulated by LF and K03, and the flux densities at 1 GHz from our own data (Table 6.2.3). We have summed over all sub-components which were given the same label (W or E,

respectively) by LF, except, as discussed below, at 0.61 GHz, where we recognise one of the components as N, and at 0.33 GHz, where we think the single flux density listed by LF should in fact be ascribed to a combination of all components. LF and K03 both have data at 2.3 GHz and 8.4 GHz. The morphologies in their images appear to match well, and while their tabulated flux densities differ at the 20 % level, the uncertainties do not obscure the trends on which we wish to focus; we simply use the average of the two available measurements in Figure 6.7, with a bar to show the range between them.

The northeastern region, which we have called N, is clearly distinguishable in the 1.67 GHz image of LF, where it consists of rather extended emission at a distance of roughly 30–55 mas from region E, to the north and northeast, in position angles roughly between  $0^\circ$  and  $30^\circ$  as seen from E; the position angle of region N as seen from W is about  $65^\circ$ . Note that this corresponds well with the position of N in our data (see Table 6.2.3; with respect to E, the distance of N at 1049 MHz is 41 mas, in a position angle of  $16^\circ$ ). There are, understandably, no model components tabulated by LF for this extended emission. From the contour levels and extent of the emission, our very rough estimate of the total flux density of N is 75 mJy, which we have indicated with a factor of 2 margin towards both lower and higher values in Figure 6.7.

Region N is also unmistakably present in the 0.61 GHz image of LF. Even though, for their own analysis, LF have included it as part of E, the third 0.61 GHz model component tabulated by LF (with flux density 0.11 Jy) clearly forms part of N, given its position relative to E. The model component might only represent part the total flux density from that area, and it is thus indicated as a lower limit in Figure 6.7.

At 0.33 GHz, LF have modeled the source as a single Gaussian, which they ascribed fully to E. However, in their image we find good evidence for the presence of all three components, W, E, and N. The image is clearly extended and elongated, and the western side is the fainter part. We believe this is W; all other data establish that W has a more inverted broad-band spectrum and is fainter than E at all frequencies below 8.4 GHz (see Figure 6.7). Unfortunately, E and N are difficult to disentangle in the 0.33 GHz image, both because of the lower VLBI resolution, and because of scatter-broadening, although LF may have overestimated the amount of interstellar scattering at 0.33 GHz when they took the entire visible structure to be due to E. We find that the overall position angle of the contour image is  $75^\circ$ – $85^\circ$ . This suggests that the location of the centroid of the bright, eastern part of the source is influenced by significant contributions from both E (in  $PA \sim 100^\circ$  from W) and N (in  $PA \sim 65^\circ$  from W). Thus, we show in Figure 6.7 a plausible but by no means unique decomposition of the total flux density of the single model component fitted by LF; to indicate our uncertainty, no marker symbols are drawn.

Components W and E, we believe, are thus separately visible at all frequencies, while component N is visible in the images up to 1.67 GHz. Above 1 GHz, where the linear resolution is sufficient and the impact of interstellar scattering negligible, “component” E shows considerable substructure. At the highest observing frequencies, 8.4 GHz and 15.4 GHz, “component” W is seen to have compact substructure as well. Where measurable, the intrinsic angular sizes of W or its sub-components are considerably smaller than those

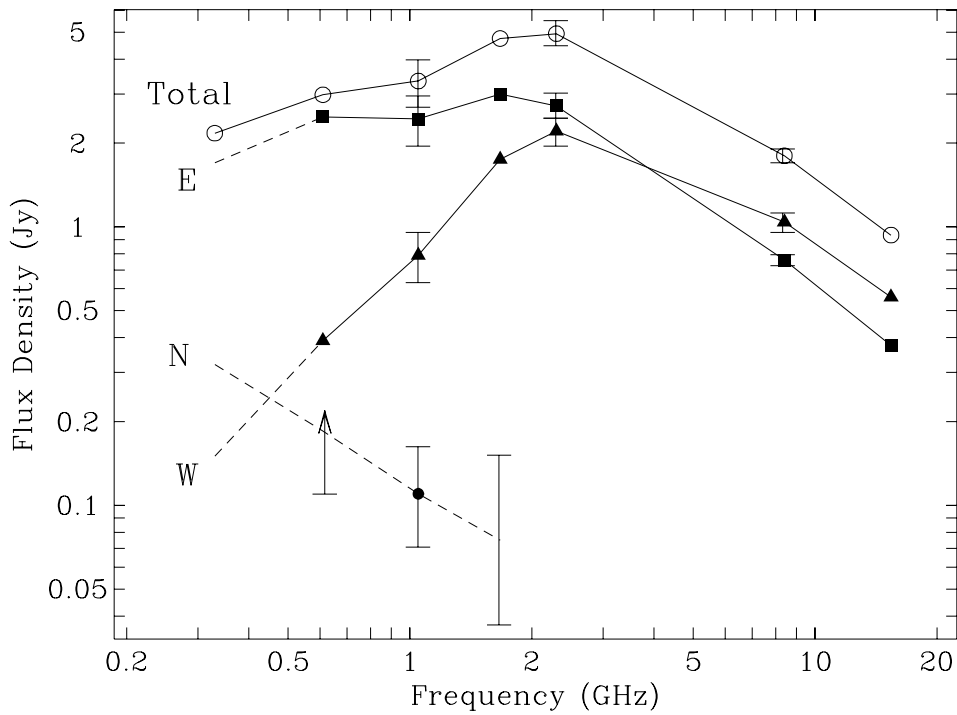


**Figure 6.7—.** Continuum component flux densities at multiple frequencies, based on data at 0.33, 0.61, 1.67, 2.3, and 8.4 GHz from LF, at 2.3, 8.4, and 15.4 GHz from K03, and at 1.049 GHz from our own observations. See Section 6.4 for details.

of E or its sub-components. Also, from Figure 6.7, W clearly has the most inverted low-frequency spectrum, and very likely also the highest peak frequency and the flattest high-frequency spectrum.

N has quite the opposite properties: it is the most extended and does not appear to have much compact substructure; its broad-band radio spectrum is probably steep over the full frequency range (although with large uncertainties from the data of LF). Thus, W, E, and N, successively are in a sequence of decreasing compactness, steepening high frequency spectral index, and decreasing peak frequency.

## 6.5 Discussion

### 6.5.1 B2050+364: a one-sided core-jet structure ?

The three regions W, E, and N show a progressive change of compactness and of spectral shape which is not typical for compact double-lobed radio sources, but rather for core-jet radio sources, where relativistic beaming and opacity effects lead to a one-sided observed

structure. Furthermore, the relative alignment of the three regions is also compatible with a one-sided core-jet source. The very compact sub-components of W seen at the highest frequencies are aligned roughly, but not exactly, along the line towards E. The relative disposition of the substructures in E at various frequencies suggests that this may well be radio emission from shocks at the location of a sudden bend in a single jet, which is first visible at W, and after bending at E continues towards the more extended emission region N. The jet could be at a fairly small angle to the line of sight, such that the deprojected angle of the bend at E need not be large; this is seen in many other core-jet sources. Due to its substructure, E has a somewhat unusual convex broad-band radio spectrum, peaked at frequencies of a few GHz. We find that B2050+364 is set apart from many other GPS/CSS sources by the fact that at all GHz frequencies its total flux density is dominated by two emission regions, W and E, which are rather compact and widely separated, i.e., each one spans only a small fraction of the distance between them. Genuine double-lobed GPS/CSS sources can show compact hot spots at the two ends, but then in addition they typically have clearly visible, often dominant, extended emission regions (the lobes). Region N in B2050+364, on the other hand, is rather faint, even at the lowest frequencies, and as such would be rather atypical if it were a lobe beyond its putative hot-spot E. A convincing counter-lobe is not seen. Classical core-jet sources, on the other hand, do often show a faint extended emission region beyond a shock at a bend in the jet.

We think that it is, furthermore, plausible that the sub-components of W may be at or adjacent to the traditional radio core. Many core-jet radio sources show a few bright knots in the innermost jet. The overall apparent separation velocity between W and E at 1.67 GHz has been delimited by LF to be no faster than  $c$ . However, this limit is still several times faster than what seems to be typical in CSOs (e.g. Gugliucci et al. 2005), and it also does not rule out that some sub-components might even show superluminal motions, as is sometimes seen in other sources, where stationary radio components are thought to mark regions of either confinement or bending in a jet, while other radio features may be moving with a flow or due to traveling disturbances. It is possible that the sub-components of W are still part of the inner jet, with the true core being somewhat further to the west, perhaps at a more compact radio component, as yet unseen due to a spectrum which is significantly inverted as a result of synchrotron self-absorption, free-free absorption, or a combination of both, as is probably the case in several other compact radio sources (e.g., Kameno et al. 2003). It would be interesting to attempt to monitor the positions of some of the well-defined sub-components in the W and E regions at high frequency.

In most well-known two-sided GPS/CSS sources, at the relatively high frequency of 15 GHz synchrotron self-absorption and/or free-free absorption do not fully hide the central core component (to a reasonable dynamic range of a hundred, say). However, even higher frequency observations would be useful before definitely ruling out the existence of a more inverted-spectrum core component between W and E, in which case the radio source might be two-sided after all. Likewise, even if the currently imaged structure is one-sided, with the core at or near W, it is possible that further high-dynamic-range imaging could reveal emission from a second jet or lobe on the opposite side. This situation has occurred, for example, in 2352+495, a well-known CSO (Conway et al. 1992).

The original selection of B2050+364 as a Compact Double (suggesting two-sided radio emission) seems to have been the result of a similarity between W and E which is partly coincidental; we now know that their properties diverge when studied over a wider range of frequencies, and that a section further out in the jet, N, has a steeper, more typical broad-band spectrum. Several other examples are now known in which the similarity between the components of an apparent compact double breaks down when the source is studied with high enough resolution and dynamic range and at high enough frequency. Amongst the sources now considered to be one-sided is CTD93 (Shaffer et al. 1999); like B2050+364, it was a member of the original group of CDs. The identification of a centrally located core component is a crucial part of confirming whether a CD or GPS source is indeed two-sided, and therefore a CSO, rather than a one-sided core-jet source in which two emission regions happen to have comparable flux densities and sizes, and therefore roughly similar spectra (Conway et al. 1994; Wilkinson et al. 1994).

### 6.5.2 The optical redshifts and H I: infall or outflow ?

The optical spectroscopy reported by de Vries et al. (2000b) gives  $z = 0.3547$  consistently for both [O III]  $\lambda 4959$  and [O III]  $\lambda 5007$ , while H $\beta$   $\lambda 4861$  is at  $z = 0.3536$ . Thus, the observed centroid velocity of the [O III] doublet is formally about  $325 \text{ km s}^{-1}$  larger than that of H $\beta$ . We believe that this difference is probably significant. The spectral resolution was  $15 \text{ \AA}$ , but the centroid wavelengths are listed in integer  $\text{\AA}$ , i.e. with 4 significant figures. The [O III] doublet lines are narrow and clearly have an excellent signal-to-noise ratio, so the total uncertainty in the centroid of these lines could well be of order  $\pm 1 \text{ \AA}$  in wavelength, or  $\pm 0.0002$  in redshift, or  $\pm 50 \text{ km s}^{-1}$  in velocity. The observed FWHM of H $\beta$  looks like it is roughly  $50 \text{ \AA}$ , or  $2500 \text{ km s}^{-1}$ , and the line has a lower signal-to-noise ratio, so the uncertainty in its centroid is probably several times larger than for the [O III] doublet. Nevertheless, we think that the combined velocity uncertainty probably cannot account for the entire  $325 \text{ km s}^{-1}$  observed centroid velocity offset between [O III] and H $\beta$ .

The [O III] line velocity and the velocity of the deepest H I features agree to within  $10 \text{ km s}^{-1}$  (see Figure 6.4). The radio spectral resolution is  $4.5 \text{ km s}^{-1}$ , and the H I absorption features are present at high signal-to-noise, so the uncertainty in this match is dominated by the optical data, and we believe that the offset of the [O III] velocity from that of the deep H I feature is not significant.

The VLBI data show that there is atomic gas at the [O III] velocity spanning a projected distance of several hundred parsecs, and probably overlapping in projection with the radio core. This makes it likely that the [O III] emission is from a conventional narrow line region (NLR) surrounding the active nucleus, rather than from an isolated cloud moving with a fairly high peculiar velocity. In Section 6.5.3 some less conventional possibilities are discussed, but we believe these are less plausible. A substantial centroid offset from the systemic velocity of the host galaxy seems in general more likely for the broad line region (BLR), which shows the kinematics of gas under the immediate local influence of the active galactic nucleus, than for a region with an extent of several hundred parsecs. Thus, we have adopted the [O III] redshift,  $z = 0.3547$ , as the redshift of the host galaxy, and the zero point of the velocity scale used for our main analysis. This means that both the H $\beta$  line

and the lower opacity H I absorption features extend to negative velocities (i.e. outflowing, approaching the observer); in the restframe, the velocity offset of H $\beta$  is  $-244 \text{ km s}^{-1}$ .

The H I absorbers in B2050+364 thus appear to be somewhat different than in PKS 1549–79 (Tadhunter et al. 2001) and B1221–42 (Morganti, priv.comm.). In those objects the velocity of the H I line does not coincide with the optical redshift of the [O III] line, but rather with the [O II] line. Because of its lower ionisation level, one might expect [O II] to originate in a larger region and perhaps to be more representative of the systemic velocity than [O III].

### 6.5.3 The locations of the H I absorbers relative to the radio source

We think that all of the H I absorption may well occur in the same region as the radio source, in the inner kiloparsec of the host galaxy, and that the presence of this atomic gas might have some connection with the active nucleus, or with the radio morphology. Below we argue that an association of the narrow, deep H I component with the NLR in B2050+364 is plausible, and that the broader H I absorption towards region W could be related to the BLR.

The atomic gas is probably not kinematically disturbed very much as a result of interaction and bending of the jet at E. The absorption profile there only has two narrow components, and moreover, the dominant deep line is rather similar to the one at W, where no bending of the jet is visible. If the jet at E does impact and disturb clouds containing atomic hydrogen, these probably do not cover the radio source as seen along our line-of-sight.

The sharp, deep absorption features at low velocity are at first sight the most puzzling to explain. The integrated peak opacity in B2050+364, 16 %, is the third deepest in the sample of 41 CSS and GPS sources analysed by Pihlström et al. (2003). Based on the anti-correlation of peak opacity with linear size in that sample,  $\leq 1$  % absorption would be more typical for a projected extent of  $\sim 300$  pc. Conversely, the FWHM of the integrated deep H I absorption feature in B2050+364,  $16 \text{ km s}^{-1}$ , is the narrowest in the sample, where most of the FWHM are in the range of fifty to several hundred  $\text{km s}^{-1}$ , with no obvious dependence on source linear size.

Because the remarkably high peak opacity is partly balanced by a remarkably low FWHM, the integrated column depth lies only mildly above the anti-correlation with linear size in the sample of Pihlström et al. (2003): assuming uniform coverage and a spin temperature  $T_{sp} \sim 100$  K, as is often thought to prevail in typical ISM conditions, we obtain  $N(\text{H I}) \sim 5 \times 10^{20} (T_{sp}/100) \text{ cm}^{-2}$ ; column depths for the individual features are listed in Table 6.2.4.

The most likely location for this H I absorption is in the neutral cores of the clouds in the NLR, given the excellent correspondence with the velocity centroid of the [O III] line, and the projected extent of at least 300 pc.

Taking  $n_{\text{H I}} = 100 \text{ cm}^{-3}$  as a rough estimate of the atomic gas density in NLR clouds, and using the 300 pc transverse extent covered by the absorbers as an estimate of the

line-of-sight depth through the NLR as well, this would imply that clouds are present along about 1 % of the pathlength. The key distinguishing property, then, is the low kinematic dispersion. The main direction of motion and/or rotation in the NLR of B2050+364 is evidently perpendicular to our line-of-sight, and coherent in velocity to  $\sim 10 \text{ km s}^{-1}$  over several hundred parsecs both along the line-of-sight and transverse to it. It is this velocity coherence which allows a deep, narrow absorption line to build up. Thus, it seems unlikely that the absorption is related to directly inflowing gas, feeding the nucleus, because the velocity is so similar over a region substantially larger than typical accretion regions.

On the other hand, the absorption features of comparatively low opacity but spanning a broader observed velocity range (to nearly  $-200 \text{ km s}^{-1}$ ) occur only towards W, which we believe is most likely to be at or close to the nucleus (see Section 6.5.3). It is plausible that this shows neutral hydrogen which is either being entrained by the inner jet of B2050+364, or is flowing out from the accretion region. Perhaps this atomic gas is related to the BLR in B2050+364, particularly since the  $H\beta$  centroid, while subject to considerable uncertainty, is probably also at a negative velocity of a few hundred  $\text{km s}^{-1}$ . The neutral gas, especially that part of it which happens to be visible in absorption, is likely to sample only a part of the velocity profile of the ionised gas. The broader part of the H I profile clearly has several distinct kinematic components (a possible representation with Gaussian lines is given in Figure 6.6 and Table 6.2.4); the average opacity is  $\tau \sim 0.025$ . Assuming W to be uniformly covered gives a column depth integrated over the observed velocity range  $-50 \text{ km s}^{-1}$  to  $-180 \text{ km s}^{-1}$ , of roughly  $N(\text{H I}) \sim 6 \times 10^{20} (T_{sp}/100) \text{ cm}^{-2}$ . Making the further and surely oversimplified assumption that the absorbing atomic gas is also uniformly dense along a pathlength comparable to the total transverse extent of W ( $\sim 10 \text{ pc}$ ), then the atomic gas density would be  $n_{\text{H I}} = 20 \text{ cm}^{-3}$ , which is rather low. Unfortunately, with the EVN we cannot resolve region W at the frequency of the H I line. The optical BLR itself probably has an extent of at most 1 pc, so if the atomic gas were also confined to that region only, then its density would be perhaps two or three orders of magnitude higher, because the pathlength would decrease, the opacity and column depth would increase since the covering factor of W would be less than unity, and finally, close to the active nucleus the spin temperature could be significantly elevated.

Could the H I absorption arise instead outside the host galaxy of B2050+364 ? A chance superposition, in which the galaxy visible at the position of B2050+364 would be a foreground object rather than the host of the radio source, is *a priori* unlikely. Such a situation does exist for lensed radio sources, such as 0218+357, where the foreground lensing galaxy also leads to H I absorption (Carilli et al. 1993), but we do not think that the radio morphology of B2050+364 is suggestive of gravitational lensing.

Close to the radio position, two other galaxies of comparable brightness are visible in the images of Biretta et al. (1985); O’Dea et al. (1990). One or both of these could be a true companion to the host galaxy of the radio source. The closer neighbour, in PA  $180^\circ$ , is centred at a projected distance of only 2 arcsec (10 kpc at  $z = 0.3547$ ), and so part of its disk could well be overlapping with the radio source in projection. The other one, centred at a projected distance of 7 arcsec (35 kpc at  $z = 0.3547$ ) in PA  $-120^\circ$ , seems to show an extension (a spiral arm ?) in the direction of the radio source, and this might be another

candidate foreground absorber.

However, in any external absorber scenario considered, that other galaxy would probably have to be responsible for both the [O III] line as well as the H I absorption, given the velocity correspondence to within  $10 \text{ km s}^{-1}$ . But that would mean that the other galaxy may also have an active nucleus, or prodigious star-bursting activity, since strong [O III] emission is not usually seen in ordinary galaxies. The optical spectrum shown in de Vries et al. (2000b) suggests a high ratio of [O III] to  $H\beta$ , i.e., high ionisation gas. This would indicate ionisation by an AGN rather than a starburst. In our view the required coincidence of two active galaxies makes external absorber options much less plausible than the simple model discussed earlier that the H I absorption shows atomic hydrogen in the NLR and BLR associated with the compact radio source B2050+364.

## 6.6 Summary

We have presented and discussed VLBI continuum and spectral line data at 1049 MHz of the compact radio source B2050+364, and we have interpreted the multi-frequency continuum VLBI images of LF. Our conclusions can be summarised as follows:

- The continuum structure at 1049 MHz consists of a faint component N to the northeast, in addition to the two well-known components E and W, which constitute the original double; their flux density ratio is 3:1.
- The compact-double properties hold only over a limited frequency range. W, E, and N, in that order, have decreasing compactness, steepening low frequency spectral index, and decreasing peak frequency.
- Compactness and radio spectra, plus the alignment of substructures within W and E, suggest that B2050+364 is a one-sided core-jet originating at or near W, bending sharply (in projection) at E, and continuing towards N.
- At the high velocity end of the absorption spectrum is a deep H I line, which reaches a maximum opacity  $\tau = 0.26$  at E, with a FWHM of  $13 \text{ km s}^{-1}$ . At W it is even narrower, with a FWHM of  $10 \text{ km s}^{-1}$  and somewhat lower opacity,  $\tau = 0.21$ . At N the opacity is  $\tau \sim 0.09$ . This absorption thus covers the entire source, extending over  $> 300 \text{ pc}$ , albeit with significant differences in opacity. Implied column depths are  $N(\text{H I}) \sim 5 \times 10^{20} (T_{sp}/100) \text{ cm}^{-2}$ .
- Extending to lower velocities is lower opacity H I absorption, which only covers W. The average opacity between  $-50 \text{ km s}^{-1}$  and  $-180 \text{ km s}^{-1}$  is  $\tau \sim 0.025$ , and the estimated column depth is  $N(\text{H I}) \sim 6 \times 10^{20} (T_{sp}/100) \text{ cm}^{-2}$ .
- The centroid of the [O III] optical doublet lines,  $z = 0.3547$ , coincides to within  $10 \text{ km s}^{-1}$  with the distinct deep line at the high velocity end of the H I radio absorption line spectrum. The formal line centroid of the optical  $H\beta$  line is at an observed velocity of  $-325 \text{ km s}^{-1}$  relative to [O III].

– We believe that the uncommonly deep but also uncommonly narrow H I absorption line is likely to be due to atomic gas in the cores of NLR clouds in the inner kpc of B2050+364. Assuming NLR clouds of density  $n_{\text{H I}} = 100 \text{ cm}^{-3}$  in a region with a 300 pc radius would imply their presence along 1 % of the line-of-sight. The direction of motion and/or rotation in the NLR of B2050+364 is coherent to  $\sim 10 \text{ km s}^{-1}$  over several hundred parsecs both along the line-of-sight and transverse to it, and is largely perpendicular to our line-of-sight.

– We believe that the lower opacity absorption at W ranging to  $-200 \text{ km s}^{-1}$  is likely to be due to atomic gas which is either being entrained in the inner parsecs of the jet of B2050+364, or is flowing out from the accretion region. It is plausibly related to the BLR in B2050+364. The atomic gas density is at least  $n_{\text{H I}} = 20 \text{ cm}^{-3}$ , for a 10 pc absorbing region, but could well be as much as three orders of magnitude higher if the region is smaller.



# 7

---

## Star formation in hosts of compact radio galaxies

A. Labiano, C.P. O'Dea, P.D. Barthel, W.H. de Vries, S. A. Baum

**W**E present near ultraviolet imaging with the Hubble Space Telescope Advanced Camera for Surveys, targeting young radio galaxies (Gigahertz Peaked Spectrum and Compact Steep Spectrum sources), in search of star formation regions in their hosts. We find near UV light which could be the product of recent star formation in eight of the nine observed sources. Stellar synthesis models are consistent with a burst of star formation before the formation of the radio source. However, observations at other wavelengths and colors are needed to definitively establish the nature of the observed UV light. In the CSS sources B1443+77 and B1814–637 the near UV light is aligned with and is co-spatial with the radio source. We suggest that in these sources the UV light is produced by star formation triggered and/or enhanced by the radio source.

## 7.1 Introduction

The relationship between black hole mass and galaxy mass implies that the growth and evolution of black holes (therefore AGN) and their host galaxies must somehow be related (e.g., Gebhardt et al. 2000). Mergers and strong interactions can trigger AGN activity in a galaxy (e.g., Heckman et al. 1986; Baum et al. 1992; Israel 1998). These events can also produce instabilities in the ISM and trigger star formation (e.g., Ho 2005). Numerical simulations and models (e.g., Mellema et al. 2002; Rees 1989) suggest that the advancement of the jets through the host galaxy environment can also trigger star formation. Imaging studies un ultraviolet (UV) light of large 3CR sources find traces of episodes of star formation around the time when the radio source was triggered (i.e.  $\lesssim 10^7 - 10^8$  yr, Koekemoer et al. 1999; Allen et al. 2002; Chiaberge et al. 2002; O’Dea et al. 2001, 2003; Martel et al. 2002) suggesting a possible link between both.

Gigahertz Peaked Spectrum (GPS) and Compact Steep Spectrum (CSS) radio sources are young, smaller (GPS  $\lesssim 1$  kpc, CSS  $\lesssim 15$  kpc, for a review see O’Dea 1998) versions of the large powerful radio sources, so they are expected to exhibit signs of more recent star formation. In addition, their size makes them excellent probes of the interactions between the expanding lobes and the host. They have not yet completely broken through the host ISM, so these interactions are expected to be even more important than in the larger sources.

The near UV observations are very sensitive to the presence of hot young stars and therefore will trace recent star formation events. We have obtained high resolution HST/ACS near-UV images of these young compact sources to study the morphology and the extent of recent star formation.

This is the first time a coherent sample of GPS and CSS sources has been imaged in the near-UV. It is also the first time that the relative sizes of radio sources in well matched samples are used to study time evolution of merger-induced and jet-induced star formation.

Our sample is chosen to be representative of GPS and CSS sources with  $z \lesssim 0.5$ , nearby enough to eliminate strong effects due to evolution with cosmic time. The objects are drawn primarily from the well-defined samples of Fanti et al. (1990), Fanti et al. (2001), Stanghellini (1992) and Stanghellini et al. (1997). The comparison sample of large 3CR sources consists of FR I and FR II sources with redshifts less than 0.1 observed in the near-UV by Allen et al. (2002).

## 7.2 Observations and data reduction

We have obtained high resolution near-UV images with the High Resolution Channel (HRC) of the Advanced Camera for surveys (ACS) on board the Hubble Space Telescope, using the F330W filter. The objects observed are GPS and CSS galaxies B1117+146, B1233+418, B1345+125, B1443+77, B1607+268, B1814–637, B1934–638, B1946+708, B2352+495 (Table 7.1).

The standard ACS reduction pipeline was used to remove detector signatures such as

bias, dark current, flat field and to perform flux calibration. Each target was observed in a two-point dither pattern. The frames were combined with Multidrizzle (Koekemoer et al. 2002) to correct for geometric distortions and cosmic rays.

The two 2-D fitting code GALFIT (Peng et al. 2002) was used to parameterize the UV emission. For each image we tested different combinations of point source and Sersic profiles, allowing the sky level, position and magnitudes of all components, as well the index and effective radii of the Sersic components, to vary. The final model was chosen according to the lowest  $\chi^2$  and best residuals (with the lowest number of components). The results are summarized in Table 7.2. Figures 7.10 to 7.18 show the UV image, GALFIT model and residuals for the nine objects. These will be discussed in detail in Section 7.4.

A Sersic profile (Sersic 1963, 1968; Graham & Driver 2005, for a review),  $R^{1/n}$  is described by:

$$I(R) = I_e \exp \left[ -b_n \left( \left( \frac{R}{R_e} \right)^{1/n} - 1 \right) \right] \quad (7.1)$$

where  $I_e$  is the intensity at the effective radius,  $R_e$  (distance that encloses half of the total emission), and  $b_n$  is a constant coupled to the value of  $n$ . Special cases of the Sersic profile are those where  $n = 4$  (de Vaucouleurs profile),  $n = 1$  (exponential profile) and  $n = 0.5$  (Gaussian profile).

There are no good models of the Point Spread Function (PSF) for the ACS/HRC. To model the PSF we used the *calibration plan* observations of Cycles 12 and 13 (programs 10054 and 10374). These programs contain observations of the spectrophotometric standard stars GD71, G191B2B, GD153 and HZ 14. To model our PSF, we compared the PSF created by each of these stars in each Cycle, as well as combinations of these. In general, the differences between each PSF are subtle and do not produce major differences in the models of the sources. However, the average PSF of the spectrophotometric stars of Cycle 13 produced better point source results (lower  $\chi^2$  and residuals) so we chose to use it in our models. This PSF has a FWHM of  $\sim 1.9$  pixels, giving a resolution of  $\sim 0.05''$ . 1814+364 needs a better model for the PSF (see Figure 7.15).

GALFIT yields the coordinates of the modeled components in pixels. The conversion to RA and Dec was performed using the astrometry information stored in the header of each HST/ACS -pipeline reduced- image. The radio positions of the sources are from the literature (Table 7.2).

Unless otherwise noticed, all presented fluxes, luminosities and magnitudes are for the F330W filter passband, corrected for galactic extinction and k-correction. The magnitudes are in the STMAG system. Galactic extinction was corrected using the Galactic de-reddening curve in Cardelli et al. (1989) and the measured Galactic extinction values of Schlegel et al. (1998). K-correction (typically  $\sim 0.1, 0.2$  magnitudes) and conversion from Allen et al. (2002) filters were done following the PEGASE (Fioc & Rocca-Volmerange 1997) templates of elliptical galaxies and using the IRAF package SYNPHOT. SYNPHOT was also used for

measuring F330W magnitudes of the PEGASE and GALAXEV (Bruzual & Charlot 2003) stellar population models.

### 7.3 Nuclear and emission line contamination

Using ground-based, optical spectroscopy, Tadhunter et al. (2002) studied the nature of the UV excess in GPS, CSS and FR II sources at redshifts  $0.15 < z < 0.7$ . They found that the UV continuum in these sources has contributions of (1) nebular continuum, (2) direct AGN light, (3) scattered AGN light, and a (4) starburst component. The presence of possible emission line gas must be also considered.

The observed objects in our case are Narrow Line Radio Galaxies (NLRG) so we expect no contamination from direct light from the AGN. The main contribution from emission line gas to our observations would come from Mg II. It is usually only found in the nuclear Broad Line Region (BLR) of AGN hosts so we do not expect contamination from emission line gas either.

To make a rough estimation of the extent of the possible contamination by direct light from the AGN, we use the STIS spectrum of 3C 277.1 (presented in chapter 4), a CSS QSO that could represent our worst case scenario: when we are looking into the nucleus. In 3C 277.1, all signs from nuclear contribution (broad lines and AGN continuum) and Mg II emission disappear at 0.8 kpc from the nucleus, roughly 1.5 times the FWHM of the PSF in the STIS observations. On average, 0.8 kpc correspond to  $\sim 0.2''$  in our ACS observations and we could expect the nuclear traces to disappear closer to the center in our ACS galaxies. The C II] line is usually fainter than Mg II (Peterson 1997) in AGN (it is also not present in 3C 277.1) so it is unlikely that it is affecting our observations.

We found UV polarization observations of B1934–638 and B1345+125 but not for the rest of the sources so the presence of scattered nuclear light cannot be completely ruled out. Tadhunter et al. (2002) find AGN scattered light in  $\sim 37\%$  of their sample (including the GPS B1934–638), but in most cases it does not seem to dominate the UV emission.

B1345+125 could have highly polarized UV light, as reported by Hurt et al. (1999), but their uncertainties are too high. However, Tadhunter et al. (2005) found evidence of recent star formation and strong jet cloud interactions in B1345+125 (see also Holt et al. 2003; Surace et al. 1998).

The contribution from nebular continuum varies between 3 and 40% (Tadhunter et al. 2002). However, 3 out of the 4 CSS they studied are dominated by young stellar populations. Furthermore, for up to 50% of their sources (including GPS, CSS and FR II), the UV excess is dominated by young stellar populations. Similar results have been found for FR I and FR II sources at different redshifts (Aretxaga et al. 2001; Wills et al. 2002, 2004).

To sum up, the most probable causes of contamination in our images are scattered nuclear light and nebular continuum. However, it is most likely that their contributions are small.

Source	Catalogue	ID	Sample	Redshift	$\lambda_{3100}$	$\lambda_{3300}$	$\lambda_{3700}$	Emission lines
B1117+146	4C 14.41	G	GPS	0.326	2338	2489	2790	C II] 2326, Mg II 2800
B1233+418		G	CSS	0.25	2480	2640	2960	Mg II 2800
B1345+125	4C 12.50	G	GPS	0.12174	2764	2942	3298	Mg II 2800
B1443+77	3C 303.1	G	CSS	0.267	2447	2605	2920	C II] 2326, Mg II 2800
B1607+268	CTD 093	G	GPS	0.473	2108	2240	2512	C II] 2326
B1814-637		G	CSS	0.063	2916	3104	3481	[Ne V] 3426
B1934-638		G	GPS	0.183	2620	2790	3128	Mg II 2800
B1946+708		G	GPS	0.10083	2816	2998	3361	Mg II 2800
B2352+495	DA 611	G	GPS	0.23790	2504	2666	2989	Mg II 2800

**Table 7.1.— Redshift and wavelengths.** B1950 IAU and catalogue names, identification, GPS/CSS classification, redshift, rest-frame wavelengths covered by our observations and possible emission lines affecting our measurements. The throughput for HRC/F330W effectively covers  $\sim 3100\text{\AA}$  to  $\sim 3700\text{\AA}$ . Columns 5 to 7 give the corresponding wavelengths of these limits and the maximum throughput of the filter in the rest frame of each source.

## 7.4 UV morphology

We have modeled the UV emitting regions with GALFIT and found that all sources show at least two components, except B1117+146 (point source). The hosts of B1233+418, B1345+125, B1443+77, B1607+268, B1814-637 and B1934-638 show a combination of at least one Sersic<sup>1</sup> component (with different indices) and one or several point sources (see Table 7.2 and Figures 7.10 to 7.18). B1946+708 and B2352+495 show a combination of two and three point sources. In the near-IR, de Vries et al. (2000a) find Sersic indices  $2 \lesssim n \lesssim 5$  and effective radii  $2 \text{ kpc} \lesssim R_e \lesssim 4 \text{ kpc}$  for GPS and CSS sources. Most of our data show point sources and/or Sersic profiles with indices  $n \lesssim 2$  and radii  $R_e \lesssim 400 \text{ parsec}$ . The presence of these small clumps of near UV emission is consistent with star forming regions in the host. Before addressing the nature of the UV emission, we describe the properties of this emission in relation to other properties, for the individual sample sources.

### 7.4.1 Notes on individual sources

For our observations, the  $3\sigma$  detection limit, for a point source (FWHM  $\sim 3$  pixels) is 25.8 (no galactic extinction applied). For comparison purposes with this limit and published data, the magnitudes listed in this section and Table 7.2 have not been corrected for galactic extinction.

*B1117+146:* Identified as a GPS by O’Dea et al. (1991). The counterpart of the radio source corresponds to a  $m_R=20.1$  galaxy (de Vries et al. 1995) at  $z = 0.362$  (de Vries et al. 1998b). Radio observations (e.g., Fey & Charlot 1997) show a  $\sim 100 \text{ mas}$  double radio source. Our image shows an unresolved 24.06 magnitude source.

*B1233+418:* A CSS galaxy with a photometric R-band redshift  $z_R = 0.25$  (Fanti et al. 2004). We detect a point source with magnitude 25.43. Our image (see Figure 7.11, first panel) suggests faint extended emission towards Northeast but the errors in the GALFIT

<sup>1</sup>The Sersic profiles are used to parameterize the data, It does not necessarily imply that these UV components are galaxies.

Source	Component	RA (J2000)	Dec (J2000)	STMAG	$R_e$ (mas)	$R_e$ (pc)	Index	Ratio
B1117+146	Fey et al. (2004)	11:20:27.807 $\pm$ 0.001	+14:20:54.99 $\pm$ 0.02					
	Point source	11 20 27.7653 $\pm$ 0.0001	14 20 54.33 $\pm$ 0.06	24.06 $\pm$ 0.06				
B1233+418	Becker et al. (1995)	12:35:35.71 $\pm$ 0.03	+41:37:07.40 $\pm$ 0.32					
	Point source	12 35 35.6664 $\pm$ 0.0004	+41:37:08.18 $\pm$ 0.17	25.43 $\pm$ 0.16				
B1345+125	Sersic profile	12 35 35.677 $\pm$ 0.001	+41 37 08.23 $\pm$ 0.47	24.21 $\pm$ 0.36	100 $\pm$ 800	390 $\pm$ 3100	0.04 $\pm$ 0.6	0.06 $\pm$ 0.09
	Ma et al. (1998)	13:47:33.3616	+12:17:24.240					
	Point source	13 47 33.3981 $\pm$ 0.0001	+12 17 23.36 $\pm$ 0.04	23.77 $\pm$ 0.05				
	Sersic profile	13 47 33.3947 $\pm$ 0.0002	+12 17 23.46 $\pm$ 0.01	21.14 $\pm$ 0.02	35 $\pm$ 0.5	76 $\pm$ 1	0.33 $\pm$ 0.03	0.36 $\pm$ 0.02
B1443+77	Sersic profile	13 47 33.3950 $\pm$ 0.0001	+12 17 23.41 $\pm$ 0.06	21.20 $\pm$ 0.04	108 $\pm$ 7	234 $\pm$ 15	1.62 $\pm$ 0.13	0.76 $\pm$ 0.03
	Sersic profile	13 47 33.5272 $\pm$ 0.0003	+12 17 23.24 $\pm$ 0.21	21.84 $\pm$ 0.12	299 $\pm$ 58	647 $\pm$ 126	2.29 $\pm$ 0.38	0.54 $\pm$ 0.05
B1607+268	Rengelink et al. (1997)	14:43:14.9 $\pm$ 1.1	+77:07:28.6 $\pm$ 3.8					
	Point source	14 43 14.666 $\pm$ 0.001	+77 07 27.546 $\pm$ 0.17	25.21 $\pm$ 0.10				
	Point source	14 43 14.5832 $\pm$ 0.0004	+77 07 27.702 $\pm$ 0.06	24.06 $\pm$ 0.06				
	Sersic profile	14 43 14.656 $\pm$ 0.002	+77 07 27.430 $\pm$ 0.10	20.36 $\pm$ 0.16	1.1" $\pm$ 0.2"	4500 $\pm$ 800	2.66 $\pm$ 0.33	0.45 $\pm$ 0.02
B1814-637	Beasley et al. (2002)	16:09:13.3208	+26:41:29.036					
	Point source	16 09 13.2497 $\pm$ 0.0002	+26 41 29.514 $\pm$ 0.14	24.64 $\pm$ 0.18				
B1934-638	Sersic profile	16 09 13.2472 $\pm$ 0.0002	+26 41 29.515 $\pm$ 0.14	23.13 $\pm$ 0.14	47 $\pm$ 11	277 $\pm$ 65	3.92 $\pm$ 2.35	0.50 $\pm$ 0.10
	Ma et al. (1998)	18:19:35.003 $\pm$ 0.003	-63:45:48.194 $\pm$ 0.01					
B1946+708	Point source	18 19 35.3179 $\pm$ 0.0001	-63 45 47.117 $\pm$ 0.01	16.95 $\pm$ 0.10				
	Sersic profile	18 19 35.3175 $\pm$ 0.0001	-63 45 47.115 $\pm$ 0.01	17.11 $\pm$ 0.12	25 $\pm$ 4	30 $\pm$ 5	2.08 $\pm$ 0.31	0.07 $\pm$ 0.02
	Ma et al. (1998)	19:39:25.027 $\pm$ 0.001	-63:42:45.626					
	Point source	19 39 25.0947 $\pm$ 0.0009	-63 42 44.978 $\pm$ 0.13	23.81 $\pm$ 0.73				
B2352+495	Sersic profile	19 39 25.0935 $\pm$ 0.0001	-63 42 44.974 $\pm$ 0.02	21.75 $\pm$ 0.12	39 $\pm$ 5	119 $\pm$ 15	1.02 $\pm$ 0.33	0.13 $\pm$ 0.04
	Sersic profile	19 39 25.1032 $\pm$ 0.0007	-63 42 45.037 $\pm$ 0.06	21.08 $\pm$ 0.07	354 $\pm$ 45	1078 $\pm$ 137	2.51 $\pm$ 0.26	0.47 $\pm$ 0.02
B1946+708	Beasley et al. (2002)	19:45:53.5200 $\pm$ 0.002	+70:55:48.732					
	Point source	19 45 53.299 $\pm$ 0.002	+70 55 48.395 $\pm$ 0.38	25.81 $\pm$ 0.25				
	Point source	19 45 53.3016 $\pm$ 0.0006	+70 55 48.476 $\pm$ 0.12	24.59 $\pm$ 0.09				
	Ma et al. (1998)	23:55:09.458 $\pm$ 0.001	+49:50:08.340 $\pm$ 0.01					
B2352+495	Point source	23 55 09.4704 $\pm$ 0.0004	+49 50 07.326 $\pm$ 0.16	25.13 $\pm$ 0.16				
	Point source	23 55 09.4634 $\pm$ 0.0006	+49 50 07.507 $\pm$ 0.25	25.53 $\pm$ 0.19				
	Point source	23 55 09.4828 $\pm$ 0.0003	+49 50 07.531 $\pm$ 0.12	24.79 $\pm$ 0.10				

**Table 7.2.** *Galfit* components. The first line for each source corresponds to the most recent radio position, the rest of the lines correspond to the UV components of the GALFIT models. Errors not listed are smaller than 0.1 milliarcsec. The coordinates in the GALFIT models are from the HST coordinate system and correspond to the brightest pixel. The magnitudes are observed, not corrected from galactic extinction.  $R_e$  is the effective radius in milliarcsec except for 1443+77. Last two columns give the sersic indices and axial ratios.

model for this component are too large to be sure of its existence.

*B1345+125*: 4C +12.50. A long known peaked spectrum radio source (e.g., Véron 1971). The counterpart of this GPS source is a  $m_R=15.5$  galaxy (e.g., Stanghellini et al. 1993) at  $z = 0.12174$  (Holt et al. 2003), in a cluster of fainter galaxies (Stanghellini et al. 1993). IR images of this ULIRG show an extremely reddened source with two nuclei separated  $\sim 1.8''$  ( $\sim 4$  kpc) embedded in a common envelope and aligned roughly East-West (e.g., Scoville et al. 2000; Surace & Sanders 2000) suggesting an ongoing merger, which may have triggered the AGN (e.g., Heckman et al. 1986; Xiang et al. 2002). The western nucleus is the brightest and shows a Seyfert 2 spectrum (Gilmore & Shaw 1986). Veilleux et al. (1997) suggest that the source may have a hidden quasar. VLBI imaging shows a complex, distorted  $\sim 100$  mas ( $\sim 0.2$  kpc) source (e.g., Lister et al. 2003), roughly oriented North-South ( $PA \sim -20^\circ$ ). Older observations of B1345+125 related the radio source to the East nucleus but improved astrometry showed that it is related to the West (e.g. Stanghellini et al. 1997; Axon et al. 2000; Fanti 2000). Evans et al. (1999) study the molecular gas in B1345+125 and suggest that the molecular gas is fueling the AGN. Our UV image detects both nuclei separated by  $\sim 1.8''$ . The East component was modeled with a Sersic profile with index  $\sim 2.3$  and an effective radius  $\sim 0.3''$  and magnitude 21.84. The West nucleus shows a more complex structure: two Sersic profiles with magnitudes 21.14 and 21.20 and indices 1.6 and 0.33. This more complex structure could be due to interaction with the radio source.

Optical/NIR images (Axon et al. 2000) show an arc of emission  $\sim 1''$  North of the Western nucleus and fainter emission at  $2''$ , none of them present in our UV images. They also detect a faint tail of emission stretching from the West nucleus towards the west, present in our image and not modeled by GALFIT (see Figure 7.12). Surace et al. (1998) detect *compact blue knots* in B1345+125 around the source which they attribute to star forming regions. We detect the southern knots  $\sim 2''$  far from the nuclei but not the northern one.

*B1443+77*: 3C 303.1. The optical counterpart of this CSS corresponds to a galaxy of  $m_v \sim 20$  (e.g., Sanghera et al. 1995), at  $z = 0.267$  (Kristian et al. 1978). The VLBI map (Sanghera et al. 1995) shows a  $\sim 1.8''$  long ( $\sim 7$  kpc) double radio source aligned NW-SE (PA  $\sim 47^\circ$ ) aligned with the inner emission line gas (e.g. de Vries et al. 1999). The center of B1443+77 shows a complex structure in the optical, which could be due to an ongoing merger (e.g., de Vries et al. 1997b; Axon et al. 2000) and it also shows up in our UV image. Axon et al. (2000) and de Vries et al. (1999) find an arc of emission south of the nucleus of the source and McCarthy et al. (1995) detects circumnuclear [O III] as far as  $3''$  from the center. Our image suggests the presence of an arc of emission  $\sim 0.9''$  ( $\sim 4$  kpc) from the nucleus. The integrated magnitude of this arc is  $\sim 23$ . A region of the sky with the same area has a magnitude  $\sim 25$ . The GALFIT model of the source consists of two point sources of magnitudes 25.21 and 24.06, and a Sersic profile with index 2.66 and effective radius  $1.1''$  ( $\sim 4.5$  kpc). The arc is not modeled by GALFIT so it is visible in the residuals of Figure 7.13. B1443+77 is the best candidate in our sample to be undergoing jet induced star formation (see below).

*B1607+268*: Also known as CTD93. VLBI maps (e.g. Dallacasa et al. 1998) show a two-component,  $\sim 60$  mas, GPS source. The counterpart is a galaxy at  $z = 0.473$  (O'Dea et al. 1991) with  $m_r = 20.4$  (Stanghellini et al. 1993). We observe a 24.64 magnitude point source on top of a 23.13 magnitude de Vaucouleurs component.

*B1814-637*: VLBI imaging shows a two component CSS galaxy (e.g., Tzioumis et al. 2002). Although the radio source is small ( $\sim 0.4''$ ,  $\sim 0.3$  kpc) its radio spectrum does not peak at  $\sim 1$  GHz. The optical identification corresponds to a  $m_v=18.0$  galaxy at  $z = 0.063$  (Wall & Peacock 1985). We observe a bright, 16.95 magnitude point source on top of a 17.11 magnitude Sersic profile with index  $n \simeq 2$ . The UV object is  $\sim 2$  arcsec to the Northeast of the radio source. At this redshift,  $2'' \simeq 2.4$  kpc so it is probably the counterpart.

*B1934-638*: A long known GPS (e.g., Kellermann 1966). VLBI maps (e.g., Tzioumis et al. 1998) show two components separated by  $\sim 40''$  (0.12 kpc at  $z = 0.183$ , Tadhunter et al. 1993). *R*-band and ISO observations (Jauncey et al. 1986; Fanti et al. 2000) show a system of two galaxies, separated by  $\sim 3''$ , consistent with our observations. The GALFIT model yields two Sersic profiles of magnitudes 21.08 and 21.75 and a fainter point source with magnitude 23.81.

*B1946+708*: The counterpart is identified with a  $z = 0.10083$ ,  $m_R=16.3$  galaxy (e.g., Snellen et al. 2003a). VLBI observations of this GPS source show an elongated,  $\sim 40$  mas ( $\sim 0.07$  kpc) NE-SW structure (Taylor & Vermeulen 1997). Optical observations (Perlman et al. 2001) also suggest a NE-SW elongated source, consistent with the orientation of the two com-

ponents in our GALFIT model: two point sources (aligned NE-SW) with magnitudes 24.59 and 25.81. Perlman et al. (2001) suggest that B1946+708 may be part of a group of galaxies, the closest being at  $\sim 1'$ . These objects fall outside our field and they have unknown redshifts.

*B2352+495*: Snellen et al. (2003a) identify the counterpart of this GPS source (e.g., O'Dea 1998) with a  $z = 0.23790$ ,  $m_R = 18.2$  galaxy. VLBI observations show a complex elongated  $\sim 0.7''$  ( $\sim 0.25$  kpc) source oriented NW-SE (Pollack et al. 2003). Our ACS observations show three point sources in a circle about  $0.5''$  wide, with magnitudes 24.79, 25.13 and 25.53.

## 7.5 UV and radio properties

To better study the UV nature of our sources, we incorporate their radio properties and in addition enlarge the sample with Allen et al. (2002) 3CR FR I and FR II sources. Allen et al. (2002) data consist of STIS near-UV-MAMA snapshots (exposure time of 1440 seconds) with filters F25SRF2 and F25CN182. The radio data have been collected from the papers listed in the individual notes above, O'Dea (1998), Morganti et al. (1993) and the 3CRR on-line catalog (an update of the sample of Laing et al. 1983). The data are summarized in Table 7.3 and plotted in Figures 7.1, 7.2 and 7.3.

O'Dea & Baum (1997) found that the radio power of the GPS and CSS is independent of size and comparable to the most powerful FR II. Comparison with Zirbel & Baum (1995) and Baum et al. (1995) suggest that the Allen et al. (2002) sample may include fainter than usual FR sources or lacking  $\sim 10^{26}$  W/Hz sources. The UV luminosity of the host seems to be similar for FR sources and GPS/CSS, and independent of redshift and power, size of the radio source.

The fact that UV luminosity is not correlated with radio size (Figure 7.2) or radio power suggests that in many objects the radio source may not dominate the NUV properties of the host. However, if the expansion of the radio lobes were enhancing the UV luminosity, it could have been unnoticed by our sample. The GPS are probably too small and young to have experienced strong interactions with the host thereby enhancing the UV emission. As the radio source grows, becoming a CSS, the UV emission would increase. When the radio lobes leave the host, the shocks created by the expansion would still propagate through the ISM for some time and still trigger some star formation. As the shocks fade, star formation in the host would go back to the normal rates. This suggested qualitative behavior is illustrated by the solid line in Figure 7.2. The lack of sufficient CSS (radio sizes comparable to the host) may cause us to be missing hosts with UV emission  $\sim 10^9 L_\odot$ . We also note that the two brightest sources in our sample (B1443+77 and B1814-637) are CSS. Labiano et al. (2005) demonstrated the presence of gas ionized by the shocks from the expanding radio source in CSS sources. Furthermore, they found that B1443+77 shows the strongest contribution from shocks. We could also expect these shocks to be affecting the star formation in the host.

Table 7.3 shows the position angles of the radio and UV sources. We see that the CSS B1443+77 and B1814-637 and the GPS B1946+708 are aligned with the UV. The UV

Name	Type	Size <sub>5GHz</sub>	UV Size	Log P <sub>5GHz</sub>	Log(L/Lsun)	L <sub>UV</sub> 10 <sup>40</sup> (erg/s)	PA 5GHz	PA UV	Δ PA
B1233+418	CSS	11.6	1.2	25.56	7.12±0.11	5.1±1.3	27	66	39
B1443+77	CSS	6.9	8.1	25.86	8.66±0.06	180±25	140	116, 136, 20 <sup>a</sup>	4
B1814-637	CSS	0.50	–	25.56	8.87±0.03	290±20	156	170	14
B1117+146	GPS	0.40	0.2	26.41	7.45±0.02	11.0±0.5	120	–	–
B1345+125	GPS	0.17	0.45	25.98	7.88±0.01	29.6±0.7	120, 26	165	45
B1607+268	GPS	0.30	0.2	26.86	8.24±0.04	68±7	29	88	59
B1934-638	GPS	0.13	0.5	26.65	8.24±0.03	68±5	88	140	52
B1946+708	GPS	0.07	0.2	25.14	6.35±0.04	0.87±0.08	28	3	25
B2352+495	GPS	0.86	0.9 <sup>c</sup>	26.23	7.39±0.03	9.6±0.7	153	157, 27, 85 <sup>b</sup>	4
3C 293	FR 1	225	24.91	8.38±0.06					
3C 296	FR 1	206	24.31	7.78±0.08					
3C 310	FR 1	316	24.89	7.23 ±0.14					
3C 449	FR 1	514	23.93	7.98±0.51					
3C 465	FR 1	349	24.71	7.94±0.22					
3C 35	FR 2	960	24.75	7.42±0.45					
3C 192	FR 2	228	25.29	8.16±0.17					
3C 236	FR 2	4470	25.43	8.41±0.35					
3C 285	FR 2	267	25.00	8.40±0.06					
3C 321	FR 2	540	25.33	9.13±0.14					
3C 326	FR 2	1990	24.83	7.33±0.18					
3C 382	FR 2	204	25.19	10.35±0.22					
3C 388	FR 2	84	25.48	7.52±0.27					

**Table 7.3.– UV and 5GHz radio properties.** UV luminosity for our GPS and CSS radio galaxies compared with large extended FR sources from Allen et al. (2002). Longest linear sizes are listed in kpc. Radio and UV position angles in degrees (from North to East) of each component. Difference in radio and UV PA of the most aligned components. The radio data are from O’Dea (1998), Morganti et al. (1993) and the on-line 3CRR catalogue (Laing et al. 1983), measured at 5GHz.

<sup>a</sup> The PA of the largest angular UV scale of 1345+125 is 130°.

<sup>b</sup> The UV morphology of 2352+495 is a roughly equilateral triangle so no general PA for the complete source can be given (see Figure 7.18).

emission in B2352+495 has two components aligned with the radio source, but the unknown offset between radio and HST reference frames prevents from accurately overlaying them.

Figures 7.4, 7.5, 7.6 and 7.7 compare the alignment (difference in UV and radio position angles) of the observed GPS and CSS sources with radio size, radio power, UV luminosity and redshift. In these figures, the data point for sources with several UV angles correspond to the most aligned component.

Inspection of figure 7.4 shows that alignment is found for sources  $\gtrsim 1$  kpc, suggesting that GPS sources may be too small to show alignment. There is no clear correlation between alignment and radio power (Figure 7.5). Sources with high UV luminosity (B1443+77 and B1814-637) seem to show alignment between the UV and radio source (Figure 7.6), consistent with star formation enhanced by propagation of the radio lobes. However, more sources with sizes  $\gtrsim 1$  kpc are needed to improve the statistics.

Figure 7.8 shows that UV size and radio size are independent for most sources. However, most of the sources are GPS, and the radio sources are probably too small and young to affect the UV emission in the host. The three sources with similar UV and radio sizes are B1443+77, B1814-637 and B2352+495<sup>2</sup>. The radio source in B1233+418 is larger than the

<sup>2</sup>For the alignment discussions we use the UV components with position angle 157° in B2352+495.

Name	GALAXEV LB		GALAXEV DB		PEGASE		Average
	10 Gyr	1 Gyr	10 Gyr	1 Gyr	10 Gyr	1 Gyr	
B1117+146	$2.2 \times 10^{11}$	$2.1 \times 10^{08}$	$2.3 \times 10^{11}$	$5.5 \times 10^{09}$	$2.6 \times 10^{10}$	$8.2 \times 10^{08}$	$8.0 \times 10^{10}$
B1233+418	$5.2 \times 10^{10}$	$1.0 \times 10^{08}$	$5.6 \times 10^{10}$	$1.8 \times 10^{09}$	$1.1 \times 10^{10}$	$3.9 \times 10^{08}$	$2.0 \times 10^{10}$
B1345+125	$1.2 \times 10^{11}$	$6.7 \times 10^{08}$	$1.2 \times 10^{11}$	$6.0 \times 10^{09}$	$4.7 \times 10^{10}$	$2.2 \times 10^{09}$	$4.9 \times 10^{10}$
B1443+77	$2.0 \times 10^{12}$	$3.3 \times 10^{09}$	$2.2 \times 10^{12}$	$6.2 \times 10^{10}$	$3.7 \times 10^{11}$	$1.3 \times 10^{10}$	$7.7 \times 10^{11}$
B1607+268	$1.9 \times 10^{12}$	$1.1 \times 10^{09}$	$1.9 \times 10^{12}$	$3.2 \times 10^{10}$	$1.5 \times 10^{11}$	$4.3 \times 10^{09}$	$6.6 \times 10^{11}$
B1814-63	$1.1 \times 10^{13}$	$4.6 \times 10^{09}$	$1.1 \times 10^{13}$	$2.0 \times 10^{11}$	$7.1 \times 10^{11}$	$2.0 \times 10^{10}$	$3.8 \times 10^{12}$
B1934-638	$3.0 \times 10^{11}$	$1.1 \times 10^{09}$	$3.3 \times 10^{11}$	$1.3 \times 10^{10}$	$9.5 \times 10^{10}$	$3.9 \times 10^{09}$	$1.2 \times 10^{11}$
B1946+708	$1.4 \times 10^{09}$	$9.6 \times 10^{06}$	$1.5 \times 10^{09}$	$7.8 \times 10^{07}$	$6.2 \times 10^{08}$	$3.1 \times 10^{07}$	$6.1 \times 10^{08}$
B2352+495	$4.1 \times 10^{10}$	$9.0 \times 10^{07}$	$4.4 \times 10^{10}$	$1.5 \times 10^{09}$	$9.3 \times 10^{09}$	$3.4 \times 10^{08}$	$1.6 \times 10^{10}$
Average	$1.7 \times 10^{12}$	$1.2 \times 10^{09}$	$1.8 \times 10^{12}$	$3.6 \times 10^{10}$	$1.6 \times 10^{11}$	$4.9 \times 10^{09}$	$6.1 \times 10^{11}$
	10 Myr	1 Myr	10 Myr	1 Myr	10 Myr	1 Myr	Average
B1117+1406	$1.7 \times 10^{09}$	$1.8 \times 10^{08}$	$1.4 \times 10^{06}$	$4.4 \times 10^{06}$	$5.9 \times 10^{07}$	$2.5 \times 10^{08}$	$3.7 \times 10^{08}$
B1233+418	$1.0 \times 10^{09}$	$1.0 \times 10^{08}$	$8.3 \times 10^{05}$	$2.5 \times 10^{06}$	$3.7 \times 10^{07}$	$1.8 \times 10^{08}$	$2.3 \times 10^{08}$
B1345+125	$8.9 \times 10^{09}$	$8.2 \times 10^{08}$	$7.1 \times 10^{06}$	$2.0 \times 10^{07}$	$3.0 \times 10^{08}$	$1.4 \times 10^{09}$	$1.9 \times 10^{09}$
B1443+77	$3.2 \times 10^{10}$	$3.1 \times 10^{09}$	$2.5 \times 10^{07}$	$7.8 \times 10^{07}$	$1.1 \times 10^{09}$	$5.4 \times 10^{09}$	$7.0 \times 10^{09}$
B1607+268	$8.1 \times 10^{09}$	$8.3 \times 10^{08}$	$6.4 \times 10^{06}$	$2.2 \times 10^{07}$	$2.8 \times 10^{08}$	$1.2 \times 10^{09}$	$1.7 \times 10^{09}$
B1814-63	$3.2 \times 10^{10}$	$3.5 \times 10^{09}$	$2.6 \times 10^{07}$	$9.5 \times 10^{07}$	$1.3 \times 10^{09}$	$6.1 \times 10^{09}$	$7.2 \times 10^{09}$
B1934-638	$1.3 \times 10^{10}$	$1.2 \times 10^{09}$	$1.0 \times 10^{07}$	$3.0 \times 10^{07}$	$4.4 \times 10^{08}$	$2.1 \times 10^{09}$	$2.8 \times 10^{09}$
B1946+708	$1.3 \times 10^{08}$	$1.2 \times 10^{07}$	$1.1 \times 10^{05}$	$3.0 \times 10^{05}$	$4.4 \times 10^{06}$	$2.1 \times 10^{07}$	$2.9 \times 10^{07}$
B2352+495	$9.4 \times 10^{08}$	$9.1 \times 10^{07}$	$7.5 \times 10^{05}$	$2.3 \times 10^{06}$	$3.3 \times 10^{07}$	$1.6 \times 10^{08}$	$2.0 \times 10^{08}$
Average	$1.1 \times 10^{10}$	$1.1 \times 10^{09}$	$8.7 \times 10^{06}$	$2.8 \times 10^{07}$	$3.9 \times 10^{08}$	$1.9 \times 10^{09}$	$2.4 \times 10^{09}$

**Table 7.4.** Mass from luminosity. Mass in  $M_{\odot}$  needed to reproduce the observed F330W luminosity, according to the mass to luminosity ratio from each model. LB is the 1 Myr long burst, DB is the delta single burst model, PEGASE is the elliptical template model. The table is divided two halves corresponding to models of Gyr and Myr. Last column and last line of each block give the average mass for each source and model.

UV emission. However, the UV magnitudes for B1233+418 are close to the detection limit so we may be missing extended and fainter UV emission from the host.

If the jet is enhancing the star formation, we expect the radio source and UV emitting to be aligned and have similar sizes. Figure 7.9 reveals that three sources (B1443+77, B1814-637 and B2352+495) show alignment and similar UV and radio sizes. Therefore they are candidates for jet enhanced star forming sources. B1946+708 shows some alignment between the UV and radio components ( $\sim 25^{\circ}$ ) but the radio source seems too small to have affected the UV in the host.

## 7.6 Stellar synthesis models

GPS and CSS sources are usually associated with massive ellipticals of ages  $\sim 5$ Gyr and solar metallicities (e.g., de Vries et al. 2000a, 1998a). With this assumptions, we use stellar population synthesis models by Bruzual & Charlot (2003) using the Chabrier (Chabrier 2003) initial mass function and Padova evolutionary tracks, for a 1 Myr long burst of star formation and a delta single burst model for populations of  $10^4$ ,  $10^3$ , 10 and 1 Myr to compare our UV luminosity measurements and to estimate the mass and age of stars producing the UV emission in our sources (Table 7.4). We also compare the measurements

with the elliptical galaxy templates from PEGASE.

Inspection of Table 7.4 shows that our observations are generally consistent with models of a single instantaneous burst of  $10^6 - 10^7 M_{\odot}$ ,  $\lesssim 10$  Myr ago. However, some sources may be dominated by intermediate-age (0.1 to 1 Gyr) populations (with masses  $\sim 10^9 M_{\odot}$ , e.g., Tadhunter et al. 2005). These young and intermediate ages in our GPS/CSS sources are also consistent with stellar population ages measured in hosts of powerful radio galaxies (Raimann et al. 2005) and other CSS sources (e.g., Johnston et al. 2005).

Our observations are consistent with a scenario where originally the radio source, that is to say, the accretion event, and the starburst have been produced by the same event. The ages of GPS and CSS sources are usually between  $10^3$  and  $10^6$  (e.g., Polatidis & Conway 2003; O’Dea 1998). The apparent delay between starburst and formation of the radio source has been found in objects with possible connections between the starburst and the formation of the AGN and radio source (Raimann et al. 2005; Tadhunter et al. 2005). and is predicted by theoretical calculations of the time needed for the gas to reach the center of the galaxy after a tidal interaction (e.g., Lin et al. 1988).

## 7.7 Summary

We have obtained HST/ACS near-UV high resolution images of young radio sources: GPS and CSS galaxies. We detect near UV emission (point sources and/or clumps) in eight of the sources, consistent with the presence of recent star formation. In two CSS sources, B1443+77 and B1814–637 the near UV emission is aligned with and co-spatial with the the radio emission and we suggest that star formation has been triggered/enhanced by expansion of the radio source through the host.

The connection between the AGN and the star formation is not yet clear but our observations suggest that some connection exists. Stellar synthesis models are consistent with a burst of star formation before the formation of the radio source. The starburst and AGN activity could have been triggered by the same event.

Observations at other wavelengths and measurement of the colors are needed to further asses the nature of the observed UV properties.

### UV luminosity Vs. 5GHz Radio Power

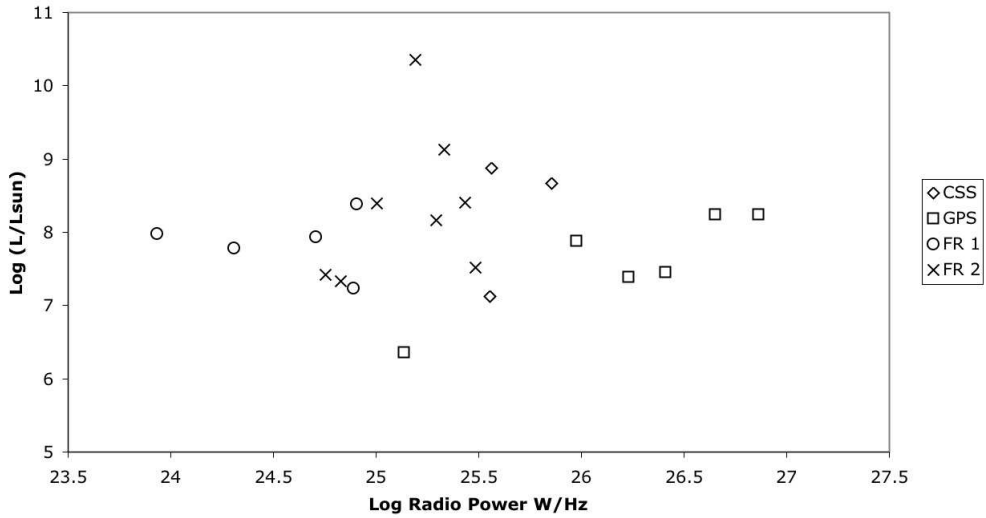


**Figure 7.1**–. UV luminosity and radio power of the combined sample of GPS/CSS and FR I, FR II from Allen et al. (2002).

### UV luminosity Vs. 5GHz Radio Size

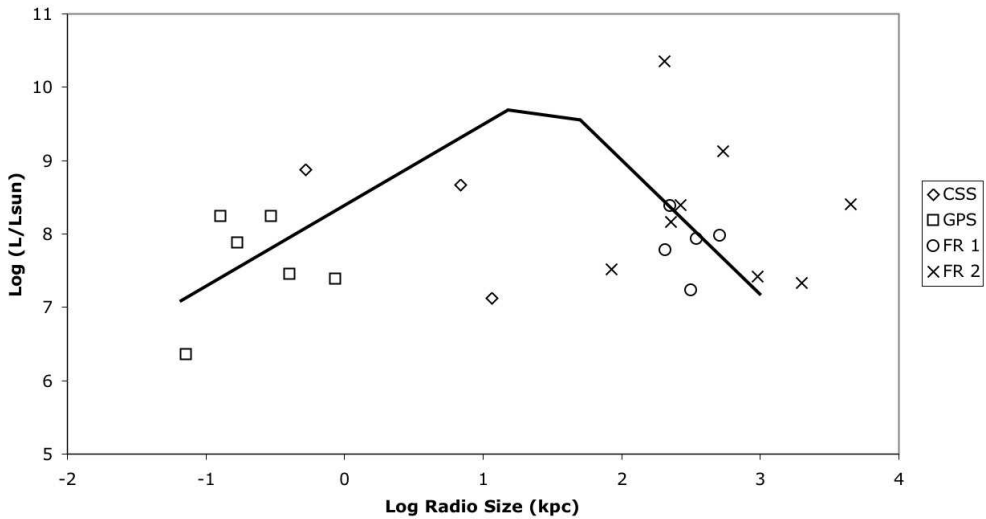


**Figure 7.2**–. As Figure 7.1, for radio size. The line represents a rough expected trend if star formation is induced by the radio lobe expansion.

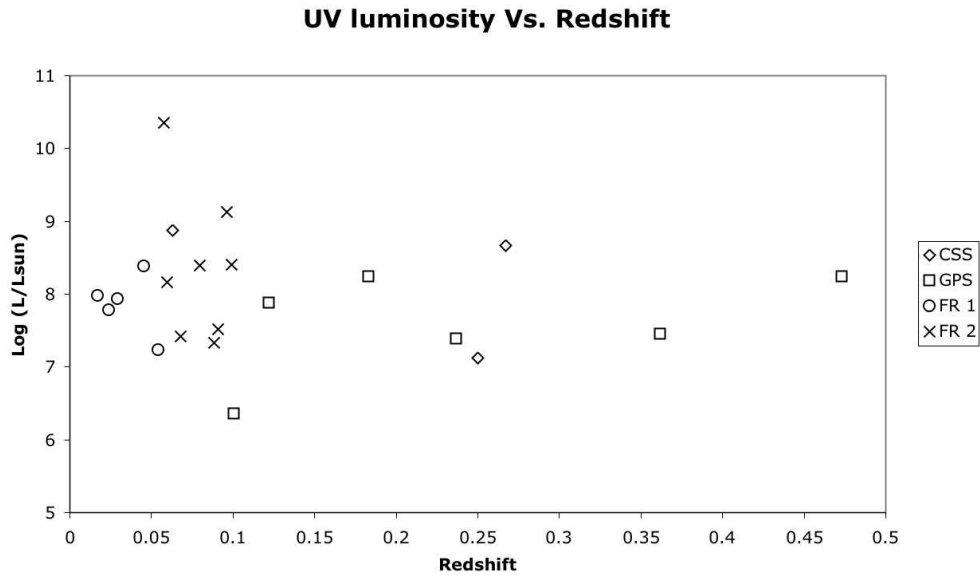


**Figure 7.3–.** As Figure 7.1, for redshift.

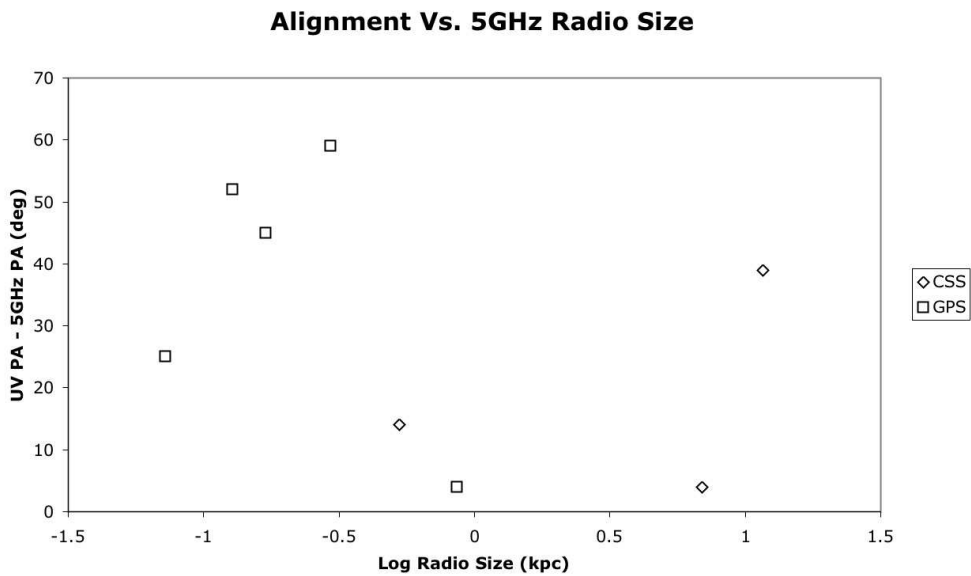


**Figure 7.4–.** Difference between the UV and radio position angles (alignment) of the GPS and CSS galaxies versus radio size.

### Alignment Vs. 5GHz Radio Power

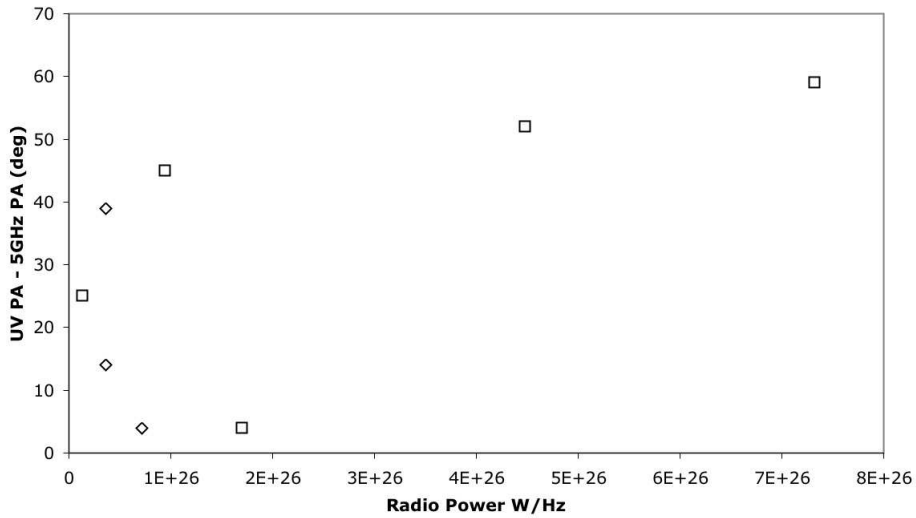


Figure 7.5—. As Figure 7.4, for radio power.

### Alignment Vs. UV luminosity

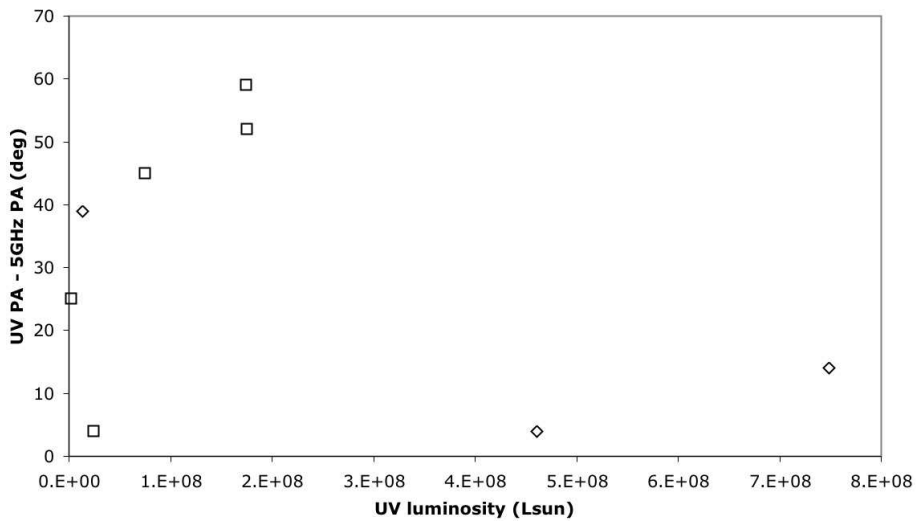
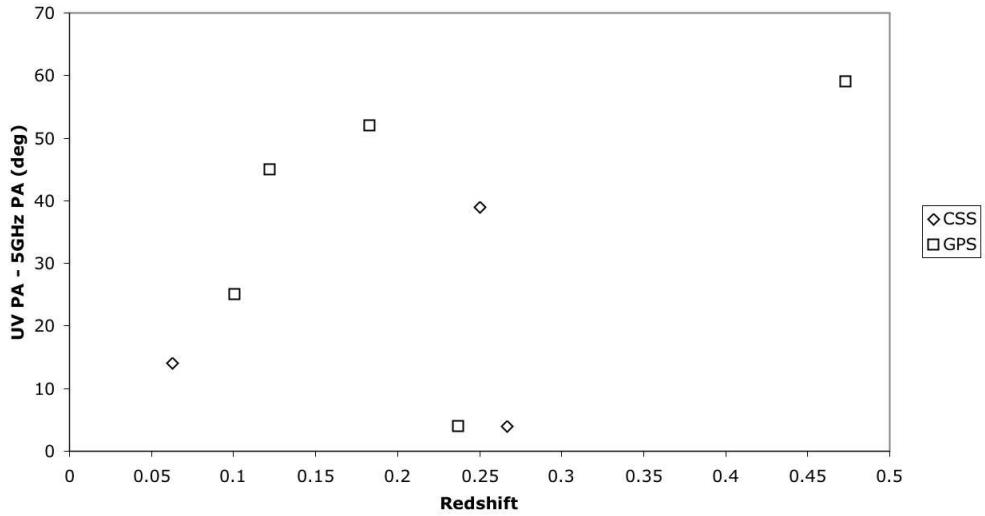


Figure 7.6—. As Figure 7.4, for UV luminosity.

### Alignment Vs. Redshift



**Figure 7.7.**— As Figure 7.4, for redshift.

### UV size Vs. 5 GHz size

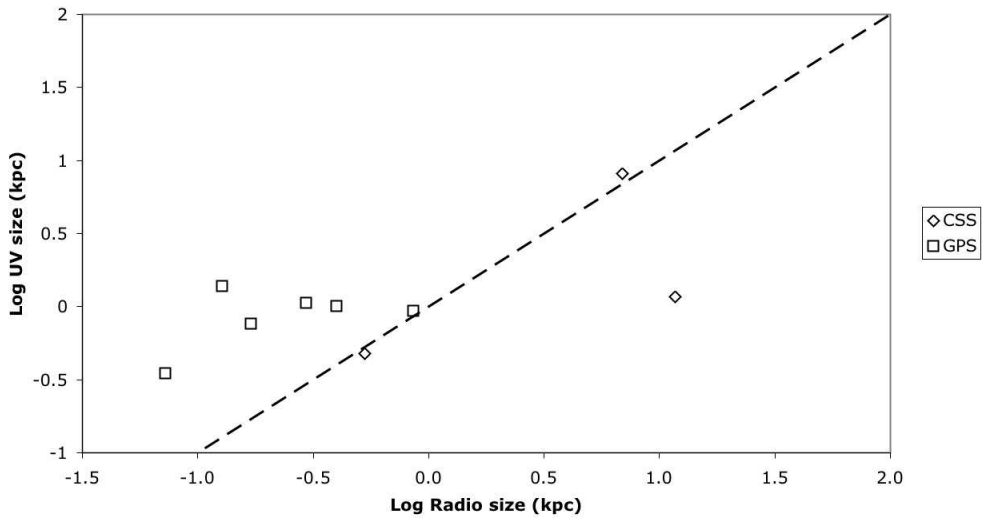


**Figure 7.8.**— UV size and radio size of GPS and CSS sources. The dashed line marks the locus of sources with equal radio and UV sizes.

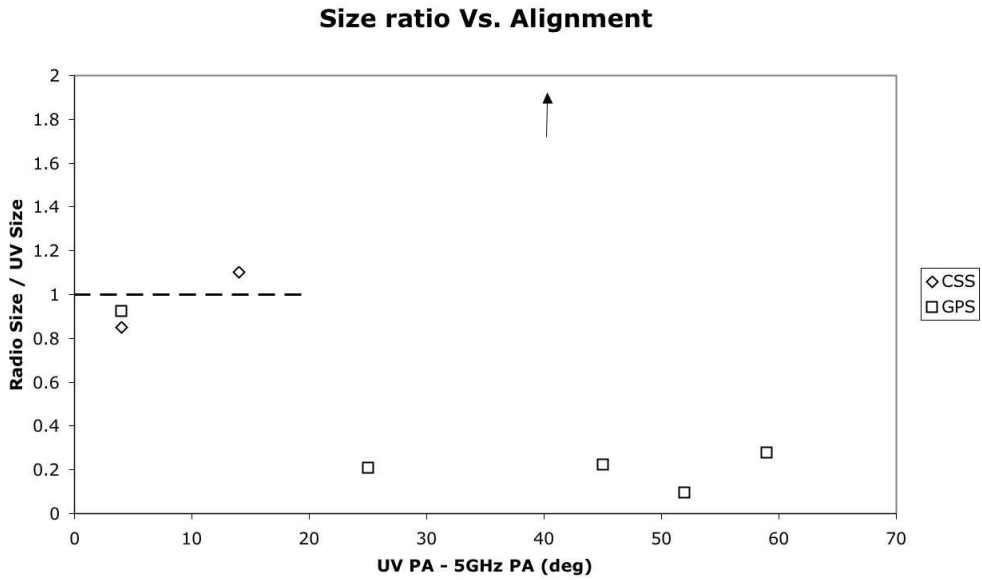


**Figure 7.9–.** Ratio of radio and UV sizes versus the alignment of the GPS and CSS sources. The dashed line marks the locus for sources with same UV and radio size and highest alignment i.e. where the radio source is most likely affecting the star formation in the host. The point for B1233+418 lies outside the plot (represented by the arrow).

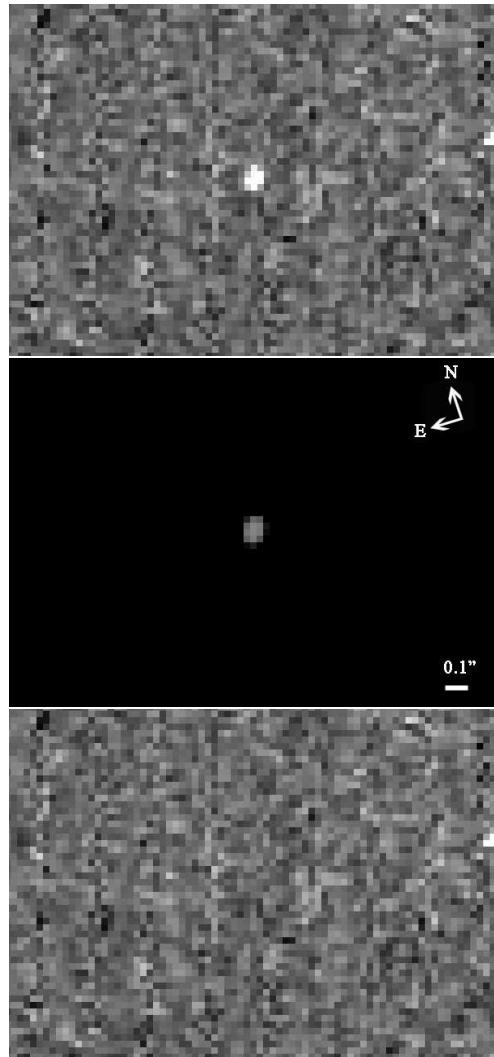


**Figure 7.10**–. Image, GALFIT model and residuals for B1117+146.

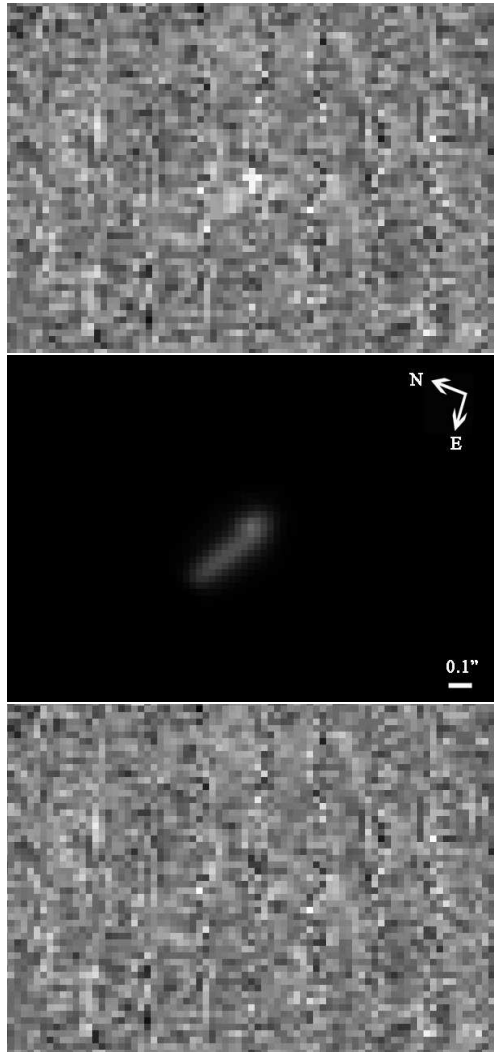


**Figure 7.11**–. Image, GALFIT model and residuals for B1233+418.

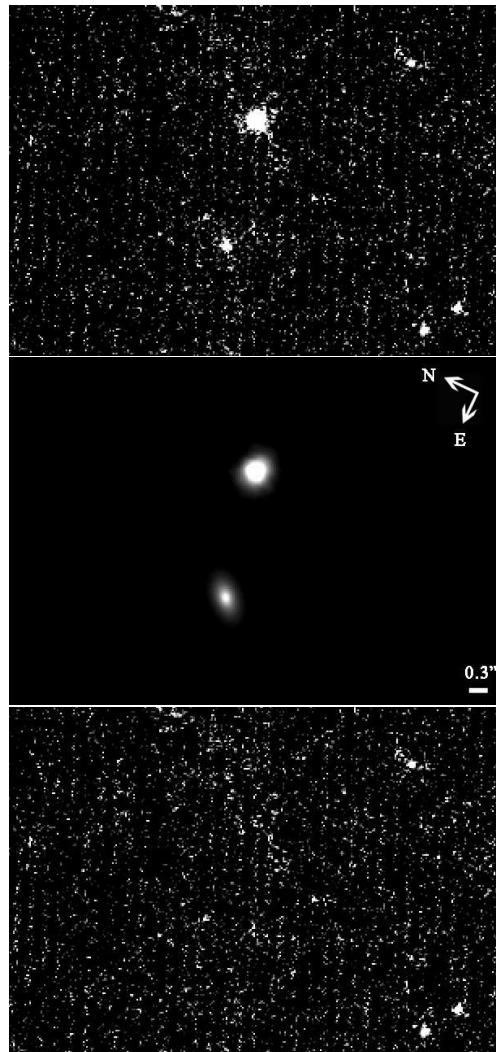


**Figure 7.12**–. Image, GALFIT model and residuals for B1345+125.

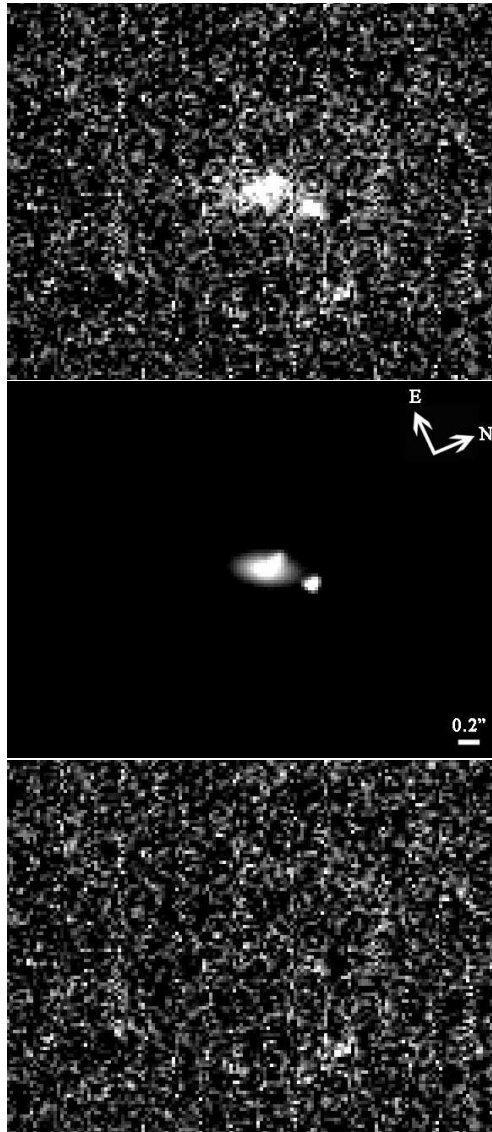


**Figure 7.13**–. Image, GALFIT model and residuals for B1443+77.

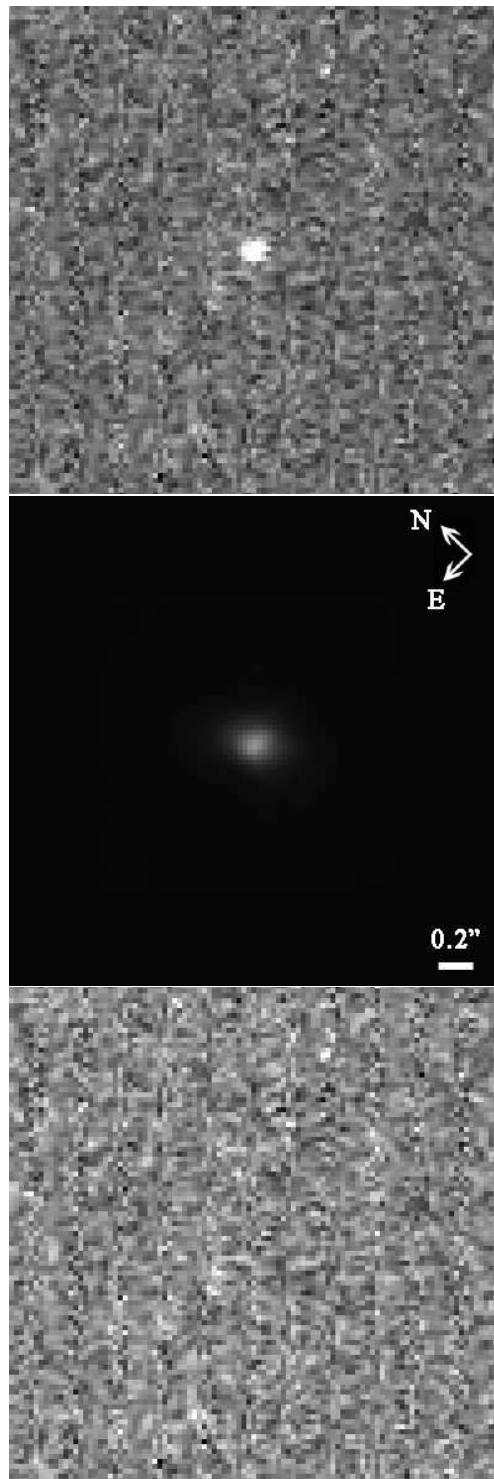


**Figure 7.14.** Image, GALFIT model and residuals for B1607+268.

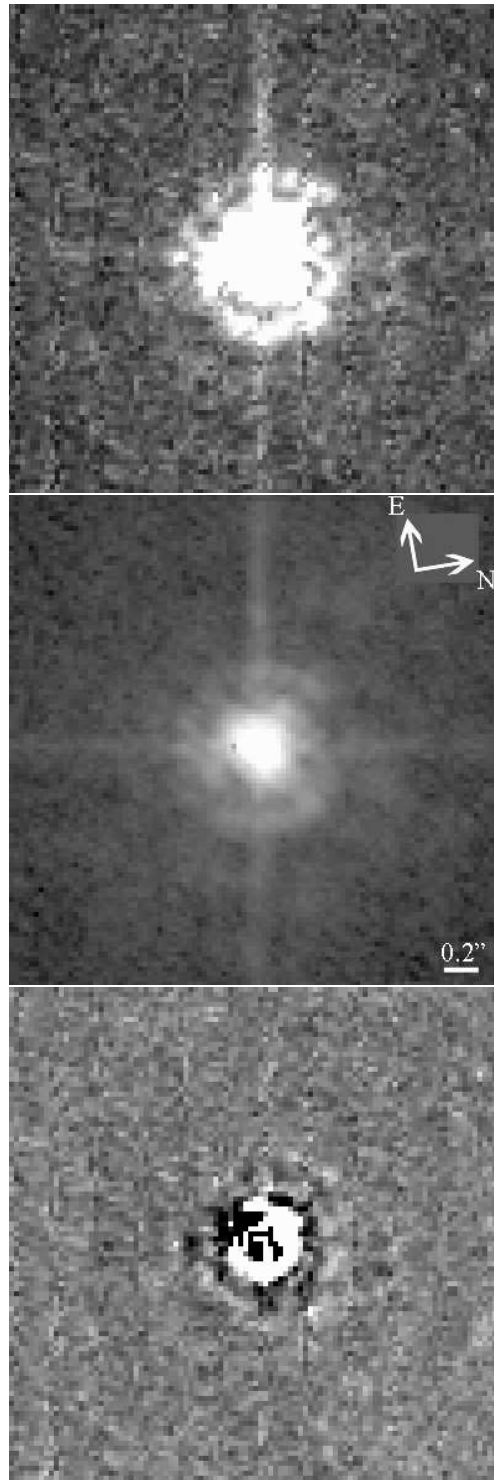


**Figure 7.15**— Image, GALFIT model and residuals for B1814–637.

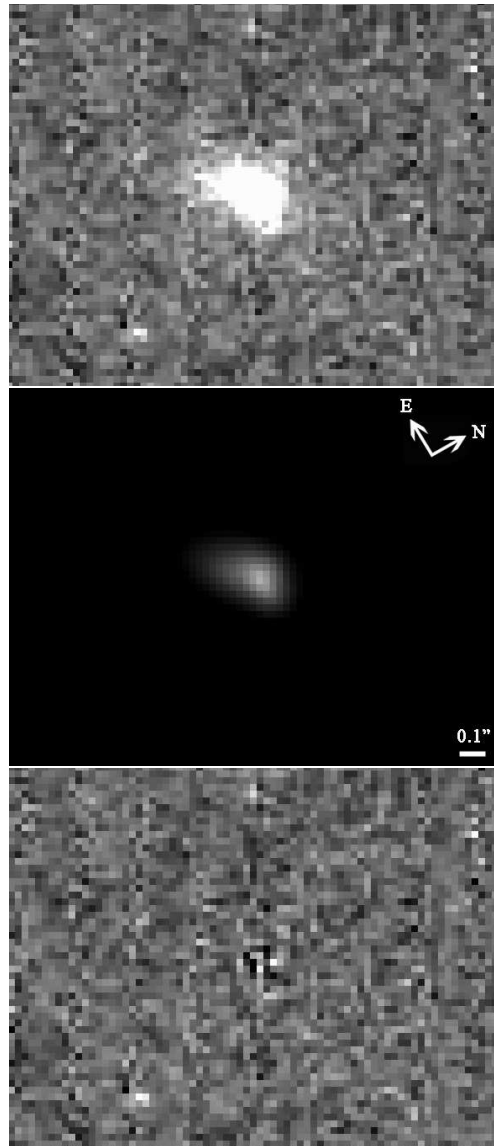


**Figure 7.16**–. Image, GALFIT model and residuals for B1934–638.

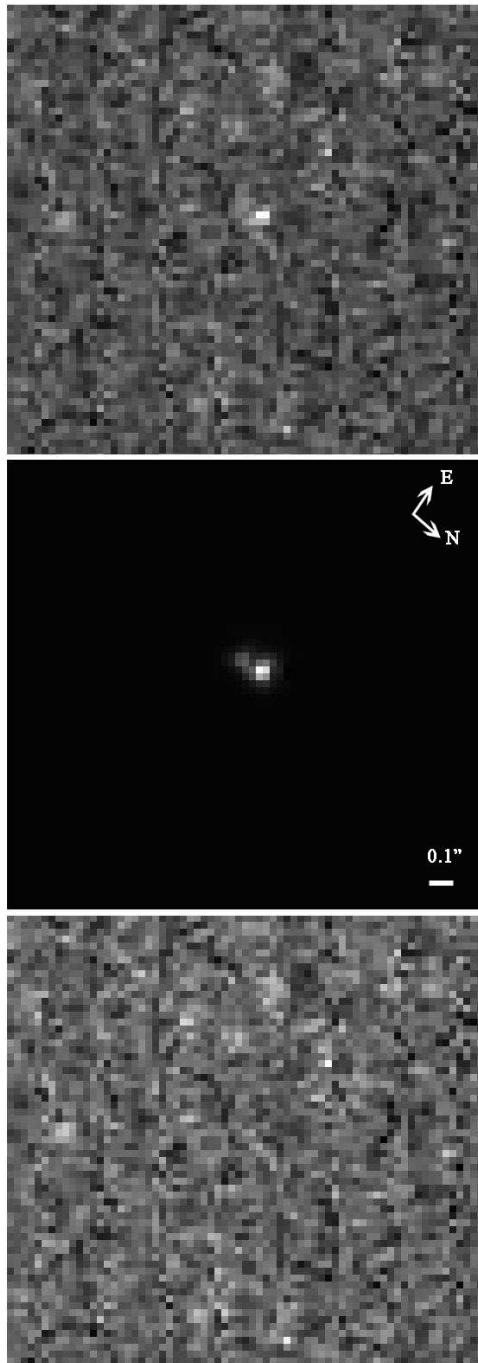


**Figure 7.17**–. Image, GALFIT model and residuals for B1946+708.

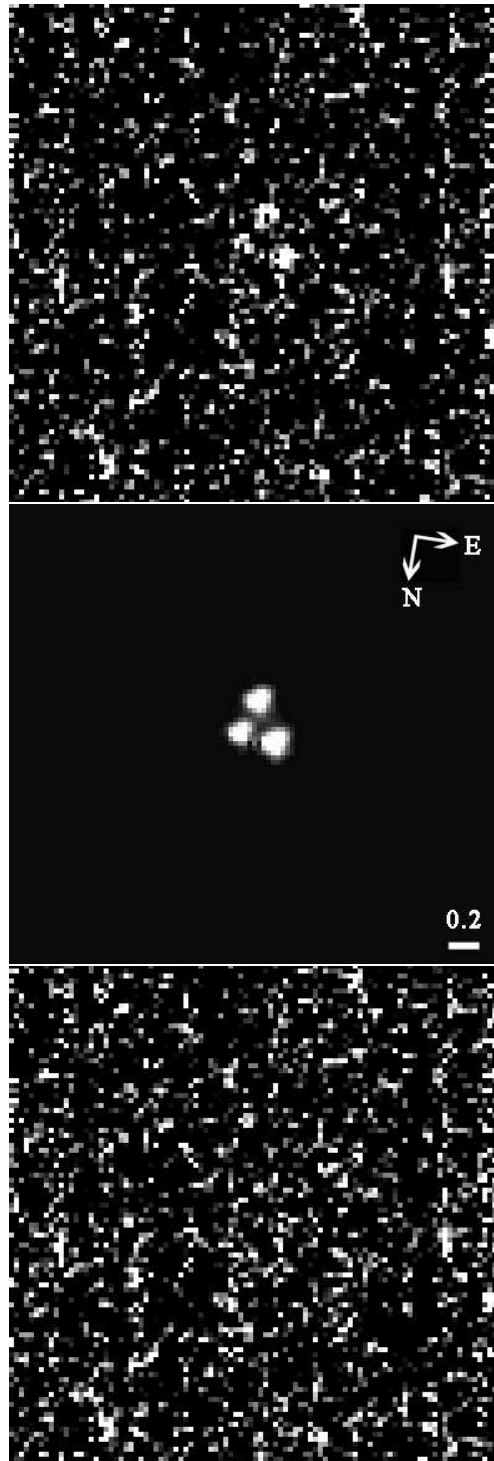


**Figure 7.18**–. Image, GALFIT model and residuals for B2352+495.



*With me poetry has not been a purpose,  
but a passion.*

Edgar Allan Poe

# 8

---

## Concluding remarks

**I**N this final chapter of the thesis, I summarize what we have learned about GPS and CSS sources in the last years. I list a few of the most (in my opinion) important questions in the field and highlight where this thesis has contributed (Section 8.1). I summarize the most important results of each chapter and what I think is the main contribution of the thesis to the field (Sections 8.2 and 8.3). I also describe some of the ongoing work in our group and suggest possible lines of future research (Section 8.4).

### 8.1 Developments in the field

In the introduction of the thesis (Section 1.7), I listed some of the questions and issues concerning compact extragalactic radio sources that had yet to be answered by the time I embarked on the project. In this section I describe the latest developments in the field and highlight the contributions from this thesis.

- *Are GPS and CSS sources young?*

The nature of GPS and CSS sources and their relation with larger radio sources has been an active issue for over thirty years (e.g., Blake 1970; van Breugel et al. 1988). In the past years (e.g., Fanti et al. 1995; Readhead et al. 1996b), growing evidence supporting the young scenario has been found. Spectral aging, energy supply arguments and, especially, measurements of expansion velocities support the young scenario (e.g., Conway 2002; Polatidis & Conway 2003; Murgia 2003; Siemiginowska et al. 2005).

However, not all GPS and CSS sources must be necessarily young. Stanghellini et al. (2005) find large scale diffuse radio structures in GPS sources, which could be the relic of a past nuclear activity phase, suggesting a recurrent source. Marecki et al. (2003) and Marecki et al. (2005) find GPS and CSS sources where the activity has recently stopped, so even though they are young, they are –as they refer to them– *dying* sources. Siemiginowska et al. (2003) observed a sample of GPS sources in X-rays and

found that some<sup>1</sup> of their hosts may have enough gas to confine them.

- *How do GPS and CSS sources evolve?*

According to the *young scenario*, GPS evolve into CSS and these into FR sources. However, it is not completely clear how this evolution takes place or if they evolve into FR I or FR II sources. Based on morphological similarities, it has been traditionally thought that they evolve into FR II. However there is no strong evidence supporting this (nor denying it) and there are models where GPS and CSS could evolve into FR I, both directly (especially if the CSS is weak, e.g., Marecki et al. 2005; Snellen et al. 2000) or through a transient FR II phase (e.g., Ghisellini & Celotti 2001).

According to the general *classic* model, GPS/CSS grow into FR sources in a self-similar way, at roughly a constant velocity through an ambient medium which declines in density as  $\rho(R) \propto R^{-2}$  while the sources decline in radio luminosity as  $L_{rad} \propto R^{-0.5}$  (e.g., Fanti et al. 1995; Begelman 1996; Readhead et al. 1996a). Most of the models developed later have been based on this one, including free-free or synchrotron self-absorption and varying the jet or the host physical parameters (e.g., Kaiser & Alexander 1997; Bicknell et al. 2003).

Modeling how the expansion takes place seems to be a matter far from solved. A few examples: Snellen et al. (2000) introduced a variation to the *classic* model where GPS would increase in luminosity as they grow into CSS, which would then dim as they expand. With this variation they could explain the observed redshift distribution of GPS/CSS. A few years later, Tinti & De Zotti (2005) describe a model that predicts that same distribution with redshift but without the increase in luminosity in the GPS to CSS phase. Another matter of discussion is the self-similar expansion. It seems a little *ad hoc* to require the jet to expand through and interact with the host while maintaining geometric relationships. Recent models (e.g., Jeyakumar et al. 2005; Saxton et al. 2005) include these interactions, and some of them obtain better predictions without including self-similar expansion (e.g., Carvalho & O’Dea 2003). However, Tschager et al. (2003) present a new sample of weak CSS sources and argue that self-similarity is an essential, intrinsic characteristic of the expansion.

The interest in modeling the expansion the radio source keeps growing and it is becoming an extremely active field. On the other hand, considerable amounts of work are being carried out with the purpose of increasing, improving and homogenizing the GPS and CSS samples, which will help addressing the problem and improving the models.

- *Free-free of synchrotron self-absorption?*

This has been a less active field but it is still surrounded by controversy. The main trend is that the peak in the radio spectra of GPS and CSS sources is due to synchrotron self-absorption (SSA, e.g., Snellen et al. 2000). However, even in sources where SSA seems to cause the peak, free-free absorption cannot completely be ruled out (e.g., Tingay & de Kool 2003). Furthermore, there are sources where the turnover seems to

---

<sup>1</sup>Some X-ray observations find that the hot gas cannot confine the GPS source (e.g., O’Dea et al. 1996b, 2000).

be produced by free-free absorption (FFA, e.g., Marr et al. 2001; Shen et al. 2005) and some models are still developed based on FFA (e.g., Kamenon et al. 2003).

- *GPS quasars*

The problem with the nature of GPS quasars is still open. The majority of the sources that are currently classified as GPS quasars could be a different type of object, unrelated to compact, *real*, GPS/CSS sources (e.g., Snellen et al. 1999; Stanghellini 2003; Bai & Lee 2005). A detailed description of the problem is given in Section 1.6 of the Introduction of this thesis. See also Snellen (1997). Most of the work carried out trying to solve this problem has focused on observing known old samples of GPS sources with better telescopes and obtaining new samples. So far, the most useful techniques for improving the samples seem to be high resolution imaging and, particularly, searches for radio spectral variability (e.g., Dallacasa et al. 2000; Jauncey et al. 2003; Tinti et al. 2005).

- *Samples of GPS and CSS sources*

Addressing most, if not all, the above issues requires good samples. During the first years of GPS/CSS research, these sources were drawn from surveys and samples targeting general radio sources (3CR for example), with selection criteria that would not necessarily apply to GPS/CSS sources. However, this has changed in the last few years and there have been projects aimed at improving old samples (e.g., de Vries et al. 1995; Stanghellini et al. 1998; Snellen et al. 1998b; de Vries et al. 2000b; Xiang et al. 2002; Rossetti et al. 2005, ; **Chapters 2 and 3** of this thesis) and obtaining new ones, targeting only (or mostly) GPS and CSS sources (e.g., Dallacasa et al. 2000; Fanti et al. 2001; Taylor & Peck 2003; Edwards & Tingay 2004). As samples get improved, enlarged and homogenized, progress is made in almost every field of research concerning GPS and CSS sources (e.g., Tschager et al. 2003; Marecki et al. 2005; Stanghellini et al. 2005; Tinti & De Zotti 2005).

- *Cold gas in GPS and CSS sources*

Many GPS, CSS and FR sources are in interacting or merging systems (e.g., de Vries et al. 2000a; Johnston et al. 2005), therefore we expect their hosts to have dense nuclear environments. Furthermore, most of the radio loud AGN seem to live in elliptical galaxies (e.g., Martel et al. 1999; Dunlop et al. 2003). Walsh et al. (1989) found that the presence of gas (and dust) in early type galaxies is correlated with the occurrence and strength of a central radio source. This gas is found both in molecular and atomic form (e.g., Knapp & Rupen 1996; Oosterloo et al. 1999). Observations at different wavelengths find central structures of gas in AGN hosts (e.g., van Gorkom et al. 1989; Verdoes Kleijn et al. 1999; Evans et al. 1999; van Langevelde et al. 2000; Morganti et al. 2001). If the gas is centrally concentrated and GPS/CSS sources are precursors (smaller versions) of FR sources, we expect GPS/CSS to show higher densities in the gas surrounding their radio lobes<sup>2</sup>. In 2003,

---

<sup>2</sup>However, extremely high densities may confine the sources.

using the recently improved Westerbork Synthesis Radio Telescopes, Vermeulen et al. (2003) and Pihlström et al. (2003) presented a study of the occurrence and properties of atomic gas associated with compact radio sources. They found that  $\sim 50\%$  of GPS and CSS sources showed HI 21 cm absorption, in contrast to normal elliptical galaxies ( $\lesssim 10\%$ , van Gorkom et al. 1989). Furthermore, they found that GPS sources tend to have higher HI column densities than CSS sources and that these densities were consistent with the young scenario. However, their data lack spatial resolution to accurately locate the HI absorption. Just a few high resolution HI observations of GPS/CSS sources were available at that time (e.g., Conway 1996; Peck & Taylor 1998; Peck et al. 1999; Peck & Taylor 2002). We are involved in a project aimed at obtain high resolution HI observations with the European VLBI Network. **Chapters 5 and 6** of this thesis are the first results of this project. Searches for molecular gas in GPS/CSS have also been carried out (e.g., O’Dea et al. 2005), finding that GPS and large radio sources have similar molecular gas contents and that GPS do not require extremely dense environments. Therefore it is unlikely that the molecular gas will confine the radio source.

- *Interaction with the host*

According to the young source scenario, a powerful radio source will grow from parsec scales to kiloparsec and megaparsec scales. However, to expand to those sizes it must cross the environment of the host galaxy. We therefore expect interaction between the radio lobes and the ISM. The first traces of interaction between GPS/CSS and their hosts were found in the emission line gas. The properties observed in [O III]  $\lambda 5007$  emission lines (Gelderman & Whittle 1994) suggested that, even though the AGN was partly photoionizing the nebula, the radio source was dominating the emission-line kinematics. A few years later, the alignment effect (similar extent for radio and optical wavelengths) seen in large radio sources (e.g. Chambers et al. 1987; McCarthy et al. 1987) was found in GPS and CSS (de Vries et al. 1997b, 1999; Axon et al. 2000). The alignment between the radio source and emission line gas suggests interaction between them, as the radio source propagates through the host. The emission line gas was found to be brighter in the center of the radio lobes and dimmed with distance. Therefore, the hypothesis adopted was that the gas inside the radio lobe had been shock-ionized while the gas outside was photoionized by the precursor gas in the shock. At the same time, the AGN could contribute to the whole system with photoionization. Cooling time arguments suggested lobe expansion velocities  $\gtrsim 1000 \text{ km s}^{-1}$  for most of the sources. In 2002, O’Dea et al. (2002) studied the kinematics of the emission line nebulae of CSS sources, finding that the radio source is accelerating the clouds of gas in the host. **Chapter 4** of this thesis continues and wraps up all previous work by studying the ionization mechanisms of three CSS sources. We compare our data with ionization models and confirm that high speed shocks are ionizing the nebula, therefore yielding evidence of jet cloud interaction. **Chapter 5** of this thesis also finds evidence of jet cloud interactions, this time through radio observations of HI absorption. **Ongoing research** by our group (not included in this thesis) finds a correlation between strength of [O III] and radio size, suggesting that the expansion of the radio source is enhancing the [O III] emission in the host. Outflows of gas induced by the AGN can also affect

the evolution of the host. They can affect even the star formation history of a galaxy (e.g., Morganti et al. 2003b; Silk & Rees 1998). Different studies are finding outflows of gas in CSS/GPS sources (e.g., Holt et al. 2003, and **Chapter 6** of this thesis). Furthermore, some cases of outflows strongly support the young scenario, as well as interactions between the radio source and the host (e.g., Tadhunter et al. 2001; Holt et al. 2005). **Chapter 7** of this thesis finds more evidence of radio source – host interaction, this time through near UV imaging: some CSS sources show jet induced star formation in their hosts.

- *The Starburst–AGN connection and the role of GPS and CSS sources*

It has been suggested that mergers and intergalactic interactions can trigger an AGN event (e.g., Heckman et al. 1986; Sanders et al. 1988; Baum et al. 1992; Israel 1998). Such a strong event can also trigger star formation in a galaxy (e.g., Ho 2005). It is also generally thought that black hole and galactic evolution are related (e.g., Silk & Rees 1998; Gebhardt et al. 2000; Begelman & Nath 2005). However, evidence of a causal connection between starbursts and AGN has yet to be found. Substantial work has been carried out trying to find it in different types of AGN (e.g., Veilleux 2001; González Delgado et al. 2001; Kauffmann et al. 2003; Ho 2005). Studies of stellar populations in the hosts of GPS, CSS and large (FR I and FR II) sources find traces of episodes of star formation by the time the radio source was formed, or earlier<sup>3</sup> (e.g., Allen et al. 2002; O’Dea et al. 2003; Morganti et al. 2003a; Raimann et al. 2005; Johnston et al. 2005; Tadhunter et al. 2005; Emonts et al. 2006).

The presumed young ages of GPS/CSS sources makes them perfect tools to study the connection between the starbursts, AGN formation and triggering of the radio source. **Chapter 7** of this thesis presents the first near-UV study of GPS and CSS sources, and looks for evidence for this connection. The results are consistent with a scenario where a strong interaction has triggered a starburst and the formation of the radio source. Studies at different wavelengths have been planned to complement these results.

## 8.2 Detailed contributions by this thesis

The work carried out in this thesis has contributed to our understanding of GPS and CSS sources and their relation to the host galaxies from different perspectives. In this section I summarize the most important contributions.

*Improving the samples of known GPS and CSS sources.* Chapters 2 and 3 are mainly devoted to identifying new GPS and CSS sources. Chapter 2 presents Very Large Array (VLA) observations of compact sources in the southern sky. Seven new CSS sources are found and a comparison between the Third Cambridge Catalogue (3C) and Molonglo Southern 4 Jy Sample (equivalent to the 3C in the Southern hemisphere) is carried out. Chapter 3 presents Very Large Telescope (VLT) deep imaging and spectroscopy of GPS candidate sources from the O’Dea et al. (1991) master list. Six optical counterparts are identified and four new redshifts are measured. Using data from these chapters and from

---

<sup>3</sup>This delay is usually consistent with the time needed for gas to be driven into the center (e.g., Lin et al. 1988).

the literature, five sources are removed from the GPS and CSS lists. Most of them were classified as GPS according to their radio spectra. However, new available data suggest that these sources are variable larger radio sources.

*Radio morphology of compact sources.* The VLA and the European VLBI Network (EVN) were used to study the morphologies of GPS and CSS sources and to compare them with observations in other wavelengths (Chapters 2, 5 and 6). VLBI radio observations allowed us to localize the atomic hydrogen in these sources and study its relation to the emission line gas. Previous studies suggested that the H I absorption could be related to the emission line gas and our results seem to confirm it. Using high resolution mapping and previous observations of a long-known GPS source we discovered a previously unseen component, changing our understanding of the source morphology: what it was thought to be a compact double, it may well be a one-sided core-jet source.

*Interaction with the host.* Chapters 4, 5, 6 and 7 study and search for interaction between the radio source and its host. The main goal is try to understand how the growth of the radio source is affecting the host it lives in, and if the properties of the host affect the evolving radio source. The small size of GPS and CSS sources makes them excellent probes to search for this interaction. Their radio lobes are still inside the host so the interaction between them is expected to be higher than in larger radio sources. We find evidence of this interaction. Our Hubble Space Telescope (HST) Space Telescope Imaging Spectrograph (STIS) spectroscopic data (Chapter 4) reveals that the shocks produced by the expanding radio source are ionizing (in some sources almost completely) the emission line gas of the host. Our EVN radio observations find H I associated with the emission line gas and outflows, supporting the interaction scenario. Using the HST Advanced Camera for Surveys we carried out the first near-UV study of GPS/CSS sources. The high spatial resolution of our images unveils complex kpc scale morphologies in the hosts of these sources. Color information is still needed. However, our first results suggest recent star formation episodes in the hosts on time scales consistent with the triggering of the radio source. Some sources show radio and UV structures that suggest star formation triggered by the expansion of the radio lobes through the host.

*Star formation and nuclear activity.* Using our optical and ultraviolet images (Chapters 3 and 7), we studied the stellar population properties of the hosts of GPS and CSS sources. The lack of colors make our results preliminary. However, these results are found to be consistent with previous studies of the stellar populations in GPS and CSS sources. Comparison with synthetic stellar population models suggest that GPS and CSS sources occur in galaxies with recent star formation and suggest a connection between nuclear activity and starburst. Furthermore, the UV images seem to imply that the expansion of the radio source can affect the star formation history of the host.

### **8.3 The bottom line: Strong interaction between radio source and host**

The main goal of this thesis is to study the interrelation of powerful radio sources with their hosts. The objects of study are GPS and CSS sources. Due to their small size, GPS/CSS

sources are excellent probes of this relation. Furthermore, their young age allows us to compare them to the larger, old radio sources and establish a time-line evolution of this relation.

This thesis combines imaging and spectroscopy of GPS/CSS sources at different wavelengths, and all our studies lead to the same conclusion: the presence and expansion of powerful radio sources clearly affect the properties and evolution of their hosts. All chapters of the thesis (excluding the sample studies) find evidence of strong interaction between the host and the radio source. Furthermore, the radio source and host can significantly affect each others evolution. However, this influence takes place in different ways. The influence that the host has on the radio source is somehow indirect. However it can completely change its destiny: depending of the contents, distribution and density of the gas, the radio source will die early, expand and grow into the large FR sources, or remain confined inside its host. In contrast, the influence of the radio source on its host seems to be more direct and takes place during its expansion through the host: the radio source will affect the kinematics and ionization of the emission line gas, and may change the star formation history of the host.

Briefly, the main results that lead to this conclusion are:

1. Presence of shock ionized gas in 3C 67, 3C 277.1 and 3C303.1 (Chapter 4).
2. HI gas associated to the emission line gas in 3C 49 and 3C 268.3 and the presence of outflows in B2050+364 (Chapters 5 and 6).
3. Possible events of star formation related to the triggering of the radio source and findings of jet induced star formation in 1814–637 and 3C 303.1, which is also the source showing the strongest contribution from shocks to the ionization of the emission line gas (Chapter 7).

## 8.4 Ongoing and future work

Much progress has been made in understanding the nature of powerful radio galaxies and GPS/CSS sources, as well as their relation to their hosts. However, there are still some puzzling questions to be answered. A few of these are clear follow-ups of the issues listed above (Section 8.1). Others may affect more general subjects such as galaxy formation and evolution, i.e. why do some galaxies harbor an AGN? Is the AGN phenomenon a phase all or just certain galaxies go through? What are the conditions needed in a galaxy to host an AGN?

The younger the radio source, the closer we are to the formation of the AGN. Therefore, GPS and CSS sources may play an important role in answering some of these questions. However, GPS and CSS sources have unanswered questions of their own. In this section I will describe some of the ongoing work we are carrying out and suggest possible lines of continuation of the research carried out in this thesis.

Large, homogeneous samples are needed to test models, solve the GPS quasar problem, test scenarios, etc. Considerable amounts of work are being carried out aiming to re-address GPS/CSS samples and obtain new ones. However, there is still much to be done, especially for the smallest and unresolved sources. High resolution VLBI imaging is needed, as well

as variability studies. Searches for extended emission are also useful as they can give an estimate of how many GPS/CSS sources are recurrent or have been interrupted. The classification of the GPS candidates in the O'Dea et al. (1991) master list is almost complete. VLT searches for optical counterparts and redshifts have proven useful. VLT images and spectroscopy will be carried out for the remaining objects still lacking identification. Measuring radio fluxes in some of these sources will help finding variable sources and sort out incorrect classifications.

Studying the gas contents and distribution will continue to constrain issues such as young versus old scenario or the free-free versus synchrotron self-absorption problems. Vermeulen et al. (2003) find H I absorption in one third of their sources. Chapters 5 and 6 yielded interesting results in both the distribution of the H I gas and the morphology of three of these GPS/CSS sources. Therefore, we expect that EVN observations of the remaining sources will also yield interesting results. In the same line of research, observations searching for molecular gas are not very frequent in GPS and CSS sources and will be planned. Techniques such as measuring the polarization properties and Faraday rotation are also useful in the study of the gas polarization of the hosts of GPS and CSS sources. X-ray observations are also yielding interesting results on gas contents, especially close to the nucleus, as well as on the strength of the AGN.

GPS and CSS are the progenitors of large radio sources. However, it is not clear how their expansion takes place. Theoretical models keep being developed. However, they are still too simple and cannot accurately reproduce the observations. Considerable amounts of work are still needed both observationally and theoretically to be able to reproduce in detail the expansion of the radio lobes, how they interact with the host, etc. We are carrying out a comparison of these models, as well as jet expansion models with a large collection of GPS/CSS and FR sources aiming to constrain the time evolution of the radio source and check the predictions from the different models.

Our ACS images are consistent with a connection between a recent starburst and the formation of the radio source. However, we lack color information to accurately establish how much of the light is from young stars. The new and soon to be launched IR space telescopes (Spitzer, ASTRO-F, HERSCHEL) provide the perfect tools for obtaining high resolution images and spectral information on the stellar composition (as well as dust and gas) of the hosts of GPS and CSS sources.

In a longer time span, the improvements in our radio observing capabilities that the Square Kilometer Array will provide will allow us to study much weaker AGN, as well as obtain information on contents and distribution of gas in the most inner regions on the AGN. In the infrared, the high resolution and extremely high sensitivity of the James Webb Space Telescope, combined with the Integral Field Spectroscopy unit of the Mid Infrared Instrument will allow us to get extremely detailed 2D maps of the properties and distribution of the emission line gas in hosts of AGN. Furthermore, it will permit such studies, not only in the nearby universe but also at high redshifts. We may be able of tracing the cosmological evolution of the interaction of powerful radio sources and their host, out to the time the first galaxies were forming.





# Nederlandse samenvatting

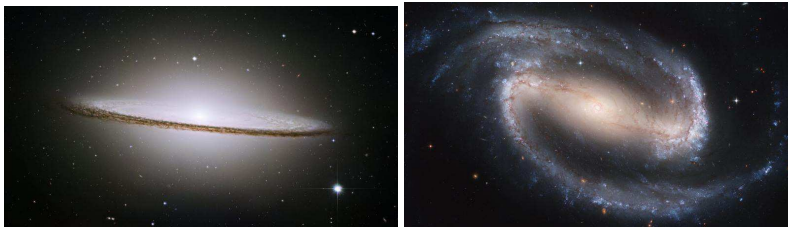
**W**ANNEER we naar een heldere nachthemel kijken zien we sterren, planeten, kometen, wolken gas en stof, en vele andere soorten objecten. De meeste van deze, net als zon en maan, maken deel uit van immense systemen, sterrenstelsels genaamd. Een sterrenstelsel is een enorm conglomeraat van sterren, gas en stof, dat door de werking van de zwaartekracht bij elkaar wordt gehouden. Zie figuur 1. Er zijn miljarden sterrenstelsels.

Dit proefschrift beschrijft een bijzonder soort van sterrenstelsel, te weten radiostelsels, welke op hun beurt deel uitmaken van de klasse "aktieve stelsels". Een actief sterrenstelsel heeft als kenmerkende eigenschap dat het centrum ervan net zo veel energie uitstraalt als het complete stelsel (en soms zelfs meer). Men spreekt ook wel van "aktieve kernen van sterrenstelsels" en denkt dat al die energie afkomstig is van het proces van inval van materie in een enorm zwaar zwart gat. Zo'n zwart gat weegt wel een miljard keer zo veel als de zon, en neemt daarbij een ruimte in van slechts enkele kilometers, in het centrum van het stelsel.

Men vermoedt dat de invallende materie een platte schijf vormt rondom het zwarte gat, de zogenaamde accretieschijf. Het is deze roterende gloeiende schijf die de grote hoeveelheden energie produceert, van radio- tot röntgenstraling. Die schijf wordt dikker verder naar buiten toe en vormt zo een dikke torus (ring), rondom de kern, in het vlak van de accretieschijf. De aanwezigheid van die torus maakt dat we de kern niet kunnen zien als we het systeem van opzij bekijken (van rechtsbeneden in de figuur op de omslag van het proefschrift). In dat geval noemen we het object een Seyfert-2 of radiostelsel, al naar de verhouding van de hoeveelheden optische en radiostraling.

Vliegt een ster of wolk gas voorbij het zwarte gat (zonder erin te vallen) dan bestaat de kans dat het magnetische veld van het zwarte gat de ster of gaswolk in zijn greep krijgt. Afhankelijk van de snelheid ervan zal de materie ofwel naar het zwarte gat worden getrokken, ofwel versneld worden naar buiten toe, in een gecollimeerde (radio)bundel, ook wel straalstroom of jet genoemd (de gele lijnen op de omslag van het proefschrift). Nemen we de kern waar vanuit een richting die dichtbij deze bundel ligt (rechter bovenhoek), dan kunnen we ongehinderd in de torus naar de accretieschijf kijken. In dat geval zien we een Seyfert-1 of – in de ultra-energetische gevallen – een quasi-stellair object (quasar).

Er zijn nog veel raadsels rond het fenomeen actief sterrenstelsel. We weten nog steeds niet hoe ze ontstaan en waarom sommige stelsels wel en andere niet een actieve kern hebben. Evenmin is duidelijk hoe zo'n object evolueert in de tijd en welke invloed de kern



**Figuur 1–.** Sterrenstelsels NGC4594 ("Sombrero") en NGC1300. De opnamen zijn gemaakt met de Hubble ruimte-telescoop (STScI/AURA).

en het moeder-sterrenstelsel op elkaar uitoefenen. Dat laatste is het hoofdonderwerp van dit proefschrift.

Onderwerp van studie vormen radiostelsels in hun eerste levensfasen, de zogenaamde GPS-objecten (leeftijd 1000 – 100.000 jaar) en de CSS-objecten (100.000 – 10.000.000 jaar jong). Vrij spoedig na de ontdekking van deze klassen van objecten stelden astronomen al vast dat ze lijken op de "normale" radiostelsels, zij het dat ze een stuk kleiner zijn. Gewone radiostelsels hebben radiobundels die zich ver buiten de moedersterrenstelsels uitstrekken; voor GPS- en CSS-objecten geldt het tegendeel. Tot vrij recent was het onduidelijk of men hier met normale radiostelsels in hun prille jeugd van doen had, op weg naar volwassenheid, of dat GPS- en CSS-objecten bijzondere gevallen waren. Hun relatief kleine afmeting zou veroorzaakt kunnen worden door een ongewoon gas- en stofrijk moederstelsel dat expansie van de radiobundels belet. De situatie is te vergelijken met met groeien in een notendop zonder door de dop te kunnen breken. Recent onderzoek van de expansiesnelheid van de radiobundels in GPS- en CSS-objecten heeft echter geleerd dat we naar alle waarschijnlijkheid met jonge objecten van doen hebben. In dit proefschrift wordt de wisselwerking tussen de jonge actieve kern en het moederstelsel nader bestudeerd.

De zich naar buiten borende bundels zullen bij hun expansie de omringende materie van het moederstelsel op hun weg vinden. Ze zullen hun weg naar buiten moeten vinden door deze materie opzij te drukken. Dat er een sterke interactie tussen de bundel en het interstellair medium ontstaat ligt dus in de lijn der verwachting. Deze interactie kan men waarnemen en vormt het belangrijkste resultaat van het promotie-onderzoek. Hoe neemt men die interactie waar? Gooit iemand een steentje in het water dan zien we rimpelingen op het oppervlak: een verstoring, veroorzaakt door het steentje. Op dezelfde manier zal een radiobundel die zijn weg naar buiten zoekt verstoringen in het omringende medium veroorzaken. Dit proefschrift beschrijft enkele CSS-objecten waar de expanderende bundels door een schokeffect het omringende gas tot gloeien brengen. Ook worden enkele CSS-objecten beschreven waarvan de bundels het gas in het moederstelsel comprimeren en tot stervorming aanzetten. De kernactiviteit oefent niet alleen krachten uit op het omringende medium, maar is tevens van invloed op de evolutie van het sterrenstelsel.

Kort gezegd, dit proefschrift vindt aanwijzingen dat de actieve kern van een sterrenstelsel het uiterlijk en de evolutie van het stelsel kan beïnvloeden.

# English Summary

WHEN we look up to the sky in a clear night, we can see stars, planets, comets, asteroids, clouds of dust and gas, and many other sorts of astronomical objects. Most of these, like the Sun and the Earth, live in big systems called *galaxies*. A galaxy is a massive system of stars, gas, and dust, together with planets and smaller bodies, bound together gravitationally (Figure 1). There are billions of galaxies.

This thesis deals with a special type of galaxies called *radio galaxies*, a sub-type of *active galaxies*. An active galaxy is one where the nucleus itself emits as much energy as (or even more than) the rest of the galaxy. They are said to have an *Active Galactic Nucleus*, or AGN. This energy is thought to be created by matter falling into an extremely massive *black hole* (1,000,000,000 times the mass of the Sun, inside a sphere of a few kilometers) on the center of the galaxy.

It is thought that the in-falling matter forms a disk around the black hole: the *accretion disk*. In fact, it is this glowing rotating disk that is producing the large amounts of energy we detect (from radio wavelengths to X-rays!). This disk is believed to widen up as we move away from the center forming a *torus* around the nucleus, in the same plane of the disk. Due to this torus, if we observe the AGN sideways (from the bottom right corner in the picture on the cover), we will not see the nucleus. In this case, we call the AGN a *Seyfert 2* or *radio galaxy*, depending on how much light is emitted in radio and optical wavelengths.

If a particle manages to fly by the black hole (and not fall into it), it may get trapped in the black hole magnetic field. Depending on the velocity of the particle, the magnetic field will push it down to the black hole or accelerate it outwards in a very collimated flow or *jet* (the yellow lines on the cover of this thesis). If we look to the AGN close to the jet line (top right corner of the cover), the torus is not in our way so we are seeing all the light produced in the AGN. In this case, we are seeing a *Seyfert 1* or a *Quasi Stellar Object* (or *quasar*) in the most luminous cases.

There are a lot of mysteries surrounding the AGN phenomenon. We still do not know how they form and why some galaxies have an active nucleus and some do not. Another issue of unclear nature is how the AGN evolves and how it affects the galaxy it lives in (the *host galaxy*). The latter issue is the top issue of the thesis.

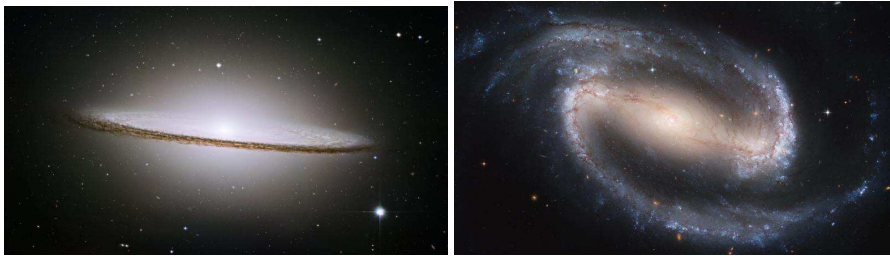


**Figure 1**–. 'The Sombrero'(left) and 'NGC1300' (right) galaxies. Images from the Hubble Heritage team (STScI/AURA).

For this, we chose to study the radio galaxies in their first phase of existence, the so called *Gigahertz Peaked Spectrum* (GPS) sources (1,000 to 100,000 years) and *Compact Steep spectrum* (CSS) sources (100,000 to 10,000,000 years). When they were first discovered, astronomers realized that these GPS and CSS radio sources looked just like the "normal" radio galaxies, but they were much smaller. Normal radio galaxies can have jets extending well outside the host, but the CSS and GPS were completely contained in their galaxies! Until recently, it was not clear if they really were normal radio galaxies "photographed" while they were growing into the large ones known, or if GPS and CSS were old radio galaxies being surrounded by a very thick environment that impeded their expansion (like growing inside a nut shell without breaking through it). Recent studies measuring the velocity of growth of jets in GPS and CSS indicated that they are most likely young radio galaxies. This thesis focuses on these young AGN to study their relation with the hosts, in the first steps of the AGN life.

The jet of the AGN will encounter the surrounding matter as it expands through the host. It will have to literally break through and sweep away all this galactic material in its way. We then expect strong interaction between the jet and the host, which we clearly detect now and becomes the main result of this thesis.

How do we find interaction? If we throw a stone in the water, we see ripples on the surface, a perturbation in the water created by the stone. In the same way, the jet expanding through the host will create perturbations in the host. We have seen CSS sources where the shocks created by the expanding jet are firing up emission in the host. Furthermore, we have seen cases of some CSS where their jets are compressing the gas in the host and triggering star formation. So the AGN is not only sweeping matter around, it is affecting the evolution of the host.

This thesis finds indications that the presence of an active nucleus in a galaxy can change the way that galaxy would appear and would evolve if the AGN was not present.

# Bibliography

- Akujor, C. E., Spencer, R. E., Zhang, F. J., Davis, R. J., Browne, I. W. A., & Fanti, C. 1991, *MNRAS*, 250, 215
- Alexander, P. 2000, *MNRAS*, 319, 8
- Alexander, P., & Leahy, J. P. 1987, *MNRAS*, 225, 1
- Allen, M. G., Sparks, W. B., Koekemoer, A., Martel, A. R., O’Dea, C. P., Baum, S. A., Chiaberge, M., Macchetto, F. D., & Miley, G. K. 2002, *ApJS*, 139, 411
- Antonucci, R. 1993, *ARA&A*, 31, 473
- Antonucci, R. R. J., & Miller, J. S. 1985, *ApJ*, 297, 621
- Aretxaga, I., Terlevich, E., Terlevich, R. J., Cotter, G., & Díaz, Á. I. 2001, *MNRAS*, 325, 636
- Axon, D. J., Capetti, A., Fanti, R., Morganti, R., Robinson, A., & Spencer, R. 2000, *AJ*, 120, 2284
- Bai, J. M., & Lee, M. G. 2005, *Journal of Korean Astronomical Society*, 38, 125
- Baker, J. C., & Hunstead, R. W. 1995, *ApJ*, 452, L95
- Baldwin, J. A., Phillips, M. M., & Terlevich, R. 1981, *PASP*, 93, 5
- Barthel, P. D. 1989, *ApJ*, 336, 606
- Baum, S. A., & Heckman, T. 1989, *ApJ*, 336, 702
- Baum, S. A., Heckman, T. M., & van Breugel, W. 1992, *ApJ*, 389, 208
- Baum, S. A., O’Dea, C. P., de Bruyn, A. G., & Murphy, D. W. 1990, *A&A*, 232, 19
- Baum, S. A., Zirbel, E. L., & O’Dea, C. P. 1995, *ApJ*, 451, 88
- Beasley, A. J., Gordon, D., Peck, A. B., Petrov, L., MacMillan, D. S., Fomalont, E. B., & Ma, C. 2002, *ApJS*, 141, 13
- Becker, R. H., White, R. L., & Helfand, D. J. 1995, *ApJ*, 450, 559
- Begelman, M. C. 1996, in *Cygnus A – Study of a Radio Galaxy*, 209
- Begelman, M. C., & Nath, B. B. 2005, *MNRAS*, 361, 1387
- Bennett, A. S. 1962, *MmRAS*, 68, 163
- Best, P. N., Peacock, J. A., Brookes, M. H., Dowsett, R. E., Röttgering, H. J. A., Dunlop, J. S., & Lehnert, M. D. 2003, *MNRAS*, 346, 1021
- Bicknell, G. V. 1995, *ApJS*, 101, 29
- Bicknell, G. V., Dopita, M. A., & O’Dea, C. P. 1997, *ApJ*, 485, 112

- Bicknell, G. V., Saxton, C. J., & Sutherland, R. S. 2003, *Publications of the Astronomical Society of Australia*, 20, 102
- Biretta, J. A., Schneider, D. P., & Gunn, J. E. 1985, *AJ*, 90, 2508
- Blake, G. M. 1970, *Astrophys. Lett.*, 6, 201
- Bridle, A. H. 1984, *AJ*, 89, 979
- Bruzual, G., & Charlot, S. 2003, *MNRAS*, 344, 1000
- Burgess, A. M. 1998, *The Molonglo Southern 4 Jy Sample: the brightest radio sources in the southern sky* (PhD thesis, University of Sydney)
- Burgess, A. M., & Hunstead, R. W. 2006a, *AJ*, 131, 100
- . 2006b, *AJ*, 131, 133
- Cardelli, J. A., Clayton, G. C., & Mathis, J. S. 1989, *ApJ*, 345, 245
- Carilli, C. L., Rupen, M. P., & Yanny, B. 1993, *ApJ*, 412, L59
- Carvalho, J. C. 1985, *MNRAS*, 215, 463
- . 1994, *A&A*, 292, 392
- . 1998, *A&A*, 329, 845
- Carvalho, J. C., & O'Dea, C. P. 2003, *Publications of the Astronomical Society of Australia*, 20, 98
- Chabrier, G. 2003, *PASP*, 115, 763
- Chambers, K. C., Miley, G. K., & van Breugel, W. 1987, *Nature*, 329, 604
- Chiaberge, M., Macchetto, F. D., Sparks, W. B., Capetti, A., Allen, M. G., & Martel, A. R. 2002, *ApJ*, 571, 247
- Clark, N. E., Axon, D. J., Tadhunter, C. N., Robinson, A., & O'Brien, P. 1998, *ApJ*, 494, 546
- Conway, J. E. 1996, *The second workshop on Gigahertz peaked spectrum and compact steep spectrum radio sources*, Leiden Univ, ed. I. Snellen, R. T. Schilizzi, H. A. J. Rttgering, M. N. Bremer (Leiden: Publ JIVE), 198
- . 2002, *New Astronomy Review*, 46, 263
- Conway, J. E., Myers, S. T., Pearson, T. J., Readhead, A. C. S., Unwin, S. C., & Xu, W. 1994, *ApJ*, 425, 568
- Conway, J. E., Pearson, T. J., Readhead, A. C. S., Unwin, S. C., Xu, W., & Mutel, R. L. 1992, *ApJ*, 396, 62
- Costa, E. 2001, *A&A*, 367, 719
- Dallacasa, D., Bondi, M., Alef, W., & Mantovani, F. 1998, *A&AS*, 129, 219
- Dallacasa, D., Stanghellini, C., Centonza, M., & Fanti, R. 2000, *A&A*, 363, 887
- de Ruiter, H. R., Arp, H. C., & Willis, A. G. 1977, *A&AS*, 28, 211
- de Vries, W. H. 1999, Ph.D. Thesis, University of Groningen
- de Vries, W. H., Barthel, P. D., & Hes, R. 1995, *A&AS*, 114, 259
- de Vries, W. H., Barthel, P. D., & O'Dea, C. P. 1997a, *A&A*, 321, 105
- de Vries, W. H., O'Dea, C. P., Barthel, P. D., Fanti, C., Fanti, R., & Lehnert, M. D. 2000a, *AJ*, 120, 2300
- de Vries, W. H., O'Dea, C. P., Barthel, P. D., & Thompson, D. J. 2000b, *A&AS*, 143, 181
- de Vries, W. H., O'Dea, C. P., Baum, S. A., & Barthel, P. D. 1999, *ApJ*, 526, 27

- de Vries, W. H., O'Dea, C. P., Baum, S. A., Perlman, E., Lehnert, M. D., & Barthel, P. D. 1998a, *ApJ*, 503, 156
- de Vries, W. H., O'Dea, C. P., Baum, S. A., Sparks, W. B., Biretta, J., de Koff, S., Golombek, D., Lehnert, M. D., Macchetto, F., McCarthy, P., & Miley, G. K. 1997b, *ApJS*, 110, 191
- de Vries, W. H., O'Dea, C. P., Perlman, E., Baum, S. A., Lehnert, M. D., Stocke, J., Rector, T., & Elston, R. 1998b, *ApJ*, 503, 138
- De Young, D. S. 1991, *ApJ*, 371, 69
- . 1993, *ApJ*, 402, 95
- . 1997, *ApJ*, 490, L55
- Dennison, B., Broderick, J. J., Thomas, M., Booth, R. S., Brown, R. L., & Condon, J. J. 1984, *A&A*, 135, 199
- di Serego-Alighieri, S., Danziger, I. J., Morganti, R., & Tadhunter, C. N. 1994, *MNRAS*, 269, 998
- Dopita, M. A., & Sutherland, R. S. 1996, *ApJS*, 102, 161
- . 2003, *Astrophysics of the diffuse universe* (*Astrophysics of the diffuse universe*, Berlin, New York: Springer, 2003. Astronomy and astrophysics library, ISBN 3540433627)
- Dunlop, J. S., McLure, R. J., Kukula, M. J., Baum, S. A., O'Dea, C. P., & Hughes, D. H. 2003, *MNRAS*, 340, 1095
- Edge, D. O., Shakeshaft, J. R., McAdam, W. B., Baldwin, J. E., & Archer, S. 1959, *MmRAS*, 68, 37
- Edwards, P. G., & Tingay, S. J. 2004, *A&A*, 424, 91
- Elvis, M. 2000, *ApJ*, 545, 63
- Elvis, M., Risaliti, G., & Zamorani, G. 2002, *ApJ*, 565, L75
- Emonts, B. et al, 2006, in preparation
- Eracleous, M., & Halpern, J. P. 2004, *ApJS*, 150, 181
- Evans, A. S., Kim, D. C., Mazzarella, J. M., Scoville, N. Z., & Sanders, D. B. 1999, *ApJ*, 521, L107
- Fanaroff, B. L., & Riley, J. M. 1974, *MNRAS*, 167, 31P
- Fanti, C. 2000, in *EVN Symposium 2000, Proceedings of the 5th european VLBI Network Symposium held at Chalmers University of Technology, Gothenburg, Sweden, June 29 - July 1, 2000*, Eds.: J.E. Conway, A.G. Polatidis, R.S. Booth and Y.M. Pihlström, published by Onsala Space Observatory, p. 73
- Fanti, C., Branchesi, M., Cotton, W. D., Dallacasa, D., Fanti, R., Gregorini, L., Murgia, M., Stanghellini, C., & Vigotti, M. 2004, *A&A*, 427, 465
- Fanti, C., Fanti, R., Dallacasa, D., Schilizzi, R. T., Spencer, R. E., & Stanghellini, C. 1995, *A&A*, 302, 317
- Fanti, C., Pozzi, F., Dallacasa, D., Fanti, R., Gregorini, L., Stanghellini, C., & Vigotti, M. 2001, *A&A*, 369, 380
- Fanti, C., Pozzi, F., Fanti, R., Baum, S. A., O'Dea, C. P., Bremer, M., Dallacasa, D., Falcke, H., de Graauw, T., Marecki, A., Miley, G., Röttgering, H., Schilizzi, R. T., Snellen, I., Spencer, R. E., & Stanghellini, C. 2000, *A&A*, 358, 499
- Fanti, R., Fanti, C., Schilizzi, R. T., Spencer, R. E., Nan Rendong, Parma, P., van Breugel,

- W. J. M., & Venturi, T. 1990, *A&A*, 231, 333
- Fath, E. A. 1909, *Lick Observatory Bulletin*, 5, 71
- Ferland, G. J., Korista, K. T., Verner, D. A., Ferguson, J. W., Kingdon, J. B., & Verner, E. M. 1998, *PASP*, 110, 761
- Fey, A. L., & Charlot, P. 1997, *ApJS*, 111, 95
- Fey, A. L., Ma, C., Arias, E. F., Charlot, P., Feissel-Vernier, M., Gontier, A.-M., Jacobs, C. S., Li, J., & MacMillan, D. S. 2004, *AJ*, 127, 3587
- Fey, A. L., & Mutel, R. L. 1993, *ApJ*, 404, 197
- Fioc, M., & Rocca-Volmerange, B. 1997, *A&A*, 326, 950
- Frank, J., King, A., & Raine, D. J. 2002, *Accretion Power in Astrophysics: Third Edition (Accretion Power in Astrophysics, by Juhan Frank and Andrew King and Derek Raine, pp. 398. ISBN 0521620538. Cambridge, UK: Cambridge University Press, February 2002.)*
- Fugmann, W., Meisenheimer, K., & Roeser, H.-J. 1988, *A&AS*, 75, 173
- Gebhardt, K., Bender, R., Bower, G., Dressler, A., Faber, S. M., Filippenko, A. V., Green, R., Grillmair, C., Ho, L. C., Kormendy, J., Lauer, T. R., Magorrian, J., Pinkney, J., Richstone, D., & Tremaine, S. 2000, *ApJ*, 539, L13
- Gelderman, R., & Whittle, M. 1994, *ApJS*, 91, 491
- Ghisellini, G., & Celotti, A. 2001, *A&A*, 379, L1
- Gilmore, G., & Shaw, M. A. 1986, *Nature*, 321, 750
- Ginzburg, V. L., & Syrovatskii, S. I. 1965, *ARA&A*, 3, 297
- . 1969, *ARA&A*, 7, 375
- González Delgado, R. M., Heckman, T., & Leitherer, C. 2001, *ApJ*, 546, 845
- Gopal-Krishna, & Wiita, P. J. 2002, *New Astronomy Review*, 46, 357
- Graham, A. W., & Driver, S. P. 2005, *Publications of the Astronomical Society of Australia*, 22, 118
- Gugliucci, N. E., Taylor, G. B., Peck, A. B., & Giroletti, M. 2005, *ApJ*, 622, 136
- Heckman, T. M., Miley, G. K., van Breugel, W. J. M., & Butcher, H. R. 1981, *ApJ*, 247, 403
- Heckman, T. M., O’Dea, C. P., Baum, S. A., & Laurikainen, E. 1994, *ApJ*, 428, 65
- Heckman, T. M., Smith, E. P., Baum, S. A., van Breugel, W. J. M., Miley, G. K., Illingworth, G. D., Bothun, G. D., & Balick, B. 1986, *ApJ*, 311, 526
- Ho, L. C. 2005, *ArXiv Astrophysics e-prints*, astro-ph/0511157
- Hodges, M. W., & Mutel, R. L. 1987, in *Superluminal Radio Sources*, 168–173
- Holt, J., Tadhunter, C. N., & Morganti, R. 2003, *MNRAS*, 342, 227
- . 2005, *ArXiv Astrophysics e-prints*, astro-ph/0509129
- Hurt, T., Antonucci, R., Cohen, R., Kinney, A., & Krolik, J. 1999, *ApJ*, 514, 579
- Israel, F. P. 1998, *A&A Rev.*, 8, 237
- Jansky, K. G. 1932, *Proc. IRE*, 20, 1920
- Jauncey, D. L., King, E. A., Bignall, H. E., Lovell, J. E. J., Kedziora-Chudczer, L., Tzioumis, A. K., Tingay, S. J., Macquart, J.-P., & McCulloch, P. M. 2003, *Publications of the Astronomical Society of Australia*, 20, 151

- Jauncey, D. L., White, G. L., Batty, M. J., & Preston, R. A. 1986, *AJ*, 92, 1036
- Jeyakumar, S., Wiita, P. J., Saikia, D. J., & Hooda, J. S. 2005, *A&A*, 432, 823
- Johnston, H. M., Hunstead, R. W., Cotter, G., & Sadler, E. M. 2005, *MNRAS*, 356, 515
- Kaiser, C. R., & Alexander, P. 1997, *MNRAS*, 286, 215
- Kaiser, C. R., Dennett-Thorpe, J., & Alexander, P. 1997, *MNRAS*, 292, 723
- Kameno, S., Inoue, M., Wajima, K., Sawada-Satoh, S., & Shen, Z.-Q. 2003, *Publications of the Astronomical Society of Australia*, 20, 213
- Kauffmann, G., Heckman, T. M., Tremonti, C., Brinchmann, J., Charlot, S., White, S. D. M., Ridgway, S. E., Brinkmann, J., Fukugita, M., Hall, P. B., Ivezić, Ž., Richards, G. T., & Schneider, D. P. 2003, *MNRAS*, 346, 1055
- Kellermann, K. I. 1964, *ApJ*, 140, 969
- . 1966, *Australian Journal of Physics*, 19, 195
- Kellermann, K. I., Sramek, R., Schmidt, M., Shaffer, D. B., & Green, R. 1989, *AJ*, 98, 1195
- Kent, S. M. 1985, *PASP*, 97, 165
- Kewley, L., Dopita, M., Evans, Groves, B., Sutherland, R., Binette, Allen, M., & Leitherer, C. 2005 in prep.,
- Knapp, G. R., & Rupen, M. P. 1996, *ApJ*, 460, 271
- Koekemoer, A. M., Fruchter, A. S., Hook, R. N., & Hack, W. 2002, in *The 2002 HST Calibration Workshop : Hubble after the Installation of the ACS and the NICMOS Cooling System*, Proceedings of a Workshop held at the Space Telescope Science Institute, Baltimore, Maryland, October 17 and 18, 2002. Edited by Santiago Arribas, Anton Koekemoer, and Brad Whitmore. Baltimore, MD: Space Telescope Science Institute, 2002, p. 339
- Koekemoer, A. M., O’Dea, C. P., Sarazin, C. L., McNamara, B. R., Donahue, M., Voit, G. M., Baum, S. A., & Gallimore, J. F. 1999, *ApJ*, 525, 621
- Kondratko, P. T., Greenhill, L. J., & Moran, J. M. 2005, *ApJ*, 618, 618
- Kriss, G. 1994, in *ASP Conf. Ser. 61: Astronomical Data Analysis Software and Systems III*, 437
- Kristian, J., Sandage, A., & Katem, B. 1978, *ApJ*, 219, 803
- Krolik, J. H. 1999, *Active galactic nuclei : from the central black hole to the galactic environment* (Princeton, NJ: Princeton University Press, 1999.)
- Labiano, A., O’Dea, C. P., Gelderman, R., de Vries, W. H., Axon, D. J., Barthel, P. D., Baum, S. A., Capetti, A., Fanti, R., Koekemoer, A. M., Morganti, R., & Tadhunter, C. N. 2005, *A&A*, 436, 493
- Laing, R. A., & Bridle, A. H. 2004, *MNRAS*, 348, 1459
- Laing, R. A., Riley, J. M., & Longair, M. S. 1983, *MNRAS*, 204, 151
- Landolt, A. U. 1992, *AJ*, 104, 372
- Large, M. I., Mills, B. Y., Little, A. G., Crawford, D. F., & Sutton, J. M. 1981, *MNRAS*, 194, 693
- Lazio, T. J. W., & Fey, A. L. 2001, *ApJ*, 560, 698
- Ledlow, M. J., & Owen, F. N. 1996, *AJ*, 112, 9
- Lin, D. N. C., Pringle, J. E., & Rees, M. J. 1988, *ApJ*, 328, 103

- Lister, M. L. 2003, *ApJ*, 599, 105
- Lister, M. L., Kellermann, K. I., Vermeulen, R. C., Cohen, M. H., Zensus, J. A., & Ros, E. 2003, *ApJ*, 584, 135
- Ludke, E., Garrington, S. T., Spencer, R. E., Akujor, C. E., Muxlow, T. W. B., Sanghera, H. S., & Fanti, C. 1998, *MNRAS*, 299, 467
- Ma, C., Arias, E. F., Eubanks, T. M., Fey, A. L., Gontier, A.-M., Jacobs, C. S., Sovers, O. J., Archinal, B. A., & Charlot, P. 1998, *AJ*, 116, 516
- Magorrian, J., Tremaine, S., Richstone, D., Bender, R., Bower, G., Dressler, A., Faber, S. M., Gebhardt, K., Green, R., Grillmair, C., Kormendy, J., & Lauer, T. 1998, *AJ*, 115, 2285
- Marecki, A., Barthel, P. D., Polatidis, A., & Owsianik, I. 2003, *Publications of the Astronomical Society of Australia*, 20, 16
- Marecki, A., Thomasson, P., Mack, K. ., & Kunert-Bajraszewska, M. 2005, *ArXiv Astrophysics e-prints*, astro-ph/0510773
- Marr, J. M., Taylor, G. B., & Crawford, F. 2001, *ApJ*, 550, 160
- Martel, A. R., Baum, S. A., Sparks, W. B., Wyckoff, E., Biretta, J. A., Golombek, D., Macchetto, F. D., de Koff, S., McCarthy, P. J., & Miley, G. K. 1999, *ApJS*, 122, 81
- Martel, A. R., Sparks, W. B., Allen, M. G., Koekemoer, A. M., & Baum, S. A. 2002, *AJ*, 123, 1357
- Mathews, T. A., Bolton, J. G., Greenstein, J. L., Münch, G., & Sandage, A. R. 1961, *S&T*, 21, 148
- McCarthy, P. J., Spinrad, H., & van Breugel, W. 1995, *ApJS*, 99, 27
- McCarthy, P. J., van Breugel, W., & Kapahi, V. K. 1991, *ApJ*, 371, 478
- McCarthy, P. J., van Breugel, W., Spinrad, H., & Djorgovski, S. 1987, *ApJ*, 321, L29
- Meier, D. L. 2002, *New Astronomy Review*, 46, 247
- Mellema, G., Kurk, J. D., & Röttgering, H. J. A. 2002, *A&A*, 395, L13
- Melrose, D. B. 1996, in *IAU Symp. 175: Extragalactic Radio Sources*, 423
- Morganti, R., Killeen, N. E. B., & Tadhunter, C. N. 1993, *MNRAS*, 263, 1023
- Morganti, R., Oosterloo, T. A., Capetti, A., de Ruiter, H. R., Fanti, R., Parma, P., Tadhunter, C. N., & Wills, K. A. 2003a, *A&A*, 399, 511
- Morganti, R., Oosterloo, T. A., Tadhunter, C. N., van Moorsel, G., Killeen, N., & Wills, K. A. 2001, *MNRAS*, 323, 331
- Morganti, R., Tadhunter, C. N., Dickson, R., & Shaw, M. 1997, *A&A*, 326, 130
- Morganti, R., Tadhunter, C. N., Oosterloo, T. A., Holt, J., Tzioumis, A., & Wills, K. 2003b, *Publications of the Astronomical Society of Australia*, 20, 129
- Moy, E., & Rocca-Volmerange, B. 2002, *A&A*, 383, 46
- Murgia, M. 2003, *Publications of the Astronomical Society of Australia*, 20, 19
- Murgia, M., Fanti, C., Fanti, R., Gregorini, L., Klein, U., Mack, K.-H., & Vigotti, M. 1999, *A&A*, 345, 769
- Mutel, R. L., & Hodges, M. W. 1986, *ApJ*, 307, 472
- Mutel, R. L., Hodges, M. W., & Phillips, R. B. 1985, *ApJ*, 290, 86
- Nan, R., Schilizzi, R. T., Fanti, C., & Fanti, R. 1991, *A&A*, 252, 513

- Neff, S. G., Roberts, L., & Hutchings, J. B. 1995, *ApJS*, 99, 349
- O'Dea, C. P. 1998, *PASP*, 110, 493
- . 2002, *New Astronomy Review*, 46, 41
- O'Dea, C. P., & Baum, S. A. 1997, *AJ*, 113, 148
- O'Dea, C. P., Baum, S. A., & Gallimore, J. F. 1994, *ApJ*, 436, 669
- O'Dea, C. P., Baum, S. A., & Morris, G. B. 1990, *A&AS*, 82, 261
- O'Dea, C. P., Baum, S. A., & Stanghellini, C. 1991, *ApJ*, 380, 66
- O'Dea, C. P., de Vries, W. H., Koekemoer, A. M., Baum, S. A., Axon, D. J., Barthel, P. D., Capetti, A., Fanti, R., Gelderman, R., Morganti, R., & Tadhunter, C. N. 2003, *Publications of the Astronomical Society of Australia*, 20, 88
- O'Dea, C. P., de Vries, W. H., Koekemoer, A. M., Baum, S. A., Morganti, R., Fanti, R., Capetti, A., Tadhunter, C. N., Barthel, P. D., Axon, D. J., & Gelderman, R. 2002, *AJ*, 123, 2333
- O'Dea, C. P., De Vries, W. H., Worrall, D. M., Baum, S. A., & Koekemoer, A. 2000, *AJ*, 119, 478
- O'Dea, C. P., Gallimore, J., Stanghellini, C., Baum, S. A., & Jackson, J. M. 2005, *AJ*, 129, 610
- O'Dea, C. P., Koekemoer, A. M., Baum, S. A., Sparks, W. B., Martel, A. R., Allen, M. G., Macchetto, F. D., & Miley, G. K. 2001, *AJ*, 121, 1915
- O'Dea, C. P., Stanghellini, C., Baum, S. A., & Charlot, S. 1996a, *ApJ*, 470, 806
- O'Dea, C. P., Worrall, D. M., Baum, S. A., & Stanghellini, C. 1996b, *AJ*, 111, 92
- Oosterloo, T., Morganti, R., & Sadler, E. 1999, *Publications of the Astronomical Society of Australia*, 16, 28
- Osterbrock, D. E. 1989, *Astrophysics of gaseous nebulae and active galactic nuclei* (Research supported by the University of California, John Simon Guggenheim Memorial Foundation, University of Minnesota, et al. Mill Valley, CA, University Science Books, 1989, 422 p.)
- Owen, F. N., & Laing, R. A. 1989, *MNRAS*, 238, 357
- Owsianik, I., & Conway, J. E. 1998, *A&A*, 337, 69
- Pacholczyk, A. G. 1970, *Radio astrophysics. Nonthermal processes in galactic and extragalactic sources* (Series of Books in Astronomy and Astrophysics, San Francisco: Freeman, 1970)
- Parma, P., de Ruiter, H. R., & Cameron, R. A. 1991, *AJ*, 102, 1960
- Peck, A. B., & Taylor, G. B. 1998, *ApJ*, 502, L23
- . 2002, *New Astronomy Review*, 46, 295
- Peck, A. B., Taylor, G. B., & Conway, J. E. 1999, *ApJ*, 521, 103
- Peng, C. Y., Ho, L. C., Impey, C. D., & Rix, H.-W. 2002, *AJ*, 124, 266
- Penston, M. V., Robinson, A., Alloin, D., Appenzeller, I., Aretxaga, I., Axon, D. J., Baribaud, T., Barthel, P., Baum, S. A., Boisson, C., de Bruyn, A. G., Clavel, J., Colina, L., Dennefeld, M., Diaz, A., Dietrich, M., Durret, F., Dyson, J. E., Gondhalekar, P., van Groningen, E., Jablonka, P., Jackson, N., Kollatschny, W., Laurikainen, E., Lawrence, A., Masegosa, J., McHardy, I., Meurs, E. J. A., Miley, G., Moles, M., O'Brien, P., O'Dea, C., del Olmo, A., Pedlar, A., Perea, J., Perez, E., Perez-Fournon, I., Perry, J., Pilbratt, G., Rees, M.,

- Robson, I., Rodriguez-Pascual, P., Rodriguez Espinosa, J. M., Santos-Lleo, M., Schilizzi, R., Stasinska, G., Stirpe, G. M., Tadhunter, C., Terlevich, E., Terlevich, R., Unger, S., Vila-Vilaro, V., Vilchez, J., Wagner, S. J., Ward, M. J., & Yates, G. J. 1990, *A&A*, 236, 53
- Perlman, E. S., Stocke, J. T., Conway, J., & Reynolds, C. 2001, *AJ*, 122, 536
- Peterson, B. M., ed. 1997, *An introduction to active galactic nuclei* (Cambridge, New York: Cambridge University Press)
- Phillips, R. B., & Mutel, R. L. 1981, *ApJ*, 244, 19
- . 1982, *A&A*, 106, 21
- Pihlström, Y. M., Conway, J. E., & Vermeulen, R. C. 2003, *A&A*, 404, 871
- Polatidis, A. G., & Conway, J. E. 2003, *Publications of the Astronomical Society of Australia*, 20, 69
- Pollack, L. K., Taylor, G. B., & Zavala, R. T. 2003, *ApJ*, 589, 733
- Raimann, D., Storchi-Bergmann, T., Quintana, H., Hunstead, R., & Wisotzki, L. 2005, *MNRAS*, 1022
- Readhead, A. C. S., & Hewish, A. 1976, *MNRAS*, 176, 571
- Readhead, A. C. S., Taylor, G. B., Pearson, T. J., & Wilkinson, P. N. 1996a, *ApJ*, 460, 634
- Readhead, A. C. S., Taylor, G. B., Xu, W., Pearson, T. J., Wilkinson, P. N., & Polatidis, A. G. 1996b, *ApJ*, 460, 612
- Readhead, A. C. S., Xu, W., Pearson, T. J., Wilkinson, P. N., & Polatidis, A. G. 1994, in *Compact Extragalactic Radio Sources*, 17
- Rees, M. J. 1984, *ARA&A*, 22, 471
- . 1989, *MNRAS*, 239, 1P
- Rees, M. J., Phinney, E. S., Begelman, M. C., & Blandford, R. D. 1982, *Nature*, 295, 17
- Rengelink, R. B., Tang, Y., de Bruyn, A. G., Miley, G. K., Bremer, M. N., Roettgering, H. J. A., & Bremer, M. A. R. 1997, *A&AS*, 124, 259
- Risaliti, G., Woltjer, L., & Salvati, M. 2003, *A&A*, 401, 895
- Rossetti, A., Mantovani, F., Dallacasa, D., Fanti, C., & Fanti, R. 2005, *A&A*, 434, 449
- Salgado, J. F., Altschuler, D. R., Ghosh, T., Dennison, B. K., Mitchell, K. J., & Payne, H. E. 1999, *ApJS*, 120, 77
- Sanders, D. B., Soifer, B. T., Elias, J. H., Madore, B. F., Matthews, K., Neugebauer, G., & Scoville, N. Z. 1988, *ApJ*, 325, 74
- Sanghera, H. S., Saikia, D. J., Ludke, E., Spencer, R. E., Foulsham, P. A., Akujor, C. E., & Tzioumis, A. K. 1995, *A&A*, 295, 629
- Saxton, C. J., Bicknell, G. V., Sutherland, R. S., & Midgley, S. 2005, *MNRAS*, 359, 781
- Schlegel, D. J., Finkbeiner, D. P., & Davis, M. 1998, *ApJ*, 500, 525
- Scoville, N. Z., Evans, A. S., Thompson, R., Rieke, M., Hines, D. C., Low, F. J., Dinshaw, N., Surace, J. A., & Armus, L. 2000, *AJ*, 119, 991
- Sersic, J. L. 1963, *Boletin de la Asociacion Argentina de Astronomia La Plata Argentina*, 6, 41
- . 1968, *Atlas de galaxias australes* (Cordoba, Argentina: Observatorio Astronomico, 1968)
- Seyfert, C. K. 1943, *ApJ*, 97, 28

- Shaffer, D. B., Kellermann, K. I., & Cornwell, T. J. 1999, *ApJ*, 515, 558
- Shen, Z.-Q., Shang, L.-L., Cai, H.-B., Chen, X., Jiang, D. R., Chen, Y.-J., Liu, X., Yang, R., Kameno, S., & Hirabayashi, H. 2005, *ApJ*, 622, 811
- Shepherd, M. C. 1997, in *ASP Conf. Ser. 125: Astronomical Data Analysis Software and Systems VI*, 77
- Shields, G. A. 1999, *PASP*, 111, 661
- Siemiginowska, A., Aldcroft, T. L., Bechtold, J., Brunetti, G., Elvis, M., & Stanghellini, C. 2003, *Publications of the Astronomical Society of Australia*, 20, 113
- Siemiginowska, A., Cheung, C. C., LaMassa, S., Burke, D. J., Aldcroft, T. L., Bechtold, J., Elvis, M., & Worrall, D. M. 2005, *ApJ*, 632, 110
- Silk, J., & Rees, M. J. 1998, *A&A*, 331, L1
- Slipher, V. M. 1917, *Lowell Observatory Bulletin*, 3, 59
- Snellen, I., & Schilizzi, R. 2002, *New Astronomy Review*, 46, 61
- Snellen, I. A. G. 1997, Ph.D. Thesis, University of Leiden
- Snellen, I. A. G., Bremer, M. N., Schilizzi, R. T., Miley, G. K., & van Ojik, R. 1996, *MNRAS*, 279, 1294
- Snellen, I. A. G., Lehnert, M. D., Bremer, M. N., & Schilizzi, R. T. 2002, *MNRAS*, 337, 981  
—. 2003a, *MNRAS*, 342, 889
- Snellen, I. A. G., Mack, K.-H., Schilizzi, R. T., & Tschager, W. 2003b, *Publications of the Astronomical Society of Australia*, 20, 38
- Snellen, I. A. G., Schilizzi, R. T., Bremer, M. N., de Bruyn, A. G., Miley, G. K., Röttgering, H. J. A., McMahon, R. G., & Perez Fournon, I. 1998a, *MNRAS*, 301, 985
- Snellen, I. A. G., Schilizzi, R. T., Bremer, M. N., Miley, G. K., de Bruyn, A. G., & Röttgering, H. J. A. 1999, *MNRAS*, 307, 149
- Snellen, I. A. G., Schilizzi, R. T., de Bruyn, A. G., Miley, G. K., Rengelink, R. B., Röttgering, H. J., & Bremer, M. N. 1998b, *A&AS*, 131, 435
- Snellen, I. A. G., Schilizzi, R. T., Miley, G. K., de Bruyn, A. G., Bremer, M. N., & Röttgering, H. J. A. 2000, *MNRAS*, 319, 445
- Spergel, D. N., Verde, L., Peiris, H. V., Komatsu, E., Nolta, M. R., Bennett, C. L., Halpern, M., Hinshaw, G., Jarosik, N., Kogut, A., Limon, M., Meyer, S. S., Page, L., Tucker, G. S., Weiland, J. L., Wollack, E., & Wright, E. L. 2003, *ApJS*, 148, 175
- Spinrad, H., Marr, J., Aguilar, L., & Djorgovski, S. 1985, *PASP*, 97, 932
- Stanghellini, C. 1992, Ph.D. Thesis, University of Bologna  
—. 2003, *Publications of the Astronomical Society of Australia*, 20, 118
- Stanghellini, C., Baum, S. A., O'Dea, C. P., & Morris, G. B. 1990, *A&A*, 233, 379
- Stanghellini, C., Dallacasa, D., O'Dea, C. P., Baum, S. A., Fanti, R., & Fanti, C. 2001, *A&A*, 377, 377
- Stanghellini, C., O'Dea, C. P., Baum, S. A., Dallacasa, D., Fanti, R., & Fanti, C. 1997, *A&A*, 325, 943
- Stanghellini, C., O'Dea, C. P., Baum, S. A., & Laurikainen, E. 1993, *ApJS*, 88, 1
- Stanghellini, C., O'Dea, C. P., Dallacasa, D., Baum, S. A., Fanti, R., & Fanti, C. 1998, *A&AS*, 131, 303

- Stanghellini, C., O'Dea, C. P., Dallacasa, D., Cassaro, P., Baum, S. A., Fanti, R., & Fanti, C. 2005, *A&A*, 443, 891
- Stickel, M., Rieke, G. H., Kuehr, H., & Rieke, M. J. 1996, *ApJ*, 468, 556
- Storchi-Bergmann, T., Wilson, A. S., Mulchaey, J. S., & Binette, L. 1996, *A&A*, 312, 357
- Surace, J. A., & Sanders, D. B. 2000, *AJ*, 120, 604
- Surace, J. A., Sanders, D. B., Vacca, W. D., Veilleux, S., & Mazzarella, J. M. 1998, *ApJ*, 492, 116
- Tadhunter, C., Dickson, R., Morganti, R., Robinson, T. G., Wills, K., Villar-Martin, M., & Hughes, M. 2002, *MNRAS*, 330, 977
- Tadhunter, C., Robinson, T. G., González Delgado, R. M., Wills, K., & Morganti, R. 2005, *MNRAS*, 356, 480
- Tadhunter, C., Wills, K., Morganti, R., Oosterloo, T., & Dickson, R. 2001, *MNRAS*, 327, 227
- Tadhunter, C. N., Morganti, R., di Serego-Alighieri, S., Fosbury, R. A. E., & Danziger, I. J. 1993, *MNRAS*, 263, 999
- Tadhunter, C. N., Robinson, A., & Morganti, R. 1989, in *Extranuclear Activity in Galaxies*, 293
- Taylor, G. B., & Peck, A. B. 2003, *ApJ*, 597, 157
- Taylor, G. B., & Vermeulen, R. C. 1997, *ApJ*, 485, L9+
- Tingay, S. J., & de Kool, M. 2003, *AJ*, 126, 723
- Tingay, S. J., Jauncey, D. L., Reynolds, J. E., Tzioumis, A. K., King, E. A., Preston, R. A., Lovell, J. E. J., McCulloch, P. M., Costa, M. E., Nicolson, G., Koekemoer, A., Tornikoski, M., Kedziora-Chudczer, L., & Campbell-Wilson, D. 1997, *AJ*, 113, 2025
- Tinti, S., Dallacasa, D., de Zotti, G., Celotti, A., & Stanghellini, C. 2005, *A&A*, 432, 31
- Tinti, S., & De Zotti, G. 2005, *ArXiv Astrophysics e-prints*, astro-ph/0509439
- Tschager, W., Schilizzi, R., Röttgering, H., Snellen, I., Miley, G., & Perley, R. 2003, *Publications of the Astronomical Society of Australia*, 20, 75
- Tzioumis, A., King, E., Morganti, R., Dallacasa, D., Tadhunter, C., Fanti, C., Reynolds, J., Jauncey, D., Preston, R., McCulloch, P., Tingay, S., Edwards, P., Costa, M., Jones, D., Lovell, J., Clay, R., Meier, D., Murphy, D., Gough, R., Ferris, R., White, G., & Jones, P. 2002, *A&A*, 392, 841
- Tzioumis, A. K., King, E. A., Reynolds, J. E., Jauncey, D. L., Gough, R. G., Preston, R. A., Murphy, D. W., Tingay, S. J., Meier, D. L., Jones, D. L., Lovell, J. E. J., Edwards, P. G., McCulloch, P. M., Costa, M. E., Kedziora-Chudczer, L., Campbell-Wilson, D., Nicolson, G. D., & Quick, J. F. H. 1998, in *ASP Conf. Ser. 144: IAU Colloq. 164: Radio Emission from Galactic and Extragalactic Compact Sources*, 179
- Urry, C. M., & Padovani, P. 1995, *PASP*, 107, 803
- Véron, M. P. 1971, *A&A*, 11, 1
- Véron-Cetty, M. P., & Véron, P. 2000, *A&A Rev.*, 10, 81
- van Breugel, W., Nan, R., Schilizzi, R. T., Fanti, C., & Fanti, R. 1988, in *IAU Symp. 129: The Impact of VLBI on Astrophysics and Geophysics*, 115
- van Breugel, W. J. M., Fanti, C., Fanti, R., Stanghellini, C., Schilizzi, R. T., & Spencer, R. E.

- 1992, *A&A*, 256, 56
- van Gorkom, J. H., Knapp, G. R., Ekers, R. D., Ekers, D. D., Laing, R. A., & Polk, K. S. 1989, *AJ*, 97, 708
- van Langevelde, H. J., Pihlström, Y. M., Conway, J. E., Jaffe, W., & Schilizzi, R. T. 2000, *A&A*, 354, L45
- Veilleux, S. 2001, in *Starburst Galaxies: Near and Far*, 88
- Veilleux, S., & Osterbrock, D. E. 1987, *ApJS*, 63, 295
- Veilleux, S., Sanders, D. B., & Kim, D.-C. 1997, *ApJ*, 484, 92
- Verdoes Kleijn, G. A., Baum, S. A., de Zeeuw, P. T., & O'Dea, C. P. 1999, *AJ*, 118, 2592
- Vermeulen, R., Labiano, A., Barthel, P. D., Baum, S. A., R., B., de Vries, W. H., & O'Dea, C. P. a. 2005, accepted in *A&A*.
- Vermeulen, R. C., Pihlström, Y. M., Tschager, W., de Vries, W. H., Conway, J. E., Barthel, P. D., Baum, S. A., Braun, R., Bremer, M. N., Miley, G. K., O'Dea, C. P., Röttgering, H. J. A., Schilizzi, R. T., Snellen, I. A. G., & Taylor, G. B. 2003, *A&A*, 404, 861
- Wall, J. V., & Peacock, J. A. 1985, *MNRAS*, 216, 173
- Walsh, D. E. P., Knapp, G. R., Wrobel, J. M., & Kim, D.-W. 1989, *ApJ*, 337, 209
- White, G. L., Jauncey, D. L., Wright, A. E., Batty, M. J., Savage, A., Peterson, B. A., & Gulkis, S. 1988, *ApJ*, 327, 561
- White, R. L., & Becker, R. H. 1992, *ApJS*, 79, 331
- Whittle, M. 1985, *MNRAS*, 213, 1
- Wilkinson, P. N., Polatidis, A. G., Readhead, A. C. S., Xu, W., & Pearson, T. J. 1994, *ApJ*, 432, L87
- Wills, K. A., Morganti, R., Tadhunter, C. N., Robinson, T. G., & Villar-Martin, M. 2004, *MNRAS*, 347, 771
- Wills, K. A., Tadhunter, C. N., Robinson, T. G., & Morganti, R. 2002, *MNRAS*, 333, 211
- Wilson, A. S., Binette, L., & Storchi-Bergmann, T. 1997, *ApJ*, 482, L131
- Wilson, A. S., & Colbert, E. J. M. 1995, *ApJ*, 438, 62
- Wilson, A. S., Ward, M. J., & Haniff, C. A. 1988, *ApJ*, 334, 121
- Wolfe, A. M., & Burbidge, G. R. 1975, *ApJ*, 200, 548
- Wright, A., & Otrupcek, R. 1990, in *PKS Catalog (1990)*, 0
- Xiang, L., Stanghellini, C., Dallacasa, D., & Haiyan, Z. 2002, *A&A*, 385, 768
- Yu, Q., & Tremaine, S. 2002, *MNRAS*, 335, 965
- Zirbel, E. L., & Baum, S. A. 1995, *ApJ*, 448, 521



# List of Publications

## **Publications in refereed journals :**

*H I absorption in 3C49 and 3C268.3. Probing the environment of Compact Steep Spectrum and GHz Peaked Spectrum sources*

Labiano, A., Vermeulen, R., Barthel, P.D., O'Dea, C.P., Gallimore, J F., Baum, S.A., de Vries, W. H.

A&A. In press. Astro-ph/0510563

*Atomic hydrogen in the one-sided 'compact double' radio galaxy 2050+364*

Vermeulen, R., Labiano, A., Barthel, P.D., Baum, S.A., de Vries, W. H., O'Dea, C.P.

A&A. In press. Astro-ph/0510440

*HST/STIS low dispersion spectroscopy of three Compact Steep Spectrum sources. Evidence for jet-cloud interaction*

Labiano, A., O'Dea, C. P., Gelderman, R., de Vries, W. H., Axon, D. J., Barthel, P. D., Baum, S. A., Capetti, A., Fanti, R., Koekemoer, A. M., Morganti, R., Tadhunter, C. N., 2005 A&A, 436, 439.

*HST/STIS spectroscopy of CSS sources. Kinematics and ionization of the aligned nebulae*

Labiano, A., O'Dea, C. P., Gelderman, R., de Vries, W. H., Axon, D. J., Barthel, P. D., Baum, S. A., Capetti, A., Fanti, R., Koekemoer, A. M., Morganti, R., Tadhunter, C. N.

Publications of the Astronomical Society of Australia 2003, 20, 28.

## **Other publications :**

*Star formation in hosts of young radio galaxies*

Labiano, A., O'Dea, C.P., Barthel, P.D., de Vries, W.H., Baum, S.A.

New Astronomy Reviews. 2005. In press. Astro-ph/0512057

*Spectroscopy of CSS sources*

Labiano, A., O'Dea, C. P., Gelderman, R., de Vries, W. H., Axon, D. J., Barthel, P. D., Baum, S. A., Capetti, A., Fanti, R., Koekemoer, A. M., Morganti, R., Tadhunter, C. N.,

Highlights of Spanish Astrophysics, 2002, Volumen 3, 219.

*Radio Astronomy at the Robledo Deep Space Station*

Gómez, J. F., Garca-Miró, C., Labiano, A., Alberdi, A.

Highlights of Spanish Astrophysics, 2001, Volumen 2, 377.

*A stellar library of H and He line absorption profiles at high resolution*

Díaz, A. I., Álvarez, M., Mollá, M., Labiano, A., González Delgado, R. M., Pérez, E., Vílchez, J.M

Highlights of Spanish Astrophysics, 2001, Volumen 2, 105.

# Acknowledgements

Along my graduate life I have had the chance of meeting an incredible number of people who have supported me in one way or another.

The list is long so I will start from the beginning. Don Pepe y todos esos profesores que han aguantado a este empollón con sueños de astrónomo desde la infancia. The astronomy department in the Universidad Autónoma de Madrid, who hosted me since '96! Gracias por confiar en mi, Ángeles. El Seminario de Ciencias Planetarias de la Complutense. Gracias por acoger físicos, Paco! The priceless LAEFF family! Rosa, Enrique y Luis, que de una u otra forma me habéis animado desde el principio, y seguís haciéndolo! The 2001 and 2005 generations of *Kapteyners* who welcomed me and will see me off. I am sorry we have not had the chance to meet better. And, of course, the Space Telescope Science Institute, a dream came true on January 8, 2002.

I am particularly grateful to my supervisors Chris O'Dea and Peter Barthel. Thank you for believing in me from the beginning, your help, and especially your support and patience trying to get a scientist out of this student. Thanks also to your families for their hospitality on countless occasions!

And last but by no means least, much love to my Family and Friends. You have always been there for me, even through the worst times. I will not let you down.

My most sincere thanks to all of you.

*Álvaro Labiano Ortega*  
*Groningen, December 31, 2005*



IN MEMORIAM

**Julian Labiano Pérez**

7 de Enero, 1915 – 14 de Mayo, 2002

**Ángel Ortega Muga**

30 de Agosto, 1923 – 2 de Julio, 2005